
Cytoskeletal aspects of cellular migration

Dissertation
zur Erlangung des Grades
des Doktors der Naturwissenschaften
der Naturwissenschaftlich-Technischen Fakultät
der Universität des Saarlandes

vorgelegt von

Carsten Alexander Baltes

Saarbrücken
2024



UNIVERSITÄT
DES
SAARLANDES

Naturwissenschaftlich-Technische Fakultät

Tag des Kolloquiums:	13.03.2025
Dekan:	Prof. Dr.-Ing. Dirk Bähre
Berichterstatter:	Prof. Dr. Franziska Lautenschläger Jun.-Prof. Dr. Laura Aradilla Zapata (vertreten durch Prof. Dr. Roland Bennewitz)
Akad. Mitglied:	Dr. Jennifer Kasper
Vorsitz:	Prof. Dr. Albrecht Ott

Contents

Abstract	v
Zusammenfassung	vi
Acknowledgment	vii
1 Introduction	1
2 Background	3
2.1 Cell culture	3
2.1.1 RPE-1 cells	3
2.1.2 HL60 cells	4
2.1.3 MEF cells	5
2.1.4 CD4+ cells	5
2.1.5 Staining of cells	6
2.2 The cytoskeleton	10
2.2.1 Microtubules	11
2.2.2 Intermediate filaments	12
2.2.3 Actin	14
2.3 Actin binding compounds	15
2.3.1 Actin destabilizer	15
2.3.2 Actin stabilizer	17
2.4 Cellular migration	17
2.4.1 Mesenchymal migration	18
2.4.2 Amoeboid migration	19
2.5 Focal adhesion	20
3 Methods	23
3.1 Deep UV-micropatterning	23
3.2 PRIMO micropatterning	24
3.3 Fluorescence recovery after photobleaching	26

3.4	Pattern-based contractility screening and polyacrylamide gel	29
3.4.1	Calculation of contractile energy	30
3.5	PDMS microfabrications	31
3.6	Single cell force spectroscopy	31
4	Scientific context and aim of the thesis	35
5	Results	39
5.1	Additional data	50
6	Discussion	85
7	Outlook	89
8	Additional publications	91
	Bibliography	155
A	Protocols	169
A.1	Cell culture	169
A.1.1	Cell passaging	169
A.1.2	Cell seeding	170
A.1.3	Differentiation of HL60 cells	170
A.2	Fixation and staining of cells	171
A.2.1	PFA fixation	171
A.2.2	Phalloidin staining	171
A.2.3	Direct immunostaining (paxillin)	172
A.3	PDMS microfabrication and cell migration	172
A.4	PAA gel	174
A.4.1	Acryl-silanization of cover slips	174
A.4.2	Poly-acrylamide hydrogel	174
A.5	Micropatterning	175
A.5.1	PEG coating	175
A.5.2	Deep UV	176
A.5.3	PRIMO	177
A.6	Fluorescence recovery after photobleaching	177
A.6.1	BacMam treatment	178
A.6.2	FRAP measurement	178

Abstract

The ability of cells to migrate is essential for many cellular functions. To accomplish these, cells are equipped with a dynamic filamentous network called the cytoskeleton. Actin filaments are part of the cytoskeleton and play a crucial role in cellular migration. To date, actin stabilizing and destabilizing compounds have been used in migration assays, but little is known about how these compounds interact with the underlying mechanisms of cell migration. In this work, the effects of the actin stabilizer miuraenamide A (MiuA) on the migration parameters of cells are investigated. FRAP measurements reveal that the dynamic of actin filaments is reduced. Furthermore, MiuA increases the number of focal adhesions, while decreasing their average size. According to single cell force spectroscopy, MiuA also lowers adhesion force and energy. In contrast to these changes, pattern-based contractility screening reveals that MiuA has no effect on the contractile energy. As expected from these results, it is shown that adhesion-based migration is reduced, while non-adhesion-based migration remains unaffected. Taken together, this work unravels the relationship between actin stabilization, key migration parameters and the mode of migration displayed. This new knowledge can be used to design new compounds that specifically target adhesion-based migration while leaving other types of migration unaffected.

Zusammenfassung

Zelluläre Migration ist für viele biologische Funktionen unerlässlich. Um diese zu bewältigen, sind Zellen mit einem dynamischen Netzwerk, dem Zytoskelett, ausgestattet. Aktinfilamente sind Teil des Zytoskeletts und spielen eine entscheidende Rolle bei der Zellmigration. Bisher wurden Aktin stabilisierende und destabilisierende Verbindungen in Migrationsexperimenten verwendet, aber es ist wenig darüber bekannt, wie diese Verbindungen mit den zugrunde liegenden Mechanismen der Zellmigration interagieren. In dieser Arbeit wurden die Auswirkungen des Aktinstabilisators Miuraenamid A (MiuA) auf die Migrationsparameter von Zellen untersucht. FRAP-Messungen zeigen, dass die Dynamik der Aktinfilamente reduziert wird. Außerdem erhöht MiuA die Anzahl der fokalen Adhäsionen, während deren durchschnittliche Größe abnimmt. Laut Kraftspektroskopie einzelner Zellen führt MiuA zu geringeren Adhäsionskräften und -energien. Im Gegensatz zu diesen Veränderungen zeigten Messungen der Kontraktilität, dass MiuA keinen Einfluss auf die Kontraktionsenergie hat. Wie aus diesen Ergebnissen zu erwarten war, zeigt sich, dass die adhäsionsbasierte Migration reduziert ist, während die nicht-adhäsionsbasierte Migration unbeeinflusst bleibt. Insgesamt entschlüsselt diese Arbeit die Beziehung zwischen Aktinstabilisierung, wichtigen Migrationsparametern und der dazugehörigen Migration. Dieses Wissen kann genutzt werden, um Wirkstoffe zu entwickeln, die speziell auf die adhäsionsbasierte Migration abzielen.

Acknowledgment

I would like to express my deepest appreciation to Prof. Dr. Franziska Lautenschläger, for all her support and giving me the opportunity to work on these exciting projects. Without her help, high quality in management and inspiration this work would not have been possible.

I am also grateful that I had the opportunity to collaborate with so many excellent scientists from different research groups and countries. I want to thank Rhoda J Hawkins, Friederike Nolle, Annica Gad, and Karen Ullrich. A special thanks goes to Kathi M Kaiser, which I had the pleasure to be her supervisor during her master project.

I want to thank Lucina Kainka, Kristin Sander and Erbara Gjana for their support during my PhD and their association with some of my projects. Without their help and support, the results of this work would not have been possible.

I also want to thank all the current and also former members of the lab: Mona Grünewald, Christoph Anton, Enrique Araujo, Samhita Thalla, Lukas Schuster, Galia Bereau, Johanna Becher, Divyendu Thalla, Annalena Laurent, Gagan Sharma, Yannic Veit, Kevin Kaub. Their constant support and ability to create the perfect working environment helped me to progress even further in science and as a person.

Lastly I want to thank my family, especially my mother and stepfather, my partner Robert, and my friends Peter, Lena, Julia and Meelo. Their belief in me kept me motivated and allowed me to reach my goals.

There are so many more people that I want to express my deepest gratitude. But I dislike empty phrases. That is why I asked my dearest friends and colleagues to contribute to this work in a very special way. Each one of them designed their very own little heart (see below). So it is evident, that this work is also a collaboration between myself and all the people helping and supporting me during this time. Without any of you this work would not have been written.



List of Figures

2.1	Schematic drawing of direct and indirect immunostaining	8
2.2	Schematic of the baculovirus gene delivering mechanism.	10
2.3	Illustration of the cytoskeleton in eukaryotic cells	11
2.4	Schematic drawing of the structure of microtubules	13
2.5	Schematic drawing of the structure of intermediate filaments	13
2.6	Schematic drawing of the structure of actin	14
2.7	Actin turnover cycle	16
2.8	Schematic drawing of mesenchymal migration.	19
2.9	Schematic representation of amoeboid migration	20
2.10	Schematic illustration of a focal adhesion	22
3.1	Schematic drawing of the deep UV-micropatterning method	25
3.2	Schematic drawing of the PRIMO patterning technique	27
3.3	Schematic drawing of the FRAP process	28
3.4	Schematic drawing of the pattern-based contractility screening technique . .	29
3.5	Schematic illustration of PDMS microchannel fabrication.	32
3.6	Schematic drawing of the single cell force spectroscopy procedure.	33
4.1	Graphical abstract of my research question.	37
5.1	Position of nucleus in migrating cells	50
5.2	Additional data the manuscript “Modulation of Cellular Adhesion, Contractility, and Migration by MiuA”	83
6.1	Graphical abstract for the results	88
8.1	Cross section area and circularity of CD4+ cells	136
8.2	Plateau value and half time of CD4+ cells	136

Note: If not stated otherwise in the figure caption, the displayed figure has been drawn by myself.

List of abbreviations

FRAP = Fluorescence recovery after photobleaching

PaCS = Pattern-based contractility screening

MiuA = Miuraenamide A

PEG = Poly-L-lysine grafted polyethyleneglycol

PDMS = Polydimethylsiloxane

FA = Focal adhesion

DMSO = Dimethyl sulfoxide

ECM = Extracellular matrix

Note: Language checks and improvements have been performed using DeepL Writer Beta (2024). I reviewed and edited the content as needed and hereby take full responsibility for the content of this work.

Chapter 1

Introduction

From single-celled organisms to multicellular organisms, there are structures and mechanisms that have proven to be sufficiently effective to be transmitted from one generation of life to the next. One such mechanism is the capacity for movement. It is not only bacteria and other microbes that require the ability to move; multicellular organisms such as humans also rely on cellular migration as an essential biological process. In humans and other animals, there is a vast array of cells with diverse functions. The immune system, a complex system comprising numerous immune cells, serves to safeguard the body against pathogens that gain access to the internal milieu. To fulfill their mission, these cells must migrate through the body, navigating narrow spaces in search of bacteria, parasites, and other pathogens. Fibroblasts are another example of cells that must migrate within the body, where they build and maintain the extracellular matrix. Cell migration also occurs during embryonic development, where the cluster of cells that will form the human body must reorganize and form structures like the nervous system and organs.

The cytoskeleton is the primary structural element within cells that enables this type of movement. Although its composition differs in prokaryotes, archaea and eukaryotes, the general principle and functions are preserved. For the scope of this work I will focus on the cytoskeleton in eukaryotic cells, as the aim of my work is to understand the underlying mechanisms of cellular migration exerted by eukaryotic cells. There are three main types of proteins that form the cytoskeleton: microtubules, intermediate filaments, and actin filaments. The first are hollow cylindrical tubes that radiate from a common spot near the the cell's center and extend though the cell body. They are involved in a number of cellular processes, including cell division, migration, and signaling [1]. Additionally, they are present in cilia and flagella. Intermediate filaments constitute a family of proteins that share the characteristic of resistance to mechanical stress. Consequently, they are employed by the cell as a means of protection against such stress [2]. The final category of cytoskeletal filaments are actin filaments, also referred to as microfilaments. In eukaryotic cells, these filaments play a pivotal role in force generation. They are present in stress fibers

that traverse the cell, lamellipodia, and filopodia. Additionally, they constitute the actin cortex situated beneath the cell membrane. Their polar structure enables the attachment of motor proteins, which in turn generate contractile forces utilized in processes such as cell division, cell adhesion, and cell migration [3, 4].

Two principal modes of cellular migration have been identified: mesenchymal (adhesion-based) migration and amoeboid (non-adhesion-based) migration. A substantial body of research has been conducted on the underlying mechanisms and the role of the cytoskeleton in this process. Three primary migration parameters have been identified for both types of migration [5], yet their collective interaction with actin remains an understudied area. These three parameters are actin polymerization, cell adhesion, and cell contractility, all of which contribute to the migration mode ultimately displayed by the cell. Researchers employed actin-binding compounds, including jasplakinolide, latrunculin A, and cytochalasin D, to modulate the architecture and dynamics of actin filaments in living cells and reported their effects on cell migration [6, 7, 8]. However, the effects of these compounds on cell migration parameters were not discussed in detail, which raises the question of how the architecture and dynamics of the actin network interact with the underlying mechanisms of cell migration.

In this work I focus on the cytoskeleton and its role in cellular migration. I will specifically talk about actin, which is highly involved in the generation of forces and therefore a key component for cell migration. To provide context for the discussion, I will first give a comprehensive overview (see chapter 2) about the kind of cells I used and how I visualized their inner compartments. Further, I will speak about the cytoskeleton in more detail, with a particular focus on actin and actin-binding compounds. I will also explain the two different modes of cellular migration and what role actin plays there. Finally, I will talk about cellular adhesion and focus on focal adhesions, which are the connection between the cell's environment and the cytoskeleton. Next, I will explain the main methods I used during my work (see chapter 3) including micropatterning, microfabrication, fluorescence recovery after photobleaching (FRAP), pattern-based contractility screening (PaCS), and single-cell force spectroscopy. After this, I will present my findings in the form of publications or manuscripts, prepared for submission for publication (see chapter 5). Furthermore, I will include supplementary data that was not included in the original articles. I will then discuss the results in detail in chapter 6 and present an outlook for future experiments in chapter 7. Finally, I will show other articles in which I participated (see chapter 8) and present additional results that were not included.

Chapter 2

Background

The objective of this chapter is to present the fundamental biological concepts that were essential for the completion of my research. I will discuss the various cell types employed, the rationale behind their selection, and their suitability for specific experimental procedures. Moreover, an investigation of one of the fundamental compartments of an eukaryotic cell, the cytoskeleton, will be presented. I will examine the three main filament types: microtubules, intermediate filaments, and actin filaments. Furthermore, the structure and dynamics of actin filaments will be discussed in detail, as well as various actin-binding compounds. Finally, the role of actin in cell migration will be addressed with a focus on the two principal forms of cell migration and the mechanism of cell adhesion, particularly focal adhesions.

2.1 Cell culture

In this section I will address the various cell lines utilized during my studies, their cultivation methods, the staining techniques employed to visualize their internal structures, and the rationale behind my selection of these specific cell lines. The complete cell culturing protocol can be found in the appendix A.1.

2.1.1 RPE-1 cells

The hTERT-RPE-1 cell line is the most frequently utilized cell line in my research. These cells were created by Bodnar et al. in 1998, as they transfected the telomerase catalytic subunit into the genome of human retinal pigment epithelial (RPE) cells [9]. This transfection enabled the cell to proliferate further and overcome the limits of senescence, resulting in a stable long-lasting cell line.

However, their properties as epithelial cells remained, as well as the inner structure that comes alongside this. They form cellular junctions, including tight and adherence junctions, but are also able to perform cellular locomotion [10]. Additionally, it has been

demonstrated that they are capable of switching between modes of migration in response to environmental cues [11]. For these reasons, they are an important model in cell biology and are often used in studies about cellular migration, which is also the reason I mainly worked with them (see pages 42 and 54) or publication [12].

Here I will briefly describe the cell medium and conditions I used to culture the RPE-1 cells:

Cell Medium: Dulbecco's Modified Eagle Medium / Nutrient Mix F-12 (DMEM/F-12)
+ 10% Bovine fetal serum
+ 1% Penicillin and Streptomycin
+ 1% GlutaMAX (100x)

Temperature: 37 °C

Atmosphere: 5% CO₂

Additional: Keep cells always between 20% to 80% confluency

2.1.2 HL60 cells

The HL60 cell line was derived from a patient with myeloid leukemia in 1977, which is reflected in its designation as the human leukemia cell line [13]. These cells retain the capacity for differentiation, rendering them useful in numerous investigations pertaining to the immune system. They can be differentiated into neutrophils, macrophages, and other cell types [14]. For my work, I used this property and differentiated HL60 cells into neutrophils, by culturing them in DMSO for 2 days. Once differentiated into neutrophils, the cells were employed primarily for amoeboid migration experiments, as detailed in the included manuscript on page 54. They are suitable as a model organism for this as their mechanism of migration is mostly driven by contraction and friction, the two driving forces behind amoeboid migration [15] (for amoeboid migration see section 2.4.2).

As the differentiated neutrophils were used only once for the experiments and subsequently discarded, a brief overview of the compounds and environment used for culturing the undifferentiated HL60 cells is provided herewith. After differentiation, neutrophils were maintained in the same environment and cell medium until disposal.

Cell Medium: Roswell Park Memorial Institute (RPMI) 1640
+ 10% Bovine fetal serum
+ 1% Penicillin and Streptomycin
+ 1% GlutaMAX (100x)

Temperature: 37 °C

Atmosphere: 5% CO₂

Additional: Since HL60 cells are non-adherent, replace half of the medium with fresh medium every two to three days.

2.1.3 MEF cells

Mouse embryonic fibroblasts (MEF) were isolated in the early 1960's and similar to the aforementioned RPE-1 cells immortalized [16, 17]. Since then, they were part of many studies, investigating cell division, migration, and cancer, but have also been used as feeder cells for other types of cells [18, 19].

During my work I mainly used them as a role model for mesenchymal or adhesion-based migration (for mesenchymal migration see section 2.4.1). I also used them to study the influence of the actin stabilizer miuraenamides A (see section 2.3) on the size and number of focal adhesions as well as the impact of miuraenamides A on their migration behavior (see pages 42 and 54).

For cultivating MEF cells, I chose the following cell medium and culture environment:

Cell Medium: Dulbecco's Modified Eagle Medium / Nutrient Mix F-12
+ 10% Bovine fetal serum
+ 1% Penicillin and Streptomycin
+ 1% GlutaMAX (100x)

Temperature: 37 °C

Atmosphere: 5% CO₂

Additional: Keep cells always between 20% to 80% confluency

2.1.4 CD4+ cells

CD4+ (cluster of differentiation 4 plus) cells have their origin in the thymus and are part of the immune system [20]. Inside the thymus they are subjected to a series of positive and negative selection processes, which serve to guarantee that the resulting mature CD4+ cells will not exert any detrimental effects on the body. Upon successful maturation, they divide into helper T lymphocytes or regulatory T lymphocytes [20].

During the course of my studies, I received murine CD4+ cells from Karen A.M. Ullrich (Erlangen University) that had been extracted from living mice. The cells have been genetically modified to knock out interleukin 3 or interleukin 3 receptor expression. The aim of this was to ascertain whether this depletion has an impact on the actin network structure or dynamics. To this end, phalloidin staining and FRAP measurements were performed (see page 121 or publication [21] for the results). As the cells did not proliferate any further, the following list of items was used to prepare them before using them in an experiment.

Cell Medium: Roswell Park Memorial Institute (RPMI) 1640
+ 10% Bovine fetal serum
+ 1% Penicillin and Streptomycin
+ 1% GlutaMAX (100x)

Temperature: 37°C

Atmosphere: 5% CO₂

2.1.5 Staining of cells

In order to observe the internal structures of cells, including their organelles, cytoskeleton, and other components, it is necessary to utilize a visualization technique. One straightforward method for achieving this is through the use of microscopes, which serve to enhance the spatial resolution of the human eye. Unfortunately, the refractive index of the majority of cellular components is similar, which presents a challenge in distinguishing between different structures within the cell. To address this challenge, a range of techniques have been developed, including phase contrast microscopy, which does not necessitate additional sample processing. This method is inadequate for observing the finest structures inside the cell, which is why staining methods are employed to highlight proteins, structures, or organelles of interest with a specific dye. These can be observed under a bright field microscope (such as hematoxylin or eosin, used in histology) or fluorescent dyes that require external activation before emitting light at a certain wavelength.

In this work, I will focus on fluorescent dye-based staining methods. The following section will describe the various staining techniques employed in my work, and their underlying principles. The above mentioned staining techniques are: Immunostaining, DAPI and Hoechts, LifeAct, and BacMam technology.

Immunostaining

A common technique employed in cell biology for the localization and quantification of proteins involves the use of antibodies, which are linked to a fluorophore, hence the designation “immunostaining”. Antibodies are small proteins that possess a binding region and two distinct domains. Two types of immunostaining can be distinguished: direct and indirect [22]. In the direct method of immunostaining, fluorescently labeled antibodies that are specific to the protein of interest are employed. Once the antibodies have been attached to their respective proteins, it is possible to localize them through the use of fluorescence microscopy. The indirect method is based on the same principle, with the addition of a second set of antibodies. In this approach, the protein of interest is initially linked to an antibody devoid of a fluorophore (termed the primary antibody). Subsequently, a second antibody, specific to the primary antibody (termed the secondary antibody), binds. The labeling of the secondary antibody with a fluorescent dye then permits the localization of

the protein of interest to be achieved by fluorescence microscopy in a manner analogous to the aforementioned method. A diagrammatic representation of these two approaches can be seen in Figure 2.1.

The reason this technique works is due to the structure of the antibodies themselves. Antibodies used in immunostaining poses a “Y” shape consisting of two heavy and two light polypeptide chains that are linked by disulfide bonds [23]. This structure gives rise to a variable “Fab” region at the top of the “Y” shape and a constant “Fc” region at the tail [24]. Through adaptation of these regions, one can create a primary antibody, who’s Fab region binds to the protein of interest and a Fc region that is then recognized by the Fab region of a secondary antibody.

During the course of my research, I primarily employed direct antibody staining, utilizing anti-paxillin antibodies conjugated to green fluorescent protein (GFP), to quantify the size and number of focal adhesions in RPE-1 cells. The specific protocol I utilized is outlined in the Appendix A.

DAPI and Hoechst

The nucleus is one of the most prominent structures in eukaryotic cells and can take up to around 8% of the cell volume [25]. The nucleus is the site of the majority of the cell’s DNA and is encased in a double-layered membrane. Given its pivotal role in cellular function, the nucleus has long been a focal point for researchers. Its size and visibility under phase contrast microscopy facilitate the localization and tracking of overall cellular movement. To advance this into fluorescence microscopy, the two compounds utilized in my research were DAPI (4’,6-diamidino-2-phenylindole) and Hoechst (bis-benzimidazoles).

DAPI binds to the minor groove of the DNA double helix at adenine and thymine-rich regions [26] where it then undergoes a conformational change by quenching that unfolds DAPI’s fluorescent properties [27]. The molecule emits light in the blue spectrum at a maximum at 453 nm, while being mostly activated with a wavelength of 340 nm [28]. Although DAPI can enter living cells, the concentration of DAPI that is required for this makes it an unusual compound for live cell experiments [29]. Consequently, I only used DAPI in samples that had already undergone fixation (see chapter 5).

The second compound, which I mostly used for live cell imaging, i.e. tracking migrating cells (see chapter 5), is Hoechst. Similarly, to DAPI, this compound can traverse the cell membrane, albeit at a lower concentration [29]. It also targets the nucleus’ DNA and shows its fluorescent properties upon binding to the DNA, being activated at around 360 nm while emitting light at a maximum at 460 nm [30].

Although both dyes are activated with UV-light, which comes with cytotoxic effects, I only considered these while working with Hoechst, as I only used DAPI in fixed samples. This is especially important for time lapse experiments where cells are repeatedly exposed to high-energy-light.

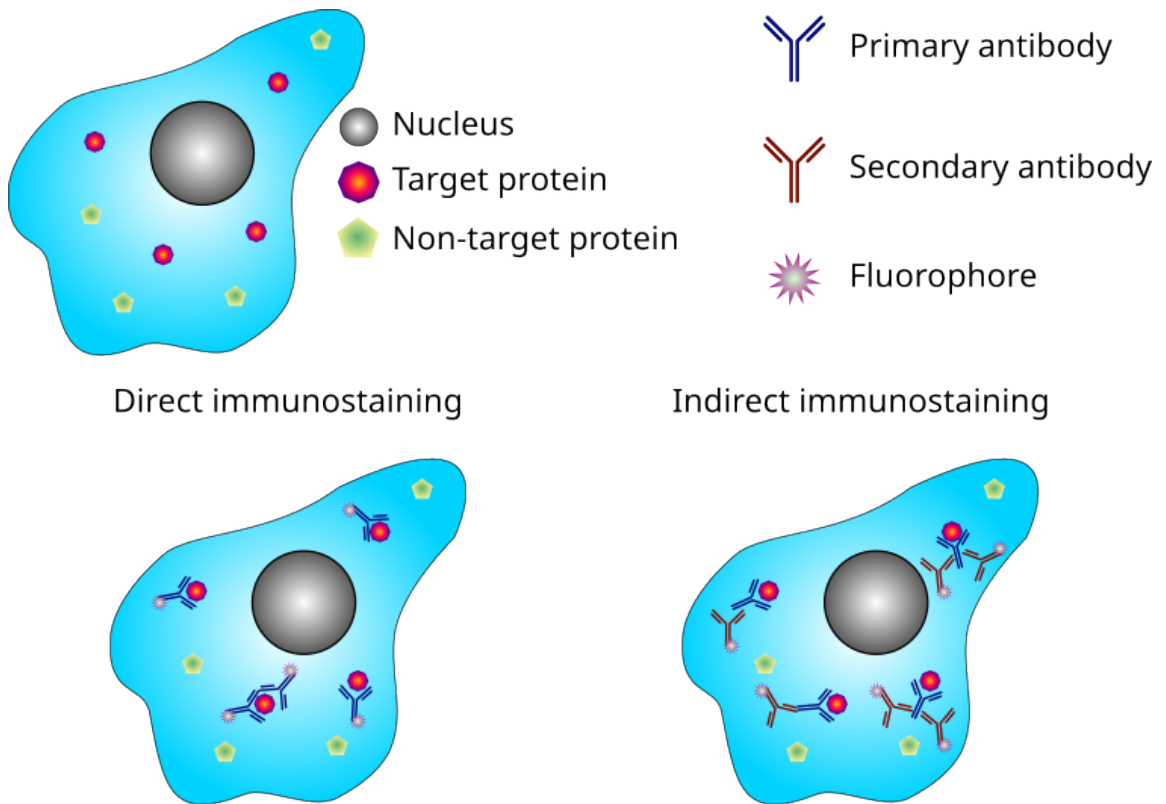


Figure 2.1: Schematic drawing of direct and indirect immunostaining. Direct immunostaining (left): Primary antibodies are linked to fluorophore and bind to their respective target proteins. Indirect immunostaining (right): Primary antibodies without fluorophores bind to their target protein. Afterwards, secondary proteins linked to a fluorophore can bind to the primary antibodies.

LifeAct

Given its high abundance, actin has been a frequent target for staining methods. However, as the aforementioned immunostaining methodology is largely applicable to fixed samples that no longer exhibit biological activity, researchers were motivated to develop a method for visualizing actin in living cells. One may utilize fluorescently labeled actin-binding compounds, such as phalloidin or jasplakinolide, which bind to F-actin and, thus, permit the localization of actin within the cell [31]. These compounds, however, also impact the architecture and dynamics of the actin network, rendering them unable to precisely display the wild-type actin network [32].

Another F-actin binding compound is called “LifeAct”, which is a 17 amino acid peptide that has first been described by Julia Riedl et al. in 2008 [33]. It derives from the actin-binding-protein 140 (Abp140), which is expressed in yeast cells (*Saccharomyces cerevisiae*) and is said to have little to no effects on the dynamics of the actin network [32]. However, this assertion has been challenged by Courtemacher et al. (2016), who demonstrated concentration-dependent effects of LifeAct on actin filaments in vitro [34]. These effects include the inhibition and promotion of actin depolymerization via cofilin depending on the used concentration of LifeAct-mCherry. Since many of my experiments were conducted using hTERT RPE-1 LifeAct-mCherry cells (see section 2.1.1), it was essential to consider these findings and ensure that a suitable control experiment was always conducted when modifying the actin network architecture and dynamics.

BacMam technology

The BacMam system has the capacity to transfect mammalian cells, a process first described by Boyce et al. in 1996 [35]. The general mechanism is illustrated in Figure 2.2. The baculovirus gains entry to the cell via endocytosis, whereupon it releases its DNA. Subsequently, the vector DNA is transported to the nucleus, where it is transcribed into mRNA. The resulting mRNA then leaves the nucleus and is translated into a functional protein. For fluorescence recovery after photobleaching (FRAP) measurements of actin filaments, fluorescent G-actin monomers are required. The BacMam system allowed me to employ a G-actin-GFP fused protein vector, consequently allowing the measurement of fluorescence levels of actin filaments in RPE-1 cells (see chapter 5 page 42) and CD4+ T-cells (see chapter 8 page 121).

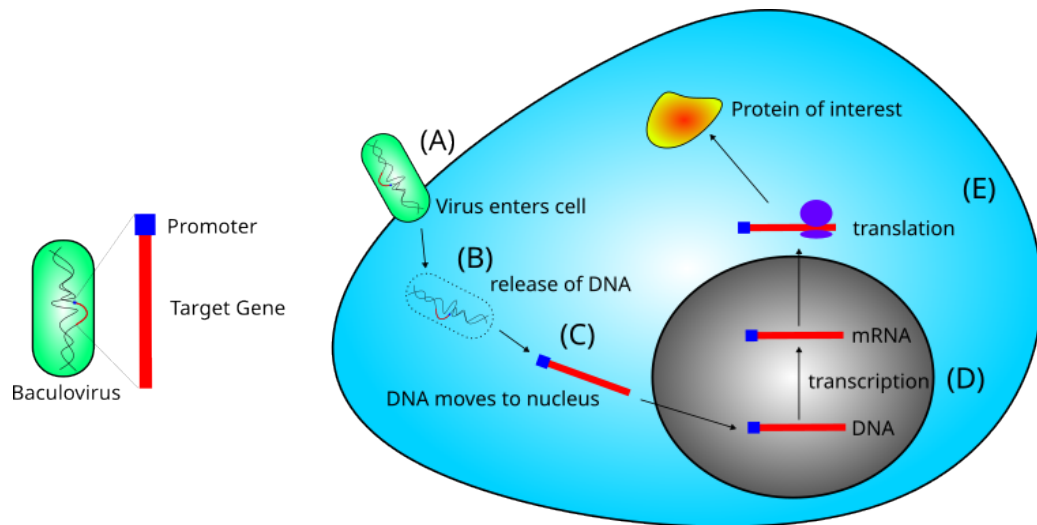


Figure 2.2: Schematic of the baculovirus gene delivering mechanism. After the baculovirus enters the cell (A), the target gene is released (B) and transported to the nucleus (C). There, it is being transcribed from DNA to mRNA (D). The mRNA then leaves the nucleus and ribosomes begin translating the mRNA into the desired protein (E).

2.2 The cytoskeleton

One important target for the above mentioned staining techniques is the cytoskeleton. The cytoskeleton is a filamentous network that is present within the majority of eukaryotic cells. It is comprised of three principal components, which can be observed in Figure 2.3:

- Microtubules are hollow cylindrical tubes that originate from the center of the cell and extend to the cell's periphery.
- Intermediate filaments constitute a family of proteins that form mechanical-resistant filaments, thereby protecting the nucleus and avoiding damage caused by mechanical stress.
- Microfilaments (also referred to as actin filaments) constitute a network that is primarily situated at the cell membrane and within fibers that traverse the cell.

Cells are capable of performing a vast array of tasks and functions. In order to fulfill these tasks, cells must be capable of movement, growth, division, search, coordination of internal processes, and a multitude of other functions. Moreover, cells are responsive to external stimuli, including stress, mechanical forces, and chemical signals. The cytoskeleton plays a pivotal role in facilitating these processes to occur.

The following section will provide a detailed account of the various cytoskeleton filaments,

explaining their structural characteristics and the processes in which they are involved. Given that actin is the protein with which I have been most concerned with during the course of my research, I have included a supplementary section in which I discuss the various compounds that interact with it (see section 2.3).

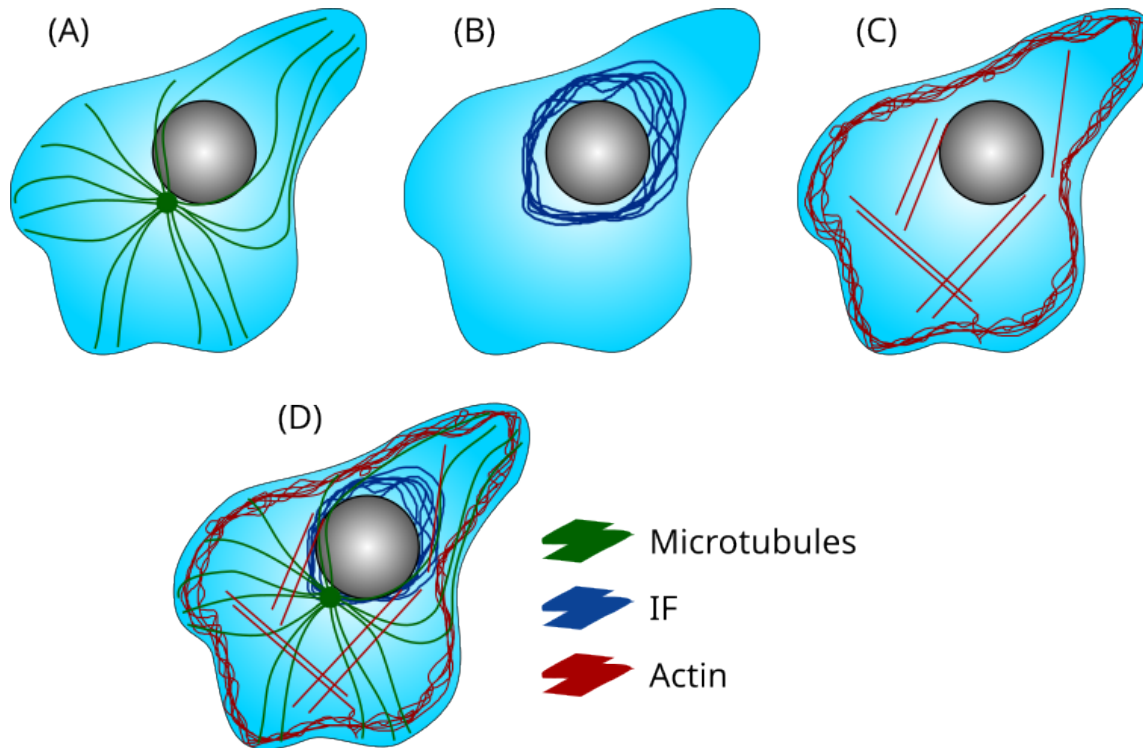


Figure 2.3: Illustration of the cytoskeleton on eukaryotic cells. (A) Microtubules. (B) Intermediate filaments. (C) Actin. (D) Merge.

2.2.1 Microtubules

Microtubules are the largest and most rigid type of filaments within the cytoskeleton. They are composed of heterodimers that are arranged in a hollow cylinder with a diameter of 25 nm[2]. Each heterodimer contains a pair of α and β tubulin monomers. These heterodimers are stacked on top of each other to form a protofilament, which then arrange laterally to create the cylindrical structure. This cylindrical structure is formed from 13 protofilaments [1]. A sketch describing the formation of microtubules from the heterodimers to the filament can be seen in Figure 2.4. Due to the asymmetrical structure of the tubulin heterodimers, microtubules themselves inherit this asymmetry, leading to their polar properties. This polarity allows one to define so called “plus” and “minus” ends. The first of

these is a fast-growing end that exposes β tubulin, while the second one exposes α tubulin, resulting in a slow-growing end. Furthermore, the polarity of microtubules allows motor proteins like kinesins and dyneins to bind to microtubules and operate a traffic system inside the cell, whereby cargo is transported alongside the microtubules.

Despite their rigid structure and high persistence length, microtubules are highly dynamic. They periodically engage in phases of growth and shrinkage. Typically, the exposed β tubulin at the plus end of a microtubule is bound to GTP (guanosine triphosphate), which over time hydrolyzes to GDP (guanosine diphosphate). This results in a conformational change and therefore a weakening of the bonds inside the lateral structure [1], which eventually leads to the disassembly of the microtubule starting from the plus end. This rapid shrinkage of the filament is called “catastrophe”, and the reversion of this phase, where the shrinkage stops and the microtubule can grow again is called “rescue”.

In addition to the aforementioned α and β tubulin, there are other isoforms that will be described briefly:

- γ tubulin.
Like α and β tubulin, γ tubulin can be found in any eukaryotic organism. This kind of tubulin is found at the nucleation site of microtubules, where it initializes the polymerization process.
- δ , ϵ and ζ tubulin.
Unlike the other types of tubulin mentioned above, these three are only present in specific organism. There they are found in flagella, cilia and basal bodies, which highlights the role of microtubules in cellular movement.

In essence, the network of microtubules is present throughout the entire cell, can be incorporated into protrusions like cilia and flagella, has a polar structure, and is highly dynamic. These properties allow microtubules to be involved in several cellular tasks like cell division, internal trafficking and cellular movement.

For cell division the microtubule network forms the so-called mitotic spindle and separates the chromosomes [36]. In cell migration, the polarization of the microtubule network works as a orientation axis for the direction of migration. Together with the regulation of internal traffic they are an essential part of cell migration and hold great importance for the ability of the cell to migrate in a persistent manner [37].

2.2.2 Intermediate filaments

The term “Intermediate filaments” (IF) describes a whole family of different proteins that place themselves in size between microtubules and actin filaments. In humans there are more than 65 known members of this category [38] that determine the mechanical properties of their respective cells. The most common types of intermediate filaments are vimentin and keratin. They are target for several studies for their ubiquitous occurrence that allows

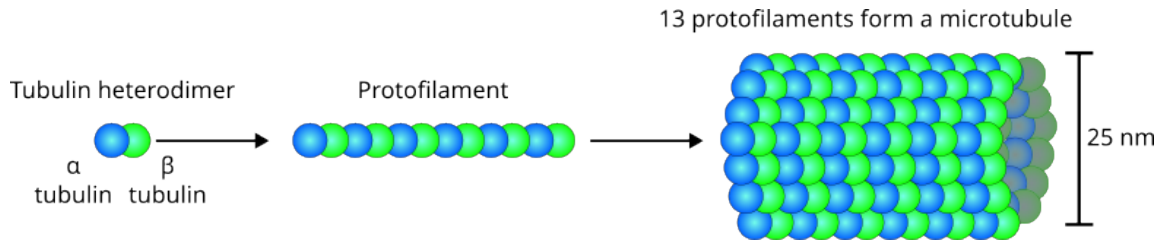


Figure 2.4: Schematic drawing of the structure of microtubules. α and β tubulin monomers form dimers, which form protofilaments. 13 of these protofilaments form a microtubule.

researchers to explore the general biophysical concept of this type of filaments. Despite the considerable diversity among the proteins comprising the intermediate filament family, they share a fundamental structure and assemble similarly. An IF monomer consists of a coiled-coil α -helix rod domain with intervening linkers. The N- and C-terminal head- and tail-domains are located at the extremities of the rod like structure [39]. Two monomers then associate to form an IF dimer [2]. Two of these dimers then form a tetramer together, which, due to the antiparallel orientation of the dimers, is now unpolar and has a size about 10 nm [39]. The formation of a protofilament, composed of eight tetramers, represents a crucial step in the formation of a fully functional intermediate filament. Figure 2.5 illustrates the steps of IF assembly from monomer to filament.

IFs serve a protective function for cells and their internal structures, including the prevention of mechanical stress. This underscores the importance of maintaining IF integrity for tissue integrity. However, since there are few pharmaceutical compounds that can inhibit them or alter their architecture and dynamics, diseases that correlate with mutated IFs have yet to be treated effectively, as evidenced by the lack of available treatments to date [2].

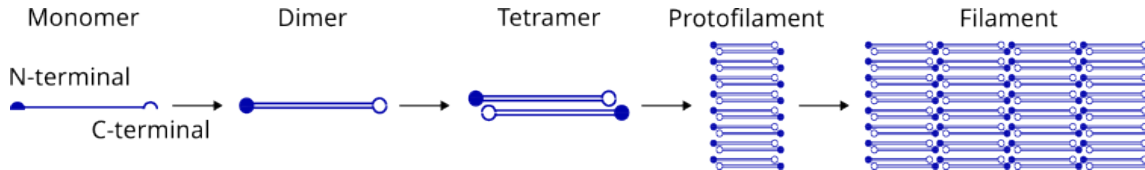


Figure 2.5: Schematic drawing of the structure of intermediate filaments. Two monomers align parallel forming a dimer. Two dimers afterwards align antiparallel to form a tetramer. Eight tetramers together form a protofilament which can then form a complete intermediate filament.

2.2.3 Actin

Actin is one of the three major proteins that form filaments inside eukaryotic cells and is also highly conserved in prokaryotes and archaea [3]. The protein contains a central cleft where ATP is bound and assimilates into a right-handed helical filament that consists of two actin strands, and reaches a diameter of approximately 6 nm [2]. A schematic representation of this can be seen in Figure 2.6. The polarity of the actin subunit (called globular actin or G-actin) results in the filament being polar as well. This enables motor proteins like myosin II to act on actin filaments in a manner analogous to kinesin and dynein on microtubules. Similarly to microtubules, the two ends of actin have different polymerization characteristics, resulting in a rapid growing “+” end and a shrinking “-” end. In contrast to microtubules, actin filaments do not originate from a single nucleation site within the cell; rather they are distributed throughout the cell. They are present in structures such as stress fibers and the actin cortex.

It is this versatility that allows actin to participate in many cellular processes. In cell adhesion, actin plays a role in the formation of focal adhesions which serve to anchor the cell to its surrounding environment. Together with motor proteins like myosin II, actin is also capable of generating contractile forces and creating a retrograde flow of actin monomers inside the cell. For cell migration these adhesion and contraction effects are essential. Furthermore, during cell division the separation of a cell into two cells finalized through a contractile ring of actin, which divides the cell into two after the mitotic spindle has segregated the chromosomes [40].

As the primary cytoskeletal filament I studied, actin will be the main topic for the following sections. There I will explain the mechanisms of its polymerization, its role in the formation of intracellular structures, and the involvement and effects of other proteins (see section 2.3). Additionally, I will address cell mechanics, specifically cell migration (see section 2.4) and cell adhesion (see section 2.5), and the function of actin in these processes.

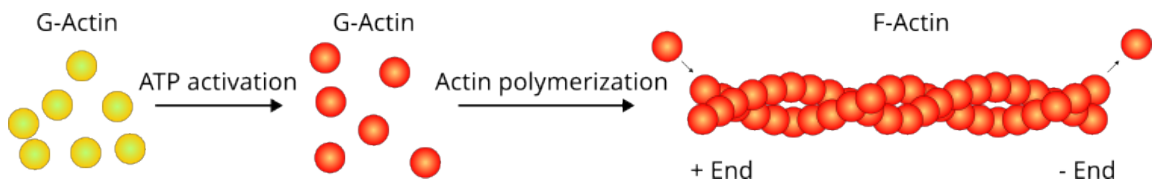


Figure 2.6: Schematic drawing of the structure of actin. ADP bound G-actin monomers get activated via ADP-ATP phosphorylation. ATP bound G-actin monomers form F-actin filaments which have a fast growing + End and a depolymerizing - End.

2.3 Actin binding compounds

Actin is a crucial protein involved in the generation of force within living cells. To fulfill this function, a multitude of proteins and other small molecules interact with actin and its various states.

In order to gain deeper understanding of these compounds I will start explaining the actin turnover cycle with regard to the cell's reservoir of ADP-bound G-actin monomers. These monomers get activated by phosphorylation into ATP-bound G-actin, from where nucleation starts. This nucleation can either be spontaneous or induced by nucleation factors like formin, resulting in actin filaments composed of F-actin. These filaments can be branched by Arp2/3 or further elongated by formin, thereby constructing an actin network throughout the entire cell. Additionally, there are capping proteins that prevent actin filaments from growing. To recycle actin monomers and refill the G-actin reservoir, actin depolymerization factors, such as cofilin, are responsible for the disassembly of actin filaments. As the ATP is dephosphorylated over time cofilin detects these changes and severs actin filaments to restore the pool of ADP-bound G-actin monomers, thereby initiating a new turnover cycle [4]. A schematic representation of this turnover cycle can be seen in Figure 2.7.

Since it is my aim to study the effects of the length of actin filaments on their migration behavior, I will now focus on actin destabilizing and stabilizing compounds. In the following sections, I will therefore discuss the origin and mechanism of the actin destabilizer latrunculin A, and the actin stabilizers phalloidin, jasplakinolide and miuraenamidine A in detail.

2.3.1 Actin destabilizer

The effects of actin depolymerizing molecules have been part of numerous studies. Although there are a lot of derivatives, for this work I will focus specifically on latrunculin A, as it has been proven a reliable compound to study the effects of a depolymerized actin network on cellular migration [2]. Additionally, I used it myself (see chapter 5), which is why I explain it in more detail.

Latrunculin A is a toxin derived from the sea sponge *latruncula magnifica* in the Red Sea. Its isolation and initial characterization were reported by Spector et al. [41] and Kashman et al. [42] in the 1980's. It is known to inhibit the polymerization of actin filaments in living cells, even at low concentrations [43]. Latrunculin A exerts its effect on actin monomers, impeding their polymerization. This results in the separation of actin filaments from their reservoir of new actin monomers without affecting the depolymerization of actin filaments via ADF/cofilin [44]. The actin destabilizing property of latrunculin A has been employed in several studies investigating biological tasks like cancer cell invasion and cell migration. In 2008 Sayed et al. showed that low dosages of latrunculin A (500nM) were sufficient to reduce cell migration in PC-3M-CT+ spheroids and suppressing activation of T47D breast

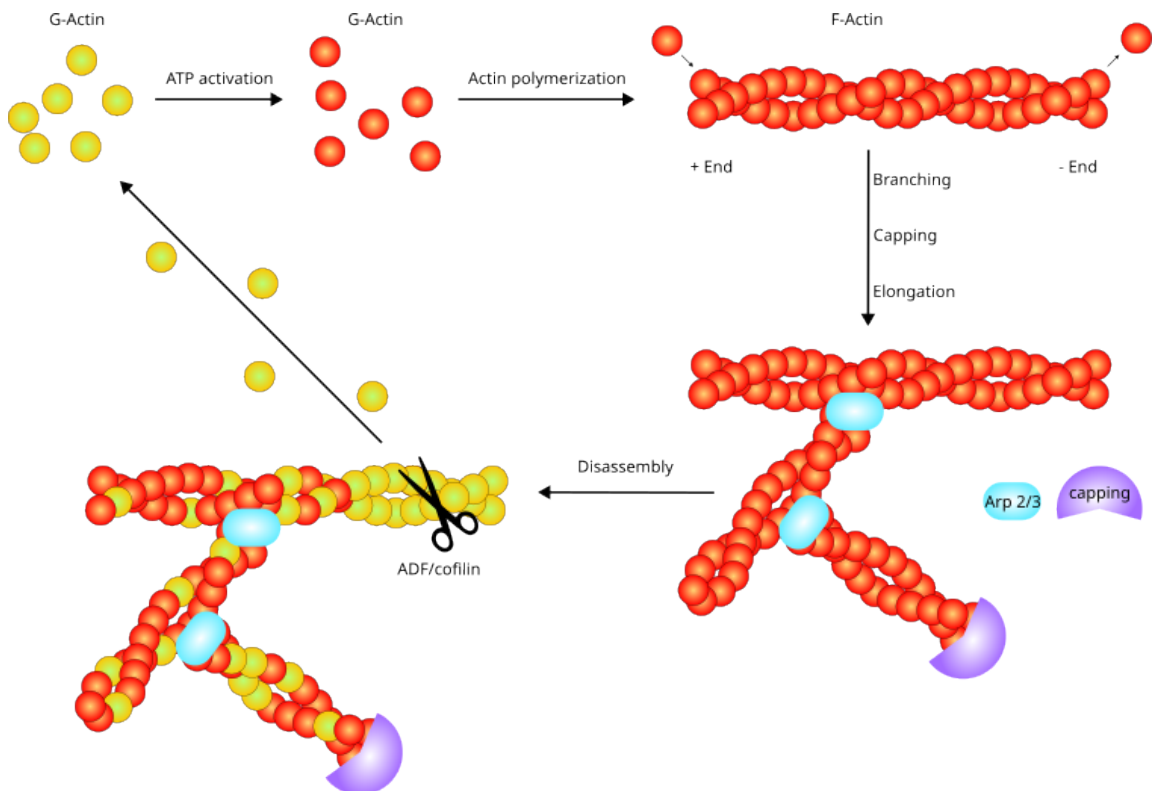


Figure 2.7: Actin turnover cycle. ADP bound G-actin starts polymerizing after activation via phosphorylation. Other actin binding molecules like Arp 2/3 or capping proteins further build up the actin network. Over time ATP is dephosphorylated and actin severing proteins like cofilin disassemble the actin network, thus restoring the G-actin pool and starting the turnover cycle again.

tumor cells [45]. Furthermore, Rekawitz et al. showed that latrunculin A can be used to regulate the chemotactic behavior in dendritic cells, enabling them to switch between adhesion-based and adhesion-independent movement [46].

2.3.2 Actin stabilizer

The stabilization of actin filaments in living cells has been a significant challenge for a long time. The most prominent actin stabilizer phalloidin is unable to enter living cells and is therefore unsuitable for live cell experiments [47]. Phalloidin is the toxin of the death cap mushroom (*amanita phalloides*) and stabilizes F-actin, thus preventing the disassembly of actin filaments. This effect is achieved by preventing the hydrolysis of ATP to ADP, which consequently reduces the dissociation rate of actin monomers from the filament [32]. Given these characteristics, phalloidin is also used in actin staining. For this a fluorophore is linked to phalloidin, which then binds to F-actin, eventually allowing researchers to visualize and localize F-actin in cells. My protocol for phalloidin staining can be seen in appendix A.

Another common actin stabilizer, jasplakinolide, is derived from marine sponges and has a comparable effect on actin filaments to that of phalloidin, as it similarly decreases the dissociation rate of actin monomers in F-actin [32]. In contrast to phalloidin, jasplakinolide is capable of entering living cells, which renders it suitable for use in live cell experiments [2]. Cramer et al. [7] used Jasplakinolide on fibroblasts and observed an increase in cell body and filopodia movement, while Ali et al. observed the opposite behavior in MDA-MB-231 cells stating that their migration speed decreases significantly [6]. Additionally Ou et al. [8] reported that varying dosages of jasplakinolide as well as varying exposure times lead to a depolymerizing effect of jasplakinolide, which is contrary to the desired stabilizing effect of actin filaments in living cells. For these reasons the usage of jasplakinolide is remains a topic of debate and necessitates further investigation.

The actin stabilizer I am going to focus on in this work is miuraenamide A as a new reliable actin stabilizer in living cells. This compound was initially isolated from a marine sponge in 2006 by Iizuka et al. [48] and subsequently synthesized by Karmann et al. in 2015 [49]. Similar to jasplakinolide, miuraenamide A can enter living cells and stabilizes actin filaments. However, unlike jasplakinolide, it does not compete with phalloidin for binding to F-actin [47]. Instead, it binds to F-actin, inducing a conformational shift that blocks the binding site of cofilin, eventually hindering cofilin from binding and therefore elongating and stabilizing actin filaments in living cells [50]. The effects of the actin stabilizer miuraenamide A are demonstrated and discussed in this work in chapter 5.

2.4 Cellular migration

A fundamental cellular process is the capacity of cells to perform locomotion, or migration. This mechanism is used in several cellular tasks and thus plays a crucial role in the

survival of multicellular organisms. Macrophages search for pathogens, fibroblasts build the extracellular matrix and maintain it, during embryonic development cells need to rearrange themselves to induce tissue formation, wounds need to be closed for which cells need to move towards each other, and so on. During their migration, cells also encounter a vast array of different tissues and environments, with varying geometries and stiffness. To adapt to these surroundings, cells possess the capacity to propel themselves forward in different ways. The two most prominent are mesenchymal and amoeboid migration. In the following I explain in more detail the mechanisms underlying these two migration modes, the role of actin within them, and the methods used to study them.

2.4.1 Mesenchymal migration

Mesenchymal migration, also known as adhesion-based migration, is one of the two modes of cell movement. This mode of migration is distinguished by its relatively slow speed, estimated at approximately $1 \mu\text{m min}^{-1}$ and the observation that cells are weakly polarized during this process [51]. The underlying mechanism of this mode of migration is the capacity of cells to adhere to their surrounding environment, utilizing these connections to pull themselves forward. For this, the cell first generates an actin-based lamellipodium, which allows actin filaments to extend even further, forming the filopodia. The side on which this structure forms is typically referred to as the leading edge. However, it is important to note that due to the initial low polarization, there might be more than one lamellipodium forming initially [51]. Focal adhesion points are created to anchor the cell to the surrounding extracellular matrix by connecting the ECM to the cytoskeleton (for more details on focal adhesions, see section 2.5). Including molecular motors like myosin II allows the cell to exert forces, propelling itself forward. Simultaneously at the rear end, which is situated on the opposite side from the leading edge, these focal adhesion points must be degraded in order to permit the cell to detach from the extracellular matrix. This process of forming new and removing old focal adhesion points eventually results in a net forward movement of the cell, as is illustrated in Figure 2.8.

Since mesenchymal migration is an adhesion based mode of migration, researchers study this cell task by creating adhesive environments for cells to migrate. This can be done in either dimension with the following exemplary approaches:

- 1D Linear tracks of e.g. fibronectin on which cells can only migrate forwards or backwards.
- 2D A coated surface (e.g. coated in fibronectin) allows cells to attach and freely move in the x-y-plane.
- 3D Cells are placed inside a gel mimicking the extracellular matrix and are able to move in any direction. Depending on the type of cells they might express a combination of different migration modes.

During my work, I mainly placed RPE-1 and MEF cells either on fibronectin coated tracks (1D migration) or let them freely migrate on a fibronectin coated glass surface (2D migration). The results of these experiments can be seen in chapter 5.

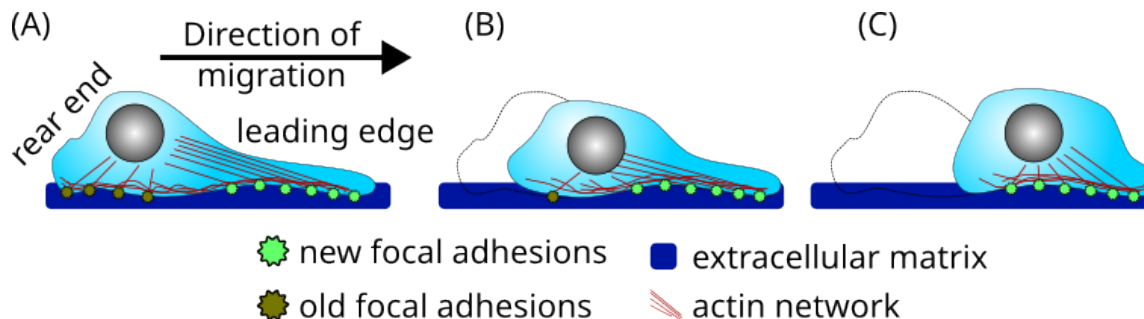


Figure 2.8: Schematic drawing of mesenchymal migration. (A) The cell body formed a leading edge where new focal adhesions are built. (B) Old focal adhesions are being degraded so the rear end starts to retract. (C) The cell body moved forwards to the position of the new focal adhesions and a new leading edge forms to repeat the cycle.

2.4.2 Amoeboid migration

In contrast to mesenchymal migration, amoeboid migration does not depend on adhesion but rather on friction, hence the alternative name friction-based migration. In this process, cells must have a high level of polarization. Given the absence of a physical attachment between the extracellular matrix and the cell, this migration is rapid with speeds reaching approximately $10 \mu\text{m s}^{-1}$ [51]. Amoeboid cell migration requires the presence of confinement or the capacity to exert forces against the external environment, thereby creating friction. This mode of migration can be compared to a climber that tries to ascend a chimney by pressing itself against the surrounding walls [11].

In amoeboid migration, the interplay between the actin network inside the cell and motor proteins like myosin II are responsible for the forward movement. Myosin II contracts the actin network, thereby creating a retrograde flow of actin that results in a higher concentration of actin at the rear of the migrating cell. This leads to a higher pressure in the back of the cell that eventually impacts the polymerization of actin and the friction the cell exerts to the environment [52] and alters the friction coefficient. In summary, elevated pressure levels impede the polymerization of actin filaments against the cell membrane. Despite the theoretical model of Hawkins et al. [52] indicating that myosin II-mediated contractility is not mandatory for amoeboid migration, its incorporation significantly enhances the speed of cells, a phenomenon that has also been observed experimentally [53].

As for mesenchymal migration, there are several approaches on how to study amoeboid migration in living cells in all three dimensions:

- 1D Linear channels made out of PDMS to confine cells.
- 2D Confining cells from the top with a so called “PDMS pillar forest” as described in Vesperini et al. [54], allowing cells to migrate in the x-y-plane.
- 3D Cells are placed inside a gel mimicking the extracellular matrix and are able to move in any direction. Depending on the type of cells they might express a combination of different migration modes.

During my work, I used RPE-1 cells and neutrophils in PEG coated PDMS microchannels to study their amoeboid migration. The results of this can be seen in chapter 5.

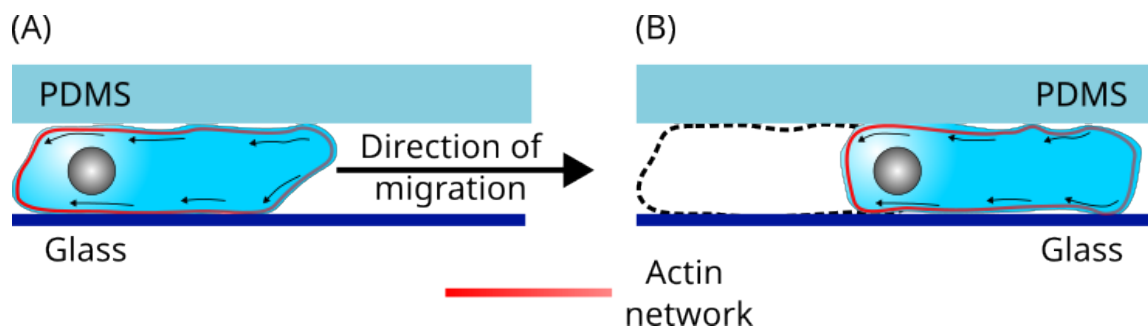


Figure 2.9: Schematic representation of amoeboid migration. A cell is confined e.g. inside a PDMS microchannel (A). The retrograde flow of actin leads to a higher concentration of actin at the back of the cells and creates friction forces, that eventually propel the cell forward (B).

2.5 Focal adhesion

One of the primary mechanisms underlying mesenchymal migration is cellular adhesion. As I studied the impact of the actin stabilizing compound MiuA on the size and number of focal adhesions and their correlation to the cells’ migratory behavior (see chapter 5), I want to describe focal adhesion sites in more detail.

Focal adhesions are integrin-based structures embedded in the cell membrane and comprise an inner and outer domain, given that integrins are transmembrane proteins. The outer domain enables interaction with the surrounding extracellular matrix (ECM), whereas the inner domain recruits proteins to establish a connection to the actin cytoskeleton. This connection between the cell’s environment and the cytoskeleton transmits signals to the nucleus, thereby influencing the cell’s migratory behavior, its proliferation and other biological functions [55].

Integrin cluster, composed of alpha- and beta-subunits, form at the cell surface and interact with the surrounding ECM. Meanwhile, intracellular proteins such as paxillin, vinculin, and talin bind to the integrins, forming focal adhesions [56]. An illustration of a focal adhesion site can be seen in Figure 2.10. The recruitment of actin filaments to these focal adhesion sites allows the transmission of forces towards the surrounding environment and the transmission of signals to the cell nucleus.

Since focal adhesions are an important part of the integrin-mediated migration, they have been the subject of many studies. In the context of mesenchymal migration, focal adhesions need to be formed at the leading edge of the cell while being disassembled at the opposite site. This turnover is achieved via a variety of factors including Rho/ROCK, microtubules, focal adhesion kinase (FAK), and dynamin [57]. Starting this process, a cell approaches an ECM filled environment, where integrins are capable of forming bonds. Short-lived nascent focal adhesions consisting of integrins, talin, paxillin, vinculin, and α -actinin, mature in an Rho/ROCK-dependent process of actin-stress regulation. The disassemble of focal adhesions at the rear end of the cell is initiated by a complex interplay between microtubules, Rho/ROCK, and focal adhesion kinase. The final stage of this process, the detachment of integrins from the substrate, is mediated by dynamin, which results in an internalization of integrins, that removes them practically from the substrate, preventing the formation of new bonds [58].

The size and shape of focal adhesions also influence the manner in which cells migrate. In 2013, Wirtz et al. stated that there is a linear correlation between the focal adhesion size and cell spreading area. Additionally, they found that the relationship between cell migration speed and focal adhesion size can be described in a two-phase model [59]. This indicates that there is an optimal focal adhesion size, from where on cellular migration is reduced regardless whether the size of focal adhesions is increased or decreased. This linear relation between focal adhesion size and force has experimentally been shown by Schwarz et al. in 2022, where they seeded fibroblasts and cardiac myocytes on an elastic substrate and fluorescently labeled their focal adhesions [60]. Substrate deformation measurements revealed the linear relation between those two parameters.

Additionally, the orientation of focal adhesions affects the locally exerted forces from the cell. Balaban et al. described this phenomenon in 2001, where they seeded fibroblasts and cardiac myocytes on a micropatterned soft substrate to influence the shape, size, and orientation of individual focal adhesions [61]. The analysis of deformations from single focal adhesions revealed a positive correlation between size and force as well as orientation and force.

These findings prompted my investigation into the size and number of focal adhesions and their impact on cell migration behavior when they migrate on a fibronectin coated surface. In contrast to the aforementioned studies, in this work I did not only look at single focal adhesions, but also the complete set of focal adhesions within the cell to study possible emerging effects (see chapter 5).

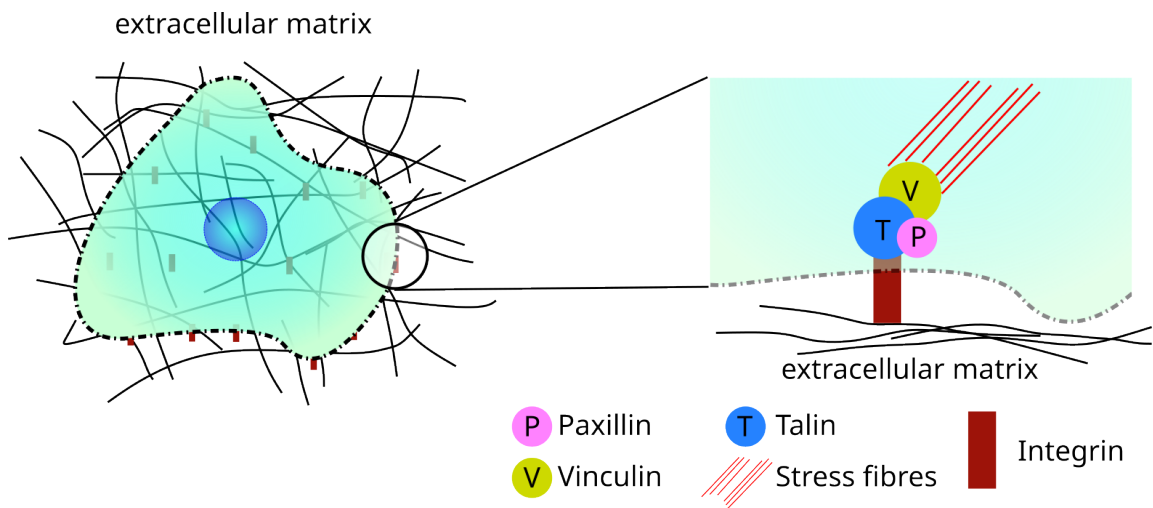


Figure 2.10: Schematic illustration of a focal adhesion. Left: A cell (cytoplasm green, nucleus blue, cell membrane dashed black) adhering to the underlying extracellular matrix (black) with its focal adhesion sites (red). Right: Zoom in to a focal adhesion site, where the transmembrane protein integrin connects to the extracellular matrix on the outside, while recruiting paxillin, vinculin and talin on the cytoplasmic side to anchor to actin stress fibers. Image taken and adapted from the manuscript “*Modulation of Cellular Adhesion, Contractility, and Migration by MiuA: A Comprehensive Analysis of Its Biochemical Impact*” (see chapter 5, page 54).

Chapter 3

Methods

In the field of biophysics, one of the primary objectives is to gather data and develop models which accurately depict the intricate biological processes occurring within cells. In order to achieve this, it is necessary to identify parameters and variables that can be measured and subjected to qualitative and quantitative analysis. Biophysicists, who cross the border between the qualitative nature of biology and the quantitative modeling of physics have devised methodologies for the examination and analysis of cellular behavior, while simultaneously developing and evaluating their models.

In this chapter, I am going to talk about the main methods used in this work. This includes micropatterning, fluorescence recovery after photobleaching, pattern-based contractility screening, migration assays, and single-cell force spectroscopy. I will explain in detail how these techniques are applied in biophysics, how they evolved, and how I employed them in my work. In addition all of my protocols can be found in the appendix A.

3.1 Deep UV-micropatterning

In conventional cell culture, cells are kept in a Petri dish or cell culture flask. Neither of these reflect the biological environment in which cells typically reside. *In vivo*, cells are embedded in a complex milieu of surrounding cells and the extracellular matrix, which constrains their motility and capacity for proliferation. Furthermore, it provides sites of adhesion, thereby influencing the overall behavior of the cell [62]. To mimic these environmental effects on cells in cell culture, the technique of micropatterning is used. This technique allows the creation of precisely defined adhesive regions among a non-adhesive area, resulting in spatially and geometrically controlled cells. Such cells express uniform shapes that facilitate their quantitative analysis.

Earlier studies have employed micropatterning for a variety of research including migration assays, cell polarity, cytokinesis, tissue architecture and other fundamental biological functions [63]. In 2002 Brock et al. investigated the effect of different geometries on the

mobility of fibroblasts and observed that the cells would create new lamellipodia primarily at the corners of the underlying patterns [64]. In the same year, Wang et al. used patterns on a polyacrylamide gel infused with fluorescent microbeads to measure the traction forces of smooth muscle cells [65]. In 2010 Kilian et al. studied the influence of geometrical cues on the differentiation of mesenchymal stem cells, where they saw that geometries that promote actomyosin activities increase osteogenesis [66]. These and many more are examples for the high versatility of the micropatterning technique and its impact on the field of biophysical studies on cells.

In my work (see Chapter 5), I used the established protocol of Azioune et al. [67], to create fibronectin patterns among an antifouling PEG layer as depicted in Figure 3.1. In a nutshell, I coated glass cover slips with a pll-g-PEG solution after plasma treatment and placed them on a photomask. The following irradiation with UV-light ($\lambda_{UV} = 200\text{ nm}$) led to a degradation of the C-O-C bounds between the poly-l-lysine and the PEG, exposing reactive carboxylate groups. After filling these gaps among the otherwise intact PEG layer with fibronectin, the obtained micropatterns were used for three different experiments:

1. Cytoskeletal organization.

In those experiments I seeded RPE-1 cells on fibronectin patterns and let them spread completely. Afterwards, I treated the cells with miuraenamides A and latrunculin A to see whether these actin binding compounds affect the architecture of the actin network inside the cells.

2. Migration assay.

Besides patterns for single cell use one can also use this technique to create adhesive lines with varying thickness for cells to migrate on. I used these lines to track the movement of RPE-1 cells under the influence of miuraenamides A.

3. Contractile energy.

As I will describe later on in section 3.4, I used deformable micropatterns to measure the contractile energy of RPE-1 cells treated with miuraenamides A and blebbistatin. For this, I prepared fibronectin micropatterns and transferred them to a soft polyacrylamide gel, before seeding the cells on top.

3.2 PRIMO micropatterning

In addition to the aforementioned technique of deep UV-micropatterning, I employed the use of the PRIMO device (Alvéole, Paris, France) to create the desired micropatterns. This technique is based on a similar principle to that of the deep UV-micropatterning method: an antifouling coating, in this case a PEG coating, is used, and the layer is degraded at certain points through the use of UV-light. The two main differences between the two techniques are that PRIMO uses longer wavelengths ($\lambda_{\text{PRIMO}} = 365\text{ nm}$) for their illumination

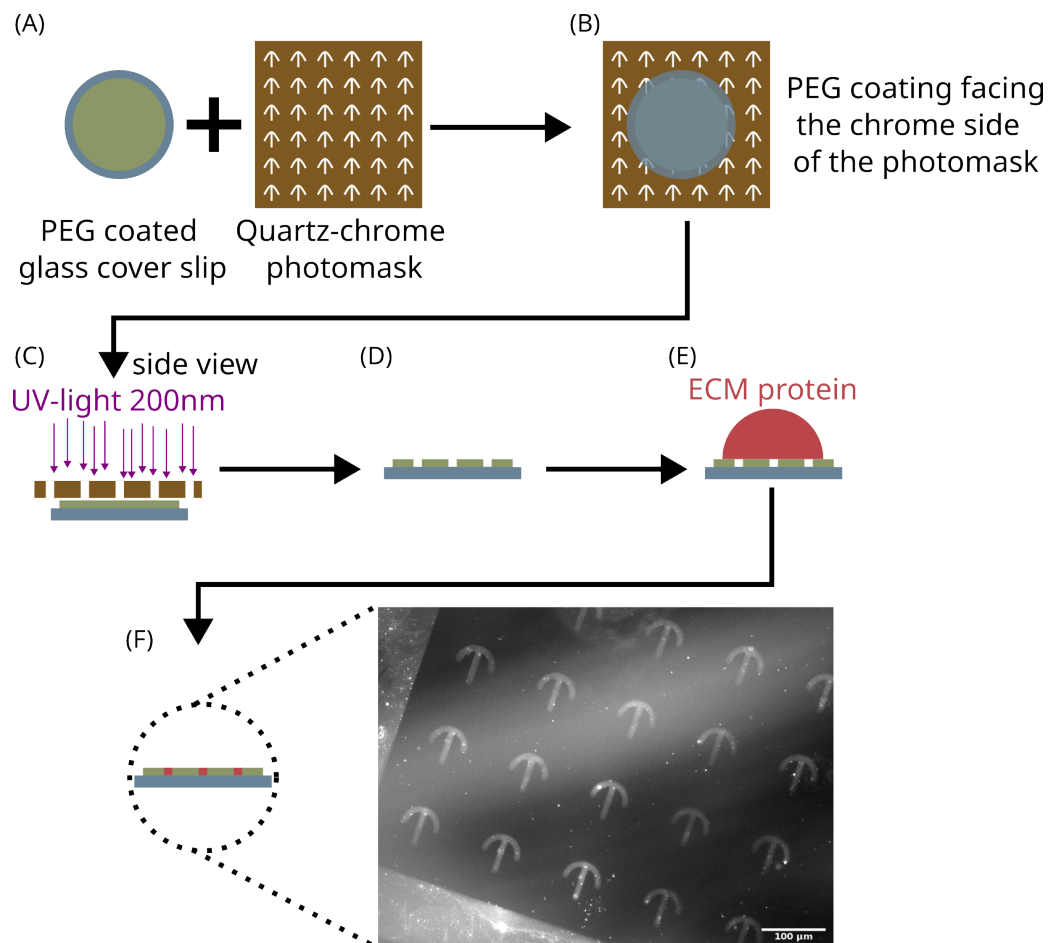


Figure 3.1: Schematic drawing of the deep UV-micropatterning method. A PEG coated glass cover slip is placed on the chrome side of a quartz-chrome photomask (B). UV-light (wavelength $\lambda = 200$ nm) irradiates through the patterns on the photomask (C), degenerating the PEG coating (D). After incubating the glass cover slip with an extracellular matrix protein, cells can adhere to the patterns (E). A representative image of a patterned glass cover slip is shown at the end of the scheme (F), where fluorescently labeled fibronectin was used to coat the patterns. The fluorescent image was taken with a Nikon eclipse ti microscope. Scale bar: 100 μm .

and that one can freely select the shape and gradient of the resulting micropattern. The longer wavelength used in this method is incapable of breaking the C-O-C bonds between the poly-l-lysine and the PEG. This is why one needs to use an additional chemical provided by the company, which they call “PLPP”. The free choice of patterns is a result of the design of the PRIMO unit. The system comprises a digital micromirror device (DMD) that redirects the incoming UV laser through the microscope’s objective in any given shape and gradient [68].

Figure 3.2 shows the process of making micropatterns using the PRIMO technique. In more detail one starts with designing their own pattern. For this I used the software Inkscape (<https://inkscape.org/>) where I took a dark background and drew the desired shapes in white color. This is due to the fact that the PRIMO device will subsequently interpret the values of each pixel and determines whether or not to illuminate that pixel. A black pixel is assigned a value of 0, indicating no illumination, while white pixels are assigned to a value of 255, indicating full illumination. This allows the creation of gradients as any value between 0 and 255 is only illuminated for a reduced amount of time, with a higher value reflecting a longer illumination time.

For the patterning itself, one prepares a glass-bottom dish or a glass cover slip coated with an antifouling layer, as previously described in section 3.1. Subsequently, the photoinitiator is added to the sample prior to the illumination. Before starting the actual patterning process, it is essential to calibrate the PRIMO device. In order to achieve this, a commercially available highlighter is used to paint an additional glass cover slip, which is then positioned beneath the microscope. Once the PRIMO patterning software “Leonardo” is opened, one must select “calibration” and the software will automatically adjust the angle and dimensions of the DMD. Following calibration, the highlighted glass is replaced with the actual sample. The digital mask is then loaded to the PRIMO device via the software and the designed mask is patterned on the glass. The photoinitiator reacts with the UV light, creating free radicals that causes the C-O-C bonds to break down in a manner similar to the deep UV-micropatterning method [68]. Following the completion of the patterning process, one needs to rinse the sample to remove any remaining PLPP, as the PLPP compound has cytotoxic effects. Subsequently, ECM proteins are added and following an hour of incubation cells can be seeded onto the patterns. Figure 3.2 (I) shows the result of such a patterning process with PRIMO.

3.3 Fluorescence recovery after photobleaching

The cytoskeleton along with numerous other structures within living tissue is a highly dynamic network that undergoes constant changes. Microtubules switch between a sudden depolymerization (called catastrophe) and a polymerization (called rescue) state. Actin filaments grow at their plus-end and shrink at their minus-end. They also grow into branched networks and get severed by actin depolymerizing factors such as cofilin. To

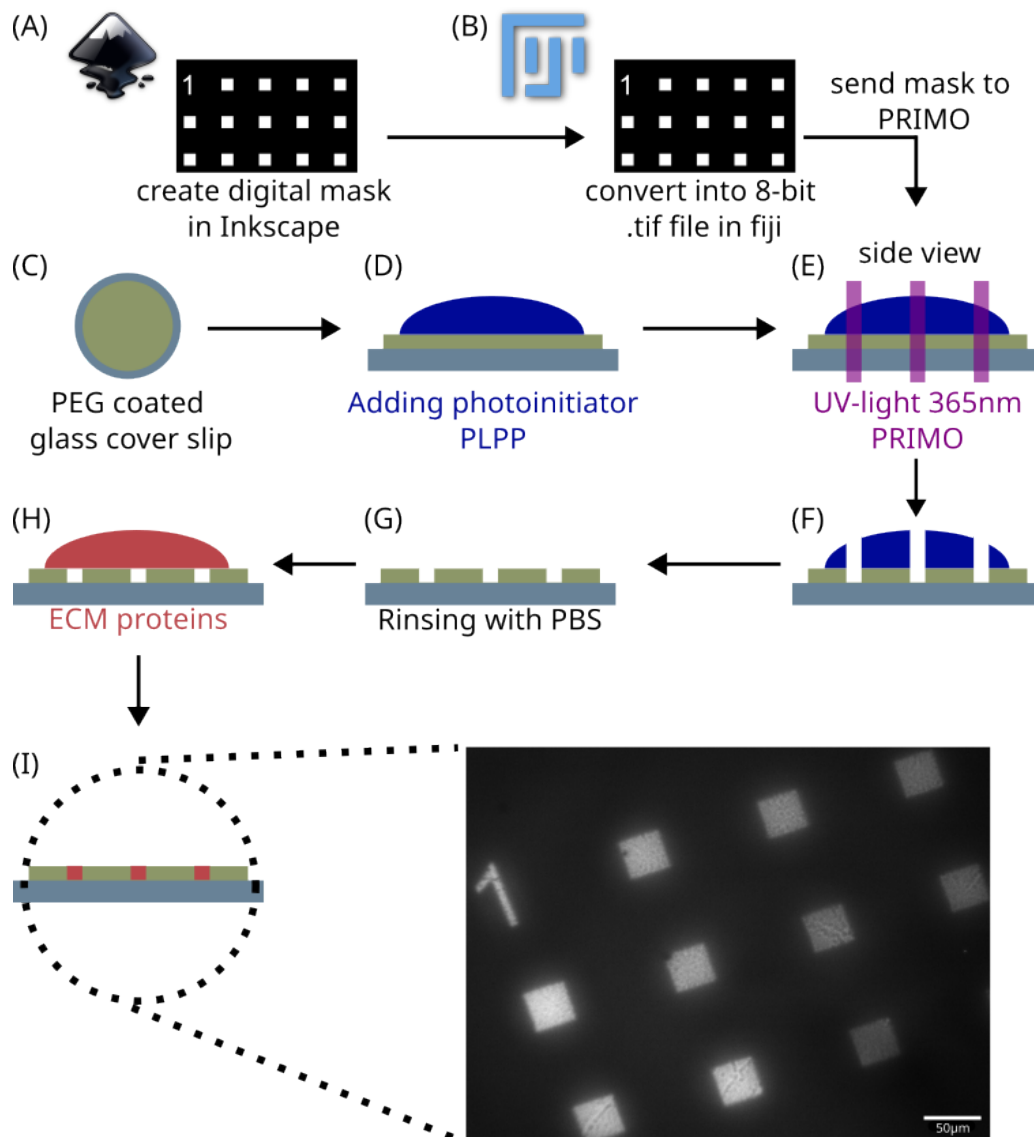


Figure 3.2: Schematic drawing of the PRIMO patterning technique. (A) First one designs a digital pattern using Inkscape. (B) This digital mask then is converted into a 8-bit .tif file using fiji. A PEG coated glass surface (C) is placed under the microscope and the photoinitiator PLPP is added (D). The earlier created digital mask is send to the PRIMO device which triggers the illumination process (E). After the illumination (F) the remaining PLPP must be rinsed several times with PBS (G). The resulted micropatterns can now be coated with an ECM protein (H). (I) Shows an fluorescent image of PRIMO pattern coated with fibronectin+BSA Alexa 555 conjugate. Scale bar $50\mu\text{m}$. Logos of Inkscape and Fiji taken from <https://inkscape.org/de/> and <https://imagej.net/software/fiji/> respectively.

study the dynamics of these and other networks, Axelrod et al. developed a technique called “fluorescence recovery after photobleaching” (short FRAP), which involves bleaching fluorescently labeled molecules within a network while monitoring the subsequent recovery of the fluorescent signal [69] as depicted in Figure 3.3.

Since then, FRAP has been used in a huge variety of studies and focused on different aspects of cell biology [70]. The first applications were on intracellular compartments like organelles and vesicles [71, 72]. Later on, FRAP was also used in studies about actin. Fritzsche et al. used this technique in 2013 to measure the turnover dynamics of the actin cortex in melanoma cells [73]. Another example for FRAP in actin networks is given by Skamrahl et al. in 2019, where they combined FRAP and AFM to measure turnover rates and cell mechanics at the same time [74].

In my work, I used FRAP to quantify the dynamics of actin filaments in RPE-1 cells (see chapter 5 page 42) and CD4+ T cells (see chapter 8 page 121). The data were analyzed according to the protocol provided by Fritzsche et al. from 2015 [75]. Here, the obtained data are characterized by two parameters: the mobile fraction a and the half recovery time τ . The data would be fitted using the following equation:

$$I_{\text{fluorescence}}(t) = a \cdot (1 - \exp(-\ln(2)(t - t_0)/\tau))$$

where t_0 denotes the point in time where the bleaching took place.

To be able to measure the fluorescence recovery of actin filaments one needs to dye G-actin instead of F-actin, which is why I used the BacMam system (described in 2.1.5).

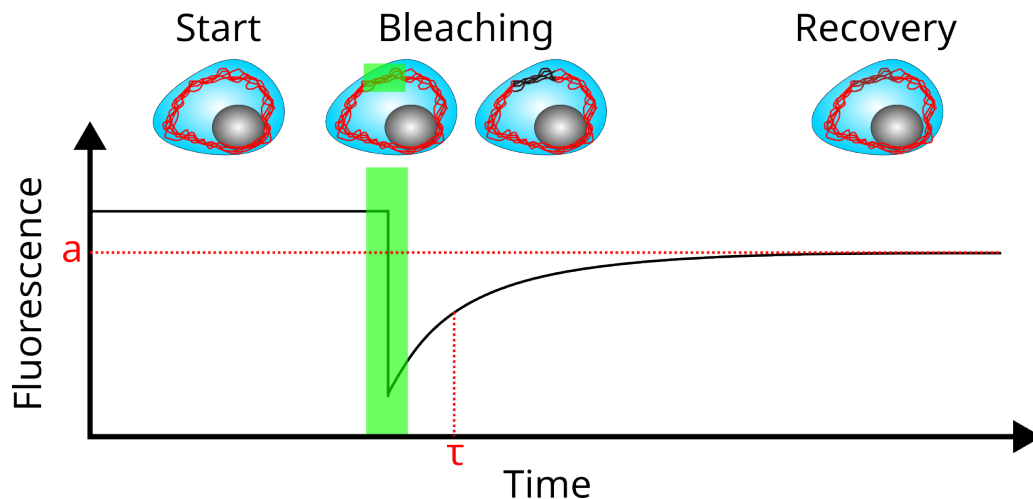


Figure 3.3: Schematic drawing of the FRAP (fluorescence after photobleaching) process. A ROI is being bleached by an intense laser to reduce the fluorescent signal in that area, which, over time, recovers. Red dashed lines indicate the mobile fraction a and the half recovery time τ

3.4 Pattern-based contractility screening and polyacrylamide gel

In traditional cell culture, cells are cultivated in a Petri dish or a cell culture flask. Both of these contain a rigid surface that does not accurately reflect the stiffness of cells in living tissue. Polyacrylamide gels are a soft substrate for cells to grow on, as their surface can be functionalized with adhesion proteins while remaining inert otherwise [76]. In 2021 Norris et al. even created a photodegradable polyacrylamide gel that allowed them to alter the stiffness of the gel while cultivating cells on it [77]. One of the most used applications for soft and purely elastic polyacrylamide gels is in traction force assays. In this technique, fluorescent microbeads are embedded into the gel and move alongside the deformations of the gel. Subsequently, if a cell is placed on the gel and starts deforming it, one can capture the position of the beads before and after the displacement, thereby enabling the calculation of the force that was needed to deform the gel. For example, in 2015 Jerrell et al. used this technique to measure the forces of cancer cells [78] and in 2010 Mann et al. improved the technique to allow prolonged observations of traction forces in murine muscle cells [79].

Once the force field has been acquired, it is possible to further calculate the contractile energy of the cells in question. However, since the described method of performing traction force assays is tedious, Ghagre et al. advanced the technique by introducing a reference-free method of calculating the contractile energy [80]. For this, one takes a patterned polyacrylamide gel with fluorescent patterns of known dimension. Following the seeding of cells, they will adhere to the patterns and start deforming the gel and, consequently, the pattern itself, as seen in Figure 3.4. This change in pattern area can then be used to calculate the contractile energy the cell needed to deform the gel.

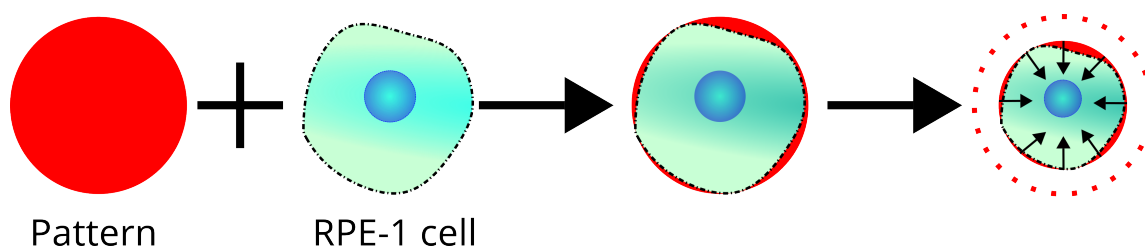


Figure 3.4: Schematic drawing of the pattern-based contractility screening technique. RPE-1 cells are placed on top of a soft patterned surface (pattern in red). After cells adhered to the pattern they start contracting and therefore deforming it. The initial outlines of the pattern are shown as red dashed lines. Image taken from the manuscript “*Modulation of Cellular Adhesion, Contractility, and Migration by MiuA: A Comprehensive Analysis of Its Biochemical Impact*” (see chapter 5, page 54).

3.4.1 Calculation of contractile energy

Ghagre et al. [80] calculated the contractile energy in their work using a Cartesian coordinate system, that describes the shift of each point of the underlying pattern in x- and y-direction. Since their and my calculations are based on the assumption of isometric deformations, I aimed to transform the mathematical question into a polar coordinate system (r, φ) . With this I could reduce the needed parameters from two (x and y) to only one (radius r) and furthermore, I was able to connect the contractile energy to the change of pattern area.

The complete calculations are part of the supplementary information of the included manuscript “*Modulation of Cellular Adhesion, Contractility, and Migration by MiuA: A Comprehensive Analysis of Its Biomechanical Impact*” and can be seen in Chapter 4 after the article itself (see page 73). Here I want to summarize the steps and give a brief description of the mathematics behind the calculation.

I calculated the contractile energy using the following equation:

$$U = \frac{1}{2} \int \vec{F} \cdot \vec{u} dA \quad (3.1)$$

where \vec{F} denotes the force field applied to the substrate.

For this, I started with the following partial differential equation (PDE):

$$(1 - 2\sigma)\Delta\vec{u} + \vec{\nabla}(\vec{\nabla} \cdot \vec{u}) = 0$$

where σ denotes the Poisson ratio and \vec{u} denotes the displacement vector.

Using harmonic functions and the boundary conditions of a flat deformable plane in the $x - y$ -plane I derived the following solution to the PDE above:

$$\vec{u} = G_{ik} * \vec{F} \quad (3.2)$$

where G_{ik} denotes Greens Tensor.

Since the displacement is isometric, I now only took the displacement at $\varphi = 0$ into account and transformed Greens tensor into polar coordinates:

$$G_{\text{polar}} = \frac{1 + \sigma}{\pi E r} \begin{pmatrix} (1 - \sigma) + \sigma & 0 \\ 0 & (1 - \sigma) \end{pmatrix} \quad | \text{ assuming } \varphi = 0$$

where E denotes the Young’s modulus (part of the boundary conditions).

As it is only possible to directly observe the displacement field but not the force field, I transformed equation 3.2 into Fourier space, inverted it and transformed it back. This allowed me to analytically solve our initial equation for the contractile energy (see equation 3.1) and obtain the following expression:

$$U_{\text{final}} = \frac{E(1 - \sigma)}{3(1 + \sigma)[(2(1 - \sigma) + \sigma)^2 - \sigma^2]} \left(\left(\frac{A_i}{\pi} \right)^{\frac{3}{2}} - \left(\frac{A'}{\pi} \right)^{\frac{3}{2}} \right)$$

where A_i denotes the initial and A' the final area of the pattern.

3.5 PDMS microfabrications

In vivo, cells demonstrate the capacity to migrate through a diverse array of different environments. They must navigate through the extracellular matrix, squeeze through epithelial sheets, and are often confined to a capillary sized level. To more accurately replicate this type of environment researchers have been using polydimethylsiloxane (PDMS) for the past decade [81]. The physical and chemical properties of PDMS are a significant factor for its widespread use in cell biology. These include transparency, biological compatibility and permeability for gases [82].

Examples of the extensive utilization of PDMS microfabrications are: the creation of three-dimensional endothelial cell layers using circular PDMS microchannels [83], the study of cell migration in a microfluidic device [84], and the study of collective cellular migration [85]. Those and numerous other studies show the versatile usage of PDMS microfabrications for cell biology and have helped to establish it as a standard technique in biophysics. In my work, I was following the established protocol of Heuzé et al. [86], which I have briefly outlined in Figure 3.5. In essence, a mixture of PDMS and a curing agent is poured onto a mold. After degassing the PDMS mixture, the mold and PDMS together are placed inside an oven to speed up the curing process. Once the PDMS is cured, it is peeled from the mold and activated with plasma to mount it to a glass surface. In the final step, an antifouling coating (like PEG) or ECM proteins can be added to either hinder or facilitate adhesion.

For this work the microchannels were used in migration assays, wherein the inside of the channels was coated with an antifouling PEG layer to enforce amoeboid migration. Similar to the migration assays on fibronectin lines, I stained the nuclei of the cells with Hoechst and tracked their position during a time lapse video. From this I calculated the mean migration speeds and persistence (see chapter 5).

3.6 Single cell force spectroscopy

The process of cellular adhesion represents a fundamental aspect of cellular mechanics. It is essential for a number of biological processes, including migration, tissue development, and wound healing. Therefore, understanding the mechanism behind adhesion is an important subject in many studies. Initial attempts to measure the adhesion of cells included the usage of trypsin, a digestive enzyme, which degrades the adhesion proteins [87]. A more sophisticated approach is the usage of atomic force microscopy (AFM), where a nanoscale-sized cantilever is used to lift cells from their substrate to measure the adhesion force they exerted towards their environment. This method allowed a more quantitative analysis of cell adhesion behavior than trypsinization, although it resulted in a low throughput, as only one cell could be measured at a time [88]. In 2009, Meister et al. [89] combined an atomic force microscope (AFM) system with a microfluidic device. The use of a hollow cantilever enabled the researchers to exert greater control over the pressure applied to

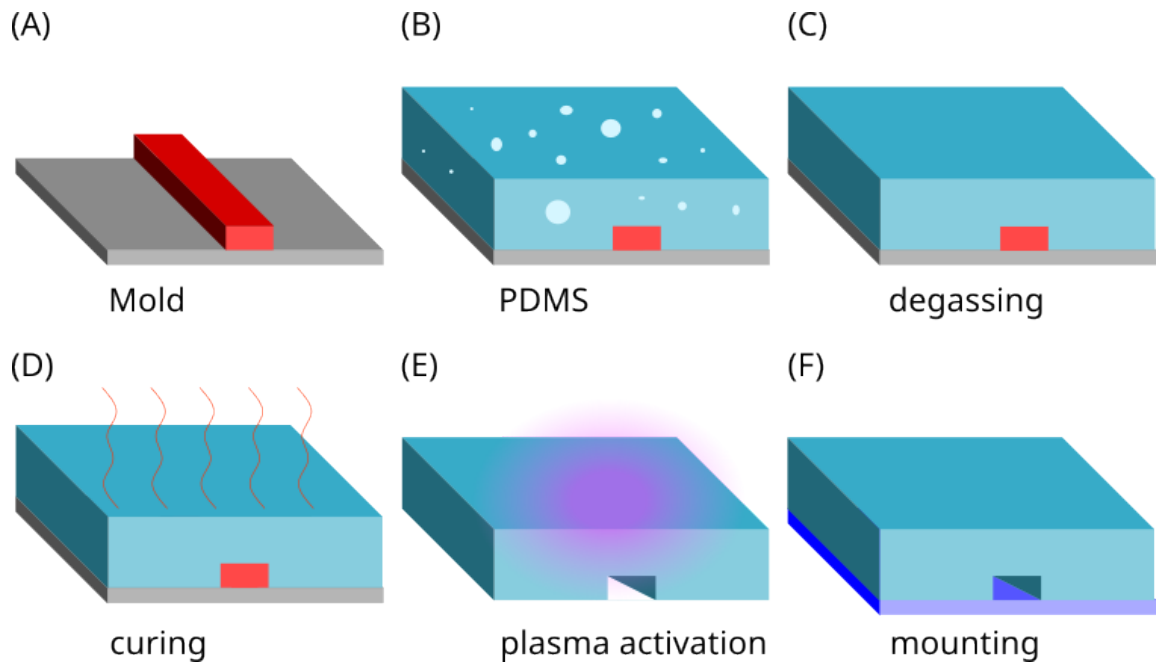


Figure 3.5: Schematic illustration of PDMS microchannel fabrication. A mold (A) is filled with PDMS (B) and degassed (C) in a degassing chamber. The PDMS is then placed in an oven for curing (D). After curing the PDMS chip is removed from the mold and activated by plasma treatment (E) before being mounted on a glass coverslip (F).

the cells, thus facilitating a more precise analysis of the adhesion process. The general idea is shown in Figure 3.6, where a hollow cantilever approaches an adhered cell, applies negative pressure after contact, and lifts the cell until it is completely detached from the substrate. The obtained force-distance curve (example see Figure 3.6 panel (D)) contains three parameters to analyze:

1. Adhesion force.
The maximal force needed to remove the cell from the substrate is characterized by the lowest tip point of the curve.
2. Adhesion energy.
The area between the base line and the force-distant curve indicates the adhesion energy the cell had while attached to the environment.
3. Rupture length.
The two points the force-distance curve crosses the base line mark the distance needed for the cantilever to lift before the cell was completely detached from the substrate.

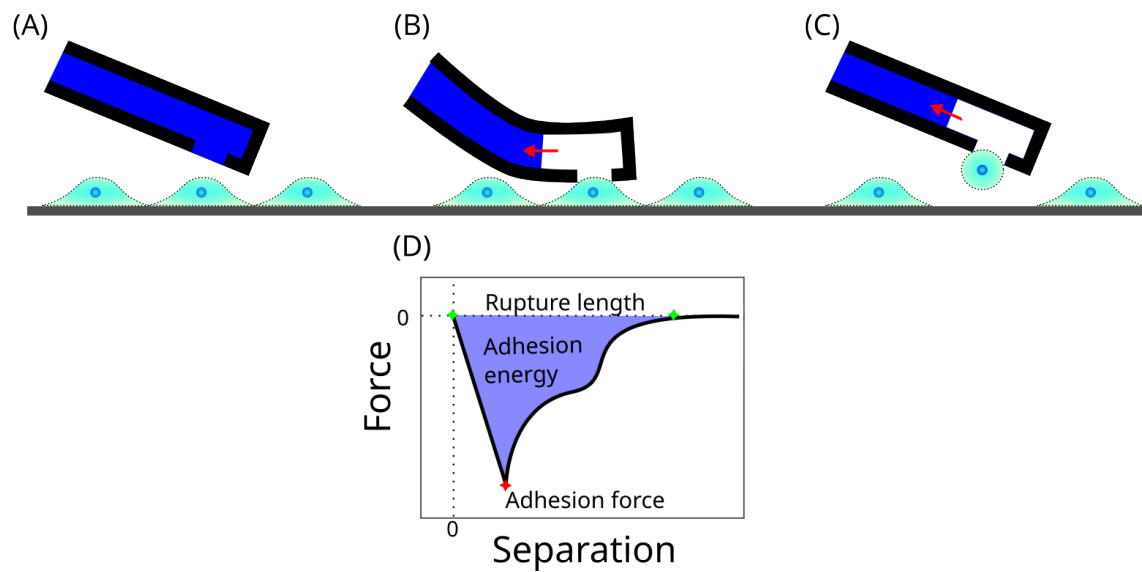


Figure 3.6: Schematic drawing of the single-cell force spectroscopy procedure. A hollow cantilever approaches a cell (A). After applying negative pressure (B) the cell can be lift until it is completely detached from the surface (C). A corresponding curve for a typical single cell force spectroscopy measurement is shown to illustrate how the adhesion force, energy and rupture length (D) are obtained.

Chapter 4

Scientific context and aim of the thesis

In this chapter I am going to briefly explain the scientific context surrounding my work and pose the scientific question I was trying to answer during my research.

The capacity of cells to move is crucial for many biological processes. Immune cells must locate and pursue pathogens, fibroblasts construct and maintain the extracellular matrix, in embryonic development, stem cells must reorganize to proceed in tissue development, and in response to an injury cells must migrate towards each other to close the wound. These examples show the broad field of the cells use in cellular migration.

Due to its importance in cell biology, a lot of research has been conducted on the matter and many different study designs and approaches have been made to better understand the underlying mechanism of cellular migration. One of the main proteins involved in this is actin, which serves as the main cytoskeletal filament responsible for the generation of forces in cells. Consequently, many studies have been dedicated to targeting the architecture and dynamics of the actin filament network. To provide a concise overview, I will present a few representative examples in the following.

In 2008, El Sayed et al. treated breast tumor cells with various concentrations of the actin depolymerizers latrunculin A and B to see whether this affects the migration and invasive properties of the cells. The authors report that dosages of 500 nM are sufficient to reduce migration by a factor of three and that dosages ranging from 50 nM to 1 μ M reduce invasive activities in these cells [45]. In 2006 Hayot et al. investigated the impact of cytochalasin D, an alternative actin destabilizer on the migration properties of tumor cells. The treatment of cells cells with cytochalasin D resulted in a reduction in actin polymerization dynamic and reduced migration, in both migration assays and wound healing assays [90].

In conclusion, the disruption of the actin network impedes cell migration. One potential explanation for this phenomenon ist that actin is involved in both cell contractility and

adhesion. Consequently, a disruption of this network could lead to a malfunctioning of these cell mechanics, resulting in cells that are unable to adhere or contract. This effectively addresses the two main mechanisms responsible for cell migration.

On the other hand, the stabilization of actin filaments has not been the subject of as much research. The two most prominent actin stabilizers are phalloidin and jasplakinolide. The first is unable to pass through the cell membrane, which significantly limits its utility for observations in living cells. In contrast, the latter one has been used in several studies that have demonstrated its effect to be highly sensitive to the used dosage and time of exposure. In a study from Hayot et al. the effects of jasplakinolide on the migration of MCF-7 cells and A549 cells were investigated. The results of the study were contradictory. While jasplakinolide treatment reduced migration in MCF-7 cells, it significantly increased migration in A549 cells [90]. Furthermore, a delayed toxicity has been reported when using jasplakinolide [2]. Other studies also focused on the effects of jasplakinolide on cell migration. In 2021 Ali et al. showed that MDA-MB-231 cells treated with jasplakinolide reduced their expression of adhesion proteins, consequently leading to a reduction of their migratory capacities [6]. In conclusion, jasplakinolide generally reduces cell migration but also requires a precise handling to obtain reproducible results. This may explain the observed results that on a first glance seem to contradict each other. However, since small fluctuations in dosage and exposure time seem to have significant effects, the reported results may simply reflect this.

In this work I am going to present a comprehensive overview of the role of the actin network, its architecture and dynamics, and its contribution to the mechanism of cellular migration. Specifically, I am looking at the effects of the actin stabilizing compound miuraenamamide A in RPE-1 cells, MEFs and neutrophils. I explain which of the migration parameters (actin polymerisation, cellular adhesion, and cellular contractility) listed by Lämmermann et al. [5] are affected and how they influence the different modes of migration. A better understanding of cellular migration and its underlying mechanisms is important for further research. For example, to design pharmaceutical compounds that target one specific mode of migration, it is necessary to know which cellular processes need to be altered and how to address them. Figure 4.1 shows a graphical abstract of my research question, which will be discussed later on in chapter 6. The three migration parameters described by Lämmermann et al. are actin polymerization, cell adhesion, and cell contractility. Depending on which of these parameters dominates, the cell display another mode of migration. For example, a cell that shows a high level of adhesion, is more likely to migrate in a mesenchymal way, whereas a cell with higher contraction might be more likely to migrate in an amoeboid manner. In my work, I am going to describe the effects of MiuA on these parameters and therefore explain why and how MiuA, with its actin stabilizing effects, influences cell migration.

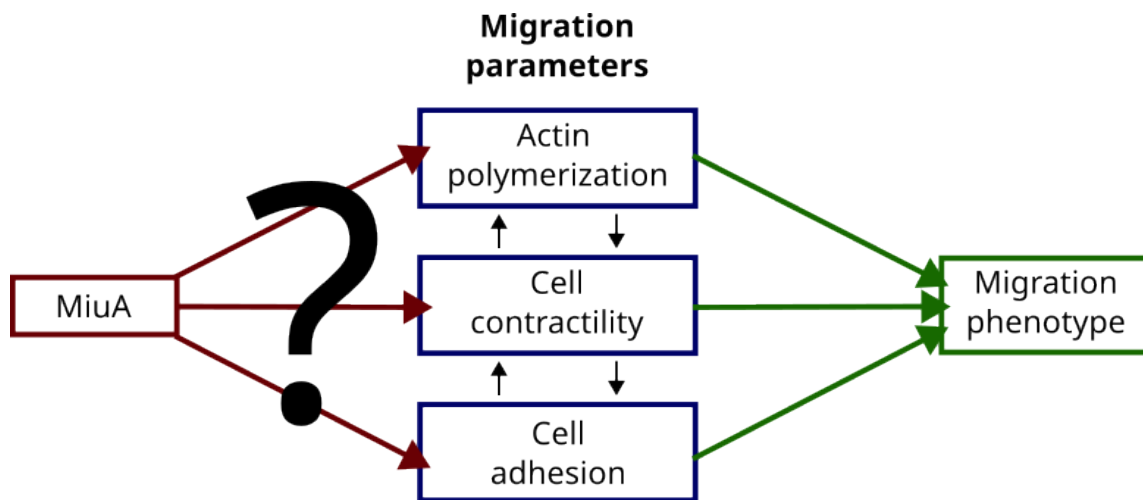


Figure 4.1: Graphical abstract of my research question. The exact impact of MiuA on the three main migration parameters is not well studied. These parameters together decide which mode of migration the cell performs. The question is how the effect of MiuA influences migration parameters and how this eventually impacts the mode of migration.

Chapter 5

Results

In this chapter I want to present my research findings, which have been published or are currently under the process of submission.

During my work, I was aiming to better understand the relation between the length of actin filaments in migrating cells and their mode of migration. For this, I looked at RPE-1 cells, MEF cells and neutrophils and tracked their migratory behavior under the influence of the actin stabilizing compound miuraenamamide A. To further understand the results I studied the effects of miuraenamamide A on their migration mechanics, including adhesion, actin filament length and dynamics, and contractile energy. For this, I measured the length of actin filaments in RPE-1 and MEF cells and conducted FRAP experiments on the actin filaments of RPE-1 cells. Furthermore, I analyzed the focal adhesions of RPE-1 and MEF cells adhered to a fibronectin coated surface and additional single cell force spectroscopy on RPE-1 cells was employed. Lastly I performed pattern based contractility screening and used my newly derived formula to calculate the contractile energy of RPE-1 cells.

The exact methods, results and discussion can be seen in the following two articles:

1. *Actin stabilization in cell migration* [12].
See page 42.
Published in “Frontiers in Cell and Developmental Biology” in 2022.
Additionally, I present data about the positioning of the nucleus in migrating cells treated with MiuA. This can be seen on page 50.
2. *Modulation of Cellular Adhesion, Contractility, and Migration by MiuA: A Comprehensive Analysis of Its Biomechanical Impact*.
See page 54 for the manuscript and page 73 for the detailed calculation of the contractile energy.
Manuscript is in submitting process as of November 2024.
Additionally, I present data that has not been included in the manuscript, as the experiments are not yet finished. This can be seen on page 82.

Faculty of Natural Sciences and Technology

Cumulative form of the dissertation

Template for the confirmation of the proportion of co-authors

Title of the dissertation (working title):

Cytoskeletal aspects of cellular migration

Article to be included:

Actin stabilization in cell migration

ORIGINAL RESEARCH article

Front. Cell Dev. Biol., 11 August 2022

Sec. Cell Adhesion and Migration

Volume 10 - 2022 | <https://doi.org/10.3389/fcell.2022.931880>Quality of the publication:

Research article

Review process or publication status:

Accepted and published

Explanation of the contributions of the co-authors:**Carsten Alexander Baltes:** Designed experiments, prepared Figures (Figure 2, Figure 3, Figure 4, Figure 5, Figure 6, Figure S1, Figure S2, Figure S3) and wrote the manuscript.

Performed the following experiments and their corresponding analysis:

▮	RPE-1 and MEF preparation and cell culture:	100%
▮	Preparation of micropatterns:	100%
▮	Actin filament length measurements:	100%
▮	Fibronectin coating of covers slips:	100%
▮	Migration experiments (RPE-1 and MEF):	100%
▮	Cell viability assay (MTT assay):	100%
▮	Immunostaining of focal adhesions (paxillin):	100%
▮	Fluorescence recovery after photobleaching (FRAP) experiments:	100%
▮	Coding (python3 scripts):	100%

Divyendu Goud Thalla: supervised the study for the following experiments:

- ▮ Immunostaining of focal adhesions (paxillin)
- ▮ Cell viability assay (MTT assay)

Uli Kazmaier: Provided the miuraenamide A compound. Improved the manuscript and prepared Figures (Figure 1)**Franziska Lautenschläger:** Generated concepts, designed experiments, and improved the manuscript. Secured funding and supervised the study.

Signature of the doctoral candidate
(Carsten Alexander Baltes)



Signature of the co-authors

Co-author	Signature
Divyendu Goud Thalla	
Uli Kazmaier	
Franziska Lautenschläger	



OPEN ACCESS

EDITED BY

Claudia Tanja Mierke,
Leipzig University, Germany

REVIEWED BY

Silvia C. Finnermann,
Fordham University, United States
Dave Gau,
University of Pittsburgh, United States

*CORRESPONDENCE

Franziska Lautenschläger,
f.lautenschlaeger@physik.uni-saarland.

SPECIALTY SECTION

This article was submitted to Cell
Adhesion and Migration,
a section of the journal
Frontiers in Cell and Developmental
Biology

RECEIVED 29 April 2022

ACCEPTED 08 July 2022

PUBLISHED 11 August 2022

CITATION

Battes C, Thalla DG, Kazmaier U and
Lautenschläger F (2022), Actin
stabilization in cell migration.
Front. Cell Dev. Biol. 10:931880.
doi: 10.3389/fcell.2022.931880

COPYRIGHT

© 2022 Battes, Thalla, Kazmaier and
Lautenschläger. This is an open-access
article distributed under the terms of the
[Creative Commons Attribution License
\(CC BY\)](https://creativecommons.org/licenses/by/4.0/). The use, distribution or
reproduction in other forums is
permitted, provided the original
author(s) and the copyright owner(s) are
credited and that the original
publication in this journal is cited, in
accordance with accepted academic
practice. No use, distribution or
reproduction is permitted which does
not comply with these terms.

Actin stabilization in cell migration

Carsten Battes¹, Divyendu Goud Thalla¹, Uli Kazmaier² and
Franziska Lautenschläger^{1,3*}

¹Experimental Physics, Saarland University, Saarbrücken, Germany, ²Organic Chemistry, Saarland University, Saarbrücken, Germany, ³Centre for Biophysics, Saarland University, Saarbrücken, Germany

Actin is a cytoskeletal filament involved in numerous biological tasks, such as providing cells a shape or generating and transmitting forces. Particularly important for these tasks is the ability of actin to grow and shrink. To study the role of actin in living cells this dynamic needs to be targeted. In the past, such alterations were performed by destabilizing actin. In contrast, we used the natural compound miuraenamamide A in living retinal pigmented epithelial (RPE-1) cells to stabilize actin filaments and show that it decreases actin filament dynamics and elongates filament length. Cells treated with miuraenamamide A increased their adhesive area and express more focal adhesion sites. These alterations result in a lower migration speed as well as a shift of nuclear position. We therefore postulate that miuraenamamide A is a promising new tool to stabilize actin polymerization and study cellular behavior such as migration.

KEYWORDS

actin, migration, miuraenamamide, nucleus, adhesion

Introduction

Actin is one of the most preserved proteins in eukaryotic cells and is therefore involved in many cellular functions like cell division, migration, signaling and adhesion (Thomas and John, 2009). This variety of tasks illustrates its importance within living cells. Therefore, researchers are interested in understanding its role and its relevance by altering its properties and investigating the corresponding cellular behavior. To alter actin properties, actin binding compounds like phalloidin, latrunculin and jasplakinolide have been used (Figure 1). While actin depolymerizing compounds such as latrunculin have been part on many studies on the actin network, studying the effects of stabilized filaments remains challenging. The two most prominent compounds to stabilize actin filaments were phalloidin and jasplakinolide, both carrying major disadvantages: Phalloidin is not able to pass the cell membrane (Risinger and Du, 2020) which limits its use to fixed cells and the effect of jasplakinolide heavily relies on the used concentration and time scales (Ou et al., 2002). To bypass these disadvantages, we decided to use the alternative natural compound miuraenamamide A (MiuA), which was isolated in 2006 from slightly halophilic marine myxobacterium (Iizuka et al., 2006). The structural relationship to jasplakinolide forced us to develop a total synthesis of MiuA (Wang et al., 2019) as well as other derivatives (Moser et al., 2017; Gegenfurtner et al., 2018) for structure-activity studies. By the synthetic protocols developed, miuraenamamides are accessible on the gram scale for

biological studies, e. g., regarding their possible binding mode (Wang et al., 2019), their effect on cell migration under chemotaxis (Moser et al., 2017) and their regulatory effects on gene expression (Gegenfurtner et al., 2018). Modifications to the structure of MiuA have also been shown to reverse the stabilizing properties of MiuA into a destabilizing compound (Wang et al., 2021), increasing its versatility.

In this study, we show the quantitative effects which MiuA has on the dynamics of actin filaments, as well as on the length of actin filaments in living cells. We additionally observed that treated cells occupied a larger area when allowed to freely spread and that their number of focal adhesions increased. We further found that MiuA treatment led to repositioning of the nucleus towards the cell center during migration and that cell migration speed decreased.

Material and methods

UV-patterning

We used two different types of patterns: “crossbow” patterns, that forced single cells to transform into a polarized shape and straight lines with a thickness of 10 μm to observe migration in 1D. For the production of the micropatterns, PEG-coated glass cover slips were placed on a photomask and illuminated with UV light according to the protocol of Azioune et al. (2010). We activated the photomask for 5 min before placing any glass objects on it and afterward put it back in for another 6 min. A fibronectin (concentration 25 $\mu\text{g}/\text{ml}$) solution (purchased from Thermo Fisher) was used to fill the holes among the PEG layer to create adhesive islands. For this procedure, the UV treated glass cover slips were placed upside down on a fibronectin droplet and kept either at room temperature for 1 h or placed in a sealed box inside a refrigerator (+ 4°C) overnight.

Cell culture

RPE-1 cells transfected with LifeAct mCherry [as described by Maiuri et al. (2015)] and mouse embryonic fibroblasts (MEFs) were cultured at 37.5°C and 5% CO₂ in Dulbecco’s Modified Eagle Medium Nutrient Mix F12 with 10% FBS, 1% GlutaMax and 1% Streptomycin + Penicillin (ThermoFisher). The RPE-1 cells were kindly given by the lab of Matthieu Piel, Institut Curie, Paris. The MEFs were kindly given by Dr. Jennifer Kasper, Leibniz Institut für neue Materialien, Saarbrücken.

Miuraenamide A treatment

Miuraenamide A used in this study was obtained by total synthesis as reported previously (Karmann et al., 2015). It was

given to cells 1 h prior to life cell imaging or fixation with PFA. Concentrations of MiuA were chosen to be 20 nM in each experiment. For this, MiuA has been added to the cell culture medium (DMEM/F12) which was given to cells and incubated for the duration of the experiments.

Fixation of cells

Cell medium was removed, and cells were washed with PBS before adding a 4% PFA solution for 10 min. After that PFA was removed and samples were washed in PBS for 5 more minutes 3 times. Samples were then mounted with Fluoromount G + DAPI (Thermo Fisher) on a microscope slide, sealed with nail polish and stored at +4°C, protected from light.

Paxillin staining

For visualization of focal adhesions, we took samples (RPE-1 LifeAct-mCherry) after the fixation with 4% PFA and dissolved the cell membrane. For this we used a 0.1% solution of TritonX-100 and put cells in it for 10 min. After three times washing with PBS we added a 3% BSA solution to them to block on specific binding for at least 1 h. A 1:1000 solution of paxillin antibodies (ThermoFisher, catalog nb. PA-34910) and 3%BSA was then added to the cells for another hour prior to washing with PBS and mounting the samples with Fluoromount G + Dapi on a microscope slide.

Fluorescence microscopy

Fixed cells were imaged with a ZEISS Axio observer using a $\times 63$ magnification oil objective. Life cell imaging was performed with a Nikon Eclipse Ti microscope using a $\times 10$ magnification objective. Inside the microscope incubation chamber the temperature was set to 37°C and the CO₂ concentration was set to 5%. The whole setup was allowed to stabilize at this temperature and CO₂ concentration 1 h prior to the start of the experiments. Cell migration was observed by treating RPE-1 LifeAct mCherry cells with 250 ng/ml of Hoechst for 30 min before beginning the experiments and then taking pictures of them every 5 min.

Actin staining for FRAP measurements and FRAP measurements

Dynamics of the actin network were measured by fluorescence recovery after photobleaching (FRAP) using a Zeiss LSM880 microscope. RPE-1 wild type cells were treated with BacMam2.0 (Thermo Fisher) at least 2 days before the experiment.

The amount of BacMam used was set to 60 μL per 100,000 cells. Samples were placed in a glass bottom dish and were allowed to spread for at least 3 h before starting the FRAP measurements. Light with a wavelength of 405 nm was used to achieve the bleaching effects on single actin filaments. The parameters for the experiment were acquired using the protocol by [Fritzsche and Charras \(2015\)](#). Fluorescence intensity in areas of bleaching events was measured by the microscope software itself. A second and third ROI were set to measure the overall bleaching effect on the cell and the background signal. Final graphical presentation and statistical tests were performed using a home written Python3 script.

MTT-assay

5,000 RPE-1 cells were placed inside several wells of a 96 well plate and the following five different conditions were chosen for testing:

- 1 μL DMSO per 1 ml medium, as (negative) control MiuA (20 nM, 40 nM and 60 nM)
- 10 $\mu\text{g}/\text{mg}$ mitomycin, as (positive) control

Cells were allowed to proliferate for 48 h under their respective conditions before the medium was removed and the cells were rinsed with PBS. MTT solvent at a concentration of 0.5 $\mu\text{g}/\text{ml}$ (in cell culture medium) was added to the cells, before placing them in an incubator (37°C, 5% CO_2) for 1 h. After the MTT solution was removed and the purple crystals that formed were dissolved in 100 μL of DMSO. To achieve a homogeneous dissolution, we placed the 96-well plate on a beacon shaker for at least 30 min. The light absorption, correlating with the number of cells inside each plate was then measured using a Tecan infinite 200 Pro, which automatically measures the absorbance coefficient in each well and provides xlsx files with the collected data. The machine was set to “multi-measurement” mode, meaning that nine distinct spots inside each well were measured and an average value for the absorbance coefficient was formed for each of them. The wavelength was set to 570 nm.

Image analysis

All images were analyzed with Fiji (ImageJ) ([Schindelin et al., 2012](#)). Length of actin filaments was measured by hand using Fiji’s “line” tool. Time-lapse images of migrating cells were analyzed using the plug in “TrackMate” ([Tinevez et al., 2017](#); [Ershov et al., 2021](#)). Nuclear distances were defined as the length between the back of the cell and the center of the nucleus divided by the total length of the cell. The number and size of focal adhesions were determined by paxillin staining. Paxillin signal was put under a threshold and then analyzed with Fiji’s built-in function “Analyze particles”, giving us the number and sizes of

focal adhesions in those cells. All data were saved as csv. files and used for further analysis. Kymographs were performed using Fiji’s “Kymograph” tool.

Statistical testing

Student’s t test were conducted on all experimental data and Pearson R values were calculated using a home build Python3 script. *p*-values were calculated and assigned as follows:

- $p > 0.05$: no significance (n.s.)
- $p < 0.05$: *
- $p < 0.01$: **
- $p < 0.001$: ***

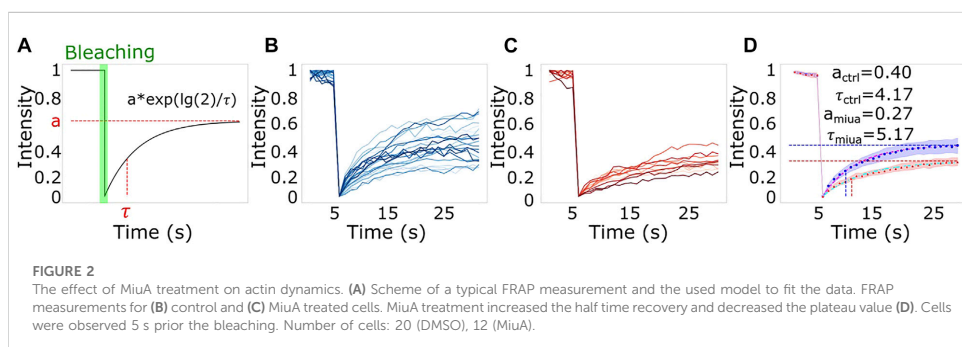
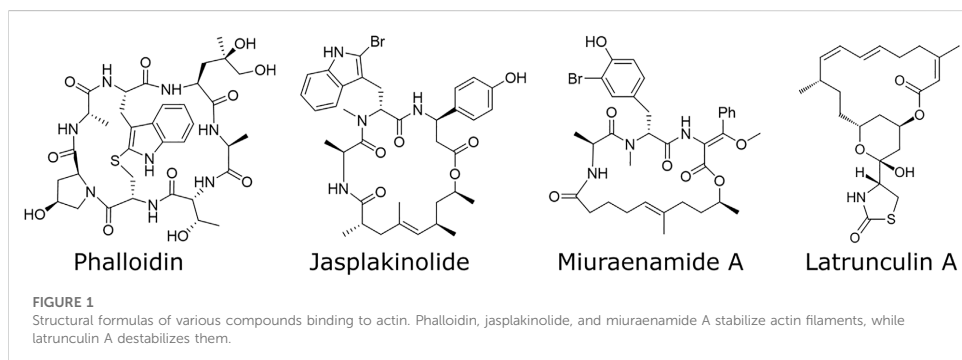
Results

MTT assay

To confirm that a concentration of 20 nM MiuA is suitable for our experiments, we conducted a MTT assay on RPE-1 cells ([Supplementary Figure S1](#)). There we could see that cells treated with 20 nM of MiuA proliferated similar to the control group, while those treated with 40 nM MiuA showed the same behavior as the positive control group, treated with mitomycin C. When we increased the concentration further to 60 nM MiuA, we observed that the number of cells was even lower than that in our positive control group. Taking this into account, we decided to use 20 nM MiuA for all our experiments in this study.

Actin dynamics

To determine whether treatment with MiuA affected on the dynamics of actin filaments, we performed fluorescent recovery after photobleaching (FRAP) measurements. For this purpose, we bleached actin fibers in RPE-1 cells transfected with BacMan2.0 and measured the time evolution of the fluorescence intensity. We used BacMam staining as it stains G-actin and thus allows us to observe the network dynamics. Using a model for the recovery of the fluorescence intensity proposed by [Fritzsche and Charras, \(2015\)](#) we found that both the plateau level and the recovery time were altered in cells treated with MiuA. An alteration of the plateau level indicates a lower fraction of restored fluorescence and an alteration of the recovery time indicates a changing rate of exchanging actin monomers. Since upon treatment with MiuA, the plateau level decreased and the half-time recovery time increased ([Figure 2](#)), we concluded that MiuA treatment slows actin dynamics.

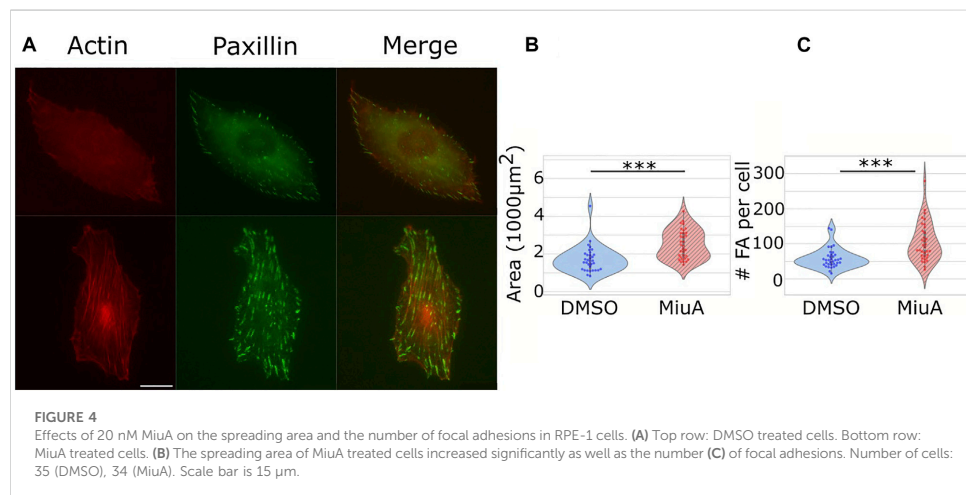
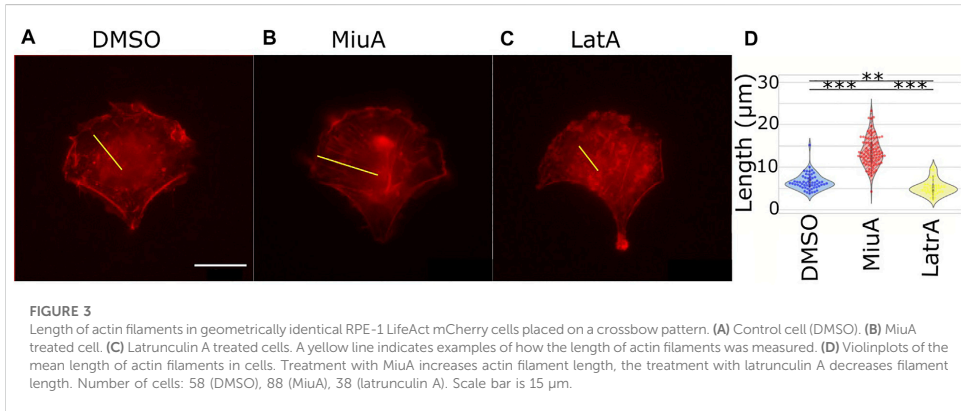


Length of actin filaments

Because actin filament dynamics might influence the length of actin filaments, we next wanted to compare actin filament length depending on MiuA. Therefore, we first aimed to obtain geometrically identical cells so that we could compare similar structures (Théry, 2010). We placed RPE-1 cells that express LifeAct mCherry as a fluorescent dye on crossbow micropatterns (Figure 3). Once cells had a similar shape, compared the length of actin filaments in cells treated with 20 nM MiuA with the length of actin filaments in untreated cells. This concentration was chosen from the literature and was used throughout the study (Moser et al., 2017). Additionally, we used latrunculin A to destabilize the actin network as a negative control group. We manually analyzed the actin filament length using ImageJ. MiuA treatment resulted in a mean length of 13.57 μm compared to 6.26 μm in untreated cells and 4.89 μm in cells exposed to latrunculin A. Taken together, we can conclude that the length of actin filaments in MiuA treated cells increased significantly.

Number of focal adhesions and spreading area

We placed cells on micropatterns to compare cells which all had the same shape in order to compare the length of similar actin filaments. However, micropatterns are a rather artificial approach, which is helpful for understanding particular parameters, but is difficult to relate to the *in vivo* situation. Therefore, we next compared the adhesion of cells on 2D fibronectin coated glass surfaces. We quantified the number of focal adhesions in RPE-1 cells treated with MiuA: We stained for paxillin (Figure 4A), a protein involved in the formation of focal adhesions and counted the focal adhesions using ImageJ. Interestingly, the mean number of focal adhesions in MiuA treated cells increased from 57.829 in control cells to 103.235 in MiuA treated cells, resulting in an overall increase by a factor of 1.7 (Figure 4C). Following the number of focal adhesions, we also measured the spreading area of fully adhered cells. Consistent with the increased number of focal adhesions, MiuA treated cells occupied a significantly larger area

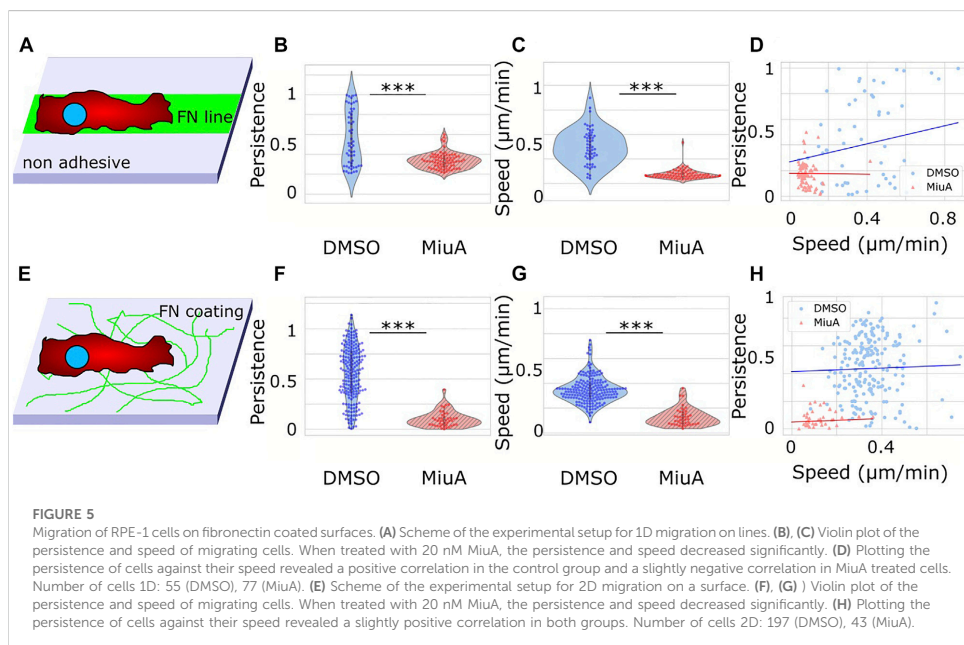


than control cells. The spreading area increased by a factor of 1.5 from 1,693.06 μm² in untreated cells to 2,605.78 μm² in MiuA treated cells (Figure 4B).

Migration behavior and position of nuclei

To understand how elongated actin filaments, a higher number of focal adhesions and larger spreading areas affect the migration behavior of RPE-1 cells, we placed cells on fibronectin lines of 10 μm width as well as on a fibronectin coated glass surface and recorded their migration behavior (Figure 5). RPE-1 cells were chosen for

their mesenchymal migration properties and their use in other migration studies (Maiuri et al., 2015; Terriac et al., 2019). We tracked cellular movements by staining the nuclei with Hoechst and taking pictures every 5 min. We analyzed the resulting trajectories using the ImageJ plug in TrackMate. Upon treatment with MiuA, cellular movement in 1D decreased significantly from 0.372 μm/min in the control case to 0.09 μm/min in the MiuA treated cells (Figure 5C) as well as the persistence of cellular movement, which decreased from 0.442 in untreated cells to 0.168 in cells exposed to MiuA (Figure 5B). Kymographs of those cells also showed a reduction in membrane activity during migration (Supplementary Figure S2). The same effect occurred in cells



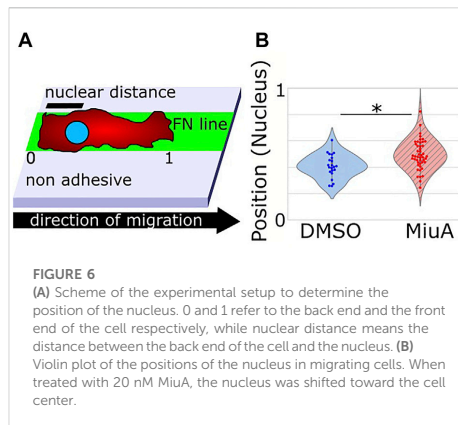
migrating on a fibronectin coated glass surface. Their speed and persistence decreased after treatment with MiuA from 0.346 $\mu\text{m}/\text{min}$ to 0.124 $\mu\text{m}/\text{min}$ and from 0.444 to 0.079, respectively (Figures 5F,G). We also calculated the Pearson R correlation value between the speed and the persistence of migrating cells (Figures 5D,H), revealing an R value of 0.35 for untreated cells and -0.01 for MiuA treated cells in 1D. In the 2D case the R value stayed the same for both conditions at 0.06.

We also performed a 2D migration experiment using MEFs and observed the same effects (Supplementary Figure S3). The mean speed and persistence of MEF cells dropped from 0.259 $\mu\text{m}/\text{min}$ and 0.311 to 0.125 $\mu\text{m}/\text{min}$ and 0.153 respectively.

Additionally, we measured the position of the nuclei in RPE-1 cells during migration on fibronectin lines. We imaged the nuclei by Hoechst staining and analyzed the position within the cell using ImageJ. Interestingly, the position of the nuclei of cells treated with MiuA significantly shifted toward the cell center (Figure 6B).

Discussion

Actin, which is omnipresent in eukaryotic cells, has various in living systems (Thomas and John, 2009). Therefore, altering aspects of actin always affects many aspects of the entire system, increasing the challenge of understanding single actions



of actin in cells such as the role of actin filament length in cell migration, proliferation etc. One way to study actin is by compounds which stabilize or destabilize actin by altering the polymerization rates. Although both types of such compounds are well known since the end of the 20th century, research has mainly focused on actin destabilizing compounds like latrunculin A or

cytochalasin D (Risinger and Du, 2020). Nevertheless, it is not sufficient to only destabilize actin, but means of stabilizing actin are needed. However, stabilizing actin filaments remains challenging, as the two most prominent compounds, phalloidin and jasplakinolide, have serious disadvantages. Phalloidin cannot pass through cell membrane, rendering it impossible to use this compound in living cells. The second compound, jasplakinolide, stabilizes actin filaments in living cells. However, this stabilizing effect relies on the concentration and the duration of treatment (Ou et al., 2002). Therefore, handling jasplakinolide is challenging and often not reproducible. In our study we used a synthetic sample of the natural compound miuraenamamide A, a secondary metabolite of a halophilic myxobacterium isolated from soil samples of the Japanese coast (Iizuka et al., 2006). This marine actin stabilizer (Ojika et al., 2008) can, similar to jasplakinolide, pass through the cell membrane and is therefore suitable for observing living cells. Due to its structural similarity to other cyclodepsipeptides, MiuA also targets actin filaments (Iizuka et al., 2006; Ojika et al., 2008; Sumiya et al., 2011; Karmann et al., 2015; Ojima et al., 2016). We therefore used MiuA to test the effect of actin stabilization on the dynamic behavior of actin inside living cells. The overall dynamics of actin filaments were decreased by treatment with MiuA. We showed that the half time recovery of actin filaments in MiuA treated cells increased in FRAP measurements meaning that the dynamics of the filaments decreased. These data are supported by the results of Florian A. Gegenfurtner and colleagues showing that the diffusion of actin monomers in the cytoplasm of MiuA treated cells is reduced when compared to the control group (Gegenfurtner et al., 2018). Following the change in actin dynamics due to MiuA, we wanted to see how the architecture of actin filaments in living cells might be affected. In 2019, Shuaijun Wang and colleagues showed that actin filaments *in vitro* exposed to MiuA increased their elongation rate and overall length, as well as the number of filaments (Wang et al., 2019). This finding matches our observations in living RPE-1 cells, where treatment with MiuA induces longer actin filaments. Because these data were taken on micropatterns, we then moved to RPE-1 cells on 2D and compared their adhesion capacity regarding number of focal adhesions and spreading area. Christina Moser et al. observed no significant change in the spreading area of HUVECs treated with MiuA after 90 min of spreading time (Moser et al., 2017). This finding is in contrast to our study, where we found that RPE-1 cells exposed to MiuA occupy a larger area than the control group. One explanation for such differences might be the different time scales used in our experiments. As we seeded the cells on fibronectin coated glass surfaces, we allowed the cells to fully adhere for at least 4 h. We then treated them with MiuA for 1 h prior to fixing the cells with 4% PFA. The longer adhesion time might explain the significant difference in the spreading area of MiuA treated cells compared to the work of Moser et al. We also counted the number of focal adhesions per cell and found a significantly increased number. Nevertheless, the interplay

between the spreading area and the number of focal adhesions remains open for further studies. Adhesion and actin are directly linked to migration. One study using MiuA investigated 2D chemotaxis in HUVECs treated with MiuA and showed no change in migration speed (Moser et al., 2017; Wang et al., 2019). However, in our study, RPE-1 and MEF cells treated with MiuA showed a significant decrease in mean speed compared to the control group. This difference between both studies might be because we investigated 1D and 2D migration on fibronectin without chemotaxis. Regarding other possibilities of altering the migration of cells, Ali et al. (2021) showed that jasplakinolide affects the phosphorylation of alpha-1-syntrophin, which in turn leads to a decrease in motility. As MiuA and jasplakinolide have a similar molecular structure (Karmann et al., 2015), MiuA might also be capable of interfering with the alpha-1-syntrophin pathway. We also reproduced the correlation between speed and persistence that have been shown by Maiuri et al. (2015). Thus fast cells in 1D migrate in a more persistent manner. The treatment with MiuA, as well as the migration on 2D surfaces in general resulted in low migration speed paired with R values close to zero, meaning we could draw no conclusion about the correlation between these two values. As actin plays an active role in the positioning of the nucleus during cell migration (Thomas and John, 2009; Gardel et al., 2010; Calero-Cuenca et al., 2018), we measured the position of the nuclei in the migrating cells while being on fibronectin lines and under treatment with MiuA. Because disassembly of actin filaments is a crucial step during mesenchymal migration (Louise, 1999) and the organization of the actin network is linked to the position of cell organelles (Gardel et al., 2010) we hypothesized that the position of the nucleus during migration might also be affected by a change in the actin network. Indeed, we measured a repositioning of the nucleus toward the cell center under MiuA treatment. Our data are supported by the finding that the treatment of fibroblasts with jasplakinolide resulted in an increase in both cell body movement and in lamellipodia (Louise, 1999). As MiuA and jasplakinolide show similar effects on the actin cytoskeleton and their molecular structures are related (Karmann et al., 2015), we assume that MiuA might also affect the mechanism responsible for positioning the nucleus. However, further investigations are needed as the mechanism itself and its link to the cytoskeleton were not revealed by our study.

In this work we show that miuraenamamide A is a powerful tool to affect the dynamics and architecture of the actin cytoskeleton. Following this finding, we showed that actin filaments play a crucial role in the positioning of nuclei in migrating cells, as treatment with MiuA induced not only longer filaments but also shifted the nucleus toward the cell center. Furthermore, we could see that longer filaments lead to cells occupying a larger area and increasing their number of focal adhesions. In the future, we and others will be able to use this tool to further understand the role of actin in living cells.

Data availability statement

The raw data supporting the conclusions of this article will be made available by the authors, without undue reservation.

Author contributions

CB, FL, and DG contributed to conception and design of the study. CB performed the experiments and the analysis of data. UK provided the compound. All authors contributed to manuscript revision, read, and approved the submitted version.

Acknowledgments

We gratefully thank Dr. Jennifer Herrmann and Prof. Dr. Rolf Müller for useful follow up discussions. We further thank the DFG for financial support (CRC 1027).

References

- Ali, R., Mir, H. A., Hamid, R., Shah, R. A., Khanday, F. A., Bhat, S. S., et al. (2021). Jaspalakinolide attenuates cell migration by impeding alpha-1-syntrophin protein phosphorylation in breast cancer cells. *Protein J.* 40 (2), 234–244. doi:10.1007/s10930-021-09963-y
- Azioune, A., Carpi, N., Tseng, Q., Théry, M., and Piel, M. (2010). "Chapter 8 - protein micropatterns: A direct printing protocol using deep UVs," *Methods Cell Biol.* 97, 133–146. doi:10.1016/S0091-679X(10)97008-8
- Calero-Cuenca, F. J., Janota, C. S., and Gomes, E. R. (2018). Dealing with the nucleus during cell migration. *Curr. Opin. Cell Biol.* 50, 35–41. doi:10.1016/j.cob.2018.01.014
- Ershov, D., Phan, M.-S., Pylvänäinen, J. W., Rigaud, S. U., Le Blanc, L., Charles-Orszag, A., et al. (2021). Bringing TrackMate into the era of machine-learning and deep-learning. *bioRxiv* 2021. doi:10.1101/2021.09.03.458852
- Fritzsche, M., and Charras, G. (2015). Dissecting protein reaction dynamics in living cells by fluorescence recovery after photobleaching. *Nat. Protoc.* 10 (5), 660–680. doi:10.1038/nprot.2015.042
- Gardel, M. L., Schneider, I. C., Aratyn-Schaus, Y., and Waterman, C. M. (2010). Mechanical integration of actin and adhesion dynamics in cell migration. *Annu. Rev. Cell Dev. Biol.* 26 (1), 315–333. doi:10.1146/annurev.cellbio.011209.122036
- Gegenfurtner, F. A., Zisis, T., Al Dana, N., Schrimpf, W., Kliesmete, Z., Ziegenhain, C., et al. (2018). Transcriptional effects of actin-binding compounds: The cytoplasm sets the tone. *Cell. Mol. Life Sci.* 75 (24), 4539–4555. doi:10.1007/s00018-018-2919-4
- Iizuka, T., Fudou, R., Jojima, Y., Ogawa, S., Yamanaka, S., Inukai, Y., et al. (2006). Miuraenamides A and B, novel antimicrobial cyclic depsipeptides from a new slightly halophilic myxobacterium: Taxonomy, production, and biological properties. *J. Antibiot.* 59 (7), 385–391. doi:10.1038/ja.2006.55
- Karmann, L., Schultz, K., Herrmann, J., Müller, R., and Kazmaier, U. (2015). Total syntheses and biological evaluation of miuraenamides. *Angew. Chem. Int. Ed. Engl.* 54 (15), 4502–4507. doi:10.1002/anie.201411212
- Louise, P. C. (1999). Role of actin-filament disassembly in lamellipodium protrusion in motile cells revealed using the drug jaspalakinolide. *Curr. Biol.* 9 (19), 1095–1105. doi:10.1016/S0960-9822(99)80478-3
- Maiuri, P., Rupprecht, J.-F., Wieser, S., Rupprecht, V., Bénichou, O., Carpi, N., et al. (2015). Actin flows mediate a universal coupling between cell speed and cell persistence. *Cell* 161 (2), 374–386. doi:10.1016/j.cell.2015.01.056
- Moser, C., Rüdiger, D., Förster, F., von Blume, J., Yu, P., Kuster, B., et al. (2017). Persistent inhibition of pore-based cell migration by sub-toxic doses of

Conflict of interest

The authors declare that the research was conducted in the absence of any commercial or financial relationships that could be construed as a potential conflict of interest.

Publisher's note

All claims expressed in this article are solely those of the authors and do not necessarily represent those of their affiliated organizations, or those of the publisher, the editors and the reviewers. Any product that may be evaluated in this article, or claim that may be made by its manufacturer, is not guaranteed or endorsed by the publisher.

Supplementary material

The Supplementary Material for this article can be found online at: <https://www.frontiersin.org/articles/10.3389/fcell.2022.931880/full#supplementary-material>

- miuraenamide, an actin filament stabilizer. *Sci. Rep.* 7 (1), 16407. doi:10.1038/s41598-017-16759-7
- Ojika, M., Inukai, Y., Kito, Y., Hirata, M., Iizuka, T., Fudou, R., et al. (2008). Miuraenamides: Antimicrobial cyclic depsipeptides isolated from a rare and slightly halophilic myxobacterium. *Chem. Asian J.* 3 (1), 126–133. doi:10.1002/asia.200700233
- Ojima, D., Yasui, A., Tohyama, K., Tokuzumi, K., Toriihara, E., Ito, K., et al. (2016). Total synthesis of miuraenamides A and D. *J. Org. Chem.* 81 (20), 9886–9894. doi:10.1021/acs.joc.6b02061
- Ou, G. S., Chen, Z. L., and Yuan, M. (2002). Jaspalakinolide reversibly disrupts actin filaments in suspension-cultured tobacco BY-2 cells. *Protoplasma* 219 (3), 168–175. doi:10.1007/s007090200018
- Risinger, A. L., and Du, L. (2020). Targeting and extending the eukaryotic druggable genome with natural products: Cytoskeletal targets of natural products. *Nat. Prod. Rep.* 37 (5), 634–652. doi:10.1039/c9np00053d
- Schindelin, J., Arganda-Carreras, I., Frise, E., Kaynig, V., Longair, M., Pietzsch, T., et al. (2012). Fiji: An open-source platform for biological-image analysis. *Nat. Methods* 9 (7), 676–682. doi:10.1038/nmeth.2019
- Sumiya, E., Shimogawa, H., Sasaki, H., Tsutsumi, M., Yoshita, K., Ojika, M., et al. (2011). Cell-morphology profiling of a natural product library identifies bisbromoamide and miuraenamide A as actin filament stabilizers. *ACS Chem. Biol.* 6 (5), 425–431. doi:10.1021/cb1003459
- Terriac, E., Schütz, S., and Lautenschläger, F. (2019). Vimentin intermediate filament rings deform the nucleus during the first steps of adhesion. *Front. Cell Dev. Biol.* 7, 106. doi:10.3389/fcell.2019.00106
- Théry, M. (2010). Micropatterning as a tool to decipher cell morphogenesis and functions. *J. Cell Sci.* 123 (24), 4201–4213. doi:10.1242/jcs.075150
- Thomas, D. P., and John, A. C. (2009). Actin, a central player in cell shape and movement. *Science* 326 (5957), 1208–1212. doi:10.1126/science.1175862
- Tinevez, J.-Y., Perry, N., Schindelin, J., Hoopes, G. M., Reynolds, G. D., Laplantine, E., et al. (2017). TrackMate: An open and extensible platform for single-particle tracking. *Methods* 115, 80–90. doi:10.1016/j.ymeth.2016.09.016
- Wang, S., Crevenna, A. H., Ugru, I., Marion, A., Antes, I., Kazmaier, U., et al. (2019). Actin stabilizing compounds show specific biological effects due to their binding mode. *Sci. Rep.* 9 (1), 9731. doi:10.1038/s41598-019-46282-w
- Wang, S., Meixner, M., Yu, L., Zhuo, L., Karmann, L., Kazmaier, U., et al. (2021). Turning the actin nucleating compound miuraenamide into nucleation inhibitors. *ACS Omega* 6 (34), 22165–22172. doi:10.1021/acsomega.1c02838

5.1 Additional data

Besides the migration data on RPE-1 and MEF cells on fibronectin lines, I also measured the position of the nucleus in migrating RPE-1 cells. As already described in the article above (see page 42), I fixed RPE-1 cells migrating on fibronectin lines and measured the distance between their back end and the center of their nuclei. I normalized this length in a way that 0 represents the back end and 1 the front end of the cell. Additionally, I placed RPE-1 cells in PDMS microchannels (size: $10 \times 10 \mu\text{m}$) and fixed them as well to measure the position of their nuclei. These data can be seen in Figure 5.1.

In both cases it is evident that the treatment with MiuA induced a shift of nuclear position towards the center of the cell. Untreated cells had their nucleus mostly in the first third of their cell body (Figure 5.1 left side), which was shifted after the treatment with MiuA (Figure 5.1). As the aforementioned article (see page 42) already discussed, I hypothesize this effect to be linked to the altered actin filament length and dynamics through MiuA. The reduction of actin polymerisation and the increase in actin filament length combined with the retrograde flow of actin might induce an accumulation of actin at the back of the cell. This might result in a higher pressure at the back, that eventually pushes the nucleus more towards the cell center.

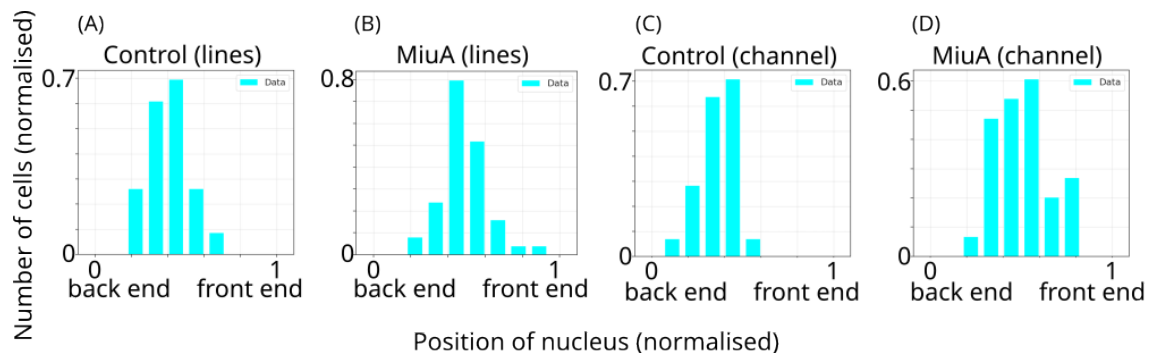


Figure 5.1: Position of nucleus in migrating RPE-1 cells. Cells on fibronectin lines (already presented in [12]) untreated (A) or treated with MiuA (B). Cells in PDMS channels (size: $10 \times 10 \mu\text{m}$) untreated (C) or treated with MiuA (D). Concentration of MiuA in all experiments: 20 nM. After treatment with MiuA the position of the nucleus is shifted towards the center of the cell in both cases: cells on fibronectin lines, and cells in PDMS channels. Number of cells: Lines: 55 (control), 77 (MiuA); Channels: 101 (control), 119 (MiuA).

Faculty of Natural Sciences and Technology**Cumulative form of the dissertation****Template for the confirmation of the proportion of co-authors**Title of the dissertation (working title):**Cytoskeletal aspects of cellular migration**Article to be included:

C. A. Baltes, F. Nolle, K. M. Kaiser, E. Gjana, K. Sander, K. Jacobs, R. J. Hawkins and F. Lautenschläger
Modulation of Cellular Adhesion, Contractility and Migration by MiuA: A Comprehensive Analysis of Its Biochemical Impact

Quality of the publication:

Research article

Review process or publication status:

To be submitted

Explanation of the contributions of the co-authors:

Carsten Alexander Baltes: Designed experiments, prepared Figures (Figure 1, Figure 2, Figure 3, Figure 4, Figure 5), wrote the manuscript and the SI document on how to derive the strain energy from changes in pattern area.

Conducted the following experiments and data analysis:

- Designing contractility screening experiment: 50%
- Preparation of hydrogels for contractility screening: 50%
- Deriving the formula for contractile energy (SI): 100%
- Pattern based contractility screening (PaCS): 100%
- Preparation and cell culture of MEF and RPE-1 cells: 60%
- Phalloidin staining of MEF cells: 100%
- Preparation of fibronectin coated lines: 100%
- Preparation of PDMS microchannels: 100%
- Migration experiments:
 - RPE-1 (fibronectin coated lines): 100%
 - RPE-1 (PEG coated PDMS channels): 100%
 - Neutrophils (PEG coated PDMS channels): 100%
- Focal adhesion experiments (RPE-1):
 - Immunostaining (paxillin): 100%
 - Measurement of focal adhesions: 100%
 - Analysis: 100%
- Focal adhesions in PEG coated PDM channels: 100%
- Coding (python3 scripts) 100%
- Trypsin assay 100%

Friederike Nolle: Wrote sections “Single-Cell Force Spectroscopy” and 50% of “Adhesion Forces” from the manuscript. Corrected and improved the manuscript.

Conducted the following experiments, analyzed and interpreted the data:

- Single-Cell force spectroscopy (Fluid FM): 100%

Kathi Michèle Kaiser: Conducted the following experiments and their respective analysis:

- Focal adhesion parameters in MEF cells: 100%
- Preparation and cell culture of MEF and RPE-1 cells: 20%

Erbara Gjana: Designed contractility screening experiments (50%) improved the manuscript and conducted the following experiments:

- Preparation of hydrogels for contractility screening: 25%

Kristin Sander: Conducted the following experiments:

- Preparation of hydrogels for contractility screening: 25%
- Preparation and cell culture of RPE-1 cells: 20%

Karin Jacobs: Supervised the single-cell force spectroscopy experiments and secured funding. Improved the manuscript.

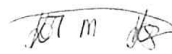
Rhoda Joy Hawkins: Supervised the calculations for the contractility screening assay.

Franziska Lautenschläger: Generated concepts, designed experiments, corrected and improved the manuscript. Secured funding and supervised the study.

Signature of the doctoral candidate
(Carsten Alexander Baltés)



Signature of the co-authors

Co-authors	Signature
Friederike Nolle	
Kathi M. Kaiser	

Erbara Gjana	
Kristin Sander	<i>K. Sander</i>
Karin Jacobs	<i>Karin Jacobs</i>
Rhoda J. Hawkins	<i>Rhoda J. Hawkins</i>
Franziska Lautenschläger	

1 Modulation of Cellular Adhesion, Contractility, and 2 Migration by MiuA: A Comprehensive Analysis of Its 3 Biomechanical Impact

4 Carsten Alexander Baltes ¹, Friederike Nolle ^{1,2}, Kathi Michèle Kaiser ¹, Erbara Gjara ¹, Kristin Sander¹,
5 Karin Jacobs ^{1,5}, Rhoda Joy Hawkins ^{3,4} and Franziska Lautenschläger ^{1,5,*}

6 ¹ Experimental Physics, Saarland University, Saarbrücken, Germany

7 ² Department of Electrical Engineering, Trier University of Applied Science, Schneidershof, Trier, Germany

8 ³ Department of Physics and Astronomy, University of Sheffield, Sheffield, United Kingdom

9 ⁴ African Institute for Mathematical Science, Accra, Ghana

10 ⁵ Centre of Biophysics, Saarland University, Saarbrücken, Germany

11 * Correspondence: f.lautenschlaeger@physik.uni-saarland.de (FL)

12 Abstract

13 Cellular adhesion and contractility are essential for cell movement. In this study, we investigate the
14 effects of actin stabilization on adhesion properties, contractility, and cell migration. For this, we use the
15 recently synthesized actin stabilizer miuraenamamide A (MiuA), which has been discussed as a more reliable
16 alternative to the otherwise commonly used actin stabilizer jasplakinolide. This work investigates the
17 number and size of focal adhesions in RPE-1 cells and uses single-cell force spectroscopy to evaluate the
18 adhesion properties of those cells after MiuA treatment. We show that MiuA increases the number of focal
19 adhesions while decreasing their size and reduces adhesion energy and force. Additional investigation on
20 its effects on the contractility of RPE-1 cells by measuring their contractile energy using pattern-based
21 contractility screening (PaCS) revealed no significant change in contractility after MiuA treatment. Finally,
22 confining RPE-1 cells in PDMS microchannels and analyzing their migration after treatment with MiuA,
23 show that neither their speed nor their persistence is affected by MiuA. To assure that these effects are not
24 specific to RPE-1 cells, we also analyzed the focal adhesions of MEF cells and the amoeboid migration of
25 neutrophils under the influence of MiuA. Both MEF cells and neutrophils showed the same results as the
26 RPE-1 cells. Our measurements indicate that, although altering focal adhesions significantly reduces
27 adhesion, it does not impact cell contractility. This finding also clarifies why amoeboid migration, which
28 operates independently of adhesion, remains unaffected. Additionally, it explains the previously observed
29 reduction in mesenchymal migration, which relies on adhesion-based mechanisms.
30

31 **Keywords:** actin; stabilization; migration; adhesion; contractility
32

33 Introduction

34
35 The ability of cells to migrate is essential for the completion of a multitude of cellular processes. To study
36 cell migration, Lämmermann et al. put forth a model that encompasses three parameters: Actin
37 polymerization, cellular adhesion, and cell contractility[1].

38 In all three parameters, the cytoskeletal protein actin plays a crucial role. It is therefore a prominent target
39 when investigating the migration behavior of cells. A variety of compounds has been employed to modify
40 the structure and dynamics of the actin network in cells. While these compounds have been used to study
41 the migration behavior of cells in general, their effects on the underlying migration parameters mentioned
42 above remain unclear.

43 Substances that depolymerize the actin network, such as cytochalasin D or latrunculin A, have been used
44 to reliably study the effects of a disassembled actin network on cellular functions, including migration [2–
45 8]. Nevertheless, the stabilization of actin filaments has proven to be a significant challenge. The two most
46 prominent actin stabilizing agents are phalloidin and jasplakinolide. The first is unable to pass through the
47 cell membrane [9], while the effectiveness of the second is dependent on the concentration used and the
48 duration of exposure, with optimal results requiring precise calibration [10].

49 Recently, a new compound, miuraenamamide A (MiuA), has been employed in studies to stabilize actin
50 filaments in living cells and in vitro [11–15]. This new tool allows the investigation on the effects of actin
51 stabilization in migration and its underlying mechanisms.

52 In an earlier study, we have already shown that MiuA reduces actin filament dynamics, thus altering the
53 first of the aforementioned migration parameters: the polymerization rate [16]. Now, we wanted to
54 understand the effects of the actin stabilizing compound MiuA on the remaining two migration parameters:
55 adhesion and contractility. We therefore performed adhesion and contractility measurements on RPE-1 and
56 partially on MEF cells which are both migrating using adhesions (mesenchymal migration).

57
58 After we confirmed that the effects of MiuA on the actin filament length is the same in RPE-1 and MEF cells
59 (Fig 1.) we measured the size and number of focal adhesions in both cell types. Focal adhesions are clusters
60 of proteins, including integrins, paxillin, vinculin, and talin [17–22]. These clusters form the connection
61 between the outer extracellular matrix and the inner actin cytoskeleton. We therefore expected that by
62 targeting actin by MiuA we would have an indirect effect on focal adhesions. And indeed, the treatment of
63 RPE-1 and MEF cells with MiuA increased the number of focal adhesions while reducing the size of
64 individual focal adhesions (Fig 2.). Since the focal adhesions are required for the cell to adhere to a substrate,
65 we also expected that an alteration of focal adhesions would reflect in alterations in the adhesion force and
66 adhesion energy, which we could confirm using single-cell force spectroscopy: Treating RPE-1 cells with
67 MiuA led to a decrease in adhesion force and energy (Fig 3.). To investigate the last migration parameter -
68 the cell contractility-, we performed pattern-based contractility screening (PaCS) on RPE-1 cells.
69 Interestingly, the treatment with MiuA did not change the contractile energy and therefore the contractility
70 of RPE-1 cells (Fig 4.). Taken together, MiuA affects the size and number of focal adhesions as well as the
71 adhesion force and energy, while leaving the contractility unaffected.

72 To combine now our results of the effect of MiuA on migration parameters with the migration itself, we
73 next compared different types of migration under the influence of MiuA.

74 In earlier work, we have tested the effect of MiuA on cells which migrate using adhesions in order to move
75 (mesenchymal migration) and saw significant reduction under the treatment of MiuA [16]. We now
76 understand this result very well, since we found the described alterations on adhesion. But would MiuA
77 then also influence migration types which do not rely on adhesion? Such a migration type is called
78 amoeboid migration, where cells move by unspecific friction forces but not by adhesions [23]. We
79 speculated that this type of migration would not be altered by MiuA. Fortunately, we were able to test
80 amoeboid migration on the same cell type as mesenchymal migration using the RPE-1 cell line, because
81 RPE-1 cells are known to be able to switch between migration modes depending on the environment [24].

82
83
84 We therefore now studied RPE-1 cells inside pll-g-PEG coated microchannels (Fig 5.), a setting which
85 forces them into amoeboid migration. We repeated the same experiments with a common model cell line

86 for amoeboid migration: with neutrophils [25]. Neutrophils serve this study as a control group to assure
 87 that the reported results on amoeboid migration are not depending on the used cell line. And as we had
 88 expected, the treatment with MiuA did not affect the migration properties of amoeboid migrating cells.
 89 Taken together, our findings suggest that the effect of MiuA on the length of actin filaments and focal
 90 adhesions is a pivotal factor in mesenchymal migration but not in amoeboid migration, as it solely
 91 influences the parameters which are essential to adhesion-based migration.

92
 93
 94

95 **Materials and Methods**

96 **Cell Culture**

97 RPE-1 cells, wildtype and transfected with the LifeAct mCherry marker (as described by Maiuri et al. in
 98 2015 [24]), and MEF cells transfected with GFP-vinculin were cultured at 37 °C and 5% CO₂ in Dulbecco's
 99 Modified Eagle Medium Nutrient Mix F12 with 10% FBS, 1% GlutaMax, and 1% Penicillin Streptomycin
 100 (Thermo Fisher). The RPE-1 cells were kindly gifted by the lab of Mathieu Piel, Institute Curie, Paris, while
 101 the MEF GFP vinculin cells were kindly given by Dr. Jennifer Kasper, Leibniz-Institute for New Materials.
 102 HL60 cells (bought from ATCC) were cultured at 37 °C and 5% CO₂ in RPMI 1640 Medium (Thermo Fisher)
 103 with 10% FBS, 1% GlutaMax, and 1% Penicillin Streptomycin (Thermo Fisher). The HL60 cells were
 104 differentiated by adding 1.3% of DMSO to the medium and incubating them for two days. A list of the cells
 105 used in this study can be seen in Table 1.

106 **Table 1.** List of the cells used in this study.

Cell line	Info	Provider	Usage
RPE-1 LifeAct mCherry	hTERT RPE-1 cells transfected with LifeAct mCherry	Lab of Matthieu Piel (Paris)	Migration assay (channels), Trypsin assay, Focal adhesion staining, FluidFM measurements
RPE-1 wt	hTERT RPE-1 cells (wildtype)	Lab of Matthieu Piel (Paris)	Contractility screening
MEF GFP vinculin	Transfected with GFP vinculin	Dr. Jennifer Kasper, Leibniz-Institute of new materials (Saarbrücken)	Focal adhesion staining, Phalloidin staining
Neutrophils	HL60 cells differentiated into neutrophils	HL60 cells bought from ATCC	Migration assay (channels), Focal adhesion staining

107

108 **Phalloidin Staining**

109 The MEF GFP vinculin cells were allowed to fully spread on a fibronectin-coated glass surface (fibronectin
 110 concentration 25 µg/ml). Then, we treated them with DMSO (control) and 5 nM of MiuA for 1 hour before
 111 we fixed them with 4% PFA, dissolved their membrane using a 0.1% Triton X100 solution, and washed
 112 them three times with PBS. We added a 3% BSA solution to block unspecific binding sites. After one hour,
 113 we added a 1:1000 solution of Phalloidin-iFluor 555 (abcam: ab176756) and 3% BSA for another hour. We
 114 then washed the cells three times with PBS and mounted them with Fluoromount G+DAPI.

115

116 **Focal Adhesion Staining**

117 We took fully spread and adhered RPE-1 LifeAct mCherry cells on fibronectin (25 µg/ml) coated glass and
118 treated them for 1 hour with DMSO (control) or 20 nM MiuA before we fixed them with 4% PFA and
119 dissolved their membrane. Additionally, we treated the RPE-1 LifeAct mCherry cells and the neutrophils
120 with DMSO (control) or 20 nM MiuA before we placed them inside PDMS microchannels (coated with 25
121 µg/ml fibronectin or 100 µg/ml pll-gPEG) and let them enter the channels. After at least 4 hours, we fixed
122 those cells too with 4% PFA and dissolved their membrane. For this, we kept the cells for 10 minutes in a
123 0.1% Triton X100 solution and washed them afterwards three times with PBS. We added a 3% BSA solution
124 to block unspecific binding sites. After one hour, we added a 1:1000 solution of paxillin polyclonal
125 antibodies (ThermoFisher PA-34910) and 3% BSA. After another hour, we washed the cells three times with
126 PBS and mounted them with Fluoromount G+DAPI. For focal adhesions in MEF GFP vinculin cells, we
127 seeded them on a glass coverslip coated with fibronectin (25 µg/ml) and put them in the incubator for at
128 least 4 hours. Once the cells were fully adhered, we treated them with MiuA (5 nM) or DMSO for 1 hour
129 before we fixed them with 4% PFA and mounted them with Fluoromount G+DAPI. All experiments have
130 been repeated three times.
131

132 **Trypsin Assay**

133 RPE-1 LifeAct mCherry cells were seeded on a glass coverslip coated with fibronectin (25 µg/ml) and
134 allowed to fully adhere. After at least four hours of spreading time, we treated the cells for one hour with
135 DMSO (control) or 20 nM of MiuA. We placed the cells inside a microscope with temperature and CO₂
136 control before we added trypsin and imaged the cells for 5 minutes. We took images every 20 seconds. The
137 experiment was repeated three times.

138 **Single-Cell Force Spectroscopy**

139 For the measurement of the adhesion forces of RPE-1LifeAct mCherry cells to fibronectin, tissue culture
140 dishes (TPP, Trasadingen, Switzerland) treated with plasma for 3 minutes were coated with fibronectin (25
141 µg/ml) and incubated for 1 hour at room temperature. After the preparation of the culture dishes, RPE-1
142 LifeAct mCherry cells (10⁶ cells/dish) were added alongside the compound of interest (DMSO or MiuA).
143 The cells were allowed to adhere to the fibronectin for 4 hours in an incubator (37 °C, 5% CO₂). To perform
144 single-cell force spectroscopy outside of a CO₂ incubator, 25 µl of HEPES per 1 ml of cell medium was
145 added to the cell medium.
146 Single-cell force measurements were performed at 37 °C using a Nanowizard IV XP AFM with a CellHesion
147 200 Head (Bruker-JPK, Santa Barbara, CA, USA), a FluidFM microfluid control system V2 Platinum
148 (Cytosurge, Glattburg, Switzerland), and a JPK PetriDishHeater. RPE-1 LifeAct mCherry cells were
149 approached (setpoint 8 nN) with a Cytosurge FluidFM micropipette (aperture 4 µm, stiffness 2 N/m) and
150 immobilized to the micropipette by a vacuum (-500 mbar) while maintaining the micropipette at a constant
151 height or force. The cells were then detached from the fibronectin by retracting the micropipette (z-length
152 50 µm, z-velocity 0.8 µm/s). An inverted-light microscope (Zeiss AG, Oberkochen, Germany) was used to
153 observe the detachment process. The force–distance curves were analyzed using JPK Data Processing
154 Software, version 7.0.128. The experiment was repeated three times.

155 **Contractility Screening**

156 We prepared micropatterned glass coverslips following the protocol of Azioune et al. [26]. First, we cleaned
157 the glass coverslips with ethanol prior to a plasma treatment lasting 3 minutes. Then, we coated the
158 coverslip with a 50 µl droplet of a 100 µg/ml pll-g-PEG solution for 1 hour at room temperature. The

159 pegylated coverslips were washed in pure water and placed on an activated quartz-chromium photomask
 160 (ROSE Fotomasken, Germany) using a 4.5 μl droplet of pure water. After 6 minutes of deep-UV irradiation
 161 (200 nm), the glass coverslips were lifted from the photomask and covered with a 50 μl droplet of a 25 $\mu\text{g}/\text{ml}$
 162 solution of fibronectin mixed with 0.1% BSA+Alexa555 (Thermo Fisher).

163 After at least 30 minutes, we prepared a solution of 200 μl acrylamide, 96 μl bis-acrylamide, and 198.5 μl
 164 PBS; vortexed it; and degassed it with nitrogen for at least 2 minutes. To this, we added 5 μl of a 10% APS
 165 (ammonium persulphate) solution and 0.5 μl TEMED (Tetramethylethylenediamine), before mixing it with
 166 a pipette. Afterwards, we pipetted 50 μl droplets on the patterned glass coverslips and placed an acryl-
 167 silanized coverslip on top. We waited at least 15 minutes before we immersed the coverslips in PBS for a
 168 minimum of 1 hour to allow the hydrogel to swell. After this, we removed the top coverslip, which was
 169 attached to the gel and the micropatterns. We seeded 100,000 RPE-1 wildtype cells on each coverslip and
 170 placed them in the incubator overnight. The next day, we treated them for 1 hour with DMSO (control) or
 171 20 nM of MiuA before we fixed the cells with 4% PFA. Each experiment was repeated three times.

172 For the analysis, we measured the change in the micropattern area and calculated the contractile energy
 173 using the following formula (derived from Ghagre et al. and *Theory of Elasticity, 3rd edition* [27,28]):
 174

$$175 \quad E_{contractile} = \frac{E(1 - \sigma)}{(1 + \sigma)((2(1 - \sigma) + \sigma)^2 - \sigma^2) \cdot 3 \cdot \pi^{\frac{3}{2}}} \left(A_i^{\frac{3}{2}} - A_f^{\frac{3}{2}} \right)$$

176 with

- 177 • E= Young's modulus
- 178 • σ = Poisson ratio (here 0.5)
- 179 • A_i = initial pattern area
- 180 • A_f = final pattern area

181

182 Our formula differs from the one used by Ghagre et al., as we reduced the necessary parameters from two
 183 to one by solving the following equilibrium equation for an elastic deformation of a substrate in the xy-
 184 plane:

185

$$186 \quad (1 - 2\sigma)\Delta\vec{u} + \vec{\nabla}(\vec{\nabla} \cdot \vec{u}) = \vec{0}$$

187

188 where we used polar coordinates to describe our displacement vector \vec{u} using only radial displacement.

189

$$190 \quad \vec{u} = (r_f - r_i) \vec{e}_r$$

191

192 The full calculations can be seen in the SI.

193 **Microfabrication of PDMS Microchannels**

194 We mixed the RTV615 A+B compound (Momentive) at a ratio of 10:1 and proceeded as described by
 195 Vesperini et al. [29]. The microchannels had a diameter of 10x10 μm for the RPE-1 LifeAct mCherry cells
 196 and 5x5 μm for the neutrophils. All the cells were treated with 250 ng/ml of Hoechst prior to imaging. The
 197 PDMS channels were coated with 100 $\mu\text{g}/\text{ml}$ poly-L-lysine-grafted poly-ethylene-glycol (=pll-g-PEG) (for
 198 the migration assays and focal adhesion staining) or 25 $\mu\text{g}/\text{ml}$ of fibronectin (for focal adhesion staining)
 199 and washed three times with PBS before they were completely submerged in cell medium. They were kept
 200 for at least one hour in the cell medium before the cells were added. For the experiments, around 100,000
 201 cells were added to one of the loading channels. The cells had already been suspended in cell medium
 202 containing only DMSO (control) or 20 nM of MiuA. Each experiment was repeated three times.
 203

204 **Microscopy**

205 The fixed samples were imaged using a ZEISS Axio observer (base version: epifluorescence, non-confocal,
206 Zeiss AG, Oberkochen, Germany) with a 63x magnification oil objective. Time-lapse images of migrating
207 cells were taken with a Nikon Eclipse Ti microscope using a 10x magnification objective. The temperature
208 inside the microscope's incubation chamber was set to 37 °C and the CO₂ level was kept at 5%. To ensure
209 that there were no fluctuations in the settings, the system was allowed to settle for one hour prior to the
210 start of the experiments. Cell movement was observed by treating living cells with 250 ng/ml Hoechst for
211 30 minutes before the start of the recording. Pictures were taken every five minutes for at least ten hours.

212 **Image Analysis**

213 Image analysis was performed with the open-source software Fiji (ImageJ) [30]. Time-lapse images of
214 migrating cells were analyzed using the plug-in TrackMate [31,32]. The number and size of the focal
215 adhesions were determined via paxillin or vinculin staining. The fluorescence signal was put under a
216 threshold and analyzed afterwards with Fiji's "Analyze particles" function.

217 **Statistical Analysis**

218 Student's t tests were conducted on all experimental data using a home-built Python script (t-test_ind-
219 function from SciPy 1.14.1). The p values were calculated and assigned as follows: no significance (n.s.)
220 $p > 0.05$, * $p < 0.05$, ** $p < 0.01$, and *** $p < 0.001$.
221 All exact p values are included in the supplementary information.
222

223 **English Correction**

224 During the preparation of this work, we used ChatGPT-3 (OpenAI, 2021) and DeepL (DeepL writer, Beta,
225 2024) to improve the language of the manuscript. After using these tools, we reviewed and edited the
226 content as needed and hereby take responsibility for the content of the publication.
227

228 **Results and Discussion**

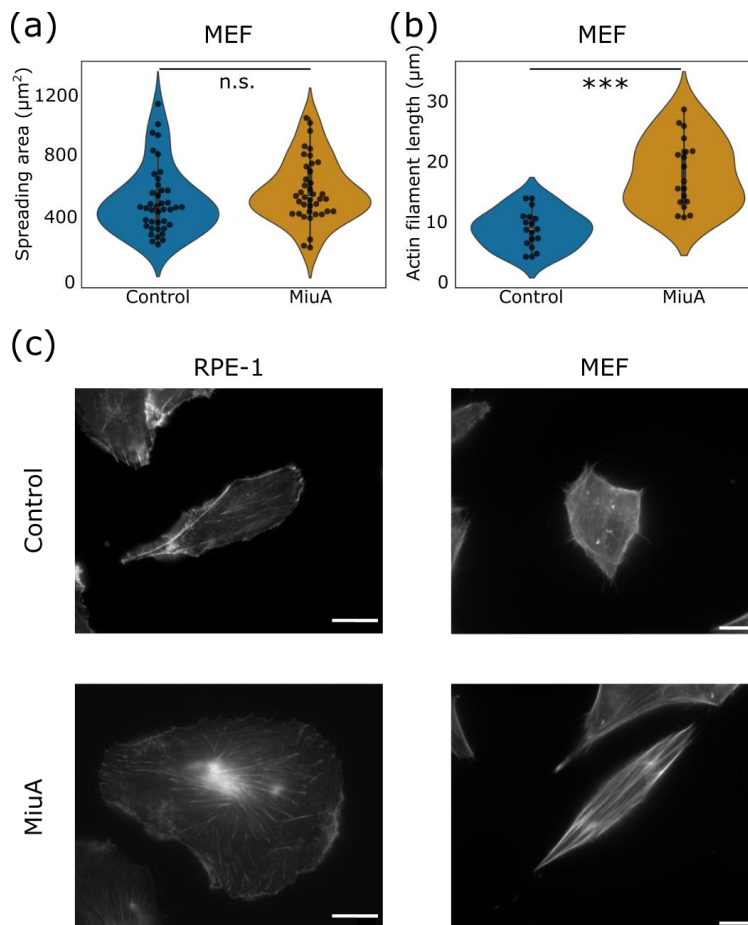
229 **Effects of Miuraenamide A on Focal Adhesions**

230 The actin stabilizer miuraenamide A was first identified in 2006 by Iizuka et al. [15] and subsequently
231 synthesized by Karmann et al. in 2015 [14]. It can enter living cells and stabilizes actin filaments by
232 modifying the conformation of actin monomers, thereby preventing the binding site of cofilin, an actin-
233 severing protein, from being accessed [11].

234 In this work, we first tested whether the actin stabilizing effect of MiuA applies to different cell lines.

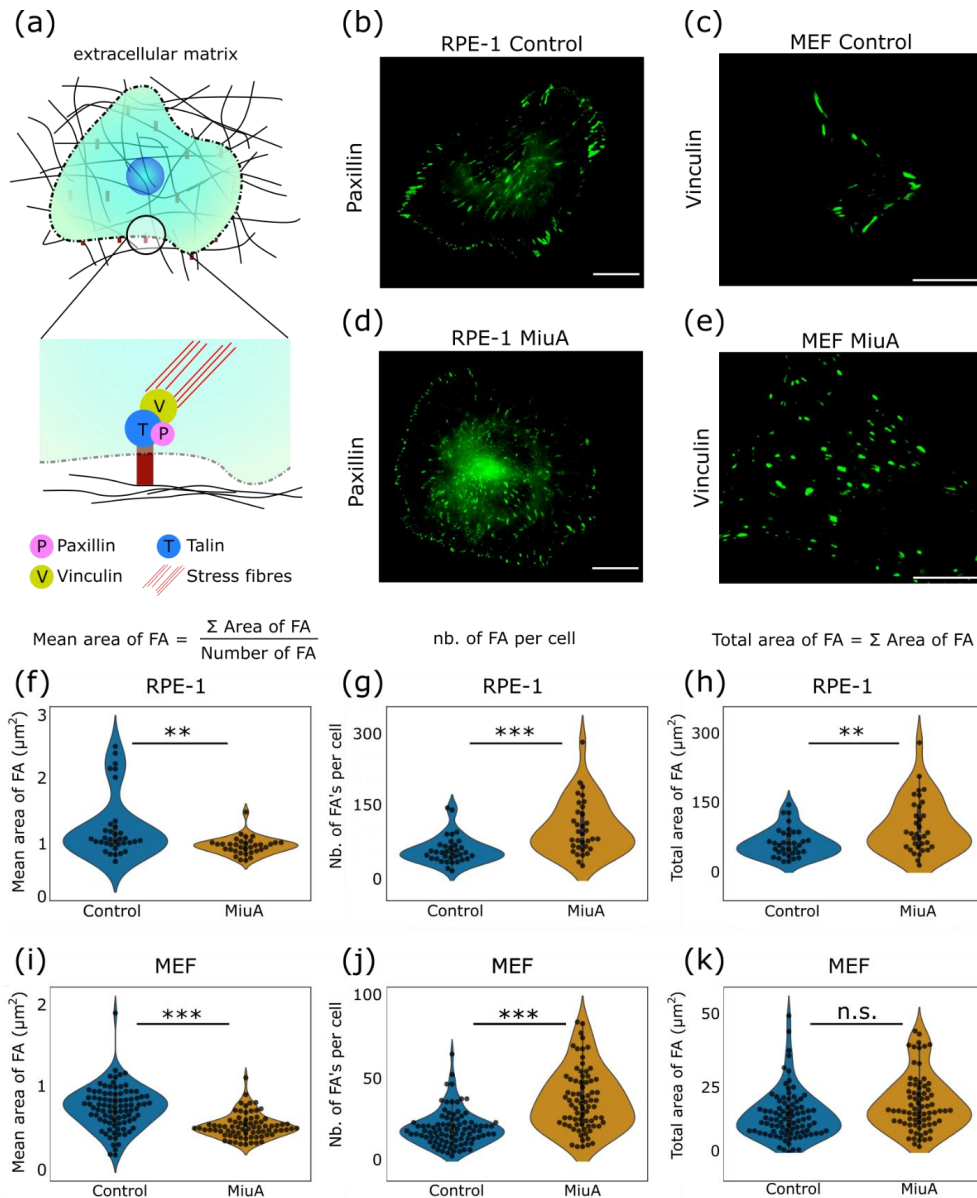
235 We already reported the actin stabilizing effect in RPE-1 cells as well as the reduction of migration in RPE-
236 1 and MEF cells when treated with MiuA [16], however the effect of MiuA on the actin filament length in
237 MEF cells was still missing. We therefore now seeded MEF GFP vinculin cells on glass cover slips coated
238 with fibronectin (25 µg/ml) and allowed them to fully adhere. We found that the MEF cells treated with
239 MiuA did not increase their spreading area (Fig. 1 (a)), remaining at around 550 µm², while the average
240 length of their actin filaments increased from 10.2 µm in untreated cells to 19.1 µm in MiuA treated cells
241 (Fig 2 (b)). This effect partially aligns with the already reported effects in RPE-1 cells [16]: A side-by-side
242 comparison (Fig. 1 (c)) shows an example of fully adhered and spread RPE-1 and MEF cells. In both cell
243 lines the average length of actin filaments increased but only RPE-1 cells showed an additional increase in

244 spreading area. Therefore, we conclude that the treatment with MiuA leads to an elongation and
245 stabilization of actin filaments within living cells regardless of the cell line.
246 Linked to actin filaments are focal adhesions, which represent the connecting side between the cytoskeleton
247 and the extracellular matrix. Although it is established that the size of focal adhesions affects the
248 composition of the stress fibers connected to them [33], the relationship between actin filament length and
249 focal adhesions remains largely unexplored.
250 This study investigates the correlation between actin filament length and focal adhesion number and size..
251 We seeded RPE-1 LifeAct mCherry and MEF GFP vinculin cells on a fibronectin-coated glass surface,
252 treated them with MiuA, and fixed them after they had fully spread (Fig 2. (a)-(e)). Analysis of their focal
253 adhesions showed that the average size of focal adhesions in cells treated with MiuA was smaller than in
254 the control group (Fig 2. (f), (i)). Their average size reduced from 1.258 μm^2 to 0.977 μm^2 in RPE-1 cells and
255 from 0.839 μm^2 to 0.603 μm^2 in MEF cells. However, the average number of focal adhesions increased
256 significantly in RPE-1 cells (Fig 2. (g)) from 57.8 to 103.2, and in MEF cells (Fig 2. (j)) from 21.5 to 39.1 after
257 treatment with MiuA. This resulted in a larger total area of focal adhesions in RPE-1 cells but not in MEF
258 cells (Fig 2. (h), (k)). Since MiuA treatment of MEF cells did not change their spreading area, as it is the case
259 in RPE-1 cells, we conclude that the total focal adhesion area normalized to the spreading area of the cells
260 did not change.
261 Since focal adhesions are crucial for the overall adhesion of cells, we next measured how the adhesion for
262 cells differ depending on the size of their focal adhesions.



263

264 **Fig 1. Effect of MiuA on actin.** (a) Spreading area of MEF GFP vinculin cells seeded on a fibronectin-coated glass
 265 surface; untreated (control) cells and cells treated with 5 nM MiuA. (b) Length of actin filament in MEF GFP vinculin
 266 spread on fibronectin-coated glass surface. (c) Representative images of the actin cytoskeleton in RPE-1 LifeAct
 267 mCherry and MEF GFP vinculin cells when treated with MiuA. Top: control cells. Bottom: MiuA treated cells (20 nM
 268 for RPE-1 LifeAct mCherry and 5 nM for MEF GFP vinculin). Actin filaments in MEF GFP vinculin cells were stained
 269 with Phalloidin-iFluor 555. Scale bar 10 μm .



270

271 **Fig 2. Effects of MiuA on focal adhesions (FAs).** (a) Scheme of a cell adhering to a fibronectin-coated surface.
 272 Epifluorescence images of focal adhesions in RPE-1 LifeAct mCherry cells with paxillin stained (b)(d) as well as MEF
 273 GFP vinculin cells (c)(e). Mean and total values of FA size and their number for RPE-1 cells (f)-(h) and MEF cells (i)-(k).
 274 In both cases, the number and mean area of focal adhesions per cell increased when using MiuA. Data on the number of
 275 focal adhesions taken from Baltes et al. [16]. A statistical analysis was performed using Student's t test. n.s.: $p > 0.05$;
 276 *: $p < 0.05$; **: $p < 0.01$; and ***: $p < 0.005$. Scale bar: 15 μm . Number of cells: RPE-1, 35 control and 34 MiuA; MEF, 90 control
 277 and 76 MiuA.

278 Adhesion Forces

279 Knowing that cells with stabilized and elongated actin filaments express more but smaller focal adhesions,
280 we next quantified the relationship between focal adhesion size and the adhesive force exerted by the cell.
281 Previous studies on single focal adhesions have shown that there is a positive correlation between the size
282 and the force that cells can exert on the underlying matrix [33–38]. However, the effect of average focal
283 adhesion size on the adhesion properties of cells as a whole remains unclear.

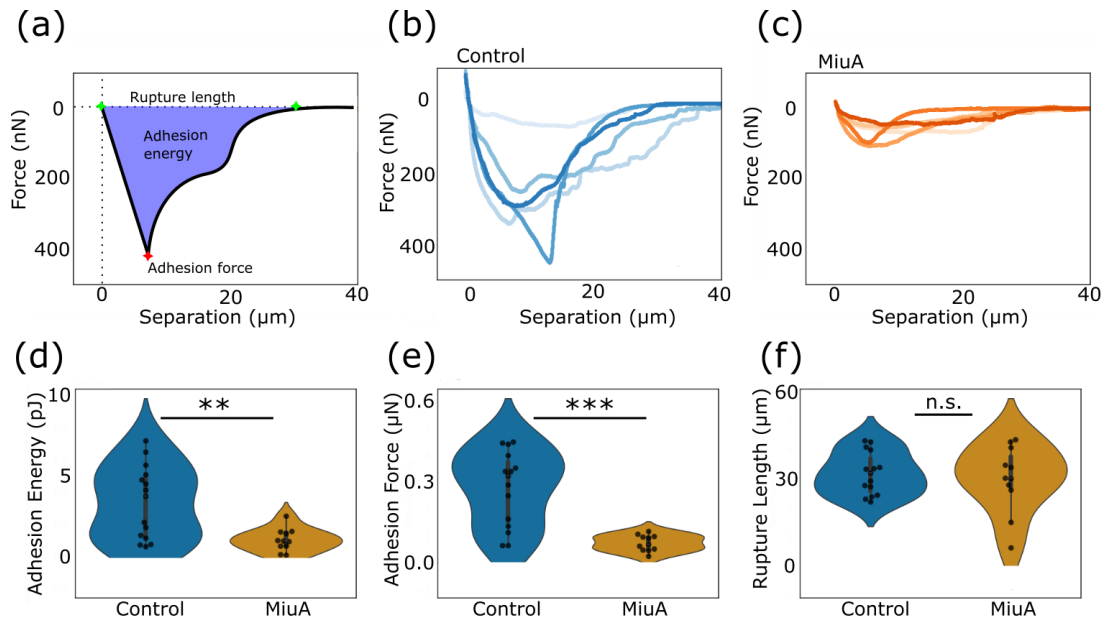
284 In order to measure the adhesion forces of cells, we performed single-cell force spectroscopy, a method well
285 suited to measure the force which is required to detach a single-cell from the substrate to which it adheres
286 [39–41] and gather force-distance curves, allowing us to calculate adhesion parameters like adhesion
287 energy, force, and rupture length (Fig 3 (a)). RPE-1 cells were seeded in a plastic bottom dish coated with
288 fibronectin (25 $\mu\text{g/ml}$) and were allowed to fully spread before force-distance curves were measured. The
289 basic structure of the force-distance curves remained unchanged, but significant differences in adhesion
290 force and energy were observed (Fig 3 (b), (c)). Comparing the specific measurement results, it is evident
291 that the addition of MiuA, significantly reduced the adhesion energy in RPE-1 cells (Fig 3 (d)), where the
292 average value dropped from 3.36 pJ in untreated cells to 1.06 pJ in MiuA treated cells. The average adhesion
293 force shows the same trend (Fig 3 (e)), where untreated cells exhibited an average adhesion force of 0.279
294 μN while MiuA treatment reduced this to approximately 0.074 μN .

295 Interestingly, despite the elongation of actin filaments, the detachment length did not seem to increase,
296 remaining within the same range at around 31 μm for both untreated and MiuA treated cells (Fig 3 (f)).
297 However, the MiuA treated cells displayed a greater spread in detachment length, which could indicate
298 increased instability of the elongated actin filaments.

299 Interestingly, when we used trypsin to detach the cells, we saw that RPE-1 cells treated with MiuA took
300 longer than the untreated cells (Fig S1). This is contrary to the expectations from the before mentioned
301 single-cell force spectroscopy measurements. We theorize that this is due to the different mechanisms used
302 by the two approaches. Using trypsin on cells and recording their detachment, correlates to a chemical effect
303 where adhesion sites are being degraded while single-cell force spectroscopy measurements physically
304 detach cells. In fact, because trypsin is a digestive enzyme that can degrade proteins such as integrins in
305 focal adhesions [42], the time it takes for cells to detach from a substrate after the addition of trypsin
306 correlates with the time of protein degradation, but not adhesion forces or energy. We speculate that due to
307 the increased number of focal adhesion sites in MiuA-treated cells, the degradation process takes longer.

308 Taken together, the pure number and area of focal adhesions does not seem to be the most decisive factor
309 for adhesion force and energy. The reduction and change in the size of the individual focal adhesions
310 appears to be much more decisive for the reduction in adhesion force and energy.

311
312



313

314 **Fig 3. Fluid force measurements (FluidFM) on RPE-1 cells.** (a) Scheme of the force–distance curve and explanation of
 315 adhesion energy, adhesion force, and rupture length. Representation of five representative force–distance curves for
 316 the control (b) and MiuA-treated cells (c). The violin plots of adhesion energy (d), adhesion force (e), and rupture length
 317 (f) show that energy and force are reduced in cells with smaller FAs, while rupture length remains unchanged. A
 318 statistical analysis was performed using Student’s t test. n.s.: $p > 0.05$; *: $p < 0.05$; **: $p < 0.01$; and ***: $p < 0.005$. Number of
 319 cells: 15 control and 11 MiuA.

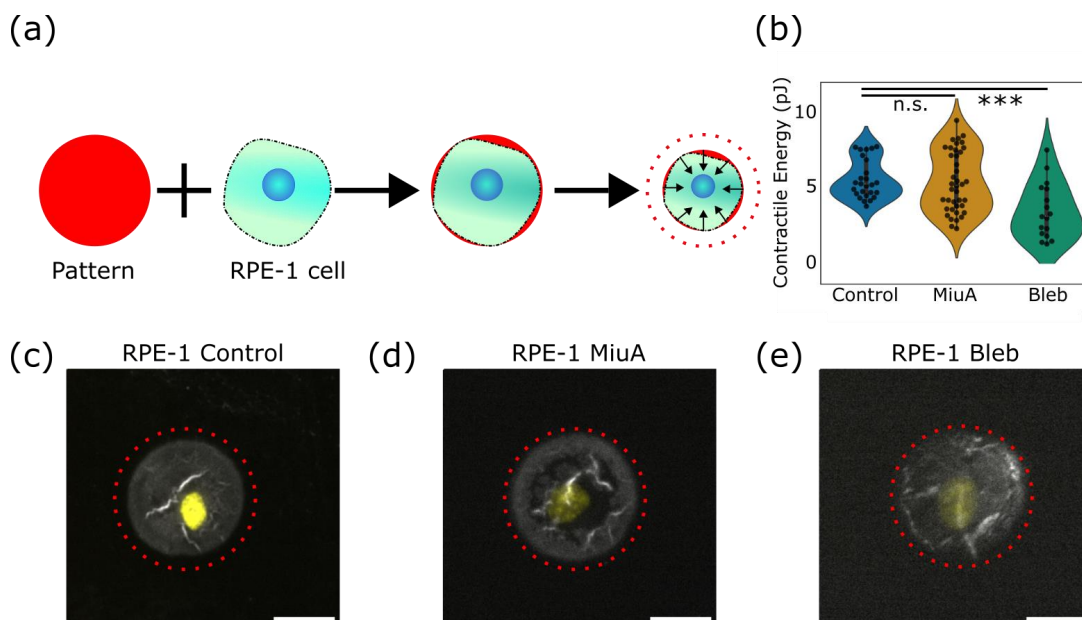
320 Cell Contractility

321 In addition to actin polymerization and cellular adhesion, cells require contraction in all types of migration
 322 [43–47]. Therefore, this work also investigates the influence of MiuA on cell contractility

323 We performed a pattern-based contractility screening assay (PaCS) [27] in which RPE-1 cells are placed on
 324 a polyacrylamide gel (Fig 4 (a)) with a stiffness of 10 kPa. Treating the surface of these gels with fibronectin
 325 allows the cells to adhere only to a specific fluorescently labeled area, known as a micropattern [26]. These
 326 micropatterns are small enough that when a cell contracts, the underlying micropattern and substrate
 327 equally deform. By monitoring this deformation, the quantification of changes in the pattern area can be
 328 detected, thus calculating the contractile energy exerted by the cell to deform the pattern.

329 Interestingly, cells treated with MiuA did not show significant changes in contractile energy compared to
 330 untreated cells (Fig 4 (b)). For untreated cells the average contractile energy was 4.907 pJ, while being
 331 slightly decreased to 4.735 pJ in MiuA treated cells. To verify the sensitivity of our assay, we also treated
 332 cells with 10 μ M blebbistatin, which inhibits the motor protein myosin II. As expected, the treatment with
 333 blebbistatin reduced the contractile energy of RPE-1 cells (Fig 4 (c)-(e)), dropping from approximately 4.80 pJ
 334 in untreated and MiuA treated cells to 2.61 pJ in blebbistatin treated cells. This gives us confidence that our
 335 PaCS assay is sensitive enough to detect changes in contractility and that MiuA did not alter this
 336 contractility.

337 We next tested how amoeboid migration was affected by MiuA.



338

339 **Fig 4. Contractile energy of RPE-1 cells on poly-acrylamide gels.** (a) Scheme of the technique, where a cell adheres to
 340 a pattern on a soft gel and deforms it, with the red dotted lines representing the initial pattern outline. (c), (d), (e)
 341 Representation of a single cell (nucleus in yellow on a soft gel pattern (grey) showing the area before deformation as a
 342 dashed circle (red). When treated with MiuA cells do not show any significant change in contractile energy (b) or pattern
 343 area after deformation, whereas treatment with blebbistatin reduces contractile energy (e) and increases pattern area
 344 after deformation compared to control. Scale bar: 20 μm . Statistical analysis was performed using Student's t test. n.s.:
 345 $p > 0.05$, *: $p < 0.05$, **: $p < 0.01$, ***: $p < 0.005$. Number of cells: Control: 38, MiuA: 40, blebbistatin: 22.

346

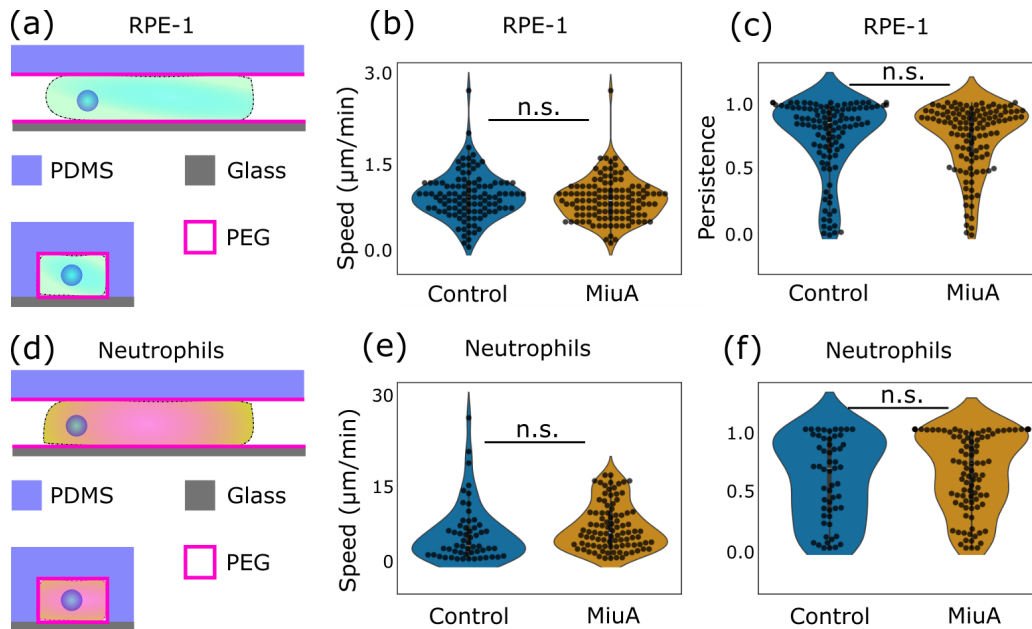
347 Cell Migration

348 Cells can migrate by a non-adhesive process known as amoeboid migration, or friction-based migration,
 349 which does not rely on adhesion but on friction and contractility [1,24,48,49]. RPE-1 cells are known to be
 350 able to switch between migration modes, depending on the environment, and neutrophils are widely used
 351 as a model system for amoeboid migration [24,25]. To investigate the effects of MiuA treatment on
 352 amoeboid migration, we used both cell lines to avoid cell line specific effects. We hypothesized that
 353 amoeboid migrating cells would not be affected by actin filament stabilization as the actin stabilizer MiuA
 354 does not change their contractility. To test this, RPE-1 cells were forced to migrate in an amoeboid mode
 355 [24], which is achieved by placing RPE-1 cells in confining microchannels and record their migration speed
 356 and persistence (Fig 5 (a)-(c)). To ensure that the observed migration mode is amoeboid, we coated the
 357 PDMS microchannels with pll-g-PEG, which is known to hinder adhesion. After seeding the cells and
 358 staining their focal adhesions, we saw that the cells inside pll-g-PEG-coated channels did indeed not express
 359 focal adhesions, unlike cells within fibronectin coated channels (Fig S2). As hypothesized, we did not find
 360 significant changes in the migration of MiuA treated RPE-1 cells in pll-g-PEG-coated channels. The
 361 measured speeds were 0.918 $\mu\text{m}/\text{min}$ and 0.858 $\mu\text{m}/\text{min}$ for untreated cells and MiuA treated cells
 362 respectively, while the persistence in both cases was 0.740. Additionally, we saw a positive correlation
 between the speed and persistence in RPE-1 cells, meaning that faster RPE-1 cells are also more persistent

364 in their movement.

365 To confirm that this behavior is general to amoeboid movement and not just a property specific to RPE-1
 366 cells, we repeated the same migration experiment in pll-g-PEG-coated channels using neutrophils (Fig 5
 367 (d)-(f)). Like RPE-1 cells, neutrophils did not change their migration speed or persistence after the treatment
 368 with MiuA significantly. Their average speed was 4.172 $\mu\text{m}/\text{min}$ in untreated cells and 5.363 $\mu\text{m}/\text{min}$ in
 369 MiuA treated cells, and their persistence was 0.577 for untreated cells and 0.636 for MiuA treated ones.
 370 Although the correlation between speed and persistence was not as high as in RPE-1 cells, neutrophils still
 371 showed the same trend in which faster cells tend to migrate in a more persistent manner. Taken together,
 372 we conclude that the actin filament stabilization effect of MiuA has no significant effect on friction-based
 373 migration, confirming our hypothesis.

374



375

376 **Fig 5. Effects of MiuA on migrating cells.** Schematic representation of amoeboid migrating cells (a, d). Under
 377 confinement, RPE-1 LifeAct mCherry cells show no differences in speed and persistence (b, c). The same results occur
 378 when neutrophils migrate in confinement (e, f). A statistical analysis was performed using Student's t test. n.s.: $p > 0.05$;
 379 *: $p < 0.05$; **: $p < 0.01$; and ***: $p < 0.005$. Number of cells: RPE-1: 109 control and 119 MiuA. Neutrophils: 56 control and
 380 102 MiuA.

381

Conclusion

382 This study investigated the interplay between actin filament length, focal adhesions, adhesion forces,
 383 adhesion energy, and cell migration and explained that they are all interrelated.

384 First, we confirmed the actin filament stabilizing effects of MiuA in MEF cells and showed that the treatment
 385 with it does indeed elongate actin filaments in MEF cells without effecting the spreading area. Thus,
 386 confirming our hypothesis that MiuA stabilizes and elongates actin filaments in living cells regardless of
 387 the used cell line in this study.

388 Second, we tested how this stabilization of actin affects the size and number of focal adhesions and found
389 an increase in number of focal adhesions while reducing the size of singular focal adhesions. We also tested
390 how the size and number of focal adhesions affect the adhesion properties of the cells. RPE-1 cells treated
391 with MiuA, therefore having more but smaller focal adhesions, adhered less, while their rupture length was
392 unaffected.

393 Furthermore, contractility measurements on RPE-1 cells revealed that MiuA does not affect the contractility.

394 We had hypothesized that the actin filament stabilization would only affect adhesion-based
395 migration (mesenchymal migration), since focal adhesions and adhesion properties were altered while
396 contractility remained unaffected. Therefore, amoeboid migration, which does not rely on adhesion, would
397 not be altered.

398 We can now confirm this hypothesis and also explain our previous findings about the reduction of
399 mesenchymal migration of RPE-1 and MEF cells (Fig S3.) [16]. Back then we hypothesized that this is due
400 to an increase in adhesion force. We can now disprove this hypothesis with the measured reduction of
401 adhesion force and energy in this work. Instead, we now conclude that the treatment with MiuA reduces
402 adhesion properties, which impedes the cell from exerting the needed forces to perform mesenchymal
403 migration.

404 On the other hand, when we placed RPE-1 cells and neutrophils in pll-g-PEG-coated microchannels and
405 forced them to migrate in an amoeboid mode, neither their speed nor their persistence changed after the
406 treatment with MiuA. Therefore, confirming our hypothesis that non-adhesion-based migration would not
407 be affected by MiuA.

408 Taken together, we conclude that MiuA treatment does only affect adhesion-based migration, but not
409 amoeboid migration in cells.

410 We showed in this work that MiuA can be used as a reliable tool to alter the cellular adhesion
411 properties in cells while leaving cellular contractility unaffected. This will lead to a better understanding of
412 the different mechanisms of migration in immune or cancer cells.

413 Acknowledgments

414 The authors want to thank Ajinkya Ghagre and Allen Ehrlicher for their advice on the soft gel patterning technique
415 PaCS, as well as Matthieu Piel and Jennifer Kasper for providing us with the used cell lines.

416 References

417

418 1. Lämmermann T, Germain RN. The multiple faces of leukocyte interstitial migration. *Semin*
419 *Immunopathol.* 2014;36: 227–251. doi:10.1007/s00281-014-0418-8

420 2. Boisvieux-Ulrich E, Lainé M-C, Sandoz D. Cytochalasin D inhibits basal body migration and ciliary
421 elongation in quail oviduct epithelium. *Cell Tissue Res.* 1990;259: 443–454. doi:10.1007/BF01740770

422 3. Bruijns RHJ, Bult H. Effects of local cytochalasin D delivery on smooth muscle cell migration and on
423 collar-induced intimal hyperplasia in the rabbit carotid artery. *Br J Pharmacol.* 2001;134: 473–483.
424 doi:10.1038/sj.bjp.0704281

425 4. Goddette DW, Frieden C. Actin polymerization. The mechanism of action of cytochalasin D. *J Biol*
426 *Chem.* 1986;261: 15974–15980. doi:10.1016/S0021-9258(18)66662-1

427 5. Schliwa M. Action of cytochalasin D on cytoskeletal networks. *J Cell Biol.* 1982;92: 79–91.
428 doi:10.1083/jcb.92.1.79

429 6. Coué M, Brenner SL, Spector I, Korn ED. Inhibition of actin polymerization by latrunculin A. *FEBS Lett.*
430 1987;213: 316–318. doi:10.1016/0014-5793(87)81513-2

431 7. Pring M, Cassimeris L, Zigmond SH. An unexplained sequestration of latrunculin A is required in
432 neutrophils for inhibition of actin polymerization. *Cell Motil.* 2002;52: 122–130. doi:10.1002/cm.10039

433 8. Hayot C, Debeir O, Van Ham P, Van Damme M, Kiss R, Decaestecker C. Characterization of the
434 activities of actin-affecting drugs on tumor cell migration. *Toxicol Appl Pharmacol.* 2006;211: 30–40.
435 doi:10.1016/j.taap.2005.06.006

436 9. Bubb MR, Senderowicz AM, Sausville EA, Duncan KL, Korn ED. Jasplakinolide, a cytotoxic natural
437 product, induces actin polymerization and competitively inhibits the binding of phalloidin to F-actin. *J*
438 *Biol Chem.* 1994;269: 14869–14871.

439 10. Risinger AL, Du L. Targeting and extending the eukaryotic druggable genome with natural products:
440 cytoskeletal targets of natural products. *Nat Prod Rep.* 2020;37: 634–652. doi:10.1039/c9np00053d

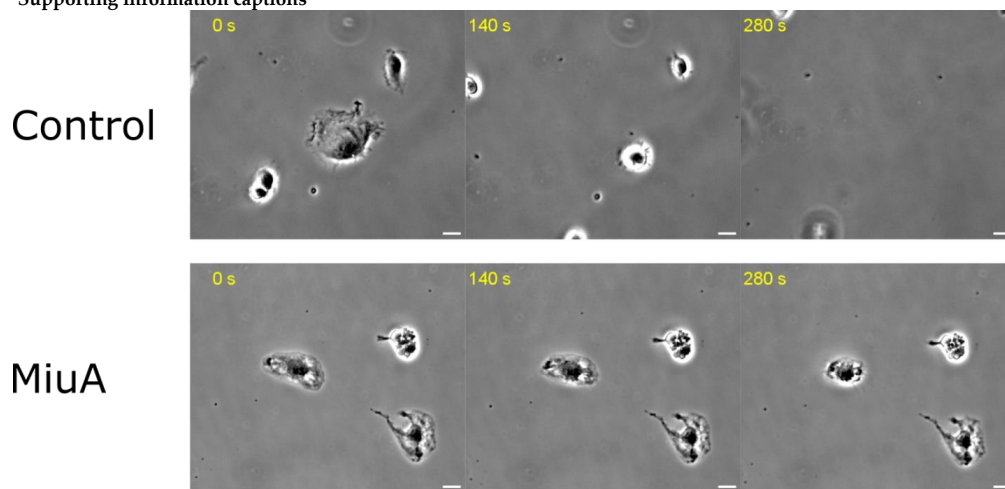
441 11. Wang S, Crevenna AH, Ugur I, Marion A, Antes I, Kazmaier U, et al. Actin stabilizing compounds show
442 specific biological effects due to their binding mode. *Sci Rep.* 2019;9: 9731. doi:10.1038/s41598-019-
443 46282-w

444 12. Moser C, Rüdiger D, Förster F, von Blume J, Yu P, Kuster B, et al. Persistent inhibition of pore-based
445 cell migration by sub-toxic doses of miuraenamides, an actin filament stabilizer. *Sci Rep.* 2017;7: 16407.
446 doi:10.1038/s41598-017-16759-7

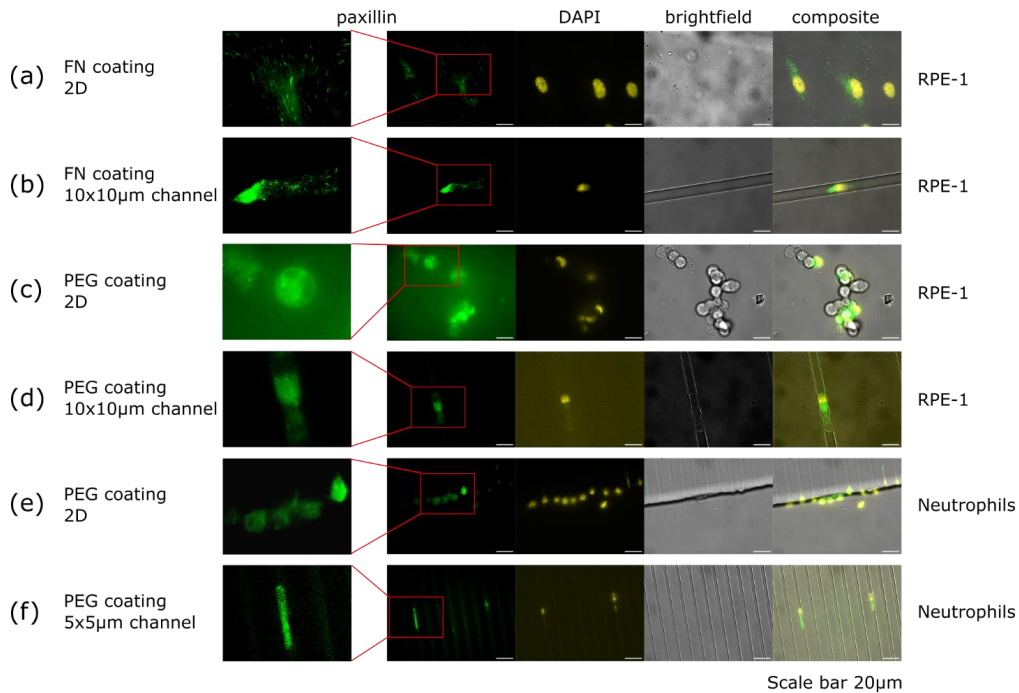
- 447 13. Sumiya E, Shimogawa H, Sasaki H, Tsutsumi M, Yoshita K, Ojika M, et al. Cell-Morphology Profiling
448 of a Natural Product Library Identifies Bisbromoamide and Miuraenamides A as Actin Filament
449 Stabilizers. *ACS Chem Biol.* 2011;6: 425–431. doi:10.1021/cb1003459
- 450 14. Karmann L, Schultz K, Herrmann J, Müller R, Kazmaier U. Total Syntheses and Biological Evaluation
451 of Miuraenamides. *Angew Chem Int Ed.* 2015;54: 4502–4507. doi:10.1002/anie.201411212
- 452 15. Iizuka T, Fudou R, Jojima Y, Ogawa S, Yamanaka S, Inukai Y, et al. Miuraenamides A and B, Novel
453 Antimicrobial Cyclic Depsipeptides from a New Slightly Halophilic Myxobacterium: Taxonomy,
454 Production, and Biological Properties. *J Antibiot (Tokyo).* 2006;59: 385–391. doi:10.1038/ja.2006.55
- 455 16. Baltes C, Thalla DG, Kazmaier U, Lautenschläger F. Actin stabilization in cell migration. *Front Cell Dev*
456 *Biol.* 2022;10: 931880. doi:10.3389/fcell.2022.931880
- 457 17. Lange JR, Fabry B. Cell and tissue mechanics in cell migration. *Exp Cell Res.* 2013;319: 2418–2423.
458 doi:10.1016/j.yexcr.2013.04.023
- 459 18. SenGupta S, Parent CA, Bear JE. The principles of directed cell migration. *Nat Rev Mol Cell Biol.*
460 2021;22: 529–547. doi:10.1038/s41580-021-00366-6
- 461 19. Legerstee K, Houtsmuller AB. A Layered View on Focal Adhesions. *Biology.* 2021;10: 1189.
462 doi:10.3390/biology10111189
- 463 20. Broussard JA, Webb DJ, Kaverina I. Asymmetric focal adhesion disassembly in motile cells. *Curr Opin*
464 *Cell Biol.* 2008;20: 85–90. doi:10.1016/j.ceb.2007.10.009
- 465 21. Wehrle-Haller B. Structure and function of focal adhesions. *Curr Opin Cell Biol.* 2012;24: 116–124.
466 doi:10.1016/j.ceb.2011.11.001
- 467 22. Wehrle-Haller B, Imhof BA. The inner lives of focal adhesions. *Trends Cell Biol.* 2002;12: 382–389.
468 doi:10.1016/S0962-8924(02)02321-8
- 469 23. Hawkins RJ, Piel M, Faure-Andre G, Lennon-Dumenil AM, Joanny JF, Prost J, et al. Pushing off the
470 Walls: A Mechanism of Cell Motility in Confinement. *Phys Rev Lett.* 2009;102: 058103.
471 doi:10.1103/PhysRevLett.102.058103
- 472 24. Liu Y-J, Le Berre M, Lautenschlaeger F, Maiuri P, Callan-Jones A, Heuzé M, et al. Confinement and
473 Low Adhesion Induce Fast Amoeboid Migration of Slow Mesenchymal Cells. *Cell.* 2015;160: 659–672.
474 doi:10.1016/j.cell.2015.01.007
- 475 25. Mihlan M, Glaser KM, Epple MW, Lämmermann T. Neutrophils: Amoeboid Migration and Swarming
476 Dynamics in Tissues. *Front Cell Dev Biol.* 2022;10. doi:10.3389/fcell.2022.871789
- 477 26. Azioune A, Carpi N, Tseng Q, Théry M, Piel M. Protein Micropatterns. *Methods in Cell Biology.*
478 Elsevier; 2010. pp. 133–146. doi:10.1016/S0091-679X(10)97008-8
- 479 27. Ghagre A, Amini A, Srivastava LK, Tirgar P, Khavari A, Koushki N, et al. Pattern-Based Contractility
480 Screening, a Reference-Free Alternative to Traction Force Microscopy Methodology. *ACS Appl Mater*
481 *Interfaces.* 2021;13: 19726–19735. doi:10.1021/acsami.1c02987

- 482 28. Landau LD, Lifshits EM, Kosevich AM, Lifshitz EM, Pitaevskii LP. Theory of Elasticity: Volume 7.
483 Elsevier; 1986.
- 484 29. Vesperini D, Montalvo G, Qu B, Lautenschläger F. Characterization of immune cell migration using
485 microfabrication. *Biophys Rev.* 2021;13: 185–202. doi:10.1007/s12551-021-00787-9
- 486 30. Schindelin J, Arganda-Carreras I, Frise E, Kaynig V, Longair M, Pietzsch T, et al. Fiji: an open-source
487 platform for biological-image analysis. *Nat Methods.* 2012;9: 676–682. doi:10.1038/nmeth.2019
- 488 31. Ershov D, Phan M-S, Pylvänäinen JW, Rigaud SU, Le Blanc L, Charles-Orszag A, et al. TrackMate 7:
489 integrating state-of-the-art segmentation algorithms into tracking pipelines. *Nat Methods.* 2022;19: 829–
490 832. doi:10.1038/s41592-022-01507-1
- 491 32. Tinevez J-Y, Perry N, Schindelin J, Hoopes GM, Reynolds GD, Laplantine E, et al. TrackMate: An open
492 and extensible platform for single-particle tracking. *Methods.* 2017;115: 80–90.
493 doi:10.1016/j.jymeth.2016.09.016
- 494 33. Goffin JM, Pittet P, Csucs G, Lussi JW, Meister J-J, Hinz B. Focal adhesion size controls tension-
495 dependent recruitment of α -smooth muscle actin to stress fibers. *J Cell Biol.* 2006;172: 259–268.
496 doi:10.1083/jcb.200506179
- 497 34. Burridge K, Guilly C. Focal adhesions, stress fibers and mechanical tension. *Exp Cell Res.* 2016;343:
498 14–20. doi:10.1016/j.yexcr.2015.10.029
- 499 35. Balaban NQ, Schwarz US, Riveline D, Goichberg P, Tzur G, Sabanay I, et al. Force and focal adhesion
500 assembly: a close relationship studied using elastic micropatterned substrates. *Nat Cell Biol.* 2001;3:
501 466–472. doi:10.1038/35074532
- 502 36. Schwarz US, Balaban NQ, Riveline D, Bershadsky A, Geiger B, Safran SA. Calculation of Forces at Focal
503 Adhesions from Elastic Substrate Data: The Effect of Localized Force and the Need for Regularization.
504 *Biophys J.* 2002;83: 1380–1394. doi:10.1016/S0006-3495(02)73909-X
- 505 37. Tapial Martínez P, López Navajas P, Lietha D. FAK Structure and Regulation by Membrane Interactions
506 and Force in Focal Adhesions. *Biomolecules.* 2020;10: 179. doi:10.3390/biom10020179
- 507 38. Gallant ND, Michael KE, García AJ. Cell Adhesion Strengthening: Contributions of Adhesive Area,
508 Integrin Binding, and Focal Adhesion Assembly. *Mol Biol Cell.* 2005;16: 4329–4340.
509 doi:10.1091/mbc.e05-02-0170
- 510 39. Sankaran S, Jaatinen L, Brinkmann J, Zambelli T, Vörös J, Jonkheijm P. Cell Adhesion on Dynamic
511 Supramolecular Surfaces Probed by Fluid Force Microscopy-Based Single-Cell Force Spectroscopy.
512 *ACS Nano.* 2017;11: 3867–3874. doi:10.1021/acsnano.7b00161
- 513 40. Gunaratnam G, Leisering R, Wieland B, Dudek J, Miosge N, L. Becker S, et al. Characterization of a
514 unique attachment organelle: Single-cell force spectroscopy of *Giardia duodenalis* trophozoites.
515 *Nanoscale.* 2024;16: 7145–7153. doi:10.1039/D4NR00122B
- 516 41. Gunaratnam G, Dudek J, Jung P, Becker SL, Jacobs K, Bischoff M, et al. Quantification of the Adhesion
517 Strength of *Candida albicans* to Tooth Enamel. *Microorganisms.* 2021;9: 2213.
518 doi:10.3390/microorganisms9112213

- 519 42. Huber R, Bode W. Structural basis of the activation and action of trypsin. *Acc Chem Res.* 1978;11: 114–
520 122. doi:10.1021/ar50123a006
- 521 43. Cramer LP. MOLECULAR MECHANISM OF ACTIN-DEPENDENT RETROGRADE FLOW IN
522 LAMELLIPODIA OF MOTILE CELLS. *Front Biosci-Landmark.* 1997;2: 260–270. doi:10.2741/A189
- 523 44. Ruprecht V, Wieser S, Callan-Jones A, Smutny M, Morita H, Sako K, et al. Cortical Contractility Triggers
524 a Stochastic Switch to Fast Amoeboid Cell Motility. *Cell.* 2015;160: 673–685.
525 doi:10.1016/j.cell.2015.01.008
- 526 45. García-Arcos JM, Ziegler J, Grigolon S, Reymond L, Shajepal G, Cattin CJ, et al. Advected percolation
527 in the actomyosin cortex drives amoeboid cell motility. *bioRxiv;* 2022. p. 2022.07.14.500109.
528 doi:10.1101/2022.07.14.500109
- 529 46. García-Arcos JM, Jha A, Waterman CM, Piel M. Blebology: principles of bleb-based migration. *Trends*
530 *Cell Biol.* 2024;0. doi:10.1016/j.tcb.2024.02.009
- 531 47. Ennomani H, Letort G, Guérin C, Martiel J-L, Cao W, Nédélec F, et al. Architecture and Connectivity
532 Govern Actin Network Contractility. *Curr Biol.* 2016;26: 616–626. doi:10.1016/j.cub.2015.12.069
- 533 48. Stricker J, Falzone T, Gardel ML. Mechanics of the F-actin cytoskeleton. *J Biomech.* 2010;43: 9–14.
534 doi:10.1016/j.jbiomech.2009.09.003
- 535 49. Hawkins RJ, Voituriez R. Mechanisms of Cell Motion in Confined Geometries. *Math Model Nat*
536 *Phenom.* 2010;5: 84–105. doi:10.1051/mmnp/20105104

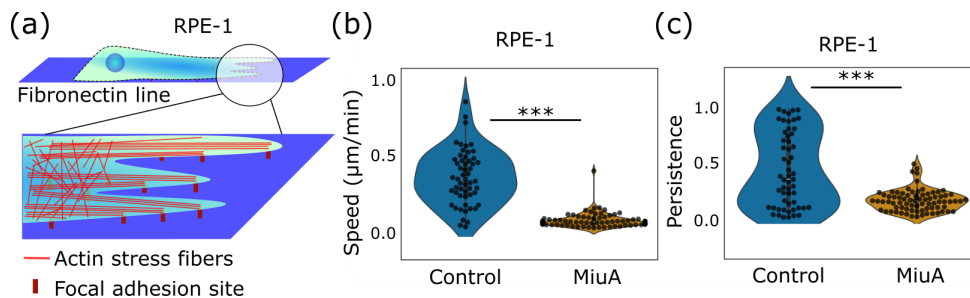
537 **Supporting information captions**

538 Scale bar 20 μm
539 **Fig S1** Trypsin assay for RPE-1 LifeAct mCherry cells. Fully spread RPE-1 LifeAct mCherry cells were trypsinized while
540 being monitored with a video microscope. Pictures were taken every 20 seconds where the time stamp (yellow label in
541 the upper left corner) denotes the time after adding trypsin. The first picture “0 s” was taken immediately after trypsin
542 was added. Top: Control cells treated with DMSO. Bottom: MiuA (20 nM) treated cells. Scale bar 20 μm .



543

544 **Fig S2** Focal adhesion staining in migrating RPE-1 LifeAct mCherry cells and neutrophils. From left to right: Paxillin
 545 immunostaining with zoomed in area (red square) in green. DAPI staining of the nucleus in yellow. Brightfield images
 546 of RPE-1 cells and neutrophils. Composite images of the paxillin, nucleus and brightfield images. From Top to bottom:
 547 (a) RPE-1 cells on 2D fibronectin (25 $\mu\text{g}/\text{ml}$) coated surface. (b) RPE-1 cells inside 10x10 μm PDMS microchannels with
 548 fibronectin coating. (c) RPE-1 cells on a PEG-coated surface. (d) RPE-1 cells in PEG-coated 10x10 μm PDMS
 549 microchannels. (e) Neutrophils on a PEG-coated 2D surface. (f) Neutrophils inside a PEG-coated 5x5 μm PDMS
 550 microchannel. Scale bars: 20 μm



551

552 **Figure S3** Effects of MiuA on mesenchymal migrating RPE-1 cells. Schematic representation of a mesenchymal
 553 migrating cell on a fibronectin line (a). On these fibronectin lines, RPE-1 LifeAct mCherry cells treated with 20 nM MiuA
 554 reduced their speed (b) and persistence (c). A statistical analysis was performed using Student's t test: n.s.: $p > 0.05$; *:
 555 $p < 0.05$; **: $p < 0.01$; and ***: $p < 0.005$. Number of cells: 55 control and 77 MiuA. Data replotted from Baltes et al. [16].

Strain energy of cells on patterns dependent only on the change of pattern area

1 Introduction

In this protocol I am going to go through most of the calculation steps needed for the analysis of cells, placed on deformable patterns. The idea of this technique origins from Ajinka Ghagre et al. (doi: <https://doi.org/10.1021/acscam.1c02987>), where they showed that it is possible to calculate the strain energy of a cell, by measuring the deformation of an underlying pattern without using fluorescent beads, as one would need in traction force microscopy. However, they only use Cartesian coordinates and propose an approximation on how the change in area correlates with the strain energy of cells. We wanted to further advance this technique by transforming the Problem in polar coordinates. There we can calculate the strain energy depending only on the change of the radius of a circle, which then allows us to directly calculate the change of area, resulting on a formula that puts strain energy and area together.

2 Background

As the authors state, most of this and the following section will be taken from "Theory of elasticity 3rd Edition" from Landau and Lifshitz. In section 4 I will start to display what we added to the technique and how we proceeded in polar coordinates.

We start with defying our **displacement vector**:

$$\vec{u} = \begin{pmatrix} u_x \\ u_y \\ u_z \end{pmatrix} = u_x \vec{e}_x + u_y \vec{e}_y + u_z \vec{e}_z \quad (1)$$

Which involves the position of each point **after** and **before** displacement

$$u_i = x' - x$$

Definition: Strain Tensor u_{ik}

$$u_{ik} = \frac{1}{2} \left(\frac{\partial u_i}{\partial x_k} + \frac{\partial u_k}{\partial x_i} + \frac{\partial u_l}{\partial x_i} \cdot \frac{\partial u_l}{\partial x_k} \right) \quad (2)$$

Where:

- $i, k, l \in 1, 2, 3$
- $x_1 = x, x_2 = y$ and $x_3 = z$
- $\sum_{i=1}^3 a_i \cdot b_i = a_i \cdot b_i$ (Einstein Notation)

Definition: Stress Tensor σ_{ik}

$$\oint \sigma_{ik} df_k = \int \frac{\partial \sigma_{ik}}{\partial x_k} dV = \int F_i dV \quad | \quad F_i = \frac{\partial \sigma_{ik}}{\partial x_k} \quad (3)$$

If we want to display the stress tensor in terms of the strain tensor it will look like this:

$$\sigma_{ik} = \frac{E}{1 + \sigma} \left(u_{ik} + \frac{\sigma}{1 - 2\sigma} u_{ll} \delta_{ik} \right) \quad (4)$$

With:

- E = Young's Modulus
- σ = Poisson ratio
- $\delta_{ik} = 1$ if $i = k$, $\delta_{ik} = 0$ else

Assuming that at equilibrium there are no internal forces (e.g. the sum of all forces is zero) and ignoring gravity, we can say:

$$\vec{F}_i = \frac{\partial \sigma_{ik}}{\partial x_k} = 0 \quad (5)$$

Using the relationship between σ_{ik} and u_{ik} we get:

$$\frac{\partial \sigma_{ik}}{\partial x_k} = \frac{E\sigma}{(1 + \sigma)(1 - 2\sigma)} \frac{\partial u_{ll}}{\partial x_i} + \frac{E}{1 + \sigma} \frac{\partial u_{ik}}{\partial x_k} \quad (6)$$

Using also:

$$u_{ik} = \frac{1}{2} \left(\frac{\partial u_i}{\partial x_k} + \frac{\partial u_k}{\partial x_i} + \underbrace{\frac{\partial u_l}{\partial x_k} \frac{\partial u_l}{\partial x_i}}_{=0, \text{ as we assume small deformations}} \right) \quad (7)$$

All together we have:

$$\frac{E}{2 \cdot (1 + \sigma)} \frac{\partial^2}{\partial x_k^2} u_i + \frac{E}{2 \cdot (1 + \sigma) \cdot (1 - 2\sigma)} \frac{\partial^2 u_l}{\partial x_i \partial x_l} = 0 \quad (8)$$

Rearranging that equation and using the following equations leaves us with a homogeneous partial differential equation

$$\frac{\partial^2 u_i}{\partial x_k^2} = \Delta \vec{u} \quad , \quad \frac{\partial u_l}{\partial x_l} = \vec{\nabla} \cdot \vec{u} \quad (9)$$

$$(1 - 2\sigma) \Delta \vec{u} + \vec{\nabla}(\vec{\nabla} \cdot \vec{u}) = 0 \quad (10)$$

3 Solving the PDE

In our case we have to deal with the following form of the PDE

$$(1 - 2\sigma) \Delta \vec{u} + \vec{\nabla}(\vec{\nabla} \cdot \vec{u}) = 0 \quad (11)$$

The right-hand side becomes zero as we do not have any intrinsic forces on the body itself, but there are forces applied to the body from the outside that appear in the solution via the boundary conditions. Our solution to the problem will be in the form of

$$\vec{u} = \vec{f} + \vec{\nabla} \phi \quad (12)$$

where \vec{f} satisfies Laplace's equation

$$\Delta \vec{f} = 0$$

and ϕ is some scalar.

If we now substitute (12) into our PDE (11) we obtain:

$$2(1 - \phi)\Delta\phi = -\vec{\nabla} \cdot \vec{f} \quad (13)$$

Imagine we only have an elastic plane in the x-y plane. That means we can write the x and y components of \vec{f} in the following way:

$$f_x = \frac{\partial g_x}{\partial z} \quad \text{and} \quad f_y = \frac{\partial g_y}{\partial z} \quad (14)$$

Since \vec{f} is a harmonic function (meaning it does satisfy the Laplace equation) also its components f_x, f_y do satisfy Laplace equation, and therefore also the functions g_x, g_y :

$$\Delta g_x = \Delta g_y = 0 \quad (15)$$

If we put all of this in our equation (13) we obtain:

$$\Delta\phi = -\frac{1}{2(1-\sigma)} \frac{\partial}{\partial z} \left(\frac{\partial g_x}{\partial x} + \frac{\partial g_y}{\partial y} + f_z \right) \quad (16)$$

As g_x, g_y, f_z are harmonic functions we can rewrite this equation introducing another harmonic function ψ :

$$\phi = -\frac{z}{4(1-\sigma)} \left(\frac{\partial g_x}{\partial x} + \frac{\partial g_y}{\partial y} + f_z \right) + \psi \quad (17)$$

With this the problem reduces to finding the functions g_x, g_y, f_z, ψ which all are harmonic functions that satisfy Laplace equation.

Introducing boundary conditions

As we have a free surface in the x-y plane, its corresponding normal vector (surface vector) is in negative z direction. Remembering that

$$\sigma_{ik} \cdot n_k = P_i$$

where P_i denotes the force (pressure) exerted in i direction.

We do not see that in our case we have

$$\begin{aligned} P_x &= -\sigma_{xz} \\ P_y &= -\sigma_{yz} \\ P_z &= -\sigma_{zz} \end{aligned}$$

If we now use the form of our stress tensor from (4) and express the components of the displacement vector \vec{u} in terms of the quantities f_z, g_x, g_y, ψ we can obtain the following boundary conditions

$$\left[\frac{\partial^2 g_x}{\partial z^2} \right]_{z=0} + \left[\frac{\partial}{\partial x} \left\{ \frac{1-2\sigma}{2(1-\sigma)} f_z - \frac{1}{2(1-\sigma)} \left(\frac{\partial g_x}{\partial x} + \frac{\partial g_y}{\partial y} \right) + 2 \frac{\partial \psi}{\partial z} \right\} \right]_{z=0} = -2(1+\sigma) \frac{P_x}{E} \quad (18)$$

$$\left[\frac{\partial^2 g_y}{\partial z^2} \right]_{z=0} + \left[\frac{\partial}{\partial y} \left\{ \frac{1-2\sigma}{2(1-\sigma)} f_z - \frac{1}{2(1-\sigma)} \left(\frac{\partial g_x}{\partial x} + \frac{\partial g_y}{\partial y} \right) + 2 \frac{\partial \psi}{\partial z} \right\} \right]_{z=0} = -2(1+\sigma) \frac{P_y}{E} \quad (19)$$

$$\left[\frac{\partial}{\partial z} \left\{ f_z - \left(\frac{\partial g_x}{\partial x} + \frac{\partial g_y}{\partial y} \right) + 2 \frac{\partial \psi}{\partial z} \right\} \right]_{z=0} = -2(1+\sigma) \frac{P_z}{E} \quad (20)$$

Since we have four unknown variables but only three equations to determine them, we can introduce another condition. The authors of "Theory of elasticity 3rd Edition" take the following condition, saying it is proven by the absence of any contradiction in the end result.

$$(1 - 2\sigma)f_z - \left(\frac{\partial g_x}{\partial x} + \frac{\partial g_y}{\partial y} \right) + 4(1 - \sigma) \frac{\partial \psi}{\partial z} = 0 \quad (21)$$

With this additional condition our equations (18) and (19) become

$$\left[\frac{\partial^2 g_x}{\partial z^2} \right]_{z=0} = -\frac{2(1 + \sigma)}{E} P_x \quad (22)$$

$$\left[\frac{\partial^2 g_y}{\partial z^2} \right]_{z=0} = -\frac{2(1 + \sigma)}{E} P_y \quad (23)$$

Having those equations is all we need to determine the harmonic functions f_z, g_x, g_y, ψ

We also do know that harmonic functions that disappear at infinity and have a normal derivative at $z = 0$ are given by the following formula:

$$h(x, y, z) = -\frac{1}{2\pi} \iint \left[\frac{\partial h(x', y', z)}{\partial z} \right]_{z=0} \frac{1}{r} dx' dy' \quad (24)$$

where $r = \sqrt{(x - x')^2 + (y - y')^2 + z^2}$

If we now seek to calculate all the components of the vector \vec{u} with regard to the set boundary conditions and setting $z = 0$ we get:

$$u_x = \frac{1 + \sigma}{2\pi Er} \left(-\frac{(1 - 2\sigma)x}{r} F_z + 2(1 - \sigma)F_x + \frac{2\sigma x}{r^2} (xF_x + yF_y) \right) \quad (25)$$

$$u_y = \frac{1 + \sigma}{2\pi Er} \left(-\frac{(1 - 2\sigma)y}{r} F_z + 2(1 - \sigma)F_y + \frac{2\sigma y}{r^2} (xF_x + yF_y) \right) \quad (26)$$

$$u_z = \frac{1 + \sigma}{2\pi Er} \left(2(1 - \sigma)F_z + (1 - 2\sigma) \frac{1}{r} (xF_x + yF_y) \right) \quad (27)$$

Definition: Green Tensor G_{ik}

To solve PDE one can use Green's function which is defined in a way that when put into the PDE, the outcome will be the Dirac delta function:

$$L := L \left(\frac{d}{dt} \right) = \sum_{k=1}^N a_k(t) \frac{d^k}{dt^k}$$

$$Ly = f$$

$$LG(t) = \delta(t)$$

$$y(t) = (G * f)(t) = \int G(t - t') \cdot f(t') dt'$$

$$Ly(t) = \int LG(t - t') f(t') dt' = \int \delta(t - t') f(t') dt' = f(t)$$

So by using Green's idea we can solve our initial PDE by rewriting \vec{u} the following way:

$$\vec{u} = G_{ik} * \vec{F} \quad (28)$$

Where G_{ik} is the **Green Tensor**.

We can extract the Green tensor for our previous set of equations for the displacement vector \vec{u} :

$$G = \frac{1 + \sigma}{2\pi Er} \begin{pmatrix} 2(1 - \sigma) + \frac{2\sigma x^2}{r^2} & \frac{2\sigma xy}{r^2} & -\frac{(1 - \sigma)x}{r} \\ \frac{2\sigma xy}{r^2} & 2(1 - \sigma) + \frac{2\sigma y^2}{r^2} & -\frac{(1 - \sigma)y}{r} \\ \frac{1 - 2\sigma}{r}x & \frac{1 - \sigma}{r}y & 2(1 - \sigma) \end{pmatrix}$$

As we are only interested in the deformation in x-y direction, we can neglect all components regarding z, leaving us with:

$$G = \frac{1 + \sigma}{2\pi Er} \begin{pmatrix} 2(1 - \sigma) + \frac{2\sigma x^2}{r^2} & \frac{2\sigma xy}{r^2} \\ \frac{2\sigma xy}{r^2} & 2(1 - \sigma) + \frac{2\sigma y^2}{r^2} \end{pmatrix} \quad (29)$$

In our case we usually obtain the displacement fields and are interested in the force that was necessary to deform our plane in such a way. For this, we need to invert equation (28), which is difficult, as we do not have a simple Matrix multiplication but a convolution of a matrix and a vector.

To facilitate this, we can perform a Fourier transformation so that the convolution would change into a multiplication, which we easily can inverse. Afterwards, performing the inverse Fourier transformation results in an equation we can use to calculate the forces that were needed for our observed displacement

$$\vec{u} = G * \vec{F} \quad \text{Fourier} \rightarrow \hat{u} = \hat{G} \cdot \hat{F} \quad \text{Inverting} \rightarrow \hat{F} = \hat{G}^{-1} \cdot \hat{u} \quad \text{reverse Fourier} \rightarrow \vec{F} = G^{-1} * \vec{u}$$

4 Polar coordiantes

Ajinka Ghagre et al. (doi: <https://doi.org/10.1021/acscam.1c02987>) managed to write a MATLAB script that performs these transformations in Cartesian coordinates. They simulate a square grid which starts with the initial area and shrinks isotopically into a smaller square grid after deformation. Thus allowing them to calculate the exerted force on the underlying substrate and therefore the strain energy

$$U = \frac{1}{2} \int \vec{f} \cdot \vec{u} dA \quad (30)$$

As in this case we loose all information about the real force and displacement field, we thought about switching from a Cartesian system into a polar system. This would reduce the needed parameters from 2 (x and y) in Cartesian to 1 (r) in polar.

To know whether we can simply transform our Green tensor, we want to derive equation 11 by assuming polar coordinates from the very beginning.

In our case we want to use cylindrical coordinates as we are going to solve our equation solely in the x-y-plane (or now in the r-φ-plane). For this we have:

$$\begin{aligned} x &= r \cdot \cos(\varphi) \\ y &= r \cdot \sin(\varphi) \\ z &= z \end{aligned}$$

And for the derivatives we find:

$$\begin{aligned}\frac{\partial r}{\partial x} &= \cos(\varphi) \\ \frac{\partial r}{\partial y} &= \sin(\varphi) \\ \frac{\partial \varphi}{\partial x} &= -\frac{1}{r} \sin(\varphi) \\ \frac{\partial \varphi}{\partial y} &= \frac{1}{r} \cos(\varphi)\end{aligned}$$

This leads us to the following relations:

$$\begin{aligned}\frac{\partial}{\partial x} &= \frac{\partial r}{\partial x} \frac{\partial}{\partial r} + \frac{\partial \varphi}{\partial x} \frac{\partial}{\partial \varphi} = \cos(\varphi) \frac{\partial}{\partial r} - \frac{\sin(\varphi)}{r} \frac{\partial}{\partial \varphi} \\ \frac{\partial}{\partial y} &= \frac{\partial r}{\partial y} \frac{\partial}{\partial r} + \frac{\partial \varphi}{\partial y} \frac{\partial}{\partial \varphi} = \sin(\varphi) \frac{\partial}{\partial r} + \frac{\cos(\varphi)}{r} \frac{\partial}{\partial \varphi}\end{aligned}\quad (31)$$

We also want to display our displacement vector \vec{u} in those polar coordinates- Looking at Figure A1 leads us to:

$$\begin{aligned}u_x &= u_r \cos(\varphi) - u_\varphi \sin(\varphi) \\ u_y &= u_r \sin(\varphi) + u_\varphi \cos(\varphi) \\ u_z &= u_z\end{aligned}$$

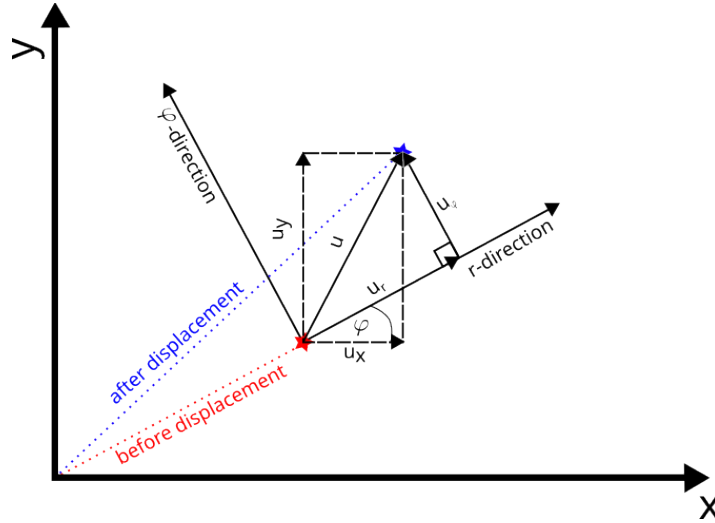


Figure A1: Visual display of the displacement vector in polar coordinates

Our strain tensor in cylindrical coordinates should therefore look as follows:

$$\begin{pmatrix} u_{rr} & u_{r\varphi} & u_{rz} \\ u_{\varphi r} & u_{\varphi\varphi} & u_{\varphi z} \\ u_{zr} & u_{z\varphi} & u_{zz} \end{pmatrix} = \begin{pmatrix} \cos(\varphi) & \sin(\varphi) & 0 \\ -\sin(\varphi) & \cos(\varphi) & 0 \\ 0 & 0 & 1 \end{pmatrix} \begin{pmatrix} u_{xx} & u_{xy} & u_{xz} \\ u_{yx} & u_{yy} & u_{yz} \\ u_{zx} & u_{zy} & u_{zz} \end{pmatrix} \begin{pmatrix} \cos(\varphi) & -\sin(\varphi) & 0 \\ \sin(\varphi) & \cos(\varphi) & 0 \\ 0 & 0 & 1 \end{pmatrix}$$

If we now put in all we know already, our tensor elements become:

$$\begin{aligned}
u_{rr} &= u_{xx} \cdot \cos(\varphi)^2 + u_{yy} \cdot \sin(\varphi)^2 + u_{xy} \cdot \sin(2\varphi) \\
u_{\varphi\varphi} &= u_{xx} \cdot \sin(\varphi)^2 + u_{yy} \cdot \cos(\varphi)^2 - u_{xy} \cdot \sin(2\varphi) \\
u_{zz} &= u_{zz} \\
u_{r\varphi} &= (u_{yy} - u_{xx}) \cdot \cos(\varphi)\sin(\varphi) + u_{xy} \cdot (\cos(\varphi)^2 - \sin(\varphi)^2) \\
u_{rz} &= u_{zx} \cdot \cos(\varphi) + u_{zy} \cdot \sin(\varphi) \\
u_{z\varphi} &= -u_{zx} \cdot \sin(\varphi) + u_{zy} \cdot \cos(\varphi)
\end{aligned}$$

Taking now together everything we know from equation (7) and (31), we obtain:

$$\begin{aligned}
u_{rrr} &= \frac{\partial u_r}{\partial r} \\
u_{\varphi\varphi\varphi} &= \frac{1}{r} \frac{\partial u_\varphi}{\partial \varphi} + \frac{u_r}{r} \\
u_{zzz} &= \frac{\partial u_z}{\partial z} \\
u_{r\varphi\varphi} &= \frac{1}{2} \left(\frac{1}{r} \frac{\partial u_r}{\partial \varphi} + \frac{\partial u_\varphi}{\partial r} - \frac{u_\varphi}{r} \right) \\
u_{rz\varphi} &= \frac{1}{2} \left(\frac{\partial u_r}{\partial z} + \frac{\partial u_z}{\partial r} \right) \\
u_{z\varphi\varphi} &= \frac{1}{2} \left(\frac{1}{r} \frac{\partial u_z}{\partial \varphi} + \frac{\partial u_\varphi}{\partial z} \right)
\end{aligned} \tag{32}$$

Using Hook's law:

$$\sigma_{ij} = \frac{E}{(1+\sigma)} \left(u_{ij} + \frac{\sigma}{(1-2\sigma)} u_{kk} \delta_{ij} \right) \tag{33}$$

The definitions of ∇ and Δ in polar coordinates:

$$\begin{aligned}
\vec{\nabla} &= \vec{e}_r \frac{\partial}{\partial r} + \frac{1}{r} \vec{e}_\varphi \frac{\partial}{\partial \varphi} + \vec{e}_z \frac{\partial}{\partial z} \\
\Delta &= \vec{\nabla} \cdot \vec{\nabla}
\end{aligned} \tag{34}$$

and knowing that at equilibrium we have:

$$\vec{\nabla} \cdot \sigma_{\text{Stress Tensor}} = 0 \tag{35}$$

we can put everything together and see, that we still end up with our PDE from above (10):

$$(1-2\sigma)\Delta\vec{u} + \vec{\nabla} \left(\vec{\nabla} \cdot \vec{u} \right) = 0$$

This means, we can solve our equation regardless of the choice of our coordinate system, which means, that one can solve the PDE as described above and transform our solution (Green Tensor) according to the designated coordinate system.

In our case we transformed the Green tensor into polar coordinates (r, φ) :

$$G_{\text{polar}} = \frac{1+\sigma}{\pi E r} \begin{pmatrix} (1-\sigma) + \sigma & 0 \\ 0 & (1-\sigma) \end{pmatrix} \quad | \text{ assuming } \varphi = 0 \tag{36}$$

We also have to transform our displacement vector \vec{u} into polar coordinates (r, φ) :

$$\vec{u}(r, \varphi) = \begin{pmatrix} r' - r \\ 0 \end{pmatrix} \tag{37}$$

Now we have to transform both of them with the following Fourier Transformation:

$$Y_{p+1,q+1} = \sum_{j=0}^{N-1} \sum_{k=0}^{M-1} \left(e^{-\frac{2\pi i}{N}} \right)^{jp} \cdot \left(e^{-\frac{2\pi i}{M}} \right)^{kq} \cdot X_{j+1,k+1} \quad (38)$$

Where Y denotes the Fourier transformed variable, X the original variable, N and M the dimensions of the Matrix respectively.

In our case we have a 2×2 Matrix G_{polar} and a 2-dimensional vector \vec{u} which plugged in equation (38) results in:

$$\hat{G}_{polar} = \frac{1+\sigma}{\pi Er} \begin{pmatrix} 2(1-\sigma)+\sigma & \sigma \\ \sigma & 2(1-\sigma)+\sigma \end{pmatrix} \quad (39)$$

↓ Inverting

$$\hat{G}_{polar}^{-1} = \frac{\pi Er}{(1+\sigma)[(2(1-\sigma)+\sigma)^2 - \sigma^2]} \begin{pmatrix} 2(1-\sigma)+\sigma & -\sigma \\ -\sigma & 2(1-\sigma)+\sigma \end{pmatrix} \quad (40)$$

$$\hat{u} = (r' - r) \begin{pmatrix} 1 \\ 1 \end{pmatrix} \quad (41)$$

Following our idea earlier on, we can now compute the force \hat{F} and afterwards perform a reverse Fourier transformation.

$$\hat{F} = \frac{2\pi Er(r' - r)2(1-\sigma)}{(1+\sigma)[(2(1-\sigma)+\sigma)^2 - \sigma^2]} \begin{pmatrix} 1 \\ 1 \end{pmatrix} \quad (42)$$

Using the formula for the reverse Fourier Transformation:

$$X_{p,q} = \frac{1}{M} \sum_{j=1}^m \frac{1}{N} \sum_{k=1}^N \left(e^{-\frac{2\pi i}{M}} \right)^{(j-1)(p-1)} \left(e^{-\frac{2\pi i}{N}} \right)^{(k-1)(q-1)} Y_{j,k} \quad (43)$$

We get:

$$\vec{F} = \frac{2\pi Er(r' - r)2(1-\sigma)}{(1+\sigma)[(2(1-\sigma)+\sigma)^2 - \sigma^2]} \begin{pmatrix} 1 \\ 0 \end{pmatrix} \quad (44)$$

5 Strain energy and pattern area

To compute the strain energy, we need the force applied to the substrate per unit of area and the displacement field as described in equation (30). By dividing our force \vec{F} by the area of the change $\pi(r' - r)^2$, we obtain the needed force \vec{f} . This results in the following integral:

$$U = \frac{1}{2} \int \vec{f} \cdot \vec{u} \, dA = \frac{1}{2} \int 2 \underbrace{\frac{E(1-\sigma)}{(1+\sigma)[(2(1-\sigma)+\sigma)^2 - \sigma^2]}}_{:=a} \cdot r \, dA \quad (45)$$

Solving this integral leads us to the following:

$$U = a \int_{r'}^{r_i} \int_0^{2\pi} r^2 \, dr \, d\varphi = \frac{2\pi a}{3} (r_i^3 - r'^3) \quad | \quad A = \frac{r^2}{\pi} \quad (46)$$

$$= \frac{2\pi a}{3} \left(\left(\frac{A_i}{\pi} \right)^{\frac{3}{2}} - \left(\frac{A'}{\pi} \right)^{\frac{3}{2}} \right) \quad (47)$$

If we now consider that we reduced our problem to a 1D problem only depending on the radius r , we need to divide this Energy by 2π , leaving us with the final expression:

$$U_{\text{final}} = \frac{a}{3} \left(\left(\frac{A_i}{\pi} \right)^{\frac{3}{2}} - \left(\frac{A'}{\pi} \right)^{\frac{3}{2}} \right) \quad (48)$$

6 Comparison between polar and Cartesian

To check whether our way of calculating the strain energy aligns with the ones from Gharge et al., we plugged in the same set of data for all three algorithms. The results can be seen in Figure A2.

Since both ways (simplified and Cartesian) were proven to fit the experimental datasets, we conclude that our solution does as well fit the data and might well be used to calculate the strain energy in cells deforming an underlying soft pattern.

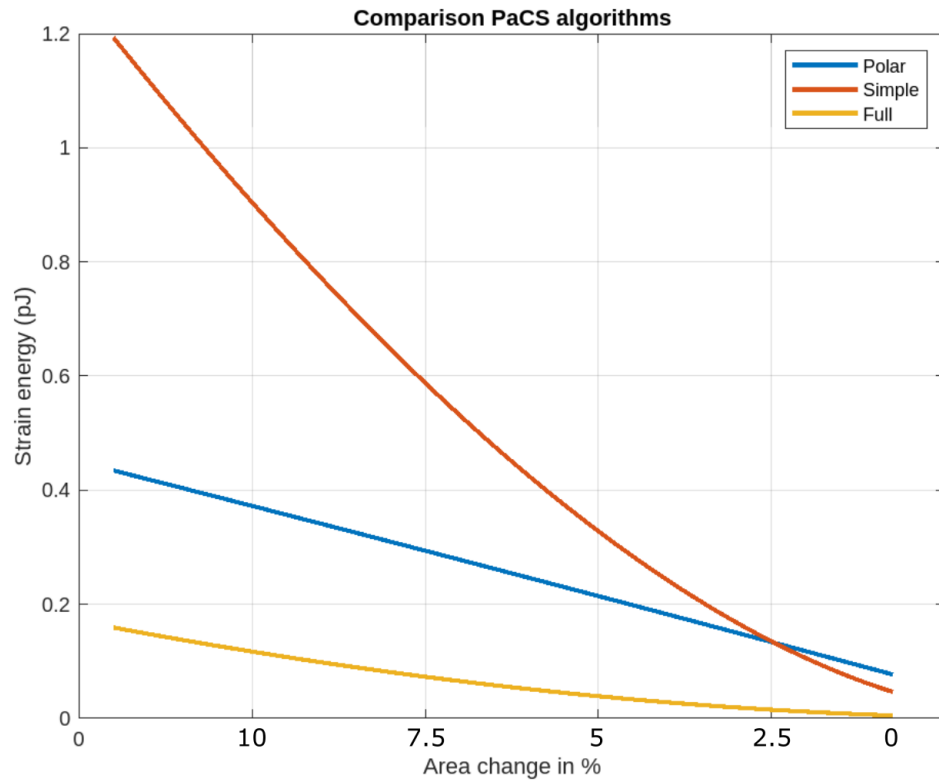


Figure A2: Comparison between the three approaches on calculating the strain Energy, showing only small deformations in the range lower than 15% (RED) simplified version, (YELLOW) Fourier transformation of mesh-grid in Cartesian coordinates. (BLUE) transformation of Green Tensor in polar coordinates. For all three cases the assumption was "small deformations".

Additional data

In addition to the presented data in the manuscript above, I also want to include my approaches on PaCS experiments on PDMS surfaces instead of polyacrylamide gel, as described in the manuscript.

Following the protocol given in the article from Gharge et al. [80] I wanted to recreate a flat PDMS surface on which I can place micropatterns. For this I placed a 50 μ L droplet of PDMS with varying ratios between PDMS and cross linker in a glass bottom dish and let it cure at 80 °C for at least one hour. After the PDMS was cured, I plasma activated the surface and incubated it with PEG for another hour at room temperature. Following the protocol for patterning with PRIMO (see 3.2) I was able to create micropatterns on top of the PDMS (see Figure 5.2 (A)). However, until now, whenever I tried to seed cells on top of the micropatens, they started to adhere everywhere, even in places that where not patterned (see Figure 5.2 (A)). Since the fibronectin coating was fluorescent I could confirm that the coating itself was intact and also limited to the pattern as it should be. Further experiments are needed to determine the cause of this adhesion. One possible explanation might be that the used poly-L-lysine PEG does break after the patterning and ECM coating process, opening spots for cells to adhere.

Additionally I wanted to measure the storage modulus of our PDMS at different levels of added cross linker. For this a rheometer was used to obtain the storage module shown in Figure 5.2 (B). From this graph it is evident that the amount of added cross linker has a huge impact on the storage module of the resulting PDMS. However, one can also see that this storage module is stable and does not change with varying shear strain.

Lastly I was also interested in the effects of MiuA on the protein expression levels of G- and F-actin. Therefore, I conducted western blot experiments and found the level of F-actin increased compared to G-actin in MiuA treated cells (as seen in Figure 5.2 (C)). As I did not repeat this experiment yet, I decided to not include this data into the manuscript, before one can be sure that the data is reproducible. Interestingly from Figure 5.2 one can see, that the overall expression levels of actin seem to increase after treatment with MiuA. It is known that MiuA has gene regulatory properties, but it has not been reported to affect the overall expression levels of actin [91].

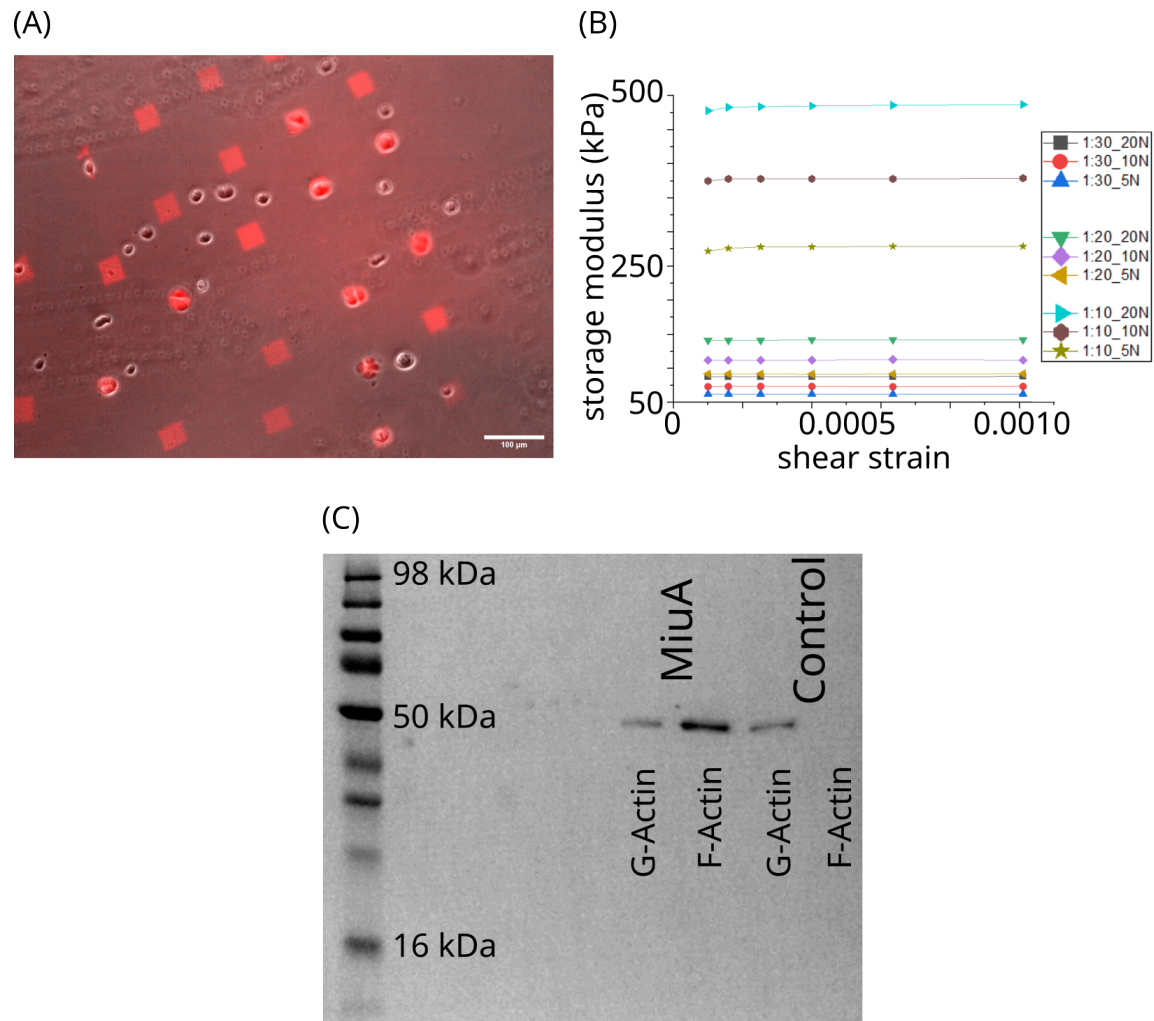


Figure 5.2: Additional data the manuscript “Modulation of Cellular Adhesion, Contractility, and Migration by MiuA”. (A) MCF-10a cells were placed on a patterned PDMS surface (pattern in red) and allowed to spread. Cells did not exclusively attach to the patterned area. (B) Rheometer measurements of the storage modulus for different ratios of PDMS to cross linker. (C) Western blot of G- and F- actin in RPE-1 cells with and without MiuA treatment. Scale bar 100 μm .

Chapter 6

Discussion

The cytoskeleton is a highly dynamic network, that spans through the entire cell. Actin is part of this network, which forms fibrous structures within the cell and the actin cortex just underneath the cell membrane. Together with motor proteins like myosin II actin filaments are capable of generating forces and contraction, thereby allowing the cell to fulfill tasks, such as cell migration. Additionally, actin is involved in other cell mechanics, like adhesion, cell division, signal transduction and phagocytosis, making it a crucial subject of investigation in scientific research.

In this chapter I am going to discuss my findings and connect the two aforementioned articles (see page 42 and 54). Since most of the discussion was already performed in the articles themselves, here I focus on answering my scientific question, that I posed in chapter 4.

In my work, I tried to gain a deeper understanding of the fundamental mechanisms underlying cellular migration. For this I looked at the effects actin filament length has on migrating cells. I used the newly synthesized actin stabilizer miuraenamamide A to study its effects on the polymerization of actin, its effect on cellular adhesion, and contractility. I performed experiments, targeting those migration parameters and were able to reason why their effects align with our hypothesis. In chapter 4 I asked the question of how actin stabilization affects migration parameters and what impact this eventually has on the different modes of migration. In addition to the graphical abstract given there, I now aim to provide at least partial answers to these questions. A brief graphical representation can be seen in Figure 6.1.

In summary, the findings in this work demonstrate that MiuA exerts actin stabilizing effects in living cells. This effect had only been reported before in vitro studies with purified actin [50]. This work now demonstrates that this effect is not contingent on the cell line, as evidenced by the successful testing of this phenomenon on RPE-1 and MEF cells. I measured the effect of MiuA on the length of actin filaments in both cell lines, when they were placed on micropatterns and found the length of their actin filaments to be increased

significantly. Other parts of the cytoskeleton did not seem to be affected by MiuA, which is consistent with the statement of Iizuka et al, that MiuA does not affect microtubules or intermediate filaments [48].

At the same time I could see that MiuA has an additional effect in RPE-1 cells, where the spreading area of RPE-1 cells increased. However, this effect did not occur in MiuA treated MEF cells. There are reports suggesting that MiuA affects genes responsible for the spreading in cells [92, 91], which would fit our observations in RPE-1 cells. An explanation for why this behavior did not occur in MEF cells, might be the lower concentration of MiuA that was used. For RPE-1 cells I always treated them with a concentration of 20 nM, which I found to be subtoxic and therefore suitable for the experiments. In MEF cells however, only 5 nM were used, as a higher toxicity of MiuA in these cells was observed during the experiments.

Additionally, FRAP measurements revealed a reduction in actin dynamics when RPE-1 cells were treated with MiuA. I think that the stabilizing effect of MiuA directly correlates with this, as the turn over cycle (as explained in chapter 2.3) and specifically the mechanism of cofilin is inhibited. This means that the reservoir of available G-actin decreases with MiuA which eventually hinders new filaments from forming or existing filaments from exchanging their subunits.

Next, I wanted to quantify the effect of MiuA on the size and number of focal adhesions. The results show that their number in both RPE-1 and MEF cells increased while their average size decreased. However, when normalizing the total focal adhesion area to the spreading area of the cells I noticed that this value did not change after treatment with MiuA, meaning that the effective adhesion area was unchanged. From there I wanted to know whether these changes have an impact on the adhesion properties. For this single-cell force spectroscopy was performed and revealed that MiuA treated cells have lower adhesion force and energy compared to control. Taken all of this together I hypothesize that actin filament length influences the geometry and distribution of focal adhesions which consequently affects the adhesion of cells. However, more research is needed to say that actin filament length affects adhesion per se, but these findings support the idea that there is an interplay between actin filament length and adhesion. Ultimately, from the presented data it seems evident that the size of single focal adhesions has a more crucial effect on the adhesion properties of cells than the overall focal adhesion area of the cell.

Contractility is the last of the three main migration parameters described by Lämmermann et al. [5], which I studied using PaCS. I found that MiuA does not change the contractility of RPE-1 cells. This is consistent with the initial hypothesis, as there are no reports about MiuA interacting with either myosin II or its respective actin binding site.

Lastly, I checked for the migration behavior of cells and could see that only adhesion based (mesenchymal) migration is affected by MiuA, while non-adhesion based (amoeboid) migration remains the same. With the previous mentioned data I can explain this behavior. Since the only migration parameter affected by the actin stabilizing effect of MiuA where essential for adhesion, I already hypothesized that only adhesion based migration would

be influenced. The reduction of adhesion force does satisfy the needed force anymore a cell needs to exert to move itself forward. Simultaneously, as there are no changes in the contractility of cells, amoeboid migration which mostly relies on contraction, did not change. Another parameter, that is not directly linked to cellular migration is the position of the nucleus in migrating cells. In my work, I saw that MiuA treated cells positioned their nucleus closer to the center than the control ones. This effect occurred in both mesenchymal and amoeboid migrating cells. This led me to the conclusion that this shift in nuclear position is only a side effect of the other influences MiuA has on the migration parameters. The most important effect might be the stabilizing effect which could lead to a build-up of actin inside the cell that pushed the nucleus more towards the center. The lower actin dynamics and longer actin filaments shown in this work support this idea. Nonetheless, it is to say that these experiments had only been employed using RPE-1 cells and their movement in both cases had been restricted to a 1D movement to facilitate the analysis of nuclear position. This kind of restriction might not reflect the environment, that cells typically reside in.

In summary, I gathered enough data that support the initial hypothesis that actin filament length has an interplay with the three main migration parameters. Although more research is needed this work already suggests that it is worth to further study this relationship. Additionally, this work shows, that compounds targeting the actin network and affecting the length of actin filaments can be used as a tool to specifically inhibit one of the two major migration modes. Especially cell lines that are capable of switching between migration modes embedded in environments allowing so are susceptible to this. This new knowledge might also help to find targets for pharmaceutical compounds and facilitates their screening with the described techniques in this work.

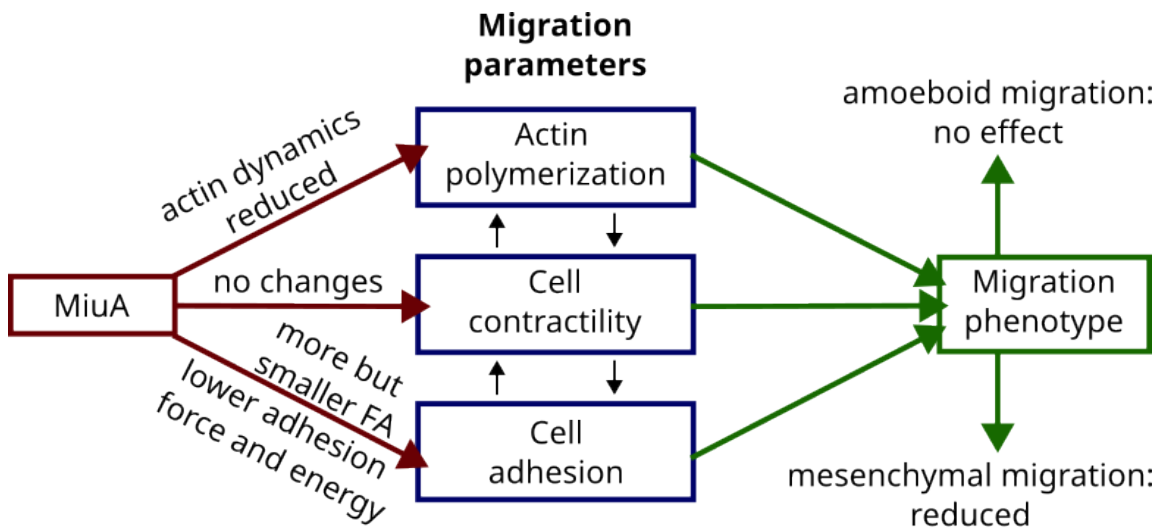


Figure 6.1: Graphical abstract for the results. The actin stabilizer MiuA reduces dynamics in actin filaments, decreases the size of focal adhesions, and increases the number of focal adhesions, but has no effect on cell contractility. The changes in these migration parameters influence the migration phenotype of the cell by only targeting adhesion based (mesenchymal) migration and leaving non-adhesion based (amoeboid) migration unaffected.

Chapter 7

Outlook

The interplay between the cytoskeleton and cell migration has been, is, and will continue to be part of many studies. Understanding the underlying mechanisms of cell migration could help us to better understand cancer, the immune system, embryonic development, and much more. In my work, I aimed to contribute to the field by examining the impact of actin stabilization on the three main migration parameters: actin polymerization, cell adhesion, and cell contractility. The data presented in this work provide compelling evidence that actin filament length is a crucial variable in the mechanism of cell migration. The observations revealed that cells with stabilized actin filaments exhibit reduced actin dynamics, reduced adhesion properties, and no change in contractility. This led to the hypothesis that adhesion-based migration is affected by stabilizing actin filaments, while non-adhesion-based migration remains unaffected, which is supported by the presented data.

Nevertheless, there are many other things to unveil about this. In the following, I will provide an overview on the next stages in the investigation of the relationship between actin filament length and cell migration behavior.

First, the precise mechanism by which the actin stabilizer miuraenamide A acts on the actin cortex remains unknown. Given its function as an actin stabilizer, it is reasonable to assume that this compound will have an effect on this structure. By employing scanning electron microscopy, expansion microscopy, or other related super-resolution microscopy techniques, one can measure the actin cortex and the effect MiuA has on it.

With regard to this it would be worthwhile to investigate the interplay between MiuA and other actin-targeting compounds. Given that MiuA impedes cofilin's ability to sever actin filaments, it would be interesting to see whether compounds like calyculin A that directly target actin monomers, can negate the stabilizing effect of MiuA. Similarly, it would then be of interest to test whether the inhibitory effect on migration could be reversed. This could provide a means of precisely modulating the effects of actin-stabilizing and destabilizing compounds, thereby enhancing the precision with which cell migration can be altered.

In addition to the structure and dynamics of the actin network itself, it is also worth to take a closer look on the formation dynamics of focal adhesion in cells. The combination of the existing technique of FluidFM with confocal fluorescence microscopy allows recording and study of focal adhesions in more detail. This would allow us to gain more insight in the role of actin filaments in all three phases of adhesion, namely the attachment, maintenance, and detachment of focal adhesions.

Another area that remains open to further investigation is the impact of actin stabilizing on migration in three-dimensional environments. For now, I only looked at 1D and 2D migration, which does not reflect the typical circumstances in living organisms. For this, one could check the migration of cells in a 3D gel where they are able to move freely in any direction. Based on the observations presented in this work, it can be postulated that the adhesion-based migration would still be inhibited while the non-adhesion-based migration would not change. Other ideas to study the migration behavior in cells would also include using a so called “soft cell confiner”, where a soft microstructure is used to confine cells. This approach would facilitate the alternation between confinement and non-confinement, compelling cells to transition between modes of migration. This would help to better understand the comprehensive interplay between migration parameters and the exhibited migration mode.

Taken together, there is still a considerable scope for further discoveries and investigation. A deeper comprehension of cell mechanics and its fundamental processes, will facilitate the prediction of how cells accomplish their biological functions. This, in turn will enable the identification of novel targets and mechanisms which pharmaceutical compounds may act. As previously stated, cellular migration is essential for cancer and metastasis, as well as the immune cells. The overarching objective in this field of research is to detect novel strategies for combating cancer and other diseases. To achieve this goal, scientists will continue to conduct research.

Chapter 8

Additional publications

In this chapter I briefly want to show additional research articles I was also involved in. The following list gives an overview about the articles, including the title, where it was published and a short description of my contribution:

1. *Metastasising Fibroblasts Show an HDAC6-Dependent Increase in Migration Speed and Loss of Directionality Linked to Major Changes in the Vimentin Interactome* [93].

See page 96.

Published in “International Journal of Molecular Science” in 2022.

My contribution: I received time lapse videos from migrating fibroblasts and analyzed their migration behavior under the influence of the HDAC6 inhibitor tubacin. Afterwards, I extracted the migration speed and persistence of the cells, performed statistical tests, and plotted the data for visualization. Finally, I discussed the results with the corresponding author and wrote section 4.11 from the article.

2. *IL-3 receptor signalling suppresses chronic intestinal inflammation by controlling mechanobiology and tissue egress of regulatory T cells* [21].

See page 121.

Published in “Gut” in 2023.

Additional experiments, which are not included in the article are also included and can be seen at page 135.

My contribution: Karen Ullrich send me murine CD4+ T cells extracted from the thymus and spleen (wild type, Interleukin 3 K.O., Interleukin 3 receptor K.O.). I visualized the actin network inside of these cells and analyzed its circularity, as well as the cross section area. Additionally, I used the BacMam technology and FRAP to measure the dynamics of the actin network. In the end, I extracted the data, performed statistical testing, and plotted the data for visualization. Finally, I wrote section “*Fluorescence recovery after photobleaching (FRAP)*” of the article and discussed the data with Karen Ullrich.

3. *Engineering Material Properties of Transcription Factor Condensates to Control Gene Expression in Mammalian Cells and Mice*[94].

See page 138.

Published in “Small” in 2024.

My contribution: In this article, I consulted Alexandra Fischer about the analysis of FRAP data. I checked her protocol and calculations, and gave a theoretical framework on which the obtained data could be discussed.

They were not part of my main research question, but nonetheless gave me the opportunity to improve my skills of the analysis of migration data, the analysis of FRAP data and performing FRAP experiments with non-adhering CD4+ T cells.

The following pages include the articles and an additional list that shows the contributions for each author in detail respectively.

Faculty of Natural Sciences and Technology**Cumulative form of the dissertation****Template for the confirmation of the proportion of co-authors**

Title of the dissertation (working title):**Cytoskeletal aspects of cellular migration**Article to be included:

Evans, C.A.; Kim, H.R.; Macfarlane, S.C.; Nowicki, P.I.A.; Baltes, C.; Xu, L.; Widengren, J.;
Lautenschläger, F.; Corfe, B.M.; Gad, A.K.B.

*Metastasising Fibroblasts Show an HDAC6-Dependent Increase in Migration Speed and Loss of
Directionality Linked to Major Changes in the Vimentin Interactome.*

Int. J. Mol. Sci. **2022**, *23*, 1961.

<https://doi.org/10.3390/ijms23041961>

Quality of the publication:

Research article

Review process or publication status:

Accepted and published

Explanation of the contributions of the co-authors:

Caroline A. Evans: Generated concepts, designed experiments, performed experiments, analyzed and interpreted them.

- Mass Spectrometry 80 %
- Protein identification and Bioinformatic analysis 100 %
- Statistical analysis 50 %

Hyejeong Rosemary Kim: Performed experiments, analyzed and interpreted them.

- Cell culture and treatment 60 %
- Preparation of enriched intermediate filament protein fraction 100 %
- Western Blot 70 %
- Live Cell Imaging 90 %
- Interpretation of migration Data 10 %

Sarah C. Macfarlane: Performed experiments, analyzed and interpreted them.

- Cell culture and treatment 40 %
- Analysed and interpreted the Cell Shape 40 %
- Live Cell Imaging 10 %
- Immunofluorescence 10 %
- Statistical analysis 25 %

Poppy I.A. Nowicki:

Analysed and interpreted the Cell Shape 60%

Carsten Alexander Baltes: prepared Figures (Figure 2 B) wrote section 4.11 *Tracking and Analysis of Migrating cells* of the manuscript and analyzed the following experiments:

- Analysis of cellular migration of fibroblasts: 100 %
- Interpretation of migration Data: 90 %
- Statistical analysis 25 %

Lei Xu: Analyzed and interpreted the following experiments:

- Super resolution STED imaging 50 %

Jerker Widengren: Analyzed and interpreted the following experiments:

- Super resolution STED imaging 20 %

Bernard M. Corfe: Generated concepts, designed experiments, analyzed and interpreted them.

- Mass Spectrometry analysis 10 %

Annica K.B. Gad: Generated concepts, designed experiments, drafted the manuscript and edited the final submission. Performed the following experiment, analyzed and interpreted them.

- Immunofluorescence staining 100 %
- Epifluorescence microscopy 80 %
- Super resolution STED imaging 30 %
- Mass Spectrometry analysis 10 %

Franziska Lautenschläger: Secured funding and supervised the analysis of cellular migration

Signature of the doctoral candidate
(Carsten Alexander Baltes)



Signature of the co-authors

Co-author	Signature
Caroline A. Evans	
Hyejeong Rosemary Kim	
Sarah C. Macfarlane	
Poppy I.A. Nowicki	

Lei Xu

Jerker Widengren

Franziska Lautenschläger



Bernard M. Corfe

Annica K.B. Gad



Note:

The original group responsible for the main part of this work does not exist anymore (29.05.2024). Annica K.B. Gad as the corresponding author and former group leader assured us that contacting the co-authors above is a major challenge as new contact details are not available.

Franziska Lautenschläger as the supervisor of Carsten A. Baltes and Annica K.B. Gad as the corresponding author for this work confirm that the list of contributions above is correct to the best of their knowledge.



Franziska Lautenschläger

Article

Metastasising Fibroblasts Show an HDAC6-Dependent Increase in Migration Speed and Loss of Directionality Linked to Major Changes in the Vimentin Interactome

Caroline A. Evans ¹, Hyejeong Rosemary Kim ², Sarah C. Macfarlane ², Poppy I. A. Nowicki ², Carsten Baltes ³, Lei Xu ⁴, Jerker Widengren ⁴, Franziska Lautenschläger ³, Bernard M. Corfe ⁵ and Annica K. B. Gad ^{2,6,*}

¹ Department of Chemical and Biological Engineering, University of Sheffield, Mappin St, Sheffield S1 3JD, UK; caroline.evans@sheffield.ac.uk

² Department of Oncology and Metabolism, The Medical School, University of Sheffield, Beech Hill Road, Sheffield S10 2RX, UK; h.r.kim@sheffield.ac.uk (H.R.K.); scmacfarlane1@sheffield.ac.uk (S.C.M.); pianowicki1@sheffield.ac.uk (P.I.A.N.)

³ Experimental Physics, NT Faculty, D2 2, Saarland University, 66123 Saarbrücken, Germany; carstenbaltes@gmx.de (C.B.); f.lautenschlaeger@physik.uni-saarland.de (F.L.)

⁴ Department of Applied Physics/Experimental Biomolecular Physics, KTH Royal Institute of Technology, SE-100 44 Stockholm, Sweden; lxu@kth.se (L.X.); jwideng@kth.se (J.W.)

⁵ Population Health Sciences Institute, Human Nutrition Research Centre, Faculty of Medical Sciences, Newcastle University, Newcastle NE2 4HH, UK; Bernard.Corfe@newcastle.ac.uk

⁶ Madeira Chemistry Research Centre, University of Madeira, 9020105 Funchal, Portugal

* Correspondence: a.k.gad@sheffield.ac.uk; Tel.: +44-114-215-9681



Citation: Evans, C.A.; Kim, H.R.; Macfarlane, S.C.; Nowicki, P.I.A.; Baltes, C.; Xu, L.; Widengren, J.; Lautenschläger, F.; Corfe, B.M.; Gad, A.K.B. Metastasising Fibroblasts Show an HDAC6-Dependent Increase in Migration Speed and Loss of Directionality Linked to Major Changes in the Vimentin Interactome. *Int. J. Mol. Sci.* **2022**, *23*, 1961. <https://doi.org/10.3390/ijms23041961>

Academic Editor: Jose Maria Gonzalez-Granado

Received: 30 November 2021

Accepted: 7 February 2022

Published: 10 February 2022

Publisher's Note: MDPI stays neutral with regard to jurisdictional claims in published maps and institutional affiliations.



Copyright: © 2022 by the authors. Licensee MDPI, Basel, Switzerland. This article is an open access article distributed under the terms and conditions of the Creative Commons Attribution (CC BY) license (<https://creativecommons.org/licenses/by/4.0/>).

Abstract: Metastasising cells express the intermediate filament protein vimentin, which is used to diagnose invasive tumours in the clinic. We aimed to clarify how vimentin regulates the motility of metastasising fibroblasts. STED super-resolution microscopy, live-cell imaging and quantitative proteomics revealed that oncogene-expressing and metastasising fibroblasts show a less-elongated cell shape, reduced cell spreading, increased cell migration speed, reduced directionality, and stronger coupling between these migration parameters compared to normal control cells. In total, we identified and compared 555 proteins in the vimentin interactome. In metastasising cells, the levels of keratin 18 and Rab5C were increased, while those of actin and collagen were decreased. Inhibition of HDAC6 reversed the shape, spreading and migration phenotypes of metastasising cells back to normal. Inhibition of HDAC6 also decreased the levels of talin 1, tropomyosin, Rab GDI β , collagen and emilin 1 in the vimentin interactome, and partially reversed the nanoscale vimentin organisation in oncogene-expressing cells. These findings describe the changes in the vimentin interactome and nanoscale distribution that accompany the defective cell shape, spreading and migration of metastasising cells. These results support the hypothesis that oncogenes can act through HDAC6 to regulate the vimentin binding of the cytoskeletal and cell–extracellular matrix adhesion components that contribute to the defective motility of metastasising cells.

Keywords: oncogenes; metastasis; cell migration; histone deacetylase 6; vimentin; vimentin interactome; fibroblasts; genome-wide mass spectrometry; stimulated emission depletion microscopy

1. Introduction

Metastasising tumour cells show increased levels of the intermediate filament protein vimentin, which has, therefore, been used to diagnose invasive tumours in the clinic for decades. Vimentin is a canonical marker of epithelial-to-mesenchymal transition (EMT), a process that occurs during embryogenesis, wound healing and cancer in which stationary cells change from a round to an elongated cell shape and become migratory. Recent findings have shown that vimentin is not only a passive marker of carcinomas and EMT, but might also induce changes in cell shape, adhesion and migration—as well as promoting

the invasion of tumour cells [1–6]. In particular, vimentin expression in epithelial cells is required and sufficient for the change from a round to an elongated cell shape, and vimentin is required for directional cell migration [7,8]. Vimentin is also required for the mechanical and adhesion properties of cells, and the metastatic spread of lung cancers [1,7–9]. This might be due, in part, to the promotion of single cell migration by vimentin, which regulates the functions of the actin microfilament and microtubule filamentous systems [9,10].

However, the molecular mechanisms through which vimentin regulates cell shape and motility remain incompletely understood. In addition to the regulation of the actin microfilament and microtubule systems, vimentin is also likely to control cell–matrix adhesions. An increasing number of observations have suggested that vimentin regulates both the inside-out control of the growth of initial focal complexes and the outside-in signalling required to form mature and large focal adhesions. For example, long and mature filaments localise to the base of relatively large cell–matrix adhesions, and this localisation to focal adhesions stabilises and promotes the mechanical strength of these adhesions. The transient depolymerisation of filamentous vimentin occurs locally, just prior to the formation of lamellipodia [11]. Accordingly, in a recent study by Ostrowska-Podhorodecka et al., binding of the cell-adhesion component talin 1 to vimentin filaments shifted the inside-out to outside-in signalling at cell–matrix adhesions, which resulted in focal adhesion maturation [12]. The loss of vimentin reduced the number and size of cell–matrix adhesions, as well as the levels of the cell-adhesion molecule integrin β 1 and the F-actin cross-linker filamin A [13]. Together with the observation that polymerisation-deficient vimentin suppresses the growth of cell–matrix adhesions via a mechanism that requires calcium-dependent, non-lysosomal calpain proteases [14], this is in line with a previously proposed model that suggests that competition between the calpain-mediated proteolysis of talin 1 and filamin A at focal adhesions is required for the growth of focal adhesions [15]. Vimentin can also promote the production of the extracellular matrix [16,17], which suggests an indirect vimentin-dependent regulation of outside-in signalling. However, the mechanisms by which vimentin regulates and integrates cell–matrix adhesion, cell shape, and motility in health and disease remain to a large extent unclear.

Vimentin is the main intermediate filament system in fibroblasts. We have previously shown that in fibroblasts, oncogenes reduce the size and increase the numbers of micrometer-sized cell–matrix adhesions [18]. This results in a more homogenous distribution of nanoscale cell–matrix adhesions, and these changes are linked to a more entangled network of vimentin filaments. The focus of this work is to describe how HDAC6 influences the spatial organization of vimentin, and the downstream consequences for intracellular signalling and cell migration—but not on the protein levels of vimentin. HDAC6 is a protein required for the RasV12 oncogene to oncogenically transform cells, and for the formation of aggresomes, cytokinesis and EMT; it is currently a key target for the development of drugs against cancer [19]. The change in cell shape from circular to elongated that accompanies EMT caused by increased levels of vimentin is also observed upon the inhibition of HDAC6 [20]. In many cell types, the directionality of cell migration correlates with migration speed [21]. We hypothesised that in our fibroblast system, oncogenes act via HDAC6 to change the vimentin interactome, and thereby the speed and the directionality of cell migration—as well as the coupling between cell speed and directionality.

These data suggest that in our fibroblast system, the transformation of B_j primary fibroblasts to metastasising cells is accompanied by the loss of the elongated cell shape, reduced cell spreading, increased cell migration speed, reduced directionality, stronger correlation between cell migration speed and reduced directionality, and changes in the nanoscale spatial distribution and the protein interactome of vimentin via an HDAC6-dependent mechanism. These observations are in line with the hypothesis that oncogenes promote the dysregulation of cell motility and metastasis via HDAC6-mediated regulation of the spatial distribution and binding of vimentin to components of cell–matrix adhesions.

2. Results

2.1. SV40T and H-RasV12 Change the Spatial Organisation of Vimentin More Than That of Actin and Tubulin

For cells to migrate from a tumour to a different site, the cell matrix adhesion and motility of the cells need to change. Although the cytoskeleton is the main determinant of these cell properties, how it contributes to metastasis is not fully understood. To determine how the three filamentous systems change during the transformation from primary fibroblasts to metastasising cells, we analysed the spatial distributions of actin microfilaments, microtubules and vimentin intermediate filaments in an isogenically matched stepwise cell model of four human cell variants that represent the transformation from primary fibroblasts to metastasising cells. Briefly (see also Materials and Methods), these are neonatal Bj human dermal fibroblasts, transformed using three well-defined genetic elements: the telomerase catalytic subunit (hTERT) in combination with two oncogenes (simian virus 40 large-T oncoprotein; V12 oncogenic allele of H-ras) [22]. These variants were as follows: (i) primary Bj fibroblasts; (ii) immortalised Bjhtert fibroblasts; (iii) cell cycle-defective BjhtertSV40T fibroblasts; and (iv) BjhtertSV40TRasV12 fibroblasts; the last of these form tumours, invade into the surrounding environment (Supplementary Figure S1), and metastasise in immunodeficient mice [23,24].

Here, we observed that at each step, all three of the cytoskeletal systems changed (Figure 1, Supplementary Figure S2). In line with previously published transcriptome data, the most pronounced change was between cell types two and three: the immortalised cell variant; and the cell cycle-defective SV40T-expressing cell variant [25]. The SV40T-expressing variant showed actin microfilament-rich lamellipodia around the cell periphery, where the microtubules were more localised towards the cell centre. In line with the literature that microtubules guide the organisation of vimentin filaments, and that vimentin can promote the assembly of microtubules, the vimentin organisation followed the distribution of the microtubules [26,27]. While thin vimentin filaments were distributed throughout the cytoplasm in an even manner in the primary and immortalised cell variants, the vimentin in the oncogene-expressing and metastasising cells showed a striking redistribution towards the cell centre—a change that was even more pronounced than the changes in actin and microtubules. The phenotypes were particularly pronounced in the fourth variant, the RasV12-expressing metastasising cells (Figure 1; Supplementary Figure S2). These cytoskeletal changes were accompanied by significant changes in cell shape and size. The oncogene-expressing and metastasising cell types showed significantly reduced cell elongation and cell size, as compared to the control (primary) cells (Figure 1). Taken together, these data suggest that changes in the spatial organisation of vimentin have a role in oncogenic cell transformation and metastasis.

2.2. HDAC6 Is Required for the Shape and Motility of Metastasising Cells

We next aimed to define the changes in cell shape, size and migration that accompany the metastatic process, and the role of HDAC6 in this process. To this end, we analysed cell shape and spreading area, the speed and directionality of cell migration, and the coupling between migration speed and directionality of metastasising cells without and with treatment with the highly potent and selective, reversible, cell-permeable HDAC6 inhibitor tubacin—as described in the Materials and Methods section. As compared to control fibroblasts, the metastasising cells showed a significantly reduced aspect ratio and increased circularity, which indicated the loss of the elongated fibroblast cell shape. This was accompanied by a reduction in the spreading area of the metastasising cells (Figure 2A), and the increased speed and reduced directionality of their migration. In particular, the correlation between increased speed and reduced directionality of migration was strengthened in the metastasising cells (Figure 2B; Supplementary Films S1 and S2). Here, tubacin-induced loss of HDAC6 activity in the metastasising cells reverted the changes in cell shape and spreading area to the controls. This also reduced the cell migration speed, increased the directionality of migration, and reduced the coupling between increased speed

and reduced directionality of the metastasising cells to that of the control cells (Figure 2; Supplementary Film S3).

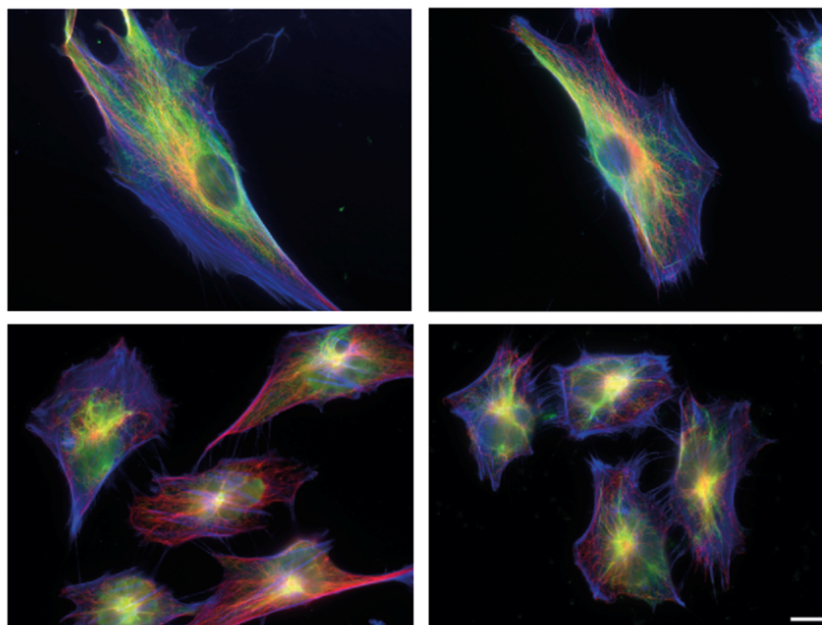


Figure 1. Cytoskeletal organisation and shape of human fibroblasts for the different stages of metastatic transformation. Immunofluorescence staining followed by Epifluorescence 2D microscopy showing Bj primary fibroblast (**top left**), Bjhtert cells (**top right**), BjhtertSV40T cells (**bottom left**) and metastasising BjhtertSV40TRasV12 cells (**bottom right**), showing vimentin (green), tubulin (red) and F-actin (blue). Scale bar, 10 μ m.

2.3. Inhibition of HDAC6 Activity Results in Loss of Nanoscale, Non-Filamentous, Short Versions of Vimentin at the Cell Periphery, and Formation of Cage-like Clusters/Asters of Filamentous Vimentin

To determine whether HDAC6 has a role in the regulation of the shape, spreading area and motility of cells via control of the spatial organisation of vimentin, we asked whether inhibition of HDAC6 activity changed the nanoscale spatial distribution of vimentin in oncogene-expressing cells. Upon inhibition of HDAC6 with tubacin (10 μ M tubacin, 4 h, 37 $^{\circ}$ C), the nanoscale, non-filamentous vimentin units at the periphery of the oncogene-expressing cells were lost and were replaced by vimentin in a dense filamentous network, which often included nanoscale ‘knots’ or ‘asters’ at the cell periphery (Figure 3; Supplementary Figure S3). At the very periphery of the oncogene-expressing metastasising cells, there were non-filamentous units of vimentin, while (as reported previously [11,18]) filamentous vimentin was visible at the end of focal adhesions—oriented towards the cell centre—and not inside focal adhesions. In the area between focal adhesions and the cell nucleus, vimentin was localised in filaments, which were occasionally arranged in similar small vimentin ring-shaped clusters or asters, as observed upon inhibition of HDAC6 (Figure 3).

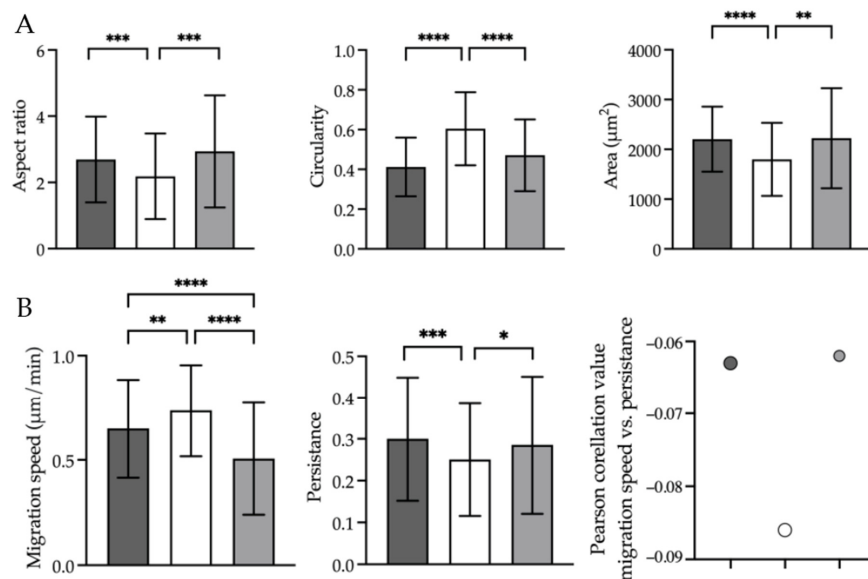


Figure 2. Oncogenes change cell shape and spreading area, speed and directionality of cell migration and speed-directionality coupling via HDAC6. (A) Epifluorescence 2D microscopy showing the aspect ratio (left), circularity (middle) and spreading area (right) of immortalised Bjhtert cells (dark grey) and metastasising BjhtertSV40TRasV12 cells without (white) and with (light grey) tubacin treatment. (B) Epifluorescence 2D live cell imaging showing the cell migration speed (left), cell migration persistence (middle) and Pearson's correlation between migration speed and persistence (right), of cells as in (A). Data are means \pm standard deviation of the total number of trajectories, shown in brackets, of Bjhtert (345), BjhtertSv40TRas without (149) and with tubacin (256), and three independent experiments. *, $p \leq 0.05$; **, $p \leq 0.01$; ***, $p \leq 0.001$; ****, $p \leq 0.0001$ (Mann-Whitney tests).

2.4. H-RasV12 and HDAC6 Activities Change the Binding of Cytoskeletal, Cell-Extracellular Matrix Adhesion Components to Vimentin Intermediate Filaments

Vimentin has been proposed to act as a platform for the binding of proteins, in order to thereby regulate intracellular signalling [28,29]. To determine how oncogenes and HDAC6 affect the vimentin interactome, and to indicate any potential regulators of the vimentin-dependent control of cell shape and motility, we analysed the vimentin interactome in the metastasising BjhtertSV40TRasV12 cells without and with tubacin treatment, and in the immortalised Bjhtert cells as a control. The intermediate filament fraction of the cell variants was first enriched to yield four subcellular fractions: membrane bound/soluble protein; cytoskeletal; highly salt-soluble supernatant; and insoluble cytoskeleton (see Materials and Methods). The levels and quality of these four fractions are shown in Figure 4A, and the final fraction—fraction 4—was enriched in vimentin relative to β -actin (Figure 4A; Supplementary Figure S4). We then analysed the protein content of this vimentin-enriched fraction 4 using a label-free quantitative proteomics approach (Supplementary Dataset 1, with 555 proteins identified and relatively quantified by ≥ 2 unique peptides). In terms of overall composition, fraction 4 contained intermediate filament proteins, of which vimentin was the most abundant. Keratin 18, lamins A and B1, plectin and pinin were also detected. Proteins associated with integrin binding and interactions with the extracellular matrix—such as integrin $\beta 1$, collagen α -1(VI), α -2(VI) and α -3(VI) chains, fibronectin, heparan sulphate proteoglycan core protein, talin 1 and CD44 antigen—were present.

Bioinformatic comparisons of these data with online vimentin-interaction data (BIOGRID interaction database; <https://thebiogrid.org/>; accessed 20 October 2021) indicated that 50 of the proteins in the dataset are known interaction partners for vimentin, including plectin, keratin 18, the sequestosome-1 aggresome protein and the 14-3-3- ζ adaptor protein YWHAZ, which induces Rac1 activity and lamellipodia formation [30,31]. Together with the co-clustering of two biological and three technical replicates for each sample in the heatmap analysis (Supplementary Figure S5), these observations provide confidence in the dataset.

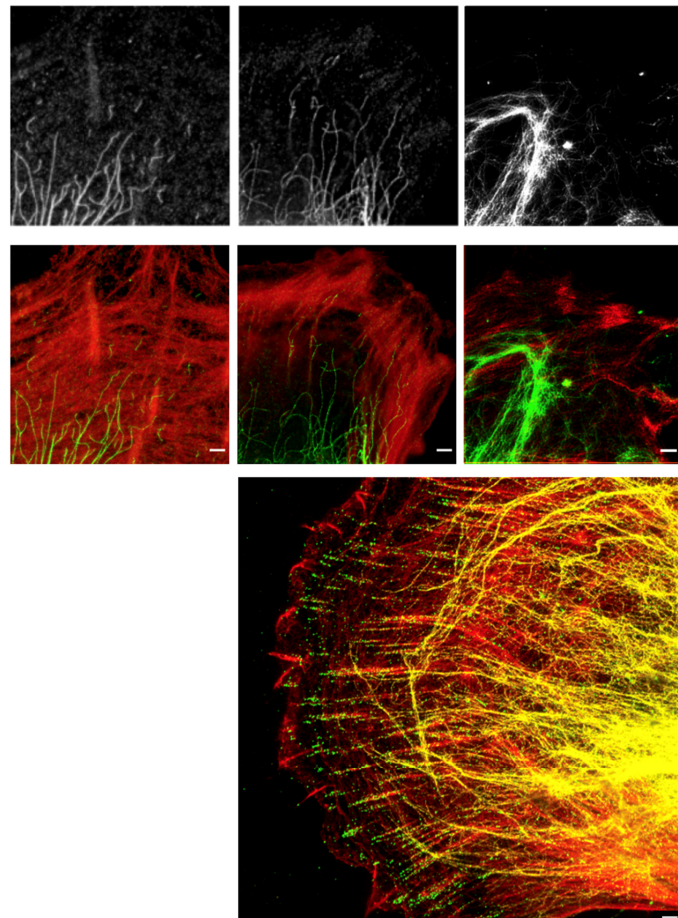


Figure 3. HDAC6 regulates the nanoscale spatial distribution of vimentin in oncogene-expressing and metastasising cells. Representative stimulated emission depletion (STED) super-resolution microscopy images of (top) immunofluorescence-stained Bjhert cells (left; immortalised) and BjhertSV40T cells (oncogene-expression) without (middle) and with (right) tubacin treatment, showing vimentin (white), (middle panel) vimentin (green) and F-actin (red) and (lower panel) a three-colour STED image of a BjhertSV40TRasV12 cell showing EGFP-vimentin (yellow), phosphotyrosine (green) and F-actin (red). Scale bars: 1 μ m.

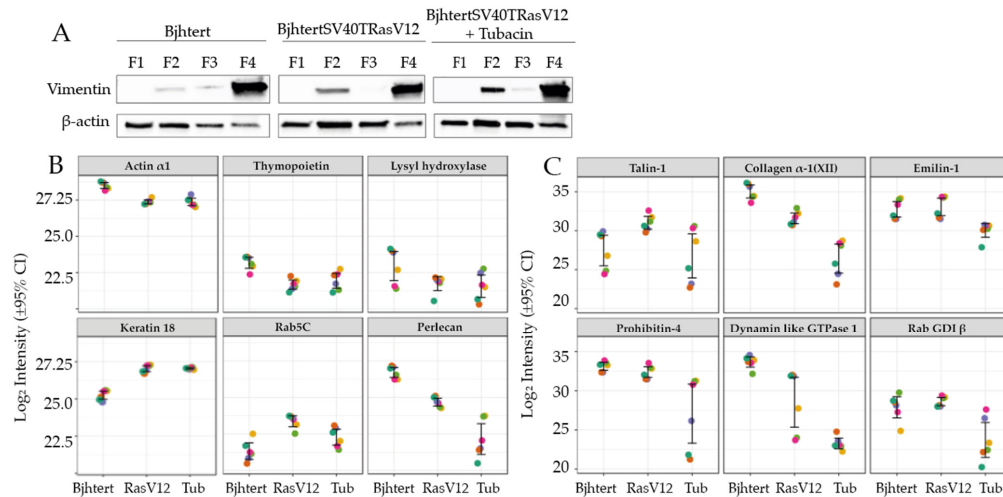


Figure 4. Vimentin interactome changes during metastatic transformation and upon inhibition of HDAC6 activity. Immortalised Bjhtert cells and metastasising BjhtertSV40TRasV12 cells without and with tubacin treatment. (A) Western blots for vimentin and actin in the cell fractions for the intermediate filament enrichment. (B,C) Mass spectrometry quantification of protein levels in the vimentin interactome in immortalised Bjhtert control cells and metastasising BjhtertSV40TRasV12 cells without (RasV12) and with (Tub) tubacin treatment. The six replicate measurements (two biological replicates, analysed in triplicate) are indicated by the coloured dots for each sample.

The vimentin interactome in the metastasising BjhtertSV40TRasV12 cells was thus characterised and compared to that of the immortalised Bjhtert cells (see Materials and Methods). We observed increased levels of 24 proteins and decreased levels of 23 proteins in the metastasising cells (Table 1, Supplementary Figures S5 and S6). BjhtertSV40TRasV12 cells showed increased levels of the intermediate filament protein keratin 18 and the small Rho GTPase Rab5C (Figure 4B), which is a protein required for the formation of focal adhesions and directed cell migration [32]. Furthermore, the vimentin interactome of these metastasising cells showed increased levels of 10 proteins associated with RNA metabolism (Supplementary Table S1), and of the glycolytic enzyme triosephosphate isomerase, the nuclear pore complex protein Nup153, and elongation factor 1- β . In contrast, the levels of the cytoskeletal components α -actin and thymopoietin were decreased (Figure 4B). The bioinformatic data mining of the interaction database identified α -actin and thymopoietin as known vimentin interactors.

Proteins associated with the organisation of the extracellular matrix were also down-regulated in the vimentin interactome of the metastasising cells: collagen type XII; collagen processing protein procollagen-lysine,2-oxoglutarate 5-dioxygenase 1/lysyl hydroxylase; fibulin 2; and heparan sulphate proteoglycan 2 (Figure 4B). We also observed decreased levels of mitochondrial voltage-dependent anion channels 1,2, ubiquitin-processing protein RuvB-like 1, and proteasome 26S non-ATPase 6 subunit (Table 1). Taken together, in the vimentin interactome of the metastasising cells there were decreased levels of extracellular-matrix, cell-surface, cell-matrix adhesion, mitochondrial ion transport and ubiquitin-processing proteins, and increased levels of keratin 18, Rab5C and proteins involved in RNA metabolism. These data for selected proteins are shown in Figure 4B.

Table 1. Changes in protein levels for all of the proteins altered in the vimentin interactome of metastasising BjhtertSV40TRasV12, relative to immortalised Bjhtert cells.

Protein	Gene	Protein ID	BjhtertSV40TRasV12 vs. Bjhtert (Fold-Change) ^a
Protein SON	SON	P18583	5.5
Neuroblast differentiation-associated protein AHNAK	AHNAK	Q09666	4.7
WD repeat-containing protein 46	WDR46	O15213	4.5
60S ribosomal protein L7-like 1	RPL7L1	Q6DKI1	4.2
Ribosome biogenesis protein BOP1	BOP1	Q14137	4.1
RNA-binding protein 8A	RBM8A	Q9Y5S9	4.0
Transcription factor BTF3	BTF3	A0A7I2YQL2	3.7
Triosephosphate isomerase	TP11	P60174	3.7
Elongation factor 1-β	EEF1B2	P24534	3.6
Keratin, type I cytoskeletal 18	KRT18	P05783	3.5
U3 small nucleolar RNA-associated protein 15 homologue	UTP15	Q8TED0	3.2
WD repeat-containing protein 75	WDR75	Q8IWA0	3.2
Guanine nucleotide-binding protein-like 3	GNL3	Q9BVP2	3.1
Nuclear pore complex protein Nup153	NUP153	P49790	3.1
DNA-directed RNA polymerase II subunit RPB3	POLR2C	P19387	3.0
U3 small nucleolar ribonucleoprotein protein MPP10	MPHOSPH10	O00566	2.9
ATP-dependent RNA helicase DDX18	DDX18	Q9NVP1	2.9
Deoxynucleotidyltransferase terminal-interacting protein 2	DNTTIP2	Q5QJE6	2.8
Ribosome production factor 2 homologue	RPF2	Q9H7B2	2.6
Ras-related protein Rab5C	RAB5C	P51148	2.6
H/ACA ribonucleoprotein complex subunit 4	DKC1	O60832	2.5
MKI67 FHA-domain-interacting nucleolar phosphoprotein	NIFK	Q9BYG3	2.4
Ribosome biogenesis protein BMS1 homologue	BMS1	Q14692	2.2
Nucleolar GTP-binding protein 1	GTPBP4	Q9BZE4	2.2
Voltage-dependent anion-selective channel protein 2	VDAC2	P45880	-2.1
Histone H2B type 2-E	HIST2H2BE	Q16778	-2.1
RuvB-like 1	RUVBL1	Q9Y265	-2.2
Actin, α skeletal muscle	ACTA1	P68133	-2.2
Bcl-2-associated transcription factor 1	BCLAF1	A0A1W2PQ43	-2.2
Testis-expressed sequence 10 protein	TEX10	Q9NXF1	-2.5
HLA class I histocompatibility antigen, Cw-7 α chain	HLA-C.1	O19617	-2.5
CD109 antigen	CD109	Q6YHK3	-2.6
Collagen α-1(XII) chain	COL12A1	D6RGG3	-2.6
HLA class I histocompatibility antigen, A-3 α chain	HLA-A	Q5SUL5	-2.6
Procollagen-lysine,2-oxoglutarate 5-dioxygenase 1/lysyl hydroxylase	PLOD1	Q02809	-2.6
Heterogeneous nuclear ribonucleoprotein H3	HNRNPH3	P31942	-2.8
Lamina-associated polypeptide 2, isoform α/ thymopoietin	TMPO	P42166	-2.9
WD repeat-containing protein 18	WDR18	U3KQC1	-2.9
Heterogeneous nuclear ribonucleoprotein U-like protein 2	HNRNPUL2-BSC12	H3BQZ7	-3.1
HLA class I histocompatibility antigen B α chain	HLA-B	Q2L6G2	-3.2
Voltage-dependent anion-selective channel protein 1	VDAC1	P21796	-3.2
Fibulin-2	FBLN2	P98095	-3.5
Basement membrane-specific heparan sulphate proteoglycan core protein	HSPG2	P98160	-4.1
Interferon-induced GTP-binding protein Mx1	MX1	A0A7P0T9R0	-4.4
26S proteasome non-ATPase regulatory subunit 6	PSMD6	Q15008	-4.6
Myosin regulatory light chain 12A	MYL12A	J3QRS3	-6.8
Interferon-induced GTP-binding protein Mx2	MX2	P20592	-8.9

^a positive value, increase; negative value, decrease.

Proteins associated with the organisation of the extracellular matrix were also down-regulated in the vimentin interactome of the metastasising cells: collagen type XII; collagen processing protein procollagen-lysine,2-oxoglutarate 5-dioxygenase 1/lysyl hydroxylase; fibulin 2; and heparan sulphate proteoglycan 2 (Figure 4B). We also observed decreased

levels of mitochondrial voltage-dependent anion channels 1,2, ubiquitin-processing protein RuvB-like 1, and proteasome 26S non-ATPase 6 subunit (Table 1). Taken together, in the vimentin interactome of the metastasising cells there were decreased levels of extracellular-matrix, cell-surface, cell-matrix adhesion, mitochondrial ion transport and ubiquitin-processing proteins, and increased levels of keratin 18, Rab5C and proteins involved in RNA metabolism. These data for selected proteins are shown in Figure 4B.

We then investigated whether the reversion of the cell shape, size and motility of metastasising cells to the control phenotype upon inhibition of HDAC6 was accompanied by a reversion of the vimentin interactome to that of the control cells. Tubacin treatment of BjHtertSV40TRasV12 cells resulted in increased levels of 9 proteins and decreased levels of 44 proteins. The global interactome in the metastasising cells was not reversed to that of the control cells; rather, the changes observed in the metastasising cells, as compared to control cells, were further enhanced by the tubacin treatment (Figure 2B, Supplementary Figures S5 and S6). Similar to oncogene expression, the tubacin treatment resulted in major decreases in the levels of cytoskeletal, cell-matrix adhesion, and extracellular matrix proteins in the vimentin interactome. However, the specific cytoskeletal and cell-matrix components were different, including talin 1, collagen type XII α -1 chain, emilin-1, prolyl 4-hydroxylase subunit β (Table 2). These proteins all have integrin binding activities, according to our bioinformatic interaction analysis using the g:Profiler tool. Of the nine proteins that increased, six (RPS9, NOP2, MRTO4, UTP6, PWP2, KRR1) are involved in the metabolism and processing of rRNA, and represent potential novel vimentin-associated proteins. Tubacin treatment reverted the levels of EEF1B2 in the metastasising cells to the levels of the control cells. In contrast, in the metastasising cells, tubacin enhanced the increase in GTP-binding protein 4 (GTPBP4), and further reduced the reduced levels of collagen α -1 (XII) chain, heparan sulphate proteoglycan 2/perlecan, dynamin-like GTPase 1 (MX1), the anion-selective ion channel proteins VDAC1 and VDAC2, and the HLA class I histocompatibility antigens (HLA-A, HLA-B) (Table 2, Figure 4C). The relative levels of vimentin were unchanged across samples (Figure S7).

Table 2. Tubacin effects (i.e., inhibition of HDAC6 activity) for all of the proteins altered in the vimentin interactome of metastasising BjHtertSV40TRasV12 cells.

Protein	Gene	Protein ID	BjHtertSV40TRasV12 with vs. without Tubacin (Fold-Change) ^a
40S ribosomal protein S23	RPS23	P62266	2.1
GTP-binding protein 4	GTPBP4	Q9BZE4	2.1
40S ribosomal protein S9	RPS9	P46781	2.2
Probable 28S rRNA (cytosine(4447)-C(5))-methyltransferase	NOP2	P46087	2.3
mRNA turnover protein 4 homologue	MRTO4	Q9UKD2	2.5
Probable ATP-dependent RNA helicase DDX56	DDX56	G3V0G3	2.7
U3 small nucleolar RNA-associated protein 6 homologue	UTP6	Q9NYH9	3.1
Periodic tryptophan protein 2 homologue	PWP2	Q15269	4.3
KRR1 small subunit processome component homologue	KRR1	Q13601	4.9
26S protease regulatory subunit 10B	PSMC6	A0A087X2I1	-2.0
Glycine-tRNA ligase	GARS	A0A6Q8PGW4	-2.1
Transitional endoplasmic reticulum ATPase	VCP	P55072	-2.1
X-ray repair cross-complementing protein 6	XRCC6	P12956	-2.1
Eukaryotic translation initiation factor 5B	EIF5B	A0A087WUT6	-2.1
T-complex protein 1 subunit γ	CCT3	B4DUR8	-2.1
Emilin-1	EMILIN1	Q9Y6C2	-2.3
Glucose-6-phosphate 1-dehydrogenase	G6PD	P11413	-2.4
Prohibitin	PHB	P35232	-2.5
Rab GDP dissociation inhibitor β	GDI2	P50395	-2.5
Tubulin-specific chaperone A	TBCA	E5RIW3	-2.5

Table 2. Cont.

Protein	Gene	Protein ID	BjhtertSv40TRasV12 with vs. without Tubacin (Fold-Change) ^a
Dolichyl-diphospho-oligosaccharide-protein glycosyltransferase 48 kDa subunit	<i>DDOST</i>	A0A0C4DGS1	−2.6
26S proteasome non-ATPase regulatory subunit 2	<i>PSMD2</i>	Q13200	−2.6
Malate dehydrogenase, mitochondrial	<i>MDH2</i>	P40926	−2.7
mRNA export factor	<i>RAE1</i>	E9PQ57	−2.7
Coatomer subunit γ -1	<i>COPG1</i>	Q9Y678	−2.8
Voltage-dependent anion-selective channel protein 2/voltage dependent anion channel 2	<i>VDAC2</i>	P45880	−2.9
Heterogeneous nuclear ribonucleoprotein R	<i>HNRNPR</i>	O43390	−2.9
Heat shock protein β -1	<i>HSPB1</i>	P04792	−3.0
Elongation factor 1- β	<i>EEF1B2</i>	P24534	−3.1
Neutral α -glucosidase AB	<i>GANAB</i>	Q14697	−3.1
Talin-1	<i>TLN1</i>	Q9Y490	−3.1
Peroxiredoxin-6	<i>PRDX6</i>	P30041	−3.2
Sodium/potassium-transporting ATPase subunit α -1	<i>ATP1A1</i>	P05023	−3.2
HLA class I histocompatibility antigen B α chain	<i>HLA-B</i>	Q2L6G2	−3.3
Flotillin-1	<i>FLOT1</i>	O75955	−3.4
Leucine-rich repeat-containing protein 59	<i>LRRC59</i>	Q96AG4	−3.4
tRNA-splicing ligase RtcB homologue	<i>RTCB</i>	Q9Y310	−3.4
Transcription intermediary factor 1- β	<i>TRIM28</i>	Q13263	−3.5
Serpin H1	<i>SERPINH1</i>	P50454	−3.6
Interferon-induced GTP-binding protein Mx1/dynamin like GTPase 1	<i>MX1</i>	A0A7P0T9R0	−3.6
Signal transducer and activator of transcription 1- α / β	<i>STAT1</i>	A0A669KB68	−3.8
Protein CutA	<i>CUTA</i>	O60888	−3.9
Protein disulphide-isomerase/collagen prolyl 4-hydroxylase β	<i>P4HB</i>	A0A7P0T8J3	−4.3
Basement-membrane-specific heparan sulphate proteoglycan core protein	<i>HSPG2</i>	P98160	−4.6
KH domain-containing, RNA-binding, signal transduction-associated protein 1	<i>KHDRBS1</i>	Q07666	−4.6
Collagen α -1(XII) chain	<i>COL12A1</i>	D6RGG3	−4.8
Tropomyosin α -4 chain	<i>TPM4</i>	P67936	−4.8
Voltage-dependent anion-selective channel protein 1	<i>VDAC1</i>	P21796	−4.9
Prothymosin α	<i>PTMA</i>	B8ZZQ6	−5.0
Protein S100-A11	<i>S100A11</i>	P31949	−5.4
C-1-tetrahydrofolate synthase, cytoplasmic	<i>MTHFD1</i>	V9GYY3	−5.7
HLA class I histocompatibility antigen, A-3 α chain	<i>HLA-A</i>	Q5SUL5	−11.6
RPLP1	<i>RPLP1</i>	P05386	−50.6

^a positive value, increase; negative value, decrease.

3. Discussion

The observation that during the metastatic transformation of cells the spatial organisation of vimentin intermediate filaments is more pronouncedly changed than that of microfilaments or microtubules highlights the possibility that vimentin has a more important role in the control of the cell–extracellular matrix adhesion and the cell shape and motility of metastasising cells than previously recognised.

This proteome analysis of the vimentin-enriched intermediate filament fraction of cells provides a global view of the vimentin interactome and indicates protein pathways and networks for future investigations. It is important to note that these interactions need to be validated using separate methods, and that differences in protein levels between interactomes does not necessarily mean that the binding of a protein to vimentin is different, because this might simply be caused by different total levels of the proteins in cells. For example, we observed reduced levels of collagen 1 and lysyl hydroxylase in the vimentin interactome of metastasising cells, as compared to the immortalised control cells; however,

this is likely due to reduced expression of these genes in the metastasising cells [25]. In contrast, the reduced levels of thymopoietin might not be due to reduced gene expression, because the expression of this gene is increased in metastasising cells, as compared to controls. Similarly, the gene expression of the protein that showed the greatest increase in the vimentin interactome of metastasising cells was reduced on the gene expression level—keratin 18 [25]. This highlights the possibility that in metastasising fibroblasts, vimentin can co-assemble with keratin 18 to form an intermediate filament variant and a cell phenotype that is intermediate between those of mesenchymal and epithelial cells. This is in line with previous reports that the co-assembly of keratin 18 and vimentin at subcellular regions in epithelial cells during EMT results in increased cell motility [27]. The muscle actin $\alpha 1$ was identified in the vimentin interactomes of all four of our cell variants and their treatments. This supports earlier observations showing that muscle actins can be incorporated into the cytoskeleton of fibroblasts [33]. Similarly, the actin crosslinkers filamin A and B were identified in all vimentin interactomes (Supplementary Dataset S1). Cells that lack filamin A show defective growth of focal adhesions, which is a phenotype that can be reversed to control cell levels by expression of a calpain-uncleavable, but not full-length, variant of talin 1 [14]. Calpain-cleavage of talin 1 has been shown to be a rate-limiting step in the turnover of cell-matrix adhesions [15,34]. These observations are in line with the model that suggests that competition between talin 1 and filamin A for binding to integrins that is controlled by calpain-mediated proteolysis is required for cell-matrix adhesions to grow [15]. We speculate that vimentin has a major role in this control, through the protection of cell-adhesion components against calpain-mediated proteolysis.

Although inhibition of HDAC6 activity in the metastasising cells resulted in a reversal of the changes to cell shape, cell migration speed and directionality, and the speed-directionality coupling of cell migration compared to control cells, this was not accompanied by a similar reversal of the protein interactions of the vimentin interactome in the metastasising cells. This is not surprising, given that tubacin treatment does not affect gene expression [22], and can therefore not be expected to fully reverse all of the oncogene-induced changes of the transcriptome and the proteome to that of the control cells. Because tubacin targets HDAC6 activity, and not protein levels, our study suggests that it is the activity, and not the levels, of HDAC6 that regulates the observed changes. The inhibition of HDAC6 resulted in a loss of binding of extracellular matrix proteins to vimentin. However, given the short timeframe of the tubacin treatment, changes in the deposition and reorganisation of the extracellular matrix are not expected to be the main contributions to the observed effects on cell shape and motility. The specific binding of talin 1 to vimentin was recently reported by Ostrowska-Podhorodecka et al. [12]; they observed that talin 1 colocalised to filamentous vimentin, and not to small fragments of vimentin, and that vimentin suppressed talin 1-dependent activation of integrin-dependent inside-out signalling, to promote outside-in signalling, focal adhesion growth and maturation. The loss of vimentin further reduced the speed of cell migration in a scrape wound assay. This indicates that by binding to and suppressing the talin 1-dependent activation of integrins, vimentin can promote outside-in signalling, growth of cell-matrix adhesions and the speed of cell migration. This concept is in line with our observations that increased levels of talin 1 in the vimentin interactome of metastasising cells are accompanied by increased cell migration speed and speed-directionality coupling, as compared to tubacin-treated cells. In contrast, the metastasising cells showed reduced directionality as compared to tubacin-treated cells. This highlights that the mechanisms by which vimentin regulates speed and directionality are separate and are mediated through different molecular mechanisms. In addition to talin 1, tubacin reduced the levels of the small Rho GTPase Rab5C in the vimentin interactome, as well as Rab GDP dissociation inhibitor β (GDI2), a GDI that inhibits Rab5C. Rab5C is required for focal adhesion formation, as it activates the calcium-dependent protease calpain 2 and increases the turnover of focal adhesion proteins, including talin 1, to promote cell migration [32,35]. It is therefore possible that GDI-inactivated Rab5C is released from vimentin upon tubacin treatment, to result in increased outside-in signalling over

focal adhesions. Tubacin also reduced the levels of the cation membrane transport protein ATP1A1 in the vimentin interactome of the metastasising cells. It is therefore possible that tubacin can increase the electrochemical gradient of cations across the plasma membrane, to induce calpain-mediated proteolysis and focal adhesion turnover and loss.

We have previously shown that in these metastasising cells, long vimentin fibres localise to the base of mature focal adhesions, and shorter vimentin fragments to the vicinity of small focal complexes, which further supports the concept that long vimentin filaments promote focal adhesion maturation and growth [11]. It is important to note that in these metastasising fibroblasts, vimentin does not show increased localisation to cell adhesion components (e.g., integrin and talin 1) within, as compared to between, focal adhesions [36]. Rather, vimentin is enriched in the proximity of, and not inside, cell-matrix adhesions. This indicates that the role of the binding of cell-adhesion components to vimentin in this cell system might be to sequester these proteins, to provide protection against proteolysis, and for their storage and timely release to control and fine-tune their functions during focal-adhesion formation and turnover, for cell shape and migration. This is in agreement with the previous observation that with treatment with Phorbol 12, 13-dibutyrate, focal adhesions rearrange into podosomes, as a distinct form of cell-matrix adhesions that first appear in subcellular areas with mature and long vimentin filaments [37].

The observation that the inhibition of HDAC6 activity results in nanoscale vimentin filaments at the very periphery of cells, and vimentin clusters and knots that are similar to small, peripheral aggresomes, is in line with previous observations that HDAC6 activity is required for the formation of perinuclear aggresomes in cells. It is therefore likely that HDAC6 activity is required for the retrograde transport of vimentin towards the nucleus that precedes the formation of the perinuclear aggresome, but not for the formation of vimentin knots or asters around defective proteins per se. This is consistent with the recent observation that vimentin is required for the localisation of proteasomes to perinuclear aggresomes [38]. We would like to highlight that the focus on HDAC6 in this study was not dictated by evidence that other HDACs do not regulate vimentin, cell adhesion or migration, but simply because of the cytoplasmic localisation of HDAC6. We have previously shown that the speed of cell migration is positively correlated with the directionality of cell migration in a wide variety of cell types [21,39]. In contrast, these fibroblasts showed a negative correlation between speed and directionality—a correlation which was significantly increased in the oncogene-expressing and metastasising cells, compared to the control cells, and reversed to that of control cells upon inhibition of HDAC6. This suggests that during the transformation of control cells to metastasising cells, a HDAC6-mediated control that ensures high speed only in directional cells is lost. We have previously shown that these metastasising cells show smaller cell-matrix adhesions and a more homogenous distribution of nanoscale adhesion complexes compared to control cells, and that these changes are accompanied by more an entangled nanoscale distribution of the vimentin filaments [18]. Therefore, we speculate that in these metastasising cells, binding to vimentin of components of cell-matrix adhesions induces calpain-mediated focal-adhesion turnover, with a shift from outside-in towards inside-out focal-adhesion signalling. This can suppress the maturation of stable and large focal adhesions that is required for elongated cell shape and directional migration, and instead results in a HDAC6-dependent, dysregulated and non-directed type of migration, which promotes metastasis.

In summary, we have identified a HDAC6-dependent control of increased speed, reduced directionality, and increased speed–directionality coupling of the migration of metastasising cells. Furthermore, we have suggested the molecular mechanisms of this control, by linking it to the vimentin interactome and the spatial distribution of vimentin, while also indicating novel vimentin-binding proteins. These findings are in line with the hypothesis that the binding of cell-matrix components to vimentin governs their functions, and they offer new avenues for investigations of how vimentin regulates cell–extracellular matrix adhesion, motility and metastasis.

4. Materials and Methods

4.1. Cell Culture and Treatments

The transformed and metastasising fibroblasts used here were previously constructed by Hahn et al. by the insertion of three well-defined genetic elements: the telomerase catalytic subunit (hTERT) in combination with two oncogenes (the simian virus 40 large-T oncoprotein; an oncogenic allele of H-ras, V12) into neonatal Bj human dermal fibroblasts [23]. These provided the control Bj primary cells, immortalised Bjhert cells, cell cycle-defective BjhertSV40T cells, and the final BjhertSV40TRasV12 variant that forms tumours that metastasise to lungs in immunodeficient mice. These cell variants can be considered as an isogenically matched model system of the transformation of primary cells to metastasising cells, and they have been characterized previously with regard to their total gene transcription and protein expression, as well as the cytoskeletal organisation and behaviour of the cells [18,25,40]. The cells were cultured as described previously [40]. BjhTertSV40TRasV12 fibroblasts were treated with 10 μ M tubacin (SML0065; SigmaAldrich, St. Louis, MO, United States) or dimethylsulphoxide and incubated at 37 °C for 4 h.

4.2. Immunofluorescence Staining, Confocal and STED Imaging and Computational Analysis of STED Images

The cells were immunostained and analysed under a microscope (AxioVert 40 CFL; Zeiss, Oberkochen, Germany). For dual colour stimulated emission depletion (STED) microscopy, the cells were imaged using a custom-built high-resolution STED microscope with a resolution of 40 nm, as described previously [3]. For triple-colour STED, the cells were transfected with an EGFP variant fused to wild-type vimentin and imaged as described previously [11].

4.3. Live-Cell Imaging

The cells were seeded at 1500 cells/well in slide chambers (543079; Greiner Bio-One Frickenhausen, Germany) and left to grow for 4 days in Dulbecco's modified Eagle's medium supplemented with 10% foetal bovine serum and 100 U/mL penicillin and 100 microg/mL streptomycin. Just prior to live-cell imaging, the medium was replaced with fresh medium containing 0.05 μ g/mL Hoechst (H3570; Invitrogen, Waltham, MA, United States) with 10 μ M tubacin (SML0065; Sigma Aldrich, St. Louis, MO, United States) or dimethylsulphoxide (BP231-100; Thermo Fisher Scientific, Waltham, MA, United States). This was followed by 24 h live-cell imaging under a microscope (Cell Discoverer 7; Zeiss, Oberkochen, Germany), with images taken every 45 min.

4.4. Invasion Assay

Matrigel in vitro cell invasion assays were performed in duplicate. A total of 5000 cells were seeded/well in a BD Biocoat Matrigel Invasion 24-well plate chambers (BD Biosciences, Franklin Lakes, NJ, United States) and incubated for 22 h. The number of invading cells per 10 \times objective field of view were counted according to the manufacturer's protocol. In parallel, the cells were seeded on tissue-culture plastic at 30 cells per mm². Then, 22 h later, the cells were trypsinized and counted using a Beckman Coulter cell counter and their proliferation rates were determined. The differences in invasion between the cell lines were normalized to this difference in proliferation rates.

4.5. Image Analysis

Cell shape was quantified using FIJI version 1.53 (<https://imagej.net/software/fiji/> (accessed on 12 October 2021)). For immunofluorescence, the images were thresholded using phalloidin staining; individual cells were selected by using the wand tracing tool and measured for shape descriptors. For quantification from images captured during live-cell imaging, images taken after 4 h were calibrated using a scale bar, and cell shape and area were quantified by manually drawing around individual cells with the free-hand selection tool.

4.6. Statistical Analysis

The statistical analysis of aspect ratios was performed in GraphPad Prism version 9.1.0 (GraphPad Prism Software, San Diego, CA, United States). All of the data were non-parametric, and therefore Mann–Whitney U tests were used to compare the experimental groups. For the migration analysis, Student's t-tests were used to determine the *p*-values between experimental conditions. A python script was written to calculate the *p*-values using the `scipy.stats` module and its function `ttest_ind()` (documentation for `ttest_ind()`): https://docs.scipy.org/doc/scipy/reference/generated/scipy.stats.ttest_ind.html (accessed on 15 October 2021). The correlation between the mean migratory speed and the persistence of each cell and under condition was obtained using python's `scipy.stats` module using the `pearsonr()` function (documentation for `pearsonr()`): <https://docs.scipy.org/doc/scipy/reference/generated/scipy.stats.pearsonr.html> (accessed on 15 October 2021).

4.7. Preparation of Enriched Intermediate Filament Protein Fraction

Cytoskeletal isolation was performed using the method of Herrmann et al., with the modification of using a mass spectrometry-compatible MS-SAFE Protease and Phosphatase Inhibitor Cocktail (Sigma-Aldrich, St. Louis, MO, United States) [41–43]. This yielded four subcellular fractions: membrane bound/soluble protein (fraction 1); cytoskeletal (fraction 2); high salt-soluble supernatant (fraction 3) and the insoluble cytoskeleton (fraction 4). Fraction 4 was dissolved in 10 M urea. Although fractions 2 and 4 contained the insoluble proteins, fraction 4 was the fraction of choice for the analysis of intermediate filament proteins, as the levels of other non-specific species were significantly reduced [42,43].

4.8. Western Blotting

The cytoskeletal isolation fractions were separated using 4% to 15% precast polyacrylamide gels (4568084; Bio-Rad, Hercules, CA, United States). The gels were then transferred onto nitrocellulose membranes (1704271; Bio-Rad, Hercules, CA, United States) using a transfer system (Trans-Blot Turbo; 1705150; Bio-Rad, Hercules, CA, United States). The blocking and developing of the membranes were carried out as previously described [44]. The antibodies used were as follows: anti-vimentin (V6389; Sigma Aldrich, St. Louis, MO, United States), pan-cytokeratin (ab8068; Abcam, Cambridge, UK), anti- β -actin (A1978; Sigma Aldrich, St. Louis, MO, United States) and Horseradish-peroxidase-conjugated goat anti-mouse secondary antibodies (GtxMu-004-DHRPX; ImmunoReagents, Raleigh, NC, United States). Membranes were stripped after imaging vimentin and pan-keratin, and exposed for 2 min to confirm that the membranes had been stripped, before incubating with β -actin antibody as a loading control.

4.9. Quantitative Proteomic, Mass Spectrometry-Based Analysis of the Vimentin Interactome

Five micrograms of each fraction 4 sample, with two biological replicates of each, were diluted to 1 M urea using 50 mM NH_4HCO_3 . The samples were reduced and alkylated by the sequential addition of 5 mM dithiothreitol and 15 mM iodoacetamide, for 30 min at room temperature and 20 min on ice, respectively. Proteins were proteolytically digested using trypsin at a ratio of 1:50, overnight at 37 °C. Following desalting using Hypercarb and C18 tips, peptides were analysed by nano-LC–MS/MS. A chromatography system was used (RSLCnano; Thermo Fisher Scientific, Waltham, MA, United States) with two solvents: solvent A (0.1% formic acid in water) and solvent B (0.08% formic acid in 80% acetonitrile). Peptides were dissolved in 0.1% (*v/v*) trifluoroacetic acid and 3% (*v/v*) acetonitrile, and two biological replicates were analysed in triplicate in randomised orders. Peptides were resolved on an C18 column (EASY-Spray PepMap RSLC; 50 cm \times 75 μm ID, 2 μm ; 40 °C; Thermo Fisher Scientific, Waltham, MA, United States) with a gradient programme delivered at 300 nL/min with 0–5 min at 3% B, then increasing from 3% B to 50% B over the next 30 min. Peptides were analysed by a mass spectrometer (Q Exactive HF hybrid quadrupole-Orbitrap; Thermo Fisher Scientific, Waltham, MA, United

States) that was programmed to be data-dependent with 10 product ion scans (centroid: resolution, 30,000; automatic gain control, 1×10^5 maximum injection time, 60 ms; isolation: normalized collision energy, 27; intensity threshold, 1×10^5) per full mass spectrometry scan (profile: resolution, 120,000; automatic gain control, 1×10^6 ; maximum injection time, 60 ms; scan range, 375–1500 *m/z*).

4.10. Protein Identification, Relative Quantification, Bioinformatic Functional Profiling and Interaction Analysis

Proteins were identified by searching the mass spectrometry data files against the *Homo sapiens* proteome database (www.uniprot.org/proteomes/UP000005640, downloaded, 2 August 2021; 78120 entries) using MaxQuant v. 1.6.4.0 with the label free quantification (LFQ) and intensity-based absolute quantification options selected [45–47]. Default settings were used with search parameters set to include the following modifications: carbamidomethyl-Cys (fixed); Met oxidation; protein N-terminal acetylation (variable); maximum of two missed tryptic cleavages. Peptide-spectrum matches and protein identifications were filtered using a target-decoy approach at a false discovery rate (FDR) of 1%. Statistical analyses were performed using LFQAnalyst (bioinformatics.erc.monash.edu/apps/LFQ-Analyst/, accessed 18 October 2021), where the LFQ intensity values were used for protein quantification [48]. Missing values were replaced by values drawn from a normal distribution of 1.8 standard deviations and a width of 0.3 for each sample (Perseus-type). Protein-wise linear models combined with empirical Bayesian statistics were used for differential expression analysis using the Bioconductor package limma, whereby the adjusted P-value cut-off was set at 0.05 and log₂ fold change cut-off was set at 1. The Benjamini–Hochberg method of FDR correction was applied. The g: Profiler tool was used for functional enrichment analysis g:Profiler (version e104_eg51_p15_3922dba) with the Benjamini-Hochberg FDR method applying a significance threshold of 0.05 [44]. The Min and Max size settings of the functional category were set to 3 and 500, respectively, with No electronic gene ontology (GO) annotations selected. GO terms for Molecular Function, Biological Process, Cellular Compartment, Kyoto Encyclopedia of Genes and Genomes (KEGG) and Reactome were assigned. The species was set to *Homo sapiens*.

4.11. Tracking and Analysis of Migrating Cells

Cell migration was analysed by tracking the cell nuclei using the Fiji plug-in of TrackMate [49]. The full documentation of this plug-in can be seen on the ImageJ wiki: <https://imagej.net/plugins/trackmate/> (accessed on 15 October 2021). The following specific settings were chosen for the tracking: Detector, Difference of Gaussian (Dog); estimated object size, 20 μm ; quality threshold, 2.0; duration of tracks, min. 18 h. All other settings remained at their default options. The tracks acquired were analysed using the in-built algorithms (<https://imagej.net/plugins/trackmate/algorithms>, accessed on 15 October 2021).

Supplementary Materials: The following supporting information can be downloaded at: <https://www.mdpi.com/article/10.3390/ijms23041961/s1>.

Author Contributions: C.A.E., B.M.C. and A.K.B.G. designed the studies; C.A.E., A.K.B.G., H.R.K., S.C.M., conducted experiments. C.A.E., B.M.C., A.K.B.G., H.R.K., S.C.M., P.I.A.N., C.B., L.X., J.W., F.L. contributed to analysing and interpreting the data. A.K.B.G. drafted the manuscript and all authors edited the final submission. All authors have read and agreed to the published version of the manuscript.

Funding: We are grateful to the University of Sheffield for funding. The QExactive HF orbitrap mass spectrometer was funded by BBSRC UK (award no. BB/M012166/1). We would further like to thank the DFG, CRC 1027 for financial support (to F.L.).

Data Availability Statement: The data presented in this study are available in the main text, references, and Supplementary Information of this Manuscript, and in the Human Protein Atlas (<https://www.proteinatlas.org> (accessed on 18 October 2021)).

Acknowledgments: The authors would like to thank William C. Hahn (Harvard Medical School) for the BJ cell line and its derivatives and the Initiative for Chemical Genetics of the National Cancer Institute (US) for tubacin. We would also like to thank Joanna Chowdry, for showing us the immunofluorescence extraction method, Jessica Medcalf for technical assistance, Ana Lopez and Toby McNally for assistance with analyses and design of the publication figures, Richard Allen, for technical support for live cell imaging, Christopher Berrie for scientific english editing, the University of Sheffield and the Fundação para a Ciência e a Tecnologia (FCT), the Portuguese Government (PEst-OE/QUI/UI0674/2013) and the Agência Regional para o Desenvolvimento da Investigação Tecnologia e Inovação (ARDITI), M1420-01-0145-FEDER-000005 Centro de Química da Madeira (CQM) (Madeira 14–20) for financial and administrative support.

Conflicts of Interest: The authors declare that they have no conflict of interest. The funders had no role in the design of the study; in the collection, analyses, or interpretation of data; in the writing of the manuscript, or in the decision to publish the results.

References

1. Eckes, B.; Dogic, D.; Colucci-Guyon, E.; Wang, N.; Maniotis, A.; Ingber, D.; Merckling, A.; Langa, F.; Aumailley, M.; Delouée, A.; et al. Impaired mechanical stability, migration and contractile capacity in vimentin-deficient fibroblasts. *J. Cell Sci.* **1998**, *111*, 1897–1907. [\[CrossRef\]](#)
2. Hendrix, M.J.; Seftor, E.A.; Seftor, R.E.; Trevor, K.T. Experimental co-expression of vimentin and keratin intermediate filaments in human breast cancer cells results in phenotypic interconversion and increased invasive behavior. *Am. J. Pathol.* **1997**, *150*, 483–495. [\[PubMed\]](#)
3. Rathje, L.-S.Z.; Nordgren, N.; Pettersson, T.; Ronnlund, D.; Widengren, J.; Aspenstrom, P.; Gad, A.K.B. Oncogenes induce a vimentin filament collapse mediated by HDAC6 that is linked to cell stiffness. *Proc. Natl. Acad. Sci. USA* **2014**, *111*, 1515–1520. [\[CrossRef\]](#)
4. Vuoriluoto, K.; Haugen, H.; Kiviluoto, S.; Mpindi, J.-P.; Nevo, J.; Gjerdrum, C.; Tiron, C.; Lorens, J.B.; Ivaska, J. Vimentin regulates EMT induction by Slug and oncogenic H-Ras and migration by governing Axl expression in breast cancer. *Oncogene* **2010**, *30*, 1436–1448. [\[CrossRef\]](#) [\[PubMed\]](#)
5. Wei, J.; Xu, G.; Wu, M.; Zhang, Y.; Li, Q.; Liu, P.; Zhu, T.; Song, A.; Zhao, L.; Han, Z.; et al. Overexpression of vimentin contributes to prostate cancer invasion and metastasis via src regulation. *Anticancer. Res.* **2008**, *28*, 327–334.
6. Zhu, Q.-S.; Rosenblatt, K.; Huang, K.-L.; Lahat, G.; Brobey, R.; Bolshakov, S.; Nguyen, T.; Ding, Z.; Belousov, R.; Bill, K.; et al. Vimentin is a novel AKT1 target mediating motility and invasion. *Oncogene* **2010**, *30*, 457–470. [\[CrossRef\]](#) [\[PubMed\]](#)
7. Helfand, B.T.; Mendez, M.G.; Murthy, S.N.P.; Shumaker, D.K.; Grin, B.; Mahammad, S.; Aebi, U.; Wedig, T.; Wu, Y.L.; Hahn, K.M.; et al. Vimentin organization modulates the formation of lamellipodia. *Mol. Biol. Cell* **2011**, *22*, 1274–1289. [\[CrossRef\]](#)
8. Richardson, A.M.; Havel, L.S.; Koyen, A.E.; Konen, J.M.; Shupe, J.; Wiles, W.; Martin, W.D.; Grossniklaus, H.E.; Sica, G.; Gilbert-Ross, M.; et al. Vimentin Is Required for Lung Adenocarcinoma Metastasis via Heterotypic Tumor Cell-Cancer-Associated Fibroblast Interactions during Collective Invasion. *Clin. Cancer Res.* **2017**, *24*, 420–432. [\[CrossRef\]](#)
9. Van Bodegraven, E.J.; Etienne-Manneville, S. Intermediate filaments against actomyosin: The David and Goliath of cell migration. *Curr. Opin Cell Biol.* **2020**, *66*, 79–88. [\[CrossRef\]](#)
10. Battaglia, R.; Delic, S.; Herrmann, H.; Snider, N.T. Vimentin on the move: New developments in cell migration. *F1000Research* **2018**, *7*, 1796. [\[CrossRef\]](#)
11. Terriac, E.; Coceano, G.; Mavajian, Z.; Hageman, T.A.G.; Christ, A.F.; Testa, I.; Lautenschläger, F.; Gad, A.K.B. Vimentin Levels and Serine 71 Phosphorylation in the Control of Cell-Matrix Adhesions, Migration Speed, and Shape of Transformed Human Fibroblasts. *Cells* **2017**, *6*, 2. [\[CrossRef\]](#)
12. Ostrowska-Podhorodecka, Z.; Ding, I.; Lee, W.; Tanic, J.; Abbasi, S.; Arora, P.D.; Liu, R.S.; Patteson, A.E.; Janmey, P.A.; McCulloch, C.A. Vimentin tunes cell migration on collagen by controlling beta1 integrin activation and clustering. *J. Cell Sci.* **2021**, *134*, jcs254359. [\[CrossRef\]](#)
13. Liu, C.Y.; Lin, H.H.; Tang, M.J.; Wang, Y.K. Vimentin contributes to epithelial-mesenchymal transition cancer cell mechanics by mediating cytoskeletal organization and focal adhesion maturation. *Oncotarget* **2015**, *6*, 15966–15983. [\[CrossRef\]](#)
14. Lynch, C.D.; Lazar, A.M.; Iskratsch, T.; Zhang, X.; Sheetz, M.P. Endoplasmic spreading requires coalescence of vimentin intermediate filaments at force-bearing adhesions. *Mol. Biol. Cell* **2013**, *24*, 21–30. [\[CrossRef\]](#)
15. Xu, Y.; Bismar, T.A.; Su, J.; Xu, B.; Kristiansen, G.; Varga, Z.; Teng, L.; Ingber, D.E.; Mammoto, A.; Kumar, R.; et al. Filamin A regulates focal adhesion disassembly and suppresses breast cancer cell migration and invasion. *J. Exp. Med.* **2010**, *207*, 2421–2437. [\[CrossRef\]](#)
16. Challa, A.A.; Stefanovic, B. A Novel Role of Vimentin Filaments: Binding and Stabilization of Collagen mRNAs. *Mol. Cell. Biol.* **2011**, *31*, 3773–3789. [\[CrossRef\]](#)
17. Challa, A.A.; Vukmirovic, M.; Blackmon, J.; Stefanovic, B. Withaferin-A Reduces Type I Collagen Expression In Vitro and Inhibits Development of Myocardial Fibrosis In Vivo. *PLoS ONE* **2012**, *7*, e42989. [\[CrossRef\]](#) [\[PubMed\]](#)

18. Rönnlund, D.; Gad, A.K.B.; Blom, H.; Aspenström, P.; Widengren, J. Spatial organization of proteins in metastasizing cells. *Cytom. Part A* **2013**, *83*, 855–865. [[CrossRef](#)] [[PubMed](#)]
19. Zhang, X.-H.; Ma, Q.; Wu, H.-P.; Khamis, M.Y.; Li, Y.-H.; Ma, L.-Y.; Liu, H.-M. A Review of Progress in Histone Deacetylase 6 Inhibitors Research: Structural Specificity and Functional Diversity. *J. Med. Chem.* **2021**, *64*, 1362–1391. [[CrossRef](#)] [[PubMed](#)]
20. Li, T.; Zhang, C.; Hassan, S.; Liu, X.; Song, F.; Chen, K.; Zhang, W.; Yang, J. Histone deacetylase 6 in cancer. *J. Hematol. Oncol.* **2018**, *11*, 111. [[CrossRef](#)] [[PubMed](#)]
21. Maiuri, P.; Rupprecht, J.-F.; Wieser, S.; Ruprecht, V.; Bénichou, O.; Carpi, N.; Coppey, M.; De Beco, S.; Gov, N.; Heisenberg, C.-P.; et al. Actin Flows Mediate a Universal Coupling between Cell Speed and Cell Persistence. *Cell* **2015**, *161*, 374–386. [[CrossRef](#)] [[PubMed](#)]
22. Witt, O.; Deubzer, H.E.; Milde, T.; Oehme, I. HDAC family: What are the cancer relevant targets? *Cancer Lett.* **2009**, *277*, 8–21. [[CrossRef](#)] [[PubMed](#)]
23. Hahn, W.C.; Counter, C.M.; Lundberg, A.S.; Beijersbergen, R.L.; Brooks, M.W.; Weinberg, R.A. Creation of human tumour cells with defined genetic elements. *Nature* **1999**, *400*, 464–468. [[CrossRef](#)] [[PubMed](#)]
24. Sun, B.; Chen, M.; Hawks, C.L.; Pereira-Smith, O.M.; Hornsby, P.J. The Minimal Set of Genetic Alterations Required for Conversion of Primary Human Fibroblasts to Cancer Cells in the Subrenal Capsule Assay. *Neoplasia* **2005**, *7*, 585–593. [[CrossRef](#)] [[PubMed](#)]
25. Danielsson, F.; Skogs, M.; Huss, M.; Rexhepaj, E.; O’Hurley, G.; Klevebring, D.; Pontén, F.; Gad, A.; Uhlen, M.; Lundberg, E. Majority of differentially expressed genes are down-regulated during malignant transformation in a four-stage model. *Proc. Natl. Acad. Sci. USA* **2013**, *110*, 6853–6858. [[CrossRef](#)]
26. Gan, Z.; Ding, L.; Burckhardt, C.J.; Lowery, J.; Zaritsky, A.; Sitterley, K.; Mota, A.; Costigliola, N.; Starker, C.; Voytas, D.; et al. Vimentin Intermediate Filaments Template Microtubule Networks to Enhance Persistence in Cell Polarity and Directed Migration. *Cell Syst.* **2016**, *3*, 500–501. [[CrossRef](#)]
27. Goldman, R.D. The role of three cytoplasmic fibers in bhk-21 cell motility. *J. Cell Biol.* **1971**, *51*, 752–762. [[CrossRef](#)]
28. Cheng, F.; Shen, Y.; Mohanasundaram, P.; Lindström, M.; Ivaska, J.; Ny, T.; Eriksson, J.E. Vimentin coordinates fibroblast proliferation and keratinocyte differentiation in wound healing via TGF-beta-Slug signaling. *Proc. Natl. Acad. Sci. USA* **2016**, *113*, E4320–E4327. [[CrossRef](#)]
29. Sanghvi-Shah, R.; Weber, G.F. Intermediate Filaments at the Junction of Mechanotransduction, Migration, and Development. *Front. Cell Dev. Biol.* **2017**, *5*, 81. [[CrossRef](#)] [[PubMed](#)]
30. Angrand, P.-O.; Segura, I.; Völkel, P.; Ghidelli, S.; Terry, R.; Brajenovic, M.; Vintersten, K.; Klein, R.; Superti-Furga, G.; Drewes, G.; et al. Transgenic Mouse Proteomics Identifies New 14-3-3-associated Proteins Involved in Cytoskeletal Rearrangements and Cell Signaling. *Mol. Cell. Proteom.* **2006**, *5*, 2211–2227. [[CrossRef](#)]
31. Oughtred, R.; Rust, J.; Chang, C.; Breitkreutz, B.J.; Stark, C.; Willems, A.; Boucher, L.; Leung, G.; Kolas, N.; Zhang, F. The BioGRID database: A comprehensive biomedical resource of curated protein, genetic, and chemical interactions. *Protein Sci.* **2021**, *30*, 187–200. [[CrossRef](#)]
32. Chen, P.-I.; Schauer, K.; Kong, C.; Harding, A.R.; Goud, B.; Stahl, P.D. Rab5 Isoforms Orchestrate a “Division of Labor” in the Endocytic Network; Rab5C Modulates Rac-Mediated Cell Motility. *PLoS ONE* **2014**, *9*, e90384. [[CrossRef](#)]
33. Velez-Delvalle, C.; Marsch-Moreno, M.; Castro-Muñozledo, F.; Galván-Mendoza, I.J.; Kuri-Harcuch, W. Epithelial cell migration requires the interaction between the vimentin and keratin intermediate filaments. *Sci. Rep.* **2016**, *6*, 24389. [[CrossRef](#)] [[PubMed](#)]
34. Franco, S.J.; Rodgers, M.A.; Perrin, B.J.; Han, J.; Bennis, D.A.; Critchley, D.R.; Huttenlocher, A. Calpain-mediated proteolysis of talin regulates adhesion dynamics. *Nat. Cell Biol.* **2004**, *6*, 977–983. [[CrossRef](#)] [[PubMed](#)]
35. Mendoza, P.A.; Silva, P.; Diaz, J.; Arriagada, C.; Canales, J.; Cerda, O.; Torres, V.A. Calpain2 mediates Rab5-driven focal adhesion disassembly and cell migration. *Cell Adhes. Migr.* **2017**, *12*, 185–194. [[CrossRef](#)]
36. Xu, L.; Braun, L.J.; Rönnlund, D.; Widengren, J.; Aspenström, P.; Gad, A.K.B. Nanoscale localization of proteins within focal adhesions indicates discrete functional assemblies with selective force-dependence. *FEBS J.* **2018**, *285*, 1635–1652. [[CrossRef](#)]
37. Gad, A.; Lach, S.; Crimaldi, L.; Gimona, M. Plectin deposition at podosome rings requires myosin contractility. *Cell Motil. Cytoskelet.* **2008**, *65*, 614–625. [[CrossRef](#)] [[PubMed](#)]
38. Morrow, C.S.; Porter, T.J.; Xu, N.; Arndt, Z.P.; Ako-Asare, K.; Heo, H.; Thompson, E.A.; Moore, D.L. Vimentin Coordinates Protein Turnover at the Aggresome during Neural Stem Cell Quiescence Exit. *Cell Stem Cell* **2020**, *26*, 558–568.e9. [[CrossRef](#)] [[PubMed](#)]
39. Shaebani, M.R.; Jose, R.; Santen, L.; Stankevics, L.; Lautenschläger, F. Persistence-Speed Coupling Enhances the Search Efficiency of Migrating Immune Cells. *Phys. Rev. Lett.* **2020**, *125*, 268102. [[CrossRef](#)]
40. Gad, A.; Thullberg, M.; Dannenberg, J.H.; te Riele, H.; Strömblad, S. Retinoblastoma susceptibility gene product (pRb) and p107 functionally separate the requirements for serum and anchorage in the cell cycle G1-phase. *J. Biol. Chem.* **2004**, *279*, 13640–13644. [[CrossRef](#)]
41. Herrmann, H.; Kreplak, L.; Aebi, U. Isolation, Characterization, and In Vitro Assembly of Intermediate Filaments. In *Methods in Cell Biology*; Academic Press: Cambridge, MA, USA, 2004; Volume 78, pp. 3–24. [[CrossRef](#)]
42. Leech, S.H.; Evans, C.A.; Shaw, L.; Wong, C.H.; Connolly, J.; Griffiths, J.R.; Whetton, A.D.; Corfe, B.M. Proteomic analyses of intermediate filaments reveals cytokeatin8 is highly acetylated—Implications for colorectal epithelial homeostasis. *Proteomics* **2008**, *8*, 279–288. [[CrossRef](#)]

43. Mackinder, M.A.; Evans, C.A.; Chowdry, J.; Staton, C.A.; Corfe, B.M. Alteration in composition of keratin intermediate filaments in a model of breast cancer progression and the potential to reverse hallmarks of metastasis. *Cancer Biomark.* **2013**, *12*, 49–64. [[CrossRef](#)] [[PubMed](#)]
44. Alkasalias, T.; Alexeyenko, A.; Hennig, K.; Danielsson, F.; Lebbink, R.J.; Fielden, M.; Turunen, S.P.; Lehti, K.; Kashuba, V.; Madapura, H.S.; et al. RhoA knockout fibroblasts lose tumor-inhibitory capacity in vitro and promote tumor growth in vivo. *Proc. Natl. Acad. Sci. USA* **2017**, *114*, E1413–E1421. [[CrossRef](#)]
45. Cox, J.; Hein, M.Y.; Lubner, C.A.; Paron, I.; Nagaraj, N.; Mann, M. Accurate Proteome-wide Label-free Quantification by Delayed Normalization and Maximal Peptide Ratio Extraction, Termed MaxLFQ. *Mol. Cell. Proteom.* **2014**, *13*, 2513–2526. [[CrossRef](#)] [[PubMed](#)]
46. Cox, J.; Mann, M. MaxQuant enables high peptide identification rates, individualized p.p.b.-range mass accuracies and proteome-wide protein quantification. *Nat. Biotechnol.* **2008**, *26*, 1367–1372. [[CrossRef](#)]
47. Schwanhäusser, B.; Busse, D.; Li, N.; Dittmar, G.; Schuchhardt, J.; Wolf, J.; Chen, W.; Selbach, M. Global quantification of mammalian gene expression control. *Nature* **2011**, *473*, 337–342, Erratum in *Nature* **2013**, *495*, 126–127. [[CrossRef](#)]
48. Shah, A.D.; Goode, R.J.A.; Huang, C.; Powell, D.R.; Schittenhelm, R.B. LFQ-Analyst: An Easy-To-Use Interactive Web Platform to Analyze and Visualize Label-Free Proteomics Data Preprocessed with MaxQuant. *J. Proteome Res.* **2019**, *19*, 204–211. [[CrossRef](#)] [[PubMed](#)]
49. Tinevez, J.-Y.; Perry, N.; Schindelin, J.; Hoopes, G.M.; Reynolds, G.D.; Laplantine, E.; Bednarek, S.Y.; Shorte, S.L.; Eliceiri, K.W. TrackMate: An open and extensible platform for single-particle tracking. *Methods* **2017**, *115*, 80–90. [[CrossRef](#)] [[PubMed](#)]

Faculty of Natural Sciences and Technology**Cumulative form of the dissertation****Template for the confirmation of the proportion of co-authors**Title of the dissertation (working title):**Cytoskeletal aspects of cellular migration**Article to be included:

Ullrich KA, Derdau J, Baltes C, et al.
IL-3 receptor signalling suppresses chronic intestinal inflammation by controlling mechanobiology and tissue egress of regulatory T cells
 Gut 2023;72:2081-2094.

Quality of the publication:

Research article

Review process or publication status:

Accepted and published

Explanation of the contributions of the co-authors:

Karen Anne-Marie Ullrich: Designed experiments, prepared figures (subfigures prepared from co-authors are depicted below), wrote the manuscript with the help of Sebastian Zundler and Markus F. Neurath (subsections written from co-authors are depicted below).

Conducted the following experiments, data analysis and visualization:

- Lamina propria mononuclear cells (LPMC) isolation from human biopsies 100%
- Isolation of peripheral blood mononuclear cells (PBMCs) from human donors 100%
- In vitro T cell stimulation and incubation with cytokines 100%
- Supervision of mouse breeding 100%
- Planning, supervision and performance of mice experiments 70%
- Cell isolation from mouse tissues 100%
- In vivo cell trafficking studies and in vivo microscopy 100%
- Recirculation studies in T cell transfer colitis 100%
- Proliferation assays 100%
- Treg suppression and polarization assays 100%
- Flow cytometry 80%
- Lightsheet microscopy sample preparation 100%
- Lightsheet microscopy 40%
- Analysis and 3D reconstruction of lightsheet microscopy 50%
- Dynamic adhesion assays 50%
- Transmigration assays 100%
- RNA-Isolation, cDNA Transcription and qPCR analysis 80%
- ELISA and multiplex assays 100%
- Rac1-Activation and G-Actin/F-Actin Assay 100%

- Immunofluorescence staining of mouse and human cryosections and cells 90%
- H/E staining of mouse colon paraffin-embedded sections 100%
- Isolation, stimulation and preparation of cells for RT-DC and AFM experiments 100%
- Isolation of cells for FRAP and SEM experiments 100%
- Further analysis and visualization of microarray, RNAseq, kinome activation analysis 100%
- Visualization/graphs 90%
- Statistics 100%

Julia Derdau: Prepared Figures (Figure 5 A-C,G and 7 A), wrote section *Real-time deformability cytometry (RT-DC) analysis* in the methods section (supplementary) of the manuscript and conducted the following experiments and their analysis:

- Real-time deformability cytometry (RT-DC) measurement 50%
- RT-DC analysis 70%
- Visualization of RT-DC analysis 100%

Carsten Alexander Baltes: Prepared Figures (Figure 4 F), wrote section *Fluorescence recovery after photobleaching (FRAP)* in the methods section (supplementary) of the manuscript and conducted the following experiments and their analysis:

- Fluorescence recovery after photobleaching (FRAP) measurements 100%
- Statistical analysis of FRAP data 100%

Alice Battistella: improved the section *Atomic force microscope (AFM) analysis of cell deformability* in the methods section (supplementary) of the manuscript and conducted the following experiments and their analysis:

- Atomic force microscope (AFM) analysis of cell deformability 30%

Gonzalo Rosso: Prepared Figures (Figure 5 D,F and 7 B), wrote section *Atomic force microscope (AFM) analysis of cell deformability* in the methods section (supplementary) of the manuscript and conducted the following experiments and their analysis:

- Atomic force microscope (AFM) analysis of cell deformability 70%

Stefan Uderhardt: Supervised light-sheet microscopy experiments, improved the manuscript, prepared Figures (Figure 6 C) and conducted the following experiments and their analysis:

- Lightsheet microscopy 50%
- Analysis and 3D reconstruction of lightsheet microscopy 50%

Lisa Lou Schulze: conducted the following experiments:

- Planning, supervision and performance of mice experiments 5%

Li-Juan Liu: Prepared data for figures (Suppl. Figure 5 A-C, Suppl. Figure 9 B and C) and conducted the following experiments and their analysis:

- Flow cytometry 20%
- Dynamic adhesion assays 50%

Mark Dedden: Prepared data for figures (Figure 1 A, 4 A-B, Suppl. Figure 6 A), wrote section *Microarray* and helped writing the section *RNA-sequencing of mouse thymocytes* in the methods section (supplementary) of the manuscript and conducted the following experiments and their analysis:

- Microarray analysis 100%
- RNA-sequencing analysis 60%

Marta Spocinska: Prepared data for figures (Suppl. Figure 10) and conducted the following experiments and their analysis:

- RNA-Isolation, cDNA Transcription and qPCR analysis 20%

Lucina Kainka: Prepared Figures (Figure 4 E), wrote section *Scanning electron microscopy (SEM)* in the methods section (supplementary) of the manuscript and conducted the following experiments and their respective analysis:

- Scanning electron microscopy (SEM) measurements 100%
- Statistical analysis of actin cortex parameters 100%

Markéta Kubánková: Supervised RT-DC measurements and improved the section *Real-time deformability cytometry (RT-DC) analysis* in the methods section (supplementary) of the manuscript.

Tanja Martina Müller: Improved the manuscript and conducted the following experiments:

- Planning, supervision and performance of mice experiments 5%

Nina-Maria Schmidt: Prepared data for figures (Figure 7 A, Suppl. Figure 9 D) and conducted the following experiments and their analysis:

- Real-time deformability cytometry (RT-DC) measurement 100%
- RT-DC analysis 70%

Emily Becker: conducted the following experiments:

- Planning, supervision and performance of mice experiments 5%

Oumaima Ben Brahim: conducted the following measurement:

- Lightsheet microscopy 10%

Imke Atreya: Supervised murine experiments and secured funding. Improved the manuscript.

Susetta Finotto: Secured funding and improved the manuscript.

Iryna Prots: Donated mice and improved the manuscript.

Stefan Wirtz: Prepared Figures (Suppl. Figure 3 C-E), wrote subsection *Oxazolone colitis with Il-3 overexpression* in the methods section (supplementary) of the manuscript and conducted the following experiments and their analysis:

- Planning, supervision and performance of mice experiments 5%
 - Oxazolone colitis with Il-3 overexpression

Benno Weigmann: Prepared Figures (Suppl. Figure 3 C-E), wrote subsection *Oxazolone colitis with Il-3 overexpression* in the methods section (supplementary) of the manuscript and conducted the following experiments and their analysis:

- Planning, supervision and performance of mice experiments 5%
 - Oxazolone colitis with Il-3 overexpression

Rocío López-Posadas: Supervised experiments, improved the manuscript and conducted the following experiment:

- Immunofluorescence staining of mouse and human cryosections and cells 10%

Raja Atreya: Supervised human experiments and secured funding. Improved the manuscript.

Arif Bülent Ekici: helped writing the section *RNA-sequencing of mouse thymocytes* in the methods section (supplementary) of the manuscript and conducted the following experiments and their analysis:

- RNA-sequencing performance 100%
- RNA-sequencing analysis 40%

Franziska Lautenschläger: Secured funding and supervised the analysis of FRAP and SEM experiments.

Jochen Guck: Supervised biophysical RT-DC and AFM experiments and secured funding. Improved the manuscript.

Markus F. Neurath: Supervised experiments and secured funding. Wrote the manuscript with the help of Karen Anne-Marie Ullrich and Sebastian Zundler.

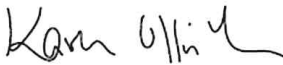
Sebastian Zundler: Generated concepts, designed experiments, supervised the study and secured funding. Wrote the manuscript with the help of Karen Anne-Marie Ullrich and Markus F. Neurath. Conducted the following experiments and their analysis:

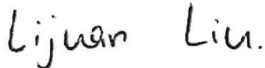
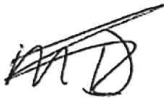
- Planning, supervision and performance of mice experiments 5%

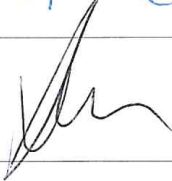
Signature of the doctoral candidate
(Carsten Alexander Baltes)



Signature of the co-authors

(co-)Author	Signature
Karen Anne-Marie Ullrich	
Julia Derdau	

Alice Battistella	
Gonzalo Rosso	No new contact information
Stefan Uderhardt	No new contact information
Lisa Lou Schulze	No new contact information
Li-Juan Liu	
Mark Dedden	
Marta Spocinska	No new contact information
Lucina Kainka	
Markéta Kubánková	
Tanja Martina Müller	
Nina-Maria Schmidt	No new contact information

Emily Becker	No new contact information
Oumaima Ben Brahim	
Imke Atreya	
Susetta Finotto	<i>Susetta Finotto</i>
Iryna Prots	No new contact information
Stefan Wirtz	No new contact information
Benno Weigmann	<i>Benno Weigmann</i>
Rocío López-Posadas	 <small>Rocío López Posadas</small>
Raja Atreya	No new contact information
Arif Bülent Ekici	<i>Arif B. Ekici</i>
Franziska Lautenschläger	

Jochen Guck	
Markus F. Neurath	
Sebastian Zundler	

Note:

Some researchers did not provide any new contact information after they left their assigned group. These people have been marked in the list above with "No new contact information".



Original research

IL-3 receptor signalling suppresses chronic intestinal inflammation by controlling mechanobiology and tissue egress of regulatory T cells

Karen Anne-Marie Ullrich ¹, Julia Derdau ¹, Carsten Baltes ², Alice Battistella ³, Gonzalo Rosso ³, Stefan Uderhardt ^{4,5,6}, Lisa Lou Schulze ¹, Li-Juan Liu ¹, Mark Dedden ¹, Marta Spocinska ¹, Lucina Kainka ², Markéta Kubánková ³, Tanja Martina Müller ^{1,6}, Nina-Maria Schmidt ¹, Emily Becker ¹, Oumaima Ben Brahim ^{4,5,6}, Imke Atreya ^{1,6}, Susetta Finotto ^{6,7}, Iryna Prots ⁸, Stefan Wirtz ^{1,6}, Benno Weigmann ^{1,6}, Rocío López-Posadas ^{1,6}, Raja Atreya ^{1,6}, Arif Bülent Ekici ⁹, Franziska Lautenschläger ^{2,10}, Jochen Guck ³, Markus F Neurath ^{1,6}, Sebastian Zundler ^{1,6}

IL-3 has been reported to be involved in various inflammatory disorders, but its role in inflammatory bowel disease (IBD) has not been addressed so far. Here, we determined IL-3 expression in samples from patients with IBD and studied the impact of *IL3* or *IL3r* deficiency on T cell-dependent experimental colitis. We explored the mechanical, cytoskeletal and migratory properties of *IL3r*^{-/-} and *IL3r*^{+/+} T cells using real-time deformability cytometry, atomic force microscopy, scanning electron microscopy, fluorescence recovery after photobleaching and *in vitro* and *in vivo* cell trafficking assays. We observed that, in patients with IBD, the levels of IL-3 in the inflamed mucosa were increased. *In vivo*, experimental chronic colitis on T cell transfer was exacerbated in the absence of IL-3 or IL-3r signalling. This was attributable to IL-3r signalling-induced changes in kinase phosphorylation and actin cytoskeleton structure, resulting in increased mechanical deformability and enhanced egress of Tregs from the inflamed colon mucosa. Similarly, IL-3 controlled mechanobiology in human Tregs and was associated with increased mucosal Treg abundance in patients with IBD. Collectively, our data reveal that IL-3 signaling exerts an important regulatory role at the interface of biophysical and migratory T cell features in intestinal inflammation and suggest that this might be an interesting target for future intervention.

INTRODUCTION

The pathogenesis of inflammatory bowel diseases (IBD) such as Crohn's disease (CD) and ulcerative colitis (UC) is still incompletely understood. According to current concepts, a multifactorial interplay of genetic susceptibility, barrier breakdown and environmental factors associated with intestinal dysbiosis triggers inadequate and pro-inflammatory immune responses in the gut resulting in tissue destruction and symptomatic disease.¹⁻³

Dissecting the mechanisms of pathologic immune cell communication via cytokines in experimental

WHAT IS ALREADY KNOWN ON THIS TOPIC

⇒ Interleukin (IL)-3 has been suggested to be involved in the pathogenesis of several immune-mediated inflammatory diseases, but its role in chronic intestinal inflammation is unclear.

WHAT THIS STUDY ADDS

⇒ IL-3 receptor signalling counteracts experimental colitis.
 ⇒ Mechanistically, IL-3 receptor signalling controls the mechanobiology of regulatory T cells (Tregs) and impedes mucosal Treg egress to restore the balance of pro-inflammatory and anti-inflammatory T cells. Thus, for the first time, we identify a factor controlling intestinal mucosal tissue egress of Tregs.
 ⇒ Our data support a fundamentally new concept of immune cell motility as a consequence of the cellular biophysical features

HOW THIS STUDY MIGHT AFFECT RESEARCH, PRACTICE OR POLICY

⇒ IL-3 emerges as a potential future therapeutic strategy in IBD.
 ⇒ Approaches locally modulating the mechanical properties of immune cells in the inflamed mucosa seem highly promising to mitigate intestinal inflammation.

► Additional supplemental material is published online only. To view, please visit the journal online (<http://dx.doi.org/10.1136/gutjnl-2023-329818>).

For numbered affiliations see end of article.

Correspondence to
 Professor Markus F Neurath, Friedrich-Alexander-Universität Erlangen-Nürnberg, Erlangen, Germany; markus.neurath@uk-erlangen.de

MFN and SZ are joint senior authors.

Received 3 March 2023
 Accepted 16 June 2023
 Published Online First
 4 August 2023



© Author(s) (or their employer(s)) 2023. Re-use permitted under CC BY-NC. No commercial re-use. See rights and permissions. Published by BMJ.

To cite: Ullrich KA-M, Derdau J, Baltes C, et al. *Gut* 2023;**72**:2081–2094.

Inflammatory bowel disease

receptors have been implicated in chronic colitis.⁵ Of note, similar roles of many of these cytokines have been described in related immune-mediated inflammatory diseases.⁶ However, despite having been described back in the 1980s^{7,8} and reported to be involved in pathologies such as experimental inflammatory arthritis,^{9,10} the role of IL-3 signalling via the IL-3 receptor (IL-3R) in the development and perpetuation of chronic intestinal inflammation remains largely unexplored.

So far, IL-3 is mainly known as a hematopoietic growth factor, which is expressed by activated T cells.¹¹ IL-3R is constitutively expressed on basophils, myeloid precursors, plasmacytoid dendritic cells as well as neoplastic mast and B cells, but the expression on regulatory T cells (Tregs) in mice⁹ and on proliferating¹² and activated T helper (Th) cells with a Th2 phenotype in the human blood¹³ has also been described.

Driven by the successful implementation and use of the anti- α 4 β 7 integrin antibody vedolizumab,^{14,15} another aspect that has gained substantial attraction in the field of IBD in recent years is immune cell trafficking. Immune cell trafficking comprises all processes controlling immune cell locomotion such as tissue homing, retention or egress.¹⁶ Although previous research led to a detailed characterisation of the interaction of surface molecules like integrins, cell adhesion molecules or selectins in cell trafficking,¹⁷ cell-intrinsic processes regulating trafficking properties have only poorly been investigated. Particularly, hampered by missing appropriate techniques until recently, cell mechanical properties such as cell elasticity have only begun to be linked with biological processes like immune cell trafficking.

In this study, we aimed to explore the role of IL-3 signalling via IL-3R in experimental colitis as well as human IBD. We show that IL-3 expression is increased in colitis in mice and humans and that IL-3r signalling in T cells alleviates chronic colitis by instructing specific mechanical properties modulating the tissue egress capacity of Tregs. Our findings suggest novel approaches for future therapy of IBD by locally modulating mechano-migratory characteristics of immune cells.

METHODS

Methods are available as online supplemental file.

RESULTS

IL-3 expression is increased in IBD

To explore the potential involvement of so far unaddressed cytokines in the pathogenesis of IBD, we re-analysed a previously published microarray data set¹⁸ including biopsies from a cohort of patients with UC, CD and non-IBD controls. Consistent with previous reports,^{19–21} the expression of cytokines like IL-17A, IL-6 or IL-26 was increased in the gut of patients with IBD (figure 1A). However, although an implication in IBD has not yet been described, we also found a significant upregulation of IL-3 both in CD and UC compared with control patients, where mucosal IL-3 expression was low. Thus, we further analysed the expression of IL-3 in colon tissue obtained from biopsies from a local patient cohort (online supplemental table 1). We detected substantially higher *IL3* messenger RNA (mRNA) expression in patients with UC or CD compared with non-IBD control donors. Moreover, *IL3* mRNA expression in patients with active disease was significantly higher than in patients with inactive disease (figure 1B). To validate this finding on protein level and to determine the source of IL-3 in the gut, we stained colonic specimens of patients with active IBD and non-IBD controls for CD4, CD14 or CD19 and IL-3. We found a marked increase

in the number of CD4⁺IL-3⁺ T cells in samples from patients with CD and UC (figure 1C), whereas only a few CD14⁺ macrophages and CD19⁺ B cells co-expressed IL-3 (figure 1D, online supplemental figure 1A). IL-3 was also detectable in the serum of patients with IBD and control donors, but without relevant differences (online supplemental figure 1B, online supplemental table 2). Thus, these data suggested that CD4⁺ T cells are a major source of IL-3 in the inflamed colon and indicated a potential involvement of IL-3 in the local signalling in the intestine in IBD.

IL-3 is selectively upregulated in the colon of mice with chronic colitis and counteracts inflammation

To address the functional role of IL-3, we explored its impact on experimental T cell transfer colitis. We did not detect *IL3* mRNA expression in intestinal tissues or lymphoid organs of unchallenged *Rag1*^{-/-} mice and only in the thymus, but not in the spleen of wild-type mice. However, *IL3* was expressed in colonic lamina propria mononuclear cells (LPMCs) of *Rag1*^{-/-} mice with colitis after the transfer of naïve CD4⁺ T cells from the spleen of wild type donor mice (figure 2A,B). Moreover, *IL3* mRNA expression by LPMCs increased over the course of transfer colitis (figure 2C). On protein level, we were also able to detect substantial secretion of IL-3 by re-stimulated LPMCs, but not splenocytes from *Rag1*^{-/-} mice with transfer colitis (figure 2D).

Having shown that IL-3 is specifically expressed in the colon during transfer colitis, we subsequently compared the phenotype of transfer colitis in *Rag1*^{-/-} mice after transfer of naïve CD4⁺ T cells from IL-3-deficient (*IL3*^{-/-}) and wild-type (*IL3*^{+/+}) mice. On colonoscopy, mice having received *IL3*^{-/-} T cells displayed increased signs of inflammation such as fibrin exudates, intestinal wall thickening and soft stool. Consistently, histological inflammation scores were higher in these mice (figure 2E) and *in vivo* imaging demonstrated the increased presence of reactive oxygen species (ROS; online supplemental figure 2A). This was accompanied by increased numbers of CD4⁺ and myeloperoxidase⁺ (MPO⁺) cells in the colon of mice that had received *IL3*^{-/-} T cells (online supplemental figure 2B).

We further sought to confirm this phenotype in another T cell-dependent colitis model. Accordingly, we performed oxazolone colitis with *IL3*^{+/+} and *IL3*^{-/-} mice and similarly observed increased signs of inflammation in *IL3*^{-/-} mice on endoscopy, histology and *in vivo* imaging of ROS (online supplemental figure 3A,B).

To address whether, consistently, the exposure to IL-3 might mitigate colitis, we chose an overexpression approach based on minicircle vectors containing IL-3 complementary DNA. This led to efficient production of IL-3 (online supplemental figure 3C) and on subsequent induction of oxazolone colitis, mice with IL-3 vector treatment lost less weight (online supplemental figure 3D) and showed lower endoscopic and histological disease activity than mice having been treated with a mock vector (online supplemental figure 3E).

Collectively, these data suggested that IL-3 alleviates experimental colitis

IL-3 receptor signalling in T cells reduces intestinal inflammation

Since T cell transfer colitis is crucially driven by T cells, we wondered whether signalling of IL-3 via IL-3r on intestinal T cells might be responsible for the above effects. Thus, we generated a new mouse line specifically lacking the IL-3 receptor (*IL3r*^{-/-}; online supplemental figure 4A–C) and isolated naïve CD4⁺

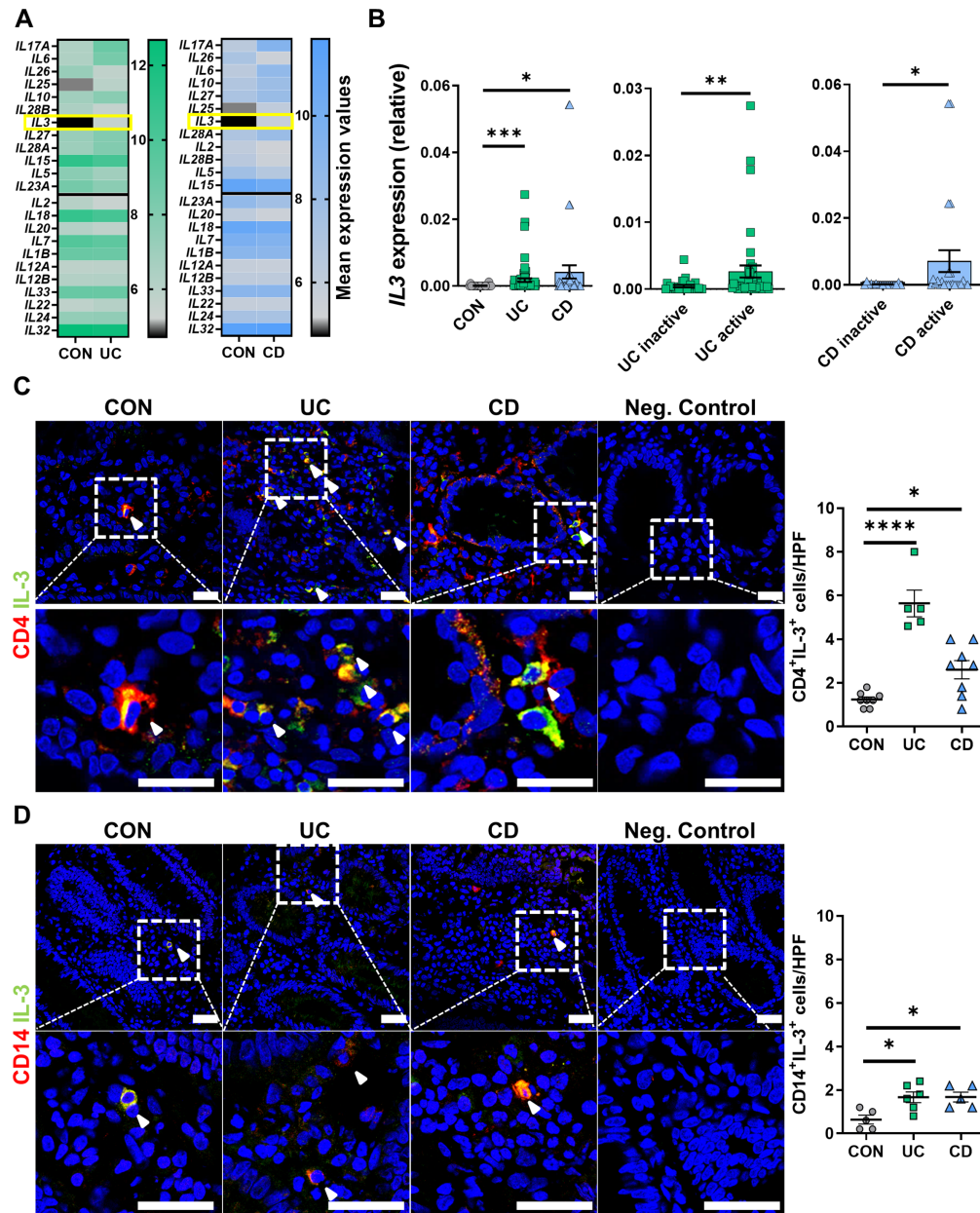


Figure 1 IL-3 is upregulated in inflamed tissue of patients with IBD. (A) Microarray analysis of the publicly available data set GSE97012: mean values of selected cytokines plotted for patients with non-IBD (CON, n=27) versus UC (left, n=22) or patients with CD (right, n=19). Genes are ordered from low to high p values (top to bottom) with the black line separating genes with and without significantly different expression (above/below). (B) *IL3* mRNA expression in colon tissue from patients with colonic CD (n=41), UC (n=68) and CON (n=21) donors as determined by qPCR. Comparison of levels between the entities (left) and comparison of levels between inactive and active disease (right); Kruskal-Wallis test with Dunn's multiple comparisons post hoc test. (C,D) Immunofluorescence of cryosections from patients with CD (n=5–8), UC (n=5–6) and CON (n=5–8) for IL-3 (green) and CD4 (C, red) or CD14 (D, red); counterstaining with Hoechst (blue). Left: representative images, white arrowheads highlight double positive cells, scale bars – 25 μ m; right: quantification of double positive cells per high power field (HPF); one-way analysis of variance with Tukey's multiple comparisons post hoc test. CD, Crohn's disease; CON, non-IBD control; IL, interleukin; mRNA, messenger RNA; qPCR, quantitative PCR; UC, ulcerative colitis.

Inflammatory bowel disease

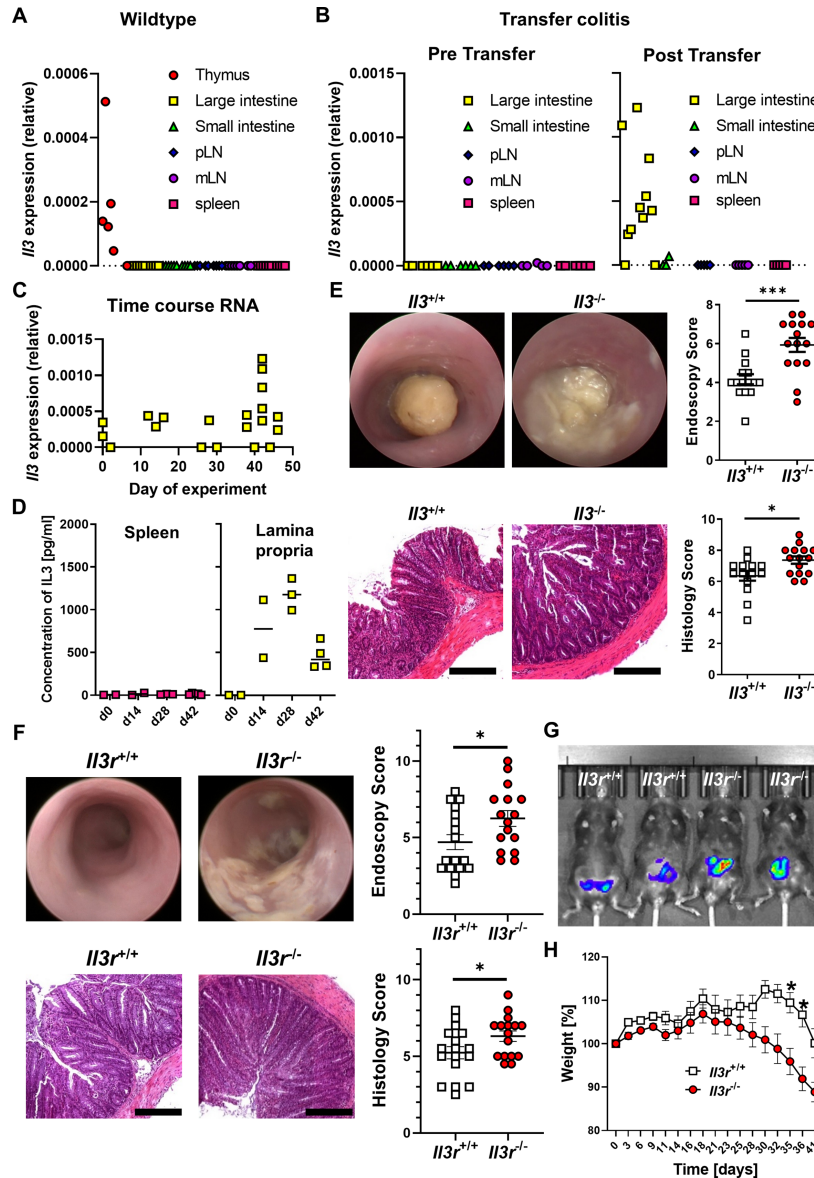


Figure 2 IL-3 alleviates T cell transfer colitis. (A) *Il3* mRNA expression in tissue from various organs of unchallenged C57BL/6J mice as determined by qPCR. n=6–10 per group. (B) *Il3* mRNA expression in tissue from various organs of unchallenged *Rag1*^{-/-} mice (pre transfer, left, n=5–6) and *Rag1*^{-/-} mice with established T cell transfer colitis (post transfer, right, n=3–11) as determined by qPCR. (C) Time course of *Il3* mRNA expression in lamina propria mononuclear cells (LPMCs) of *Rag1*^{-/-} mice with T cell transfer colitis; n=3–11 per time point. (D) Concentration of IL-3 in supernatants of splenocytes and LPMCs re-stimulated with anti-CD3/28 antibodies at different time points of T cell transfer colitis as determined by ELISA; n=2–5 per time point. (E) Colitis in *Rag1*^{-/-} mice after transfer of naive CD4⁺ T cells from *Il3*^{+/+} and *Il3*^{-/-} mice. Upper panels: histology of colon tissue. Left: representative images (scale bars – 12.5 μm), right: quantitative endoscopic and histological scores of disease severity. n=14–15 per group, unpaired t-test. (F–H) Colitis in *Rag1*^{-/-} mice after transfer of naive CD4⁺ T cells from *Il3r*^{+/+} and *Il3r*^{-/-} mice. (F) Mini-endoscopy (top) and histology of colon tissue (bottom). Left: representative images (scale bars – 12.5 μm), right: quantitative endoscopic and histological scores of disease severity. n=16–17 per group, Mann-Whitney (endoscopy) and unpaired t-test (histology). (G) Representative *in vivo* IVIS luminescence imaging of reactive oxygen species after i.p. injection of L-012. (H) Weight course. Normalisation to weight on the day adoptive T cell transfer was performed. n=16–17 per group, mixed-effects analysis with Sidak post hoc test. IL, interleukin; i.p., intraperitoneal; mLN, mesenteric lymph node; mRNA, messenger RNA; MPO, myeloperoxidase; pLN, peripheral lymph node; qPCR, quantitative PCR.

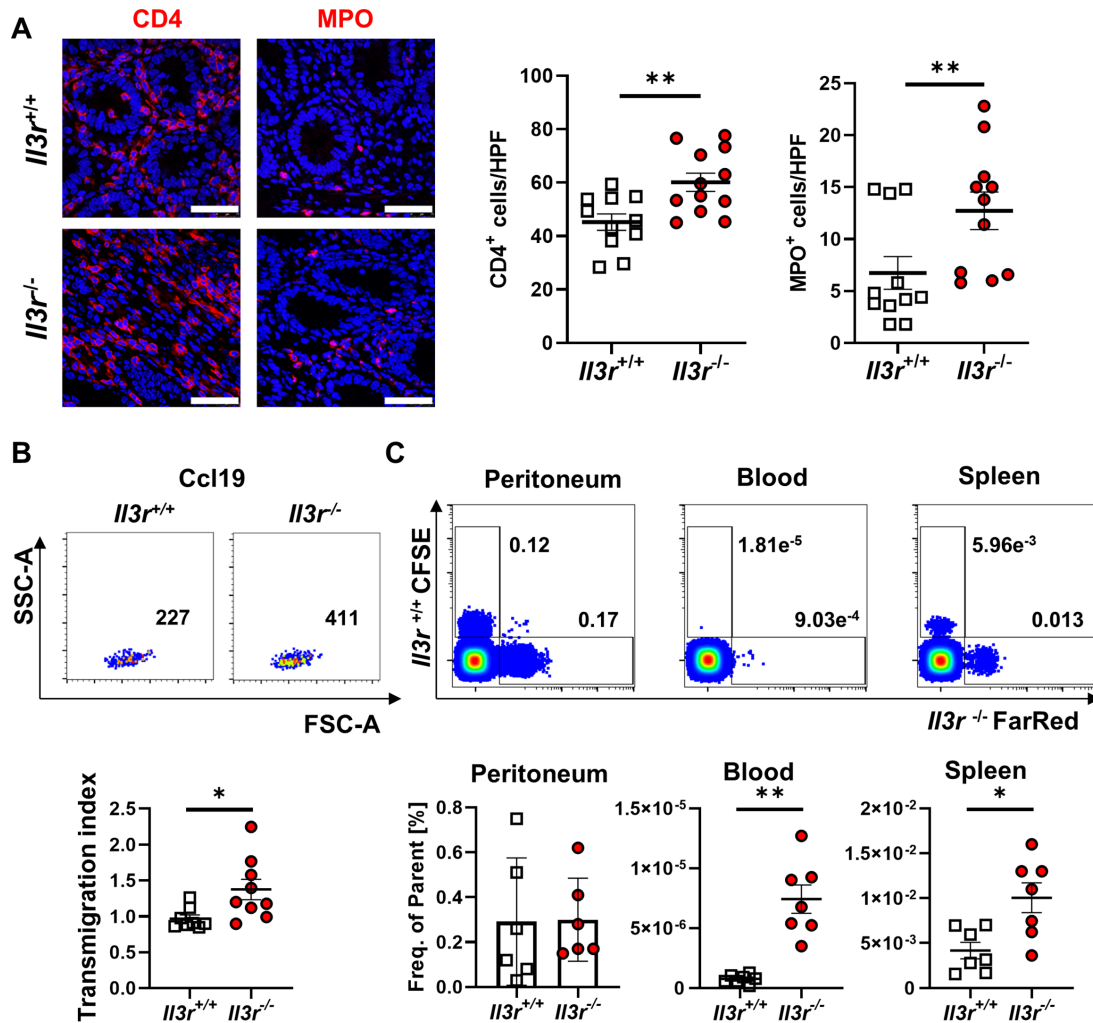


Figure 3 *Il3r* alters T cell recirculation. (A) Immunofluorescence staining for CD4 (left, red) and MPO (right, red) in colon tissue of *Rag1*^{-/-} mice after transfer of naïve CD4⁺ T cells from *Il3r*^{+/+} and *Il3r*^{-/-} mice counterstained with Hoechst (blue). Left panels: representative images, white arrows highlight CD4⁺ or MPO⁺ cells. Right panels: quantification of CD4⁺ and MPO⁺ cells per high power field (HPF). n=11–12 per group, unpaired t-test (CD4) and Mann-Whitney (MPO); scale bars – 50 µm. (B) Migration of *Il3r*^{-/-} or *Il3r*^{+/+} thymus T cells over porous membranes towards rm Ccl19. Upper panels: representative flow cytometry. Lower panel: quantification of Ccl19-specific transmigration; n=8–9 per group, Mann-Whitney test. (C) Recirculation of FarRed-stained *Il3r*^{-/-} and CFSE-stained *Il3r*^{+/+} thymus T cells after i.p. injection. Upper panels: representative flow cytometry of peritoneal, blood and splenic cells. Lower panel: quantification; n=6–7 per group, paired t-test. i.p., intraperitoneal; MPO, myeloperoxidase.

T cells from these mice for transfer colitis in *Rag1*^{-/-} mice. Consistent with the phenotype driven by *Il3r*^{-/-} T cells, mice that received *Il3r*^{-/-} CD4⁺ T cells suffered from severer T cell transfer colitis than mice that received *Il3r*^{+/+} CD4⁺ T cells as demonstrated by endoscopy, histology, *in vivo* imaging of ROS and weight course (figure 2F–H). Thus, we concluded that Il-3r signalling in T cells seems to be important for Il-3-driven effects in experimental colitis.

Il3r^{-/-}-driven transfer colitis was marked by increased accumulation of CD4⁺ and MPO⁺ cells in the inflamed colon (figure 3A). However, the number of apoptotic CD4⁺ cells in

the large intestine as determined by terminal deoxynucleotidyl transferase-mediated dUTP-biotin nick end labeling (TUNEL) staining was comparable between mice with *Il3r*^{-/-} and *Il3r*^{+/+} CD4⁺ T cells (online supplemental figure 4D), the *in vitro* proliferation of *Il3r*^{-/-} and *Il3r*^{+/+} T cells was similar (online supplemental figure 4E) and T cell differentiation as determined by the expression of key T cell transcription factors such as Tbet, Rorgt or Gata3 did not differ (online supplemental figure 4F). We therefore hypothesised that, while the local T cell turnover did not seem to be affected by *Il3r* deficiency, this might be due to altered T cell influx or efflux during trafficking.

Inflammatory bowel disease

Il3r deficiency increases T cell recirculation

To address this hypothesis, we systematically investigated key steps of intestinal T cell trafficking. Using the spleen as a major source of circulating lymphocytes potentially infiltrating the gut in analogy to transfer colitis, we did not detect any differences in the expression of integrins relevant for homing to the gut such as $\alpha 4$, $\beta 7$ or $\beta 1$ (online supplemental figure 5A). We further ruled out differential conformational regulation of $\alpha 4$ integrin dependent on Il-3r signalling (online supplemental figure 5B). Consistently, we observed no differences in the dynamic adhesion of *Il3r*^{-/-} and *Il3r*^{+/+} CD4⁺ T cells to endothelial cell adhesion molecules such as mucosal addressin cell adhesion molecule 1 (MAdCAM-1) and vascular cell adhesion molecule 1 (VCAM-1) (online supplemental figure 5C). We also employed an established *in vivo* model of T cell homing to the inflamed gut²² to study the infiltration of *Il3r*-proficient and *Il3r*-deficient CD4⁺ T cells to the inflamed colon and found no differences (online supplemental figure 5D).

Since these data made it unlikely that T cell recruitment into the inflamed tissue differs between *Il3r*^{-/-} and *Il3r*^{+/+} T cells, we considered T cell recirculation from the intestine as an alternative trafficking step controlling T cell abundance in the gut. Due to the large T cell numbers required for the assays and to mimic the local exposure to Il-3, we used T cells from the thymus (enriched for CD4⁺ T cells to >95%; online supplemental figure 5E), since Il-3 is expressed there similar to the inflamed colon (figure 2A,B). Indeed, the migration of *Il3r*^{-/-} T cells over porous membranes towards the mesenteric lymph node (mLN) chemokine Ccl19 was increased compared with *Il3r*^{+/+} cells, although the expression of *Ccr7* as the respective receptor was similar (figure 3B, online supplemental figure 5F).

Seeking to test whether the motility of these cells is also altered *in vivo*, we adoptively co-transferred differentially labelled *Il3r*^{-/-} and *Il3r*^{+/+} T cells to the peritoneum of *Rag1*^{-/-} mice and competitively measured their appearance in the spleen 72 hours later. Consistently, these analyses demonstrated that more *Il3r*^{-/-} than *Il3r*^{+/+} T cells migrated there (figure 3C) despite similar expression of various genes coding for potentially involved trafficking molecules as determined by RNA sequencing and flow cytometry (online supplemental figure 6). In synopsis, these data were consistent with a model, in which the recirculation of *Il3r*-deficient T cells is increased.

Il3r deficiency instructs altered cytoskeleton architecture and dynamics

Having shown that, we sought to identify the mechanism for increased Ccl19-directed motility and increased recirculation of *Il3r*-deficient compared with *Il3r*-proficient T cells. To this end, we profiled unchallenged *Il3r*^{-/-} and *Il3r*^{+/+} T cells from the thymus by bulk RNA sequencing,²³ which revealed 624 differentially expressed genes. Pathway enrichment analysis with the Database for Annotation, Visualization and Integrated Discovery (DAVID) demonstrated a substantial number of differentially expressed genes linked to the cytoskeleton (figure 4A,B), whereas the genes of key surface molecules involved in T cell trafficking including *Ccr7* were similarly expressed (online supplemental figure 6). This finding was consistent with the idea that cell-intrinsic processes rather than the interaction of surface molecules drive differential trafficking of *Il3r*^{-/-} and *Il3r*^{+/+} T cells.

To further investigate this idea, we performed a kinase assay assessing the activity of various kinases in unchallenged *Il3r*^{-/-} and *Il3r*^{+/+} T cells from the thymus. Overall, it showed

differential activation for numerous members of the protein tyrosine kinases (PTK) and serin/threonine kinase family (STK) for *Il3r*^{-/-} compared with *Il3r*^{+/+} cells (figure 4C). Again, pathway annotation analysis with DAVID revealed an enrichment in kinases associated with cytoskeleton regulation such as Rho kinase 1 and 2 (figure 4D).

We therefore aimed to study the Il-3r-dependent regulation and function of the cytoskeleton in more detail. Since small GTPases are known as key regulators of the cytoskeleton,²⁴ we determined their expression in *Il3r*^{+/+} and *Il3r*^{-/-} T cells by immunofluorescence, but detected no differences (online supplemental figure 7A). However, well in line with a previous study,²⁵ pull-down assays showed increased functional activity of Rac1, a Rho GTPase with particular relevance in T cells,²⁶ in *Il3r*^{-/-} compared with *Il3r*^{+/+} T cells (online supplemental figure 7B), suggesting that Rac1 function rather than Rac1 expression is a target of Il-3r signalling. To investigate how this reflects in the actual cytoskeleton architecture, we employed scanning electron microscopy and studied the actin cortex of *Il3r*^{-/-} and *Il3r*^{+/+} T cells. It turned out that the mesh-hole area of the actin cortex of *Il3r*^{-/-} T cells is substantially higher than that of *Il3r*^{+/+} T cells (figure 4E). In a further series of experiments, we additionally used fluorescence recovery after photobleaching (FRAP) to explore whether Il-3r signalling also affects the dynamics of the actin cortex. Actually, the half-time recovery period for the actin cortex of *Il3r*^{-/-} T cells was clearly longer than for *Il3r*^{+/+} T cells (figure 4F). Collectively, these data indicated that *Il3r* deficiency results in altered cytoskeleton regulation including disturbed architecture and dynamics of the actin cortex.

Il3r-deficient T cells exhibit increased deformability, which is particularly pronounced in Tregs

We then wondered how these findings might affect the postulated difference in trafficking of *Il3r*^{-/-} and *Il3r*^{+/+} T cells. Since cell deformation is an important part of T cell egress from tissues as cells cross the basement membrane and undergo reverse transendothelial migration,²⁷ we explored whether cell mechanical properties might differ. To this end, we used real-time deformability cytometry (RT-DC), a microfluidic technique suitable for high throughput assessment of cell elasticity²⁸ (figure 5A). While we observed a very homogenous phenotype of *Il3r*^{+/+} lymphocytes from thymus, transfer colitis colon and peripheral lymph nodes (pLN) with only low deformation, a subset of *Il3r*^{-/-} lymphocytes from the thymus and the inflamed colon (where Il-3 is both expressed), but not pLNs (where Il-3 is not expressed, figure 2A,B) displayed high deformability (figure 5B,C). To corroborate this finding, we employed atomic force microscopy (AFM) using a wedged cantilever measuring the forces necessary to squeeze lamina propria CD4⁺ T cells from mice with established transfer colitis. Again, we found a higher deformability of *Il3r*^{-/-} compared with *Il3r*^{+/+} T cells (i.e. less force was required for deformation; figure 5D).

In a next step, we wondered whether these alterations in cell mechanical properties might be differentially pronounced in pro-inflammatory and anti-inflammatory T cells and might thereby drive the phenotype observed in experimental colitis. Indeed, confirming previous data,⁹ we found increased expression of Il-3r on Tregs compared with non-Tregs (figure 5E). Consistently, the increase in deformability of *Il3r*^{-/-} T cells was clearly more pronounced in isolated Tregs as determined by AFM (figure 5F) as well as in CD25⁺ compared with CD25⁻ lamina propria T cells as determined by RT-DC coupled with fluorescence (figure 5G).

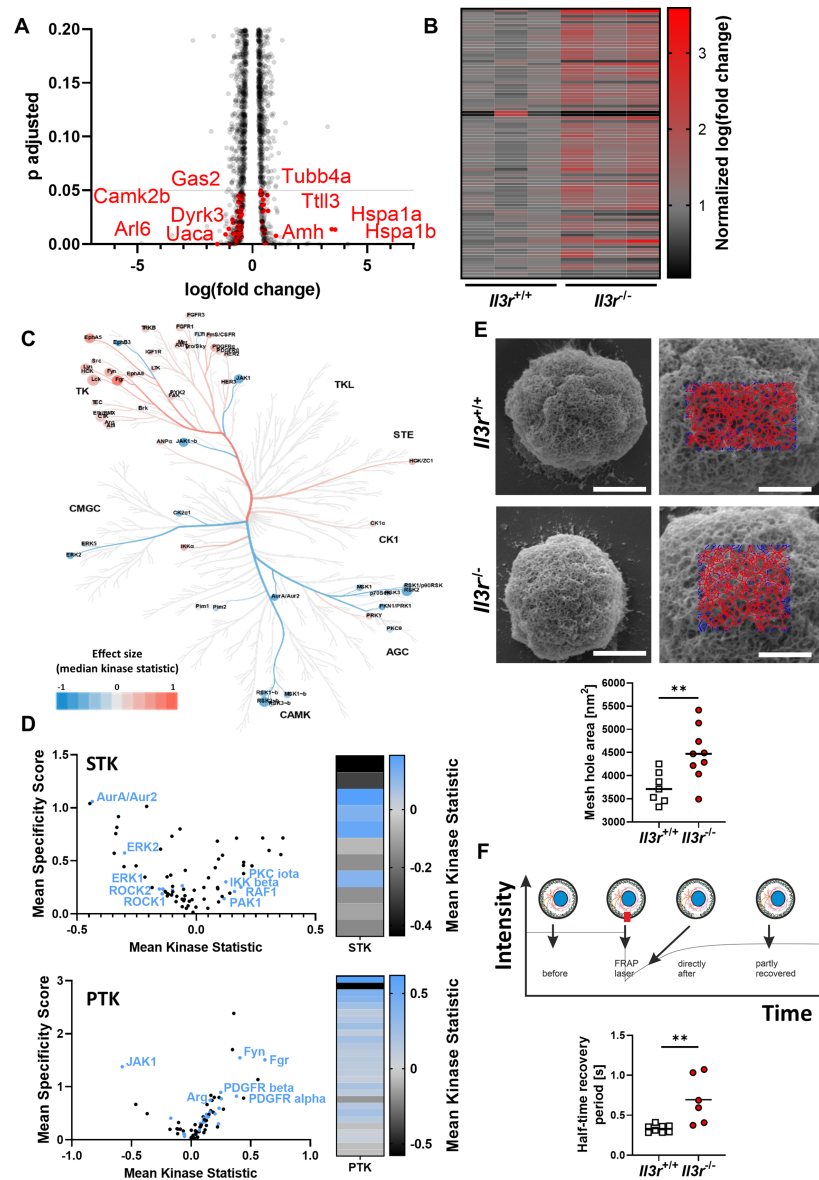


Figure 4 *I13r*-deficiency alters structure and dynamics of the cytoskeleton. (A,B) Differentially expressed genes in RNA sequencing of *I13r^{-/-}* or *I13r^{+/+}* thymus T cells (n=3 per group). (A) Volcano plot of the top 4245 regulated genes, grey line indicates significance threshold. Significantly differentially expressed cytoskeleton-related genes (as identified by Database for Annotation, Visualization and Integrated Discovery (DAVID) annotation analysis, n=90) highlighted in red, selected gene names indicated. (B) Heatmap of normalised log(fold change) of 90 cytoskeleton-related genes as identified by DAVID annotation analysis. (C) Coral Kinome Tree plotted with data from a Pamgene kinome analysis of *I13r^{-/-}* vs *I13r^{+/+}* thymus T cells. Kinases with higher activity in *I13r^{-/-}* are highlighted in red. (D) Left panels: volcano plots showing all differentially activated serin/threonine kinases (STK) and protein tyrosine kinases (PTK) in *I13r^{-/-}* versus *I13r^{+/+}* thymus T cells. Cytoskeleton-associated kinases are highlighted in blue. Right panels: heatmaps of mean kinase statistics for cytoskeleton-associated STK and PTK. (E) Scanning electron microscopy (SEM) of the actin cortex in *I13r^{-/-}* or *I13r^{+/+}* thymus T cells. Upper panels: representative SEM pictures (left, scale bars = 2 μm) and magnifications with representative FiNTA software-based quantification grids (right, scale bar = 1 μm). Lower panel: quantification of the mean mesh hole area; n=7-9 per group, unpaired t-test. (F) Fluorescence recovery after photobleaching (FRAP) of the actin cortex in *I13r^{-/-}* or *I13r^{+/+}* thymus T cells. Schematic representation of FRAP experiment (upper panel) and quantification of the half-time recovery period (lower panel); n=6-8 per group, unpaired t-test.

Inflammatory bowel disease

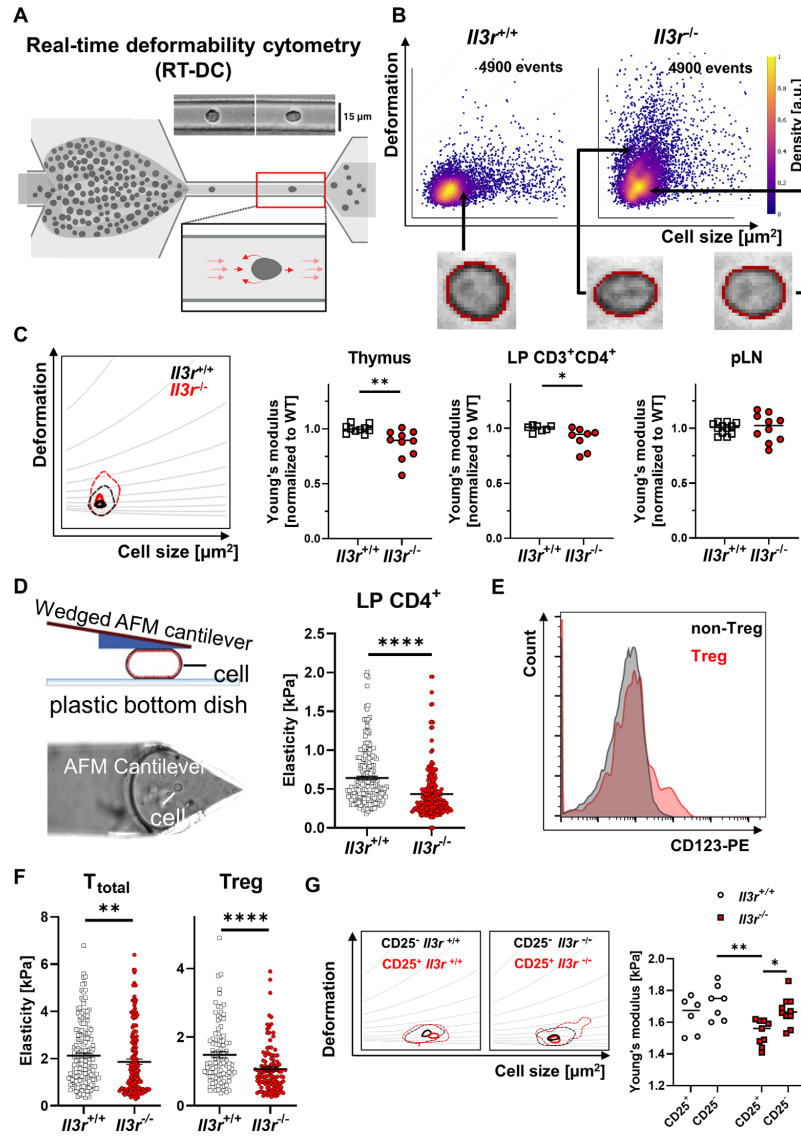


Figure 5 Increased deformability of *I13r*^{-/-} lymphocytes. (A) Schematic representation of RT-DC measurement. Cells from a reservoir are pumped through a narrow constriction in a polydimethylsiloxane (PDMS)-based microfluidic chip (15 μm capillary) and deformation ensuing due to hydrodynamic stresses is analysed; figure drawn with licensed BioRender software. (B) Representative RT-DC scatter plot of deformation versus cell size (cross-sectional area) of thymus T cells from *I13r*^{-/-} and *I13r*^{+/+} mice highlighting representative cells of the populations. (C) Representative kernel density estimate (KDE) plot (with grey isoelectricity lines) of thymus T cells from *I13r*^{-/-} and *I13r*^{+/+} mice (left) and quantification of the calculated Young's modulus of lymphocytes from thymus and pLN as well as pregated CD3⁺CD4⁺ lamina propria T cells from mice with transfer colitis. Quantification normalised to the mean of the *I13r*^{+/+} cells in each independent experiment; n=7–12 per group, Mann-Whitney test; effect size: Cohen's d=1.468 (Thymus), d=1.363 (CD3⁺CD4⁺ LP), d=0.065 (pLN). (D) Schematic representation of atomic force microscopy (AFM) cantilever and cell deformation (left). Quantification of the elasticity of CD4⁺ lamina propria lymphocytes from mice with established transfer colitis with *I13r*^{-/-} and *I13r*^{+/+} T cells by AFM; n=212 each, Mann-Whitney test. (E) Histograms of Cd123 expression on CD3⁺CD4⁺ Treg (CD25⁺CD127⁻) or non-Treg (CD25⁻) *I13r*^{+/+} thymocytes as determined by flow cytometry. Data are representative for six mice from four independent experiments. (F) Quantification of the calculated Young's modulus of total CD4⁺ and regulatory CD4⁺ T cells (right) from *I13r*^{-/-} and *I13r*^{+/+} mice by AFM; n=100–172 per group, Mann-Whitney test. (G) Representative RT-DC KDE plot (upper panel) and quantification of the calculated mean Young's modulus (lower panel) of splenic CD3⁺CD4⁺ CD25⁺ and CD25⁻ lymphocytes from *I13r*^{-/-} and *I13r*^{+/+} mice; n=6–10 per group, two-way analysis of variance with Tukey's multiple comparison test; effect size: Cohen's f=0.071. LP, lamina propria; pLN, peripheral lymph node; Treg, regulatory T cell; WT, wild-type.

Gut: first published as 10.1136/gutjnl-2023-329818 on 4 August 2023. Downloaded from <http://gut.bmj.com/> on May 27, 2024 at University Saarbruecken. Protected by copyright.

Taken together, our findings indicated that defective IL-3 signalling in T cells and particularly in Tregs modulates cell mechanical properties and increases their deformability, which might explain altered trafficking features.

Altered tissue egress of *Il3r*^{-/-} T cell to mLN in experimental colitis disturbs Treg proportions in the inflamed gut

Although demonstrating altered mechano-migratory properties of *Il3r*^{-/-} T cells, our findings did so far not answer the question, why experimental T cell transfer colitis is aggravated after transfer of *Il3r*^{-/-} cells. In view of the pronounced mechanical phenotype of *Il3r*^{-/-} Tregs, we hypothesised that their higher deformability might predispose them for increased egress from the colon to mLN compared with other T cells, which might lead to an enhanced dysbalance of pro-inflammatory and anti-inflammatory T cells in the gut.

To explore this question, we used *Rag1*^{-/-} mice with established *Il3r*^{+/+} or *Il3r*^{-/-} T cell transfer colitis and performed recirculation assays by injecting anti- $\alpha 4\beta 7$ integrin antibodies (DATK32) to block T cell gut homing and the sphingosine-1-phosphate receptor (S1PR) agonist ozanimod to block T cell recirculation from mLN. In this situation, changes occurring in the T cell composition of mLN should largely be attributable to T cell egress from the gut, since upstream and downstream pathways are unavailable (figure 6A). Consistently, whole organ imaging of mLN from mice with transfer colitis using lightsheet fluorescence microscopy demonstrated Lyve-1-expressing afferent lymph vessels and infiltrating CD4⁺ T cells (figure 6B). In further experiments, we stained mLN for Lyve-1 and CD25. Analysis by lightsheet microscopy suggested increased infiltration of *Il3r*^{-/-}, but not *Il3r*^{+/+} CD25⁺ Tregs to mLN 16 hours after combined DATK32 and ozanimod treatment compared with control mice treated with placebo (figure 6C). To quantify these changes in T cell composition, we determined the fraction of CD25⁺Foxp3⁺ Tregs in mLN and spleens of mice with transfer colitis after treatment with DATK32/ozanimod or with placebo. Interestingly, in mice with *Il3r*^{-/-} T cells, the Treg fraction in mLN, but not in spleens, increased after DATK32/ozanimod treatment compared with placebo, while it rather decreased in mice with *Il3r*^{+/+} T cells. Consistently, when we compared the ratio of Tregs in DATK32/ozanimod-treated and placebo-treated mice between *Il3r*^{+/+}-dependent and *Il3r*^{-/-}-dependent transfer colitis, we detected a significant difference in mLN, but not in spleen (figure 6D).

These data suggested that the egress of *Il3r*^{-/-} Tregs from the inflamed colon to draining mLN surpasses that of *Il3r*^{-/-} non-Tregs. To evaluate the consequences of this observation for T cell composition in the inflamed colon, we stained Foxp3 on colon cryosections from mice with transfer colitis (without additional treatment, as shown in figure 2F–H). We observed a clear reduction of Foxp3⁺ Tregs in the colon of *Rag1*^{-/-} mice with *Il3r*^{-/-} compared with *Il3r*^{+/+} T cells resulting in a decreased ratio of Tregs to total CD4⁺ T cells (figure 6E). Importantly, Treg differentiation and effector cell suppression per se were not altered by *Il3r* deficiency and addition of IL-3 (online supplemental figure 8A,B).

Thus, together, these findings suggested that aggravated inflammation in *Il3r*^{-/-}-dependent T cell transfer colitis can be explained as a result of increased Treg egress to mLN leading to reduced anti-inflammatory activity in the gut with consecutively enhanced effector T cell activity.

Il3r-dependent mechanical and migratory properties are recapitulated in human T cells and IL-3 expression in the intestine is associated to Treg abundance

We next sought to answer the question whether similar mechanisms apply for human T cells. To this end, we isolated CD4⁺ T cells from the peripheral blood, stimulated them with anti-CD3/CD28 antibodies to induce IL-3R expression (online supplemental figure 9A), and treated them with or without IL-3.

In a first series of experiments, we confirmed that IL-3 does not impact on the expression of gut homing markers or the dynamic adhesion to MAdCAM-1 and VCAM-1 similar to the situation in mice (online supplemental figure 9B,C). We then characterised their mechanical phenotype by RT-DC. Consistent with the findings in mice, IL-3-exposed T cells exhibited lower deformability, whereas IL-6 or interferon- γ did not induce similar changes (figure 7A, online supplemental figure 9D). AFM corroborated decreased deformability of IL-3-exposed cells (figure 7B). Although phalloidin staining revealed similar expression of total actin in T cells treated with or without IL-3 (online supplemental figure 9E), separation of globular (G-) and filamentous (F-) actin from these cells and subsequent western blot demonstrated increased G-actin in IL-3-unexposed CD4⁺ T cells (figure 7C). This was fitting to the concept that IL-3 signalling also triggers cytoskeletal alterations in human T cells as it does in mice.

We further aimed to investigate the impact of IL-3R signalling on human T cells on a functional level. Thus, we investigated their migration over porous membranes towards the mLN chemokines CCL19 and CCL21 on previous incubation with or without IL-3. Indeed, fewer IL-3-exposed T cells migrated through those membranes than unexposed T cells (figure 7D), suggesting that lower deformability results in reduced motility similar to the situation in mice.

Finally, we aimed at elucidating whether these mechanisms might also be relevant for human IBD. To this end, we stained LPMCs from colon biopsies of patients with IBD for flow cytometry. Importantly, we could show increased expression of IL-3R (CD123) on Tregs compared with conventional T cells in the lamina propria (figure 7E). This suggested that IL-3 released in the inflamed human gut can locally determine the mechanobiology and motility of IL-3R-expressing Tregs.

Indeed, the expression of *Il3* mRNA in the colon of patients with IBD was significantly correlated with Treg cytokines such as *IL10* or *TGFB*,²⁹ but not with pro-inflammatory mediators such as *IL13* or *IL18* (figure 7F, online supplemental figure 10). Similarly, when we stained colon samples from patients with IBD for CD4⁺Foxp3⁺ Tregs and for IL-3⁺ cells, we observed a strong correlation (figure 7G), which was consistent with the idea that IL-3 promotes mucosal residence of Tregs also in the human gut.

DISCUSSION

Various cytokines have been implicated in the pathogenesis of IBD,³⁰ but the role of IL-3 remained to be explored until now. In this study, we identify an important function of IL-3R signalling in CD4⁺ T cells in experimental colitis and human IBD.

We observed increased expression of IL-3 in the inflamed mucosa of patients with CD and UC, whereas IL-3 was barely expressed in patients without IBD. Moreover, IL-3 was strongly correlated to Treg cytokines and abundance. Thus, our data are the first to provide evidence for a key role of IL-3 in the pathogenesis of IBD.

Moreover, our findings uncovered a crucial role of IL-3 in driving Treg mechanobiology and tissue egress. To our

Inflammatory bowel disease

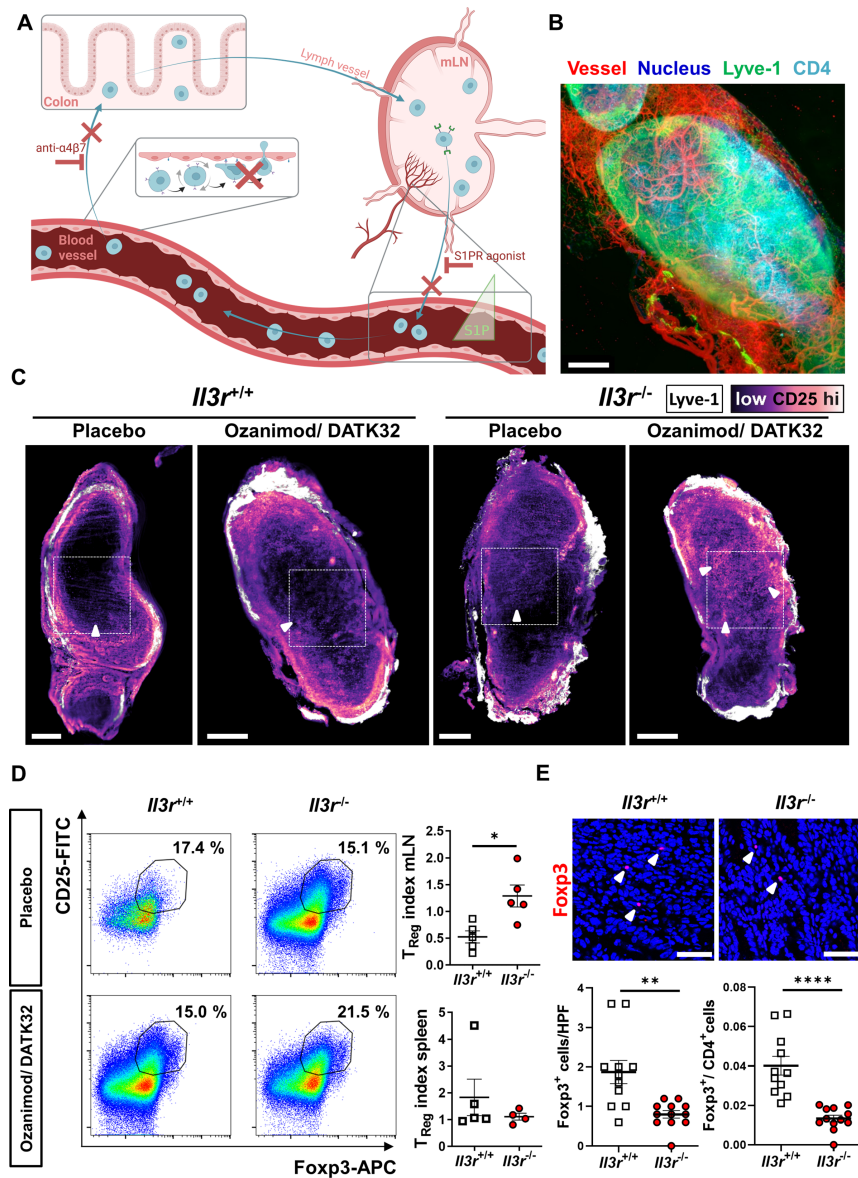


Figure 6 Enhanced recirculation of *I13r^{-/-}* regulatory T lymphocytes from the inflamed colon. (A) Schematic representation of recirculation studies in T cell transfer colitis *in vivo* (cf. main text for details); figure drawn with licensed BioRender software. (B) Representative lightsheet microscopy of *I13r^{+/+}* mLN after staining with vesseldye-CF770 (red) and with antibodies against Lyve-1-eFluor570 (green), CD4-AF647 (light blue) and counterstaining with Hoechst (dark blue); three-dimensional reconstruction with Imaris software V.9.9; scale bar = 200 μ m. (C) Representative virtual sections of mLN from *Rag1^{-/-}* mice with transfer colitis induced by *I13r^{-/-}* or *I13r^{+/+}* T cells and treated with ozanimod/DATK32 or placebo control analysed by lightsheet microscopy. Whole-organ staining with antibodies against Lyve-1-eFluor570 (white) and CD25-AF488 (scale from black to light magenta); scale bars = 400 μ m, dashed square highlights the mLN centre, white arrowheads highlight representative CD25 signal. (D) Representative flow cytometry of mLN (left, gated on $CD3^+CD4^+$) and quantification of the CD25⁺Foxp3⁺ regulatory T cell (Treg) index (right, Treg fraction in ozanimod/DATK32 per fraction in placebo) in mLN (upper panel) and spleens (lower panel). $n=4-5$ per group, Mann-Whitney test. (E) Immunofluorescence staining for Foxp3 in colon tissue of *Rag1^{-/-}* mice with transfer colitis induced by *I13r^{-/-}* or *I13r^{+/+}* T cells: Representative confocal microscopy (upper panels) and quantification of Foxp3⁺ cells as well as the ratio of Foxp3⁺ to CD4⁺ cells (stained on sequential sections, lower panels). $n=11-12$ per group, Mann-Whitney (Foxp3) and unpaired t-test (ratio); scale bars = 50 μ m, white arrowheads highlight Foxp3⁺ cells. HPF, high power field; mLN, mesenteric lymph node; S1P, sphingosine-1-phosphate; Treg, regulatory T cell.

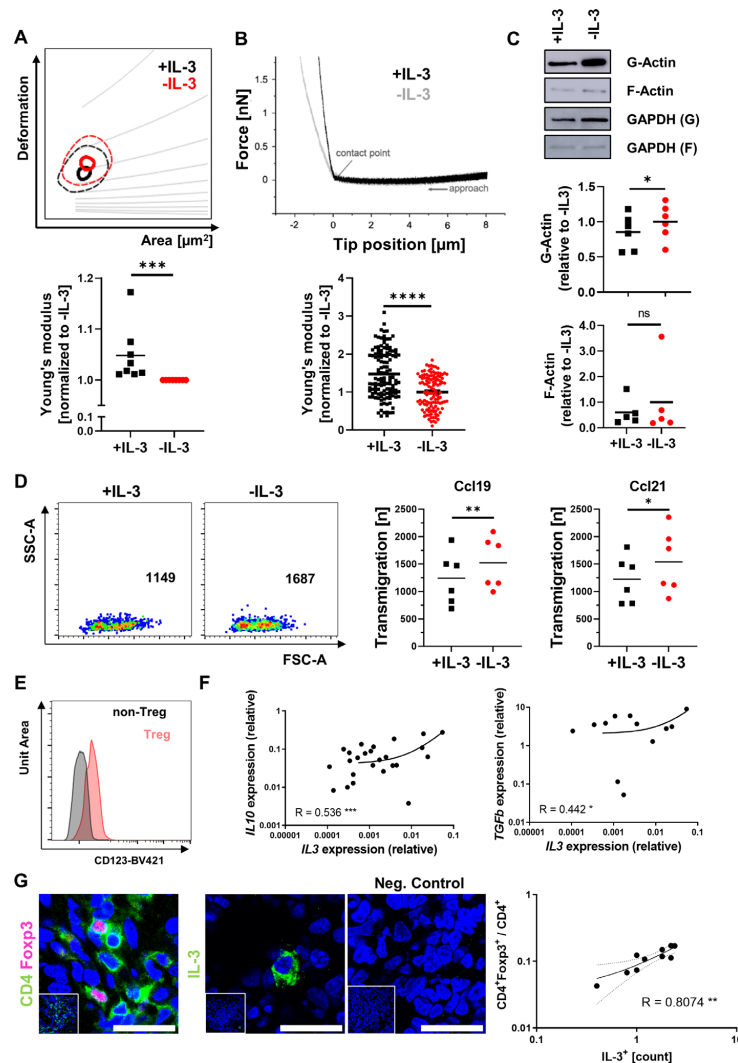


Figure 7 IL-3 stiffens human CD4⁺ T cells and correlates to Tregs in the inflamed gut. (A) Representative RT-DC kernel density estimate plot (with grey isoelasticity lines) of CD4⁺ peripheral blood T cells stimulated with anti-CD3/CD28 antibodies and treated with or without rh IL-3 (upper panel) and quantification of the calculated mean Young's modulus normalised to values of untreated samples (lower panel); n=8 per group, Wilcoxon signed-rank test; effect size: Cohen's d=1.323. (B) Representative atomic force microscopy force curve (upper panel) and quantification of the calculated Young's modulus relative to the mean of untreated cells (lower panels) of CD4⁺ peripheral blood T cells stimulated with anti-CD3/CD28 antibodies and treated with or without rh IL-3; n=59–62 per group, paired Mann-Whitney test. (C) Representative western blot analysis (upper panels) and quantification (lower panels) of G-Actin and F-Actin (as well as GAPDH control) in CD4⁺ T cells stimulated with anti-CD3/CD28 antibodies and treated with or without rh IL-3; n=5–6 per group, Wilcoxon matched pairs signed-rank test. (D) Migration of CD4⁺ peripheral blood T cells over porous membranes towards rh CCL19 or rh CCL21. Left panels: Representative flow cytometry. Right panels: Quantification of transmigration; n=6 per group, paired t-test. (E) Flow cytometry of lamina propria mononuclear cells isolated from biopsies of patients with IBD. Representative histogram of CD123 staining on CD4⁺CD25⁺Foxp3⁺ Treg cells and CD4⁺CD25⁻Foxp3⁻ non-Treg cells (left). Data are representative for five independent experiments. (F) Correlation of *IL3* mRNA with *IL10* and *TGFB1* mRNA expression as determined by qPCR in colon tissue from patients with IBD (n=21–45). Spearman's R, significance levels and a regression line are indicated. (G) Immunofluorescence of cryosections from patients with IBD (CD or UC, each n=5) for CD4 (green) and Foxp3 (magenta) or IL-3 (green); counterstaining with Hoechst (blue). Left panels: representative images, scale bars – 25 μ m; right panel: correlation of IL-3⁺ cells and CD4⁺Foxp3⁺ per total CD4⁺ cells; Spearman's R, significance levels and a regression line are indicated. CD, Crohn's disease; F-Actin, filamentous actin; G-Actin, globular actin; GAPDH, glyceraldehyde 3-phosphate dehydrogenase; IBD, inflammatory bowel disease; IL, interleukin; mRNA, messenger RNA; qPCR, quantitative PCR; rh, recombinant human; RT-DC, real-time deformability cytometry; TGF, transforming growth factor; Tregs, regulatory T cells; UC, ulcerative colitis.

Inflammatory bowel disease

knowledge, these observations identify the first factor controlling mucosal tissue egress of Tregs and suggest new avenues to specifically interfere with T cell trafficking in order to treat chronic intestinal inflammation.

We observed an increase of IL-3 expression during experimental T cell transfer colitis suggesting that IL-3 and associated IL-3R signalling not only impacts on human disease but also on experimental models of IBD. Compatibly, IL-3 had previously been linked with experimental models of several other immune-mediated inflammatory diseases such as rheumatoid arthritis, lupus erythematoses, asthma or multiple sclerosis,^{9 10 31 32} whereas insights into chronic intestinal inflammation apart from an established role on basophil expansion³³ had been lacking so far. Taking advantage of two T cell-dependent models covering different aspects of intestinal inflammation,^{34 35} our further experiments revealed that IL-3 and IL-3r signalling counteract intestinal inflammation. Regarding the marked upregulation of IL-3 expression particularly in active IBD, this might appear counterintuitive on first view. However, one has to consider that active inflammation also triggers regulatory pathways, which limit tissue destruction and may lead to resolution of inflammation.³⁶ Consistently, increased expression of the key Treg cytokine IL-10 and an increased presence of functional Tregs in active IBD have earlier been demonstrated^{29 37} and IL-3 was strongly correlated with Treg cytokines and abundance. However, in the inflammatory network present in the mucosa in IBD, such compensatory attempts fall short of controlling disease due to an even more pronounced expansion of pro-inflammatory signalling and cells.^{5 37} Thus, we interpret our findings in human IBD as the abortive effort of the intestinal immune system to mount anti-inflammatory strategies to resolve inflammation. This idea is also promoted by the virtual absence of IL-3 expression in the uninflamed gut suggesting that IL-3 does not control homeostasis, but is released as a counter-regulatory signal in inflammation.

Of note, the role of IL-3 seems to differ between different organs and contexts. Whereas detrimental effects have been suggested in diseases such as chronic inflammation of the central nervous system,³¹ other authors report a regulatory role, for example, in asthma.^{9 38 39} Importantly, many of the latter reports associate the regulatory function with Tregs. Thus, our data further underscore that the role of IL-3 in various pathologies is pleiotropic, but match well with other settings, where IL-3 restrains inflammation.

On a mechanistic level, our studies implicate IL-3 in the regulation of T cell trafficking, particularly in the prevention of Treg egress from the colon lamina propria. This observation is noteworthy for two reasons: (1) T cell egress from the intestine has barely been studied so far and (2) our data suggest that cell-intrinsic processes rather than the interaction of surface molecules orchestrate this effect.

In the light of an anti- $\alpha 4 \beta 7$ integrin antibody (vedolizumab) and an S1PR agonist (ozanimod) being available for the treatment of IBD^{14 15 40} and other anti-trafficking agents in the pipeline,^{41 42} T cell trafficking has gained increasing attraction in the field. However, while previous research extensively studied T cell homing and retention for their role in regulating the *in situ* T cell pool in the intestine,^{22 43 44} T cell egress from that pool has largely been neglected. While a role of Ccr7 and sphingosine-1-phosphate (S1P) have been demonstrated as in other organs,^{45 46} dedicated studies on local factors calibrating intestinal T cell egress in IBD are missing. This even capitalises in the so far unanswered question, whether clinically available and investigated S1PR

agonists might also impact on T cell recirculation from the mucosa in addition to recirculation from secondary lymphoid organs. Thus, our data provide important new insights into a so far understudied aspect of T cell trafficking. Of note, in line with our data suggesting that deficient *Il3r* signalling induces a preferential increase of Treg egress, a previous study has demonstrated that Treg recirculation between the colon and mLNs is vital in experimental colitis.⁴⁵

Moreover, despite recent major breakthroughs in the technical prerequisites and equipment to assess cell mechanical properties,⁴⁷ the functional role of cell mechanics for different cellular functions such as cell migration and motility has so far largely been studied in cancer,⁴⁸ but not sufficiently in T cells and in chronic inflammation. In fact, to our best knowledge, our study is the first to show the impact of a specific cytokine on the mechanical phenotype of T cells. Mechanistically, this seems to be driven by *Il3r*-dependent signalling altering the architecture and dynamics of the cytoskeleton. This is well in line with concepts previously demonstrated in other cell types.⁴⁹

While we acknowledge as a potential limitation that some of these characterisations were performed with non-intestinal T cells and under unchallenged conditions, our data on the biomechanics of lamina propria T cells and recirculation during T cell transfer colitis strongly support that this concept is relevant in intestinal inflammation. Essentially, by linking cytokine signalling-dependent T cell mechanical properties with their trafficking features and a resulting effect on chronic intestinal inflammation, we underscore that the regulation of T cell trafficking is not limited to the sole interaction of surface molecules, but importantly involves intracellular events. Thereby, we also provide a completely novel and orthogonal concept explaining aspects of the pathogenesis of chronic intestinal inflammation.

Importantly, studies with human cells and tissue recapitulated key aspects of the mechano-migratory phenotype imprinted on T cells by IL-3R signalling in mice. Thus, they suggest that a similar concept might apply in IBD. This might open avenues for novel future approaches in patients with CD and UC. In particular, since it has previously been shown that Tregs are a useful strategy for IBD therapy,^{50 51} it fuels the idea that locally modulating mechanical Treg properties with IL-3 might be a suitable and organ-selective treatment approach, for example, by application via enema or by targeted delivery through engineered commensal bacteria as previously suggested for IL-10.⁵²

Taken together, we demonstrate a beneficial role of IL-3 in chronic intestinal inflammation that is driven by alterations in the cytoskeleton promoting mucosal residence of Tregs. This suggests novel treatment approaches for IBD and stimulates necessary further studies in this direction

Author affiliations

¹Department of Medicine 1, University Hospital Erlangen and Friedrich-Alexander-Universität Erlangen-Nürnberg, Erlangen, Germany

²Experimental Physics, Saarland University, Saarbrücken, Germany

³Max Planck Institute for the Science of Light & Max-Planck-Zentrum für Physik und Medizin, Erlangen, Germany

⁴Department of Medicine 3, University Hospital Erlangen and Friedrich-Alexander-Universität Erlangen-Nürnberg, Erlangen, Germany

⁵Exploratory Research Unit, FAU Optical Imaging Competence Center, Friedrich-Alexander-Universität Erlangen-Nürnberg, Erlangen, Germany

⁶Deutsches Zentrum Immuntherapie (DZI), University Hospital Erlangen, Erlangen, Germany

⁷Department of Molecular Pneumology, University Hospital Erlangen and Friedrich-Alexander-Universität Erlangen-Nürnberg, Erlangen, Germany

⁸Dental Clinic 1 - Dental Preservation and Periodontology, University Hospital Erlangen and Friedrich-Alexander-Universität Erlangen-Nürnberg, Erlangen, Germany

⁹Institute of Human Genetics, University Hospital Erlangen and Friedrich-Alexander-Universität Erlangen-Nürnberg, Erlangen, Germany

¹⁰Center for Biophysics, Saarland University, Saarbrücken, Germany

Acknowledgements The research of TMM, IA, SF, BW, RL-P, IP, RA, MFN and SZ was supported by the Interdisciplinary Center for Clinical Research (IZKF) and the ELAN programme of the University Erlangen-Nuremberg, the Fritz-Bender-Stiftung, the Else Kröner-Fresenius-Stiftung, the DFG Collaborative Research Centers 643, 796, 1181 and TRR241, the Kenneth Rainin Foundation and the Litwin IBD Pioneers programme of the Crohn's and Colitis Foundation of America (CCFA); FL was supported by SFB 1027. The authors thank J Marcks, D Dzion, J Schuster, S Hofmann, L-S Becker, M Döbrönti, S Abuhattum, C Büttner, A Werlein, L Sologub, H Knott and A-L. Vögele for excellent support and/or technical assistance.

Contributors KAU, JD, CB, GR, SU, LLS, L-JL, MS, LK, OBB, TMM, N-MS and SZ performed the experiments. KAU, SU, MK, EB, IA, SF, IP, BW, SW, RL-P, RA, FL, JG, MFN and SZ provided clinical samples, protocols, reagents or designed experiments. ABE performed and MD analysed RNA sequencing. KAU, JD, CB, GR, SU, LLS, LK, TMM, FL, JG, MFN and SZ analysed and interpreted the data. SZ and KAU drafted the manuscript with the help of MFN. All authors critically revised the manuscript for important intellectual content. Guarantors: MFN, SZ.

Funding This work was funded by grants of the German Research Foundation (ZU 377/4-1; TRR 241 – 375876048; KFO 5024 – GB.com), the German Crohn's and Colitis Foundation (DCCV), the Interdisciplinary Center for Clinical Research (IZKF, J63), the Fritz Thyssen Stiftung (10.21.2.018MN) and the Else Kröner-Fresenius-Stiftung (2021_EKCS.23).

Competing interests MFN has served as an advisor for Pentax, Giuliani, MSD, AbbVie, Janssen, Takeda and Boehringer. SZ received honoraria from Takeda, Roche, Galapagos, Ferring, Falk, Lilly and Janssen. MFN and SZ received research support from Takeda, Shire (a part of Takeda) and Roche. JG and MK are co-founders of Rivercyte GmbH, a company that develops biomedical applications for real-time deformability cytometry. The other authors declare no conflicts of interest.

Patient and public involvement Patients and/or the public were not involved in the design, or conduct, or reporting, or dissemination plans of this research.

Patient consent for publication Not applicable.

Ethics approval This study involves human participants and was approved by ethics committee of the Friedrich-Alexander-Universität Erlangen-Nürnberg (249_13 B; 135_20B, 426_20B). Participants gave informed consent to participate in the study before taking part.

Provenance and peer review Not commissioned; externally peer reviewed.

Data availability statement Data are available in a public, open access repository. Data are available upon reasonable request. All data relevant to the study are included in the article or uploaded as supplementary information. RNA sequencing data are deposited on Zenodo (<https://doi.org/10.5281/zenodo.8068464>). All other data that support the findings of this study are either included in the article, uploaded as supplementary information or available from the corresponding author upon reasonable request.

Supplemental material This content has been supplied by the author(s). It has not been vetted by BMJ Publishing Group Limited (BMJ) and may not have been peer-reviewed. Any opinions or recommendations discussed are solely those of the author(s) and are not endorsed by BMJ. BMJ disclaims all liability and responsibility arising from any reliance placed on the content. Where the content includes any translated material, BMJ does not warrant the accuracy or reliability of the translations (including but not limited to local regulations, clinical guidelines, terminology, drug names and drug dosages), and is not responsible for any error and/or omissions arising from translation and adaptation or otherwise.

Open access This is an open access article distributed in accordance with the Creative Commons Attribution Non Commercial (CC BY-NC 4.0) license, which permits others to distribute, remix, adapt, build upon this work non-commercially, and license their derivative works on different terms, provided the original work is properly cited, appropriate credit is given, any changes made indicated, and the use is non-commercial. See: <http://creativecommons.org/licenses/by-nc/4.0/>.

ORCID iDs

Karen Anne-Marie Ullrich <http://orcid.org/0000-0003-0938-5800>

Stefan Uderhardt <http://orcid.org/0000-0002-2489-2109>

Tanja Martina Müller <http://orcid.org/0000-0003-2768-277X>

Imke Atreya <http://orcid.org/0000-0002-2708-9688>

Benno Weigmann <http://orcid.org/0000-0002-2398-0844>

Rocío López-Posadas <http://orcid.org/0000-0002-2398-5864>

Raja Atreya <http://orcid.org/0000-0002-8556-8433>

Markus F Neurath <http://orcid.org/0000-0003-4344-1474>

Sebastian Zundler <http://orcid.org/0000-0003-0888-2784>

REFERENCES

- Ananthakrishnan AN, Bernstein CN, Iliopoulos D, et al. Environmental triggers in IBD: a review of progress and evidence. *Nat Rev Gastroenterol Hepatol* 2018;15:39–49.
- Kobayashi T, Siegmund B, Le Berre C, et al. Ulcerative colitis. *Nat Rev Dis Primers* 2020;6:74.
- Tschurtschenthaler M, Adolph TE, Ashcroft JW, et al. Defective ATG16L1-mediated removal of Ire1A drives Crohn's disease-like ileitis. *J Exp Med* 2017;214:401–22.
- Torres J, Bonovas S, Doherty G, et al. ECCO guidelines on therapeutics in Crohn's disease. *Medical Treatment J Crohns Colitis* 2020;14:4–22.
- Neurath MF. Cytokines in inflammatory bowel disease. *Nat Rev Immunol* 2014;14:329–42.
- Schett G, McInnes IB, Neurath MF. Reframing immune-mediated inflammatory diseases through signature cytokine hubs. *N Engl J Med* 2021;385:628–39.
- Ihle JN, Peppersack L, Rebar L. Regulation of T cell differentiation: in vitro induction of 20 alpha-hydroxysteroid dehydrogenase in splenic lymphocytes from Athymic mice by a unique lymphokine. *J Immunol* 1981;126:2184–9.
- Fung MC, Hapel AJ, Ymer S, et al. Molecular cloning of cDNA for murine Interleukin-3. *Nature* 1984;307:233–7.
- Srivastava RK, Tomar GB, Barhanpurkar AP, et al. IL-3 attenuates collagen-induced arthritis by Modulating the development of Foxp3+ regulatory T cells. *J Immunol* 2011;186:2262–72.
- Yogesh S, Khapli SM, Srivastava RK, et al. IL-3 inhibits TNF-alpha-induced bone resorption and prevents inflammatory arthritis. *J Immunol* 2009;182:361–70.
- Dougan M, Dranoff G, Dougan SK. GM-CSF, IL-3, and IL-5 family of Cytokines: regulators of inflammation. *Immunity* 2019;50:796–811.
- Renner K, Metz S, Metzger A-M, et al. Expression of IL-3 receptors and impact of IL-3 on human T and B cells. *Cell Immunol* 2018;334:49–60.
- Kumar A, Rani L, Mhaske ST, et al. IL-3 receptor expression on activated human Th cells is regulated by IL-4, and IL-3 Synergizes with IL-4 to enhance Th2 cell differentiation. *J Immunol* 2020;204:819–31.
- Feagan BG, Rutgeerts P, Sands BE, et al. Vedolizumab as induction and maintenance therapy for ulcerative colitis. *N Engl J Med* 2013;369:699–710.
- Sandborn WJ, Feagan BG, Rutgeerts P, et al. Vedolizumab as induction and maintenance therapy for Crohn's disease. *N Engl J Med* 2013;369:711–21.
- Zundler S, Becker E, Schulze LL, et al. Immune cell trafficking and retention in inflammatory bowel disease: mechanistic insights and therapeutic advances. *Gut* 2019;68:1688–700.
- Habtezion A, Nguyen LP, Hadeiba H, et al. Leukocyte trafficking to the small intestine and colon. *Gastroenterology* 2016;150:340–54.
- Tang MS, Bowcutt R, Leung JM, et al. Integrated analysis of biopsies from inflammatory bowel disease patients identifies SAA1 as a link between mucosal microbes with TH17 and TH22 cells. *Inflamm Bowel Dis* 2017;23:1544–54.
- Moschen AR, Tilg H, Raine T. IL-12, IL-23 and IL-17 in IBD: immunobiology and therapeutic targeting. *Nat Rev Gastroenterol Hepatol* 2019;16:185–96.
- Corridoni D, Antanaviciute A, Gupta T, et al. Single-cell Atlas of colonic CD8+ T cells in ulcerative colitis. *Nat Med* 2020;26:1480–90.
- Friedrich M, Pohin M, Powrie F. Cytokine networks in the pathophysiology of inflammatory bowel disease. *Immunity* 2019;50:992–1006.
- Zundler S, Schillinger D, Fischer A, et al. Blockade of AEB7 integrin suppresses accumulation of CD8+ and Th9 lymphocytes from patients with IBD in the inflamed gut in vivo. *Gut* 2017;66:1936–48.
- Ullrich K, Dedden M, Müller TM, et al. IL-3 receptor signaling suppresses chronic intestinal inflammation by controlling Mechanobiology and tissue egress of regulatory T cells. 22 June 2023.
- Müller PM, Rademacher J, Bagshaw RD, et al. Systems analysis of RhoGEF and RhoGAP regulatory proteins reveals spatially organized RAC1 signalling from integrin adhesions. *Nat Cell Biol* 2020;22:498–511.
- Romanova LY, Alexandrov IA, Blagosklonny MV, et al. Regulation of actin cytoskeleton in lymphocytes: PKC-Delta disrupts IL-3-induced membrane ruffles downstream of Rac1. *J Cell Physiol* 1999;179:157–69.
- Tiede I, Fritz G, Strand S, et al. CD28-dependent Rac1 activation is the molecular target of azathioprine in primary human CD4+ T lymphocytes. *J Clin Invest* 2003;111:1133–45.
- James KD, Jenkinson WE, Anderson G. T-cell egress from the thymus: should I stay or should I go? *J Leukoc Biol* 2018;104:275–84.
- Otto O, Rosendahl P, Mietke A, et al. Real-time deformability cytometry: on-the-fly cell mechanical phenotyping. *Nat Methods* 2015;12:199–202.
- Wittmann Dayagi T, Werner L, Pinski M, et al. Mucosal IL-10 and IL-10 receptor expression patterns in paediatric patients with ulcerative colitis. *Int J Exp Pathol* 2021;102:4–10.
- Marafini I, Sedda S, Dinallo V, et al. Inflammatory cytokines: from discoveries to therapies in IBD. *Expert Opin Biol Ther* 2019;19:1207–17.
- Renner K, Hellerbrand S, Hermann F, et al. IL-3 promotes the development of experimental autoimmune encephalitis. *JCI Insight* 2016;1:e87157.
- Rignault-Bricard R, Machavoine F, Mecheri S, et al. IL-3-producing Basophils are required to exacerbate airway hyperresponsiveness in a murine inflammatory model. *Allergy* 2018;73:2342–51.

Inflammatory bowel disease

- 33 Gomez MR, Talke Y, Hofmann C, *et al.* Basophils control T-cell responses and limit disease activity in experimental murine colitis. *Mucosal Immunol* 2014;7:188–99.
- 34 Wirtz S, Popp V, Kindermann M, *et al.* Chemically induced Mouse models of acute and chronic intestinal inflammation. *Nat Protoc* 2017;12:1295–309.
- 35 Kiesler P, Fuss IJ, Strober W. Experimental models of inflammatory bowel diseases. *Cell Mol Gastroenterol Hepatol* 2015;1:154–70.
- 36 Chen Z, Bozec A, Ramming A, *et al.* Anti-inflammatory and immune-regulatory cytokines in rheumatoid arthritis. *Nat Rev Rheumatol* 2019;15:9–17.
- 37 Maul J, Loddenkemper C, Mundt P, *et al.* Peripheral and intestinal regulatory CD4+ CD25(high) T cells in inflammatory bowel disease. *Gastroenterology* 2005;128:1868–78.
- 38 Drube S, Müller S, Weber F, *et al.* IL-3 is essential for ICOS-L stabilization on mast cells, and sustains the IL-33-induced ROR γ ⁺ T_{reg} generation via enhanced IL-6 induction. *Immunology* 2021;163:86–97.
- 39 Krammer S, Yang Z, Zimmermann T, *et al.* An Immunoregulatory role of Interleukin-3 in allergic asthma. *Front Immunol* 2022;13:821658.
- 40 Sandborn WJ, Feagan BG, D'Haens G, *et al.* Ozanimod as induction and maintenance therapy for ulcerative colitis. *N Engl J Med* 2021;385:1280–91.
- 41 Matsuoka K, Watanabe M, Ohmori T, *et al.* A300 (Carotegrast methyl), an oral antagonist of A4-integrin, as induction therapy for patients with moderately active ulcerative colitis: a Multicentre, randomised, double-blind, placebo-controlled, phase 3 study. *Lancet Gastroenterol Hepatol* 2022;7:648–57.
- 42 Sandborn WJ, Peyrin-Biroulet L, Zhang J, *et al.* Efficacy and safety of Etrasimod in a phase 2 randomized trial of patients with ulcerative colitis. *Gastroenterology* 2020;158:550–61.
- 43 Dai B, Hackney JA, Ichikawa R, *et al.* Dual targeting of lymphocyte homing and retention through A4B7 and AEB7 inhibition in inflammatory bowel disease. *Cell Rep Med* 2021;2:100381.
- 44 Belarif L, Danger R, Keramarrec L, *et al.* IL-7 receptor influences anti-TNF responsiveness and T cell gut homing in inflammatory bowel disease. *J Clin Invest* 2019;129:121668:1910–25.:
- 45 Nakanishi Y, Ikebuchi R, Chtanova T, *et al.* Regulatory T cells with superior immunosuppressive capacity emigrate from the inflamed colon to draining lymph nodes. *Mucosal Immunol* 2018;11:437–48.
- 46 McNamee EN, Masterson JC, Veny M, *et al.* Chemokine receptor CCR7 regulates the intestinal TH1/TH17/Treg balance during Crohn's-like murine ileitis. *J Leukoc Biol* 2015;97:1011–22.
- 47 Urbanska M, Muñoz HE, Shaw Bagnall J, *et al.* A comparison of microfluidic methods for high-throughput cell deformability measurements. *Nat Methods* 2020;17:587–93.
- 48 Mierke CT. The matrix environmental and cell mechanical properties regulate cell migration and contribute to the invasive phenotype of cancer cells. *Rep Prog Phys* 2019;82:064602.
- 49 Lautenschläger F, Paschke S, Schinkinger S, *et al.* The regulatory role of cell mechanics for migration of differentiating myeloid cells. *Proc Natl Acad Sci U S A* 2009;106:15696–701.
- 50 Desreumaux P, Foussat A, Allez M, *et al.* Safety and efficacy of antigen-specific regulatory T-cell therapy for patients with refractory Crohn's disease. *Gastroenterology* 2012;143:1207–17.
- 51 Voskens C, Stoica D, Rosenberg M, *et al.* Autologous regulatory T-cell transfer in refractory ulcerative colitis with concomitant primary sclerosing cholangitis. *Gut* 2023;72:49–53.
- 52 Braat H, Rottiers P, Hommes DW, *et al.* A phase I trial with transgenic bacteria expressing Interleukin-10 in Crohn's disease. *Clin Gastroenterol Hepatol* 2006;4:754–9.

Additional data

In addition to the presented data in the article above, I also want to talk about two other experiments I carried out in the scope of this work.

Besides the dynamics of the actin cytoskeleton in CD4+ cells, I also measured the cross section area and circularity of these cells. For this, I seeded them on a V-CAM1 (concentration $5 \mu\text{g mL}^{-1}$) coated glass surface and fixed them with 4% PFA after four hours. Next I dissolved their membrane using Triton X-100 and stained their actin network via phalloidin staining. Measuring the cross-section area and the circularity in wild type, interleukin 3 (IL3)K.O. and interleukin 3 receptor K.O. (IL3 R K.O.) showed that only the cross-section area in wild type cells is significantly larger than the other cells, while all other data showed no significant difference (see Figure 8.1).

The CD4+ cells used in the article were extracted from the thymus. The thymus gland is an organ sited above the heart right behind the sternum in most mammals [95]. Its main function is to mature thymus cell lymphocytes (T cells). It accomplishes this goal by exposing immature T cells to several body own proteins and MHC immune receptors. Those cells who do not react to the body own proteins, but the MHC immune receptors are considered successfully developed and pass to the lymphatic system [96].

On top of the thymus CD4+ cells, I also received CD4+ cells which were taken from the spleen of mice and genetically altered so that they cannot express the IL3 R K.O.. I repeated the FRAP experiments as described in the respective article and measured the plateau value as well as the half time for its recovery (see Figure 8.2). The analysis of the data showed that there were no significant differences neither between the plateau values nor the half time values.

These findings did not fit the overall story of the article. This does not mean that they contradict the findings and conclusions but, they did not help explaining the observed phenomena of IL 3 R deficiency. Here I want to briefly discuss the additional results. The difference in cell sizes aligns well with literature, as interleukin 3 is a common growth factor for immune cells, that is involved in proliferation and differentiation [97]. The depletion of IL3 from these cells either by hindering them from segregating it or by removing the respective receptor, should therefore result in a reduction of proliferation and differentiation, which can be seen in Figure 8.1.

The second observation, that actin dynamics seem to be unaltered by interleukin 3 receptor knockout, can not be this easily explained. We came up with several hypothesis. First, the low number of cells we used for this experiment does not allow a coherent analysis, which could show trends, but does not hold the scientific standards one needs to apply. Second, CD4+ cells extracted from the spleen are more mature and therefore less susceptible to interleukin 3 and therefore the depletion of its respective receptor. Both are just hypothesis and further investigation would be required. However, this was not part of my main project and therefore out of scope for this thesis.

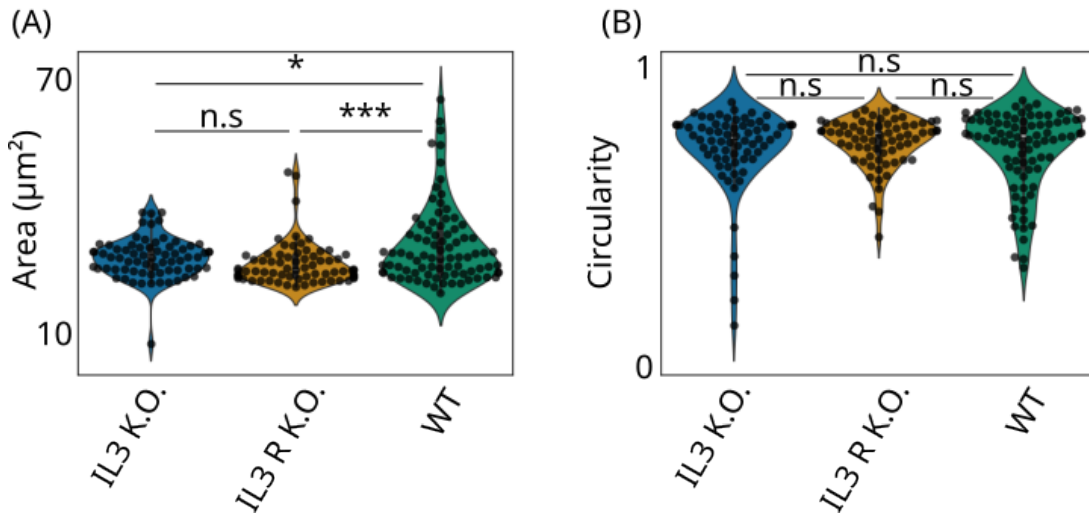


Figure 8.1: Cross section area and circularity of CD4+ cells. (A) Cross section area of CD4+ cells in wild type compared to cell with repressed IL3 (IL3 K.O.) or IL3 receptor (IL3 R K.O.) proteins, shows only a significant decrease from wild type to the other two. (B) Circularity measurements for CD4+ cells wild type, IL3 K.O. and IL3 R K.O. cells, shows no significant change between either of the three. CD4+ cells were derived from mice and extracted from the thymus. A statistical analysis was performed using Student's t test. n.s.: $p > 0.05$, *: $p < 0.05$, **: $p < 0.01$, and ***: $p < 0.005$. Number of cells: WT: 85, IL3 K.O.: 70, IL3 R K.O.: 70.

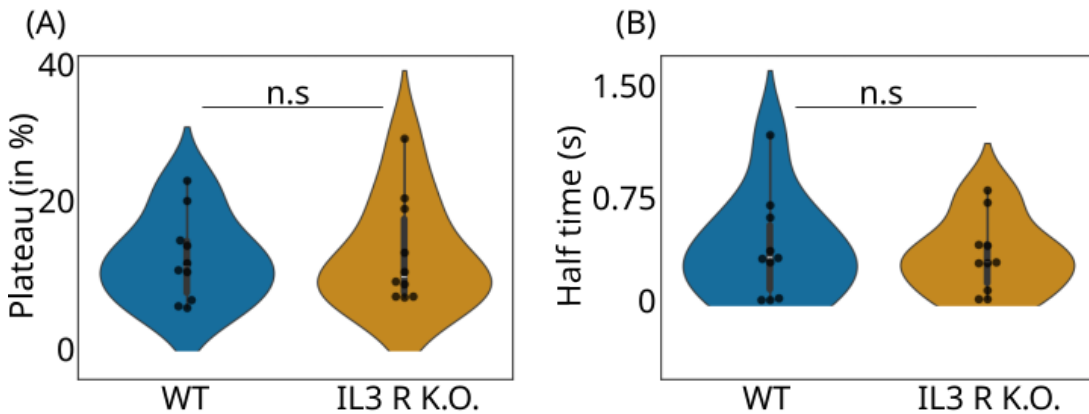


Figure 8.2: CD4+ cells extracted from the spleen instead of the thymus. FRAP measurements of CD4+ cells (spleen) show that there is no significant difference between wild type and IL3 R K.O. cells, neither for their plateau value nor their half time for recovery. A statistical analysis was performed using Student's t test. n.s.: $p > 0.05$, *: $p < 0.05$, **: $p < 0.01$, and ***: $p < 0.005$. Number of cells: WT: 10, IL3 R K.O.: 10.

Faculty of Natural Sciences and Technology**Cumulative form of the dissertation****Template for the confirmation of the proportion of co-authors**

Title of the dissertation (working title):**Cytoskeletal aspects of cellular migration**Article to be included:

A. A. Fischer, H. B. Robertson, D. Kong, M. M. Grimm, J. Grether, J. Groth, C. Baltes, M. Fliegauf, F. Lautenschläger, B. Grimbacher, H. Ye, V. Helms, W. Weber, Engineering Material Properties of Transcription Factor Condensates to Control Gene Expression in Mammalian Cells and Mice. *Small* 2024, 20, 2311834. <https://doi.org/10.1002/sml.202311834>

Quality of the publication:

Research article

Review process or publication status:

Accepted and published

Explanation of the contributions of the co-authors:**Carsten Alexander Baltes:**

Conducted no experiments for this work and was only involved in the re-evaluation and analysis of the FRAP data

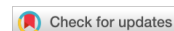
Signature of the doctoral candidate
(Carsten Alexander Baltes)



Signature of the supervisor

(Franziska Lautenschläger)





RESEARCH ARTICLE

NANO · MICRO
small

www.small-journal.com

Engineering Material Properties of Transcription Factor Condensates to Control Gene Expression in Mammalian Cells and Mice

Alexandra A.M. Fischer, Hanah B. Robertson, Deqiang Kong, Merlin M. Grimm, Jakob Grether, Johanna Groth, Carsten Baltes, Manfred Fliegau, Franziska Lautenschläger, Bodo Grimbacher, Haifeng Ye, Volkhard Helms, and Wilfried Weber*

Phase separation of biomolecules into condensates is a key mechanism in the spatiotemporal organization of biochemical processes in cells. However, the impact of the material properties of biomolecular condensates on important processes, such as the control of gene expression, remains largely elusive. Here, the material properties of optogenetically induced transcription factor condensates are systematically tuned, and probed for their impact on the activation of target promoters. It is demonstrated that transcription factors in rather liquid condensates correlate with increased gene expression levels, whereas stiffer transcription factor condensates correlate with the opposite effect, reduced activation of gene expression. The broad nature of these findings is demonstrated in mammalian cells and mice, as well as by using different synthetic and natural transcription factors. These effects are observed for both transgenic and cell-endogenous promoters. The findings provide a novel materials-based layer in the control of gene expression, which opens novel opportunities in optogenetic engineering and synthetic biology.

1. Introduction

Biomolecular condensates enable the spatial and temporal organization of cellular reactions by serving as compartments that partition molecules rapidly and selectively through phase separation.^[1,2] Recent approaches to designing biomolecular condensates have inspired a new generation of synthetic biology strategies to influence cell fate and function or to elucidate basic biological principles that rely on phase separation.^[3] Examples include the spatially controlled incorporation of synthetic amino acids into protein polymers,^[4] the control over *E.coli* biochemistry by sequestration of pathways or buffering of mRNA translation rates,^[5] the design of biochemical reaction centers to re-route molecular fluxes,^[6] the 3D organization of

A. A. Fischer, M. M. Grimm, J. Grether, J. Groth, W. Weber
Signalling Research Centres BIOSS and CIBSS
University of Freiburg
Schänzlestraße 18, 79104 Freiburg, Germany
E-mail: Wilfried.Weber@leibniz-inm.de

A. A. Fischer, M. M. Grimm, J. Grether, J. Groth, W. Weber
Faculty of Biology
University of Freiburg
Schänzlestraße 1, 79104 Freiburg, Germany

A. A. Fischer, W. Weber
Spemann Graduate School of Biology and Medicine (SGBM)
University of Freiburg
Albertstraße 21a, 79104 Freiburg, Germany

A. A. Fischer, W. Weber
INM – Leibniz Institute for New Materials
Campus D2 2, 66123 Saarbrücken, Germany

H. B. Robertson, V. Helms
Center for Bioinformatics
Saarland Informatics Campus
Saarland University
66123 Saarbrücken, Germany

D. Kong, H. Ye
Synthetic Biology and Biomedical Engineering Laboratory
Biomedical Synthetic Biology Research Center
Shanghai Key Laboratory of Regulatory Biology
Institute of Biomedical Sciences and School of Life Sciences
East China Normal University
Dongchuan Road 500, Shanghai 200241, China

J. Grether
Biberach University of Applied Sciences
Karlstraße 6–11, 88400 Biberach an der RiB, Germany

C. Baltes, F. Lautenschläger
Department of Experimental Physics and Center for Biophysics
Saarland University
66123 Saarbrücken, Germany

The ORCID identification number(s) for the author(s) of this article can be found under <https://doi.org/10.1002/smll.202311834>

© 2024 The Authors. Small published by Wiley-VCH GmbH. This is an open access article under the terms of the [Creative Commons Attribution License](#), which permits use, distribution and reproduction in any medium, provided the original work is properly cited.

DOI: [10.1002/smll.202311834](https://doi.org/10.1002/smll.202311834)

macromolecular complexes controlling genome architecture,^[7] epigenetic imprinting,^[8] or the modulation of gene expression.^[9,10]

Key driving forces for biomolecular condensate formation are the concentration of the involved molecules (such as proteins, RNA, or DNA), the biophysical properties of the involved biopolymers, as well as the multivalent interactions among them. Multivalency is often given through intrinsically disordered regions (IDRs) which are stretches of amino acids without any specific secondary structure. Proteins such as FUS^[11,12] or HNRNPA1^[13] are well-known examples, described to undergo phase separation upon reaching a critical threshold concentration. Further, an increase in the multivalency of IDR interaction, for example, through post-translational modifications or mutations, can promote the transition from the liquid state to gel- or solid-like materials.^[13–18]

Accordingly, the synthetic induction of multivalent interactions among IDRs enables the formation of biomolecular condensates on command. In a seminal study by the Brangwynne and Toettcher groups, the light-inducible homo-oligomerization of the *Arabidopsis thaliana* blue light photoreceptor Cry2 was used to increase the binding valency of IDRs and thus the formation of liquid protein condensates. By fusing IDRs to a mutant of Cry2, that forms higher-order oligomers (Cry2_{olig}), light-inducible solid-like gels were obtained, as measured by fluorescence recovery after photobleaching (FRAP). Further, as a function of the protein variant and the illumination conditions, the light-responsive formation of condensates with different material properties was observed.^[19] Since then, light-inducible formation of condensates has been applied to elucidate fundamental mechanisms and functions of phase separation,^[19,20] to optimize metabolic engineering,^[6] or to amplify biomolecular processes such as transcription activation.^[10]

Several recent studies have suggested that liquid-liquid phase separation (LLPS) of transcription factors plays important roles in the control of gene expression.^[21–25] However, the reported

effects of transcription factors undergoing LLPS range from positive^[9,10,26,27] via neutral^[28] to negative effects^[29] on gene expression, with the underlying cause for this discrepancy remaining unknown. One possible mechanism that may have led to these divergent observations could be the different material properties of the investigated transcription factor condensates. Although it has been reported that material properties influence condensate function,^[30–33] their influence on gene expression remains inconclusive.^[34–37]

In this study, we systematically engineered light-inducible transcription factor condensates with different material properties and analyzed their influence on transcription activation in mammalian cells and mice. We first performed an analysis of a synthetic transcription factor and subsequently applied the same concept to selected natural transcription factors of the NF- κ B, STAT3, and STAT6 pathways, that play pivotal roles in important processes like the immune response. We found that transcription factor condensates that exhibit rather liquid material properties have a positive effect on transgene expression levels, whereas stiffer condensates correlated with a decrease in the expression of synthetic reporter genes or endogenous promoters. These findings provide a novel concept of how biomolecular transcription factor condensates may influence gene expression. Furthermore, the molecular tools developed here may serve as an additional, material-based layer in synthetic biology for the control of target gene regulation.

2. Results

2.1. Engineering Light-Inducible Transcription Factor Condensates with Graded Material Properties

We hypothesized that altered material properties of transcription factor condensates may impact gene expression levels. To test this hypothesis, we used our previously established optogenetically-induced transcription factor condensates. This system is based on a split synthetic transcription factor comprising the DNA-binding domain TetR fused to CIBN (CIBN-TetR) and the activation domain VP16 fused to the blue light photoreceptor Cry2, further containing eYFP for visualization (Cry2-eYFP-VP16). In this configuration, illumination with blue light triggered the dimerization of CIBN and Cry2 to reconstitute a functional transcription factor.^[38] The incorporation of the FUS-derived IDR (FUS_N, Cry2-eYFP-FUS_N-VP16) led to the formation of light-inducible liquid condensates due to Cry2 homo-oligomerization. The formation of liquid condensates at the promoter site correlated with up to fivefold increased reporter gene expression compared to the non-condensed, IDR-lacking transcription factor.^[10] This increase is most likely caused by the higher concentration of activation domains within the condensate in close vicinity to the promoter (Figure 1A).^[21]

In this study, we pursued two strategies to modulate the material properties of the transcription factor condensates: first, by selecting a mutant of Cry2 that correlated with enhanced clustering (Cry2_{olig};^[39] Cry2_{olig}-eYFP-FUS_N-VP16) and second, by gradually increasing the concentration of IDRs by modularly adding a construct encoding additional FUS_N fused to Cry2_{olig} and mCherry (mCh, for visualization), by co-transfection. The construct

M. Fliegau, B. Grimbacher
Institute for Immunodeficiency
Center for Chronic Immunodeficiency (CCI)
Medical Center
Faculty of Medicine
University of Freiburg
Breisacherstr. 115, 79106 Freiburg, Germany

M. Fliegau, B. Grimbacher
CIBSS – Centre for Integrative Biological Signalling Studies
University of Freiburg
Schänzlestraße 18, 79104 Freiburg, Germany

B. Grimbacher
DZIF – German Center for Infection Research
Deutsches Zentrum für Infektionsforschung e.V.
Inhoffenstr. 7, 38124 Braunschweig, Germany

B. Grimbacher
RESIST – Cluster of Excellence 2155 to Hanover Medical School
Medizinische Hochschule Hannover
Carl-Neuberg-Str. 1, 30625 Hannover, Germany

W. Weber
Department of Materials Science and Engineering, Campus D2.2
Saarland University
66123 Saarbrücken, Germany

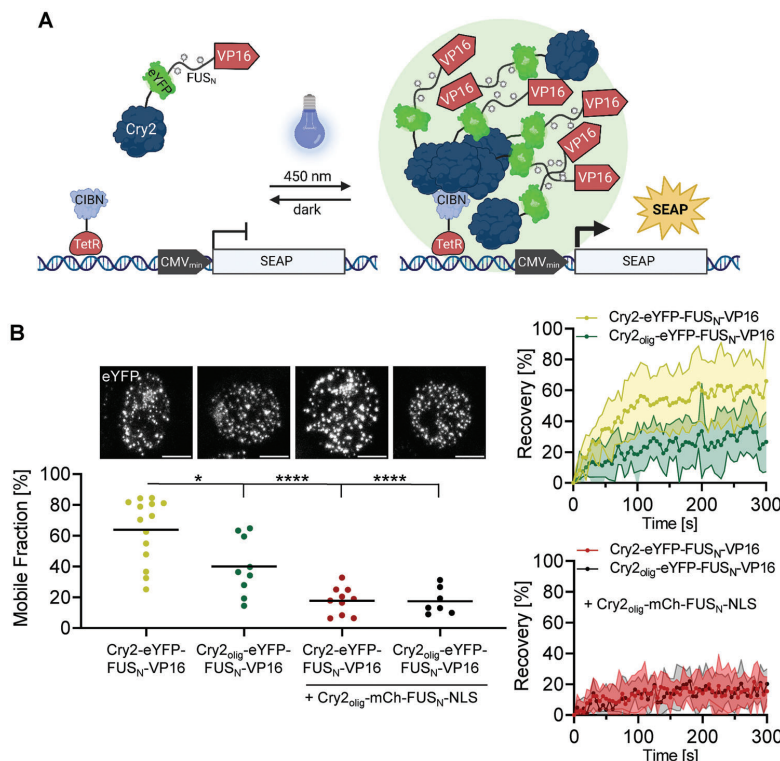


Figure 1. Design approach for tuning the material properties of transcription factor condensates. A) Design of the light-dependent transcription factor. The transcription factor consists of two parts. First, a VP16 activation domain fused to the intrinsically disordered region (IDR) FUS_N, eYFP for visualization, and the blue light photoreceptor cryptochrome 2 (Cry2). Second, the DNA-binding motif TetR fused to CIBN. Upon illumination with blue light, Cry2 binds CIBN and further undergoes homo-oligomerization, leading to multivalent interactions and the induction of LLPS. VP16 is recruited to the transcription start site provided by the CMV minimal promoter and induces reporter gene expression. B) Tuning the material properties of transcription factor condensates. To modify condensate material properties, two strategies were pursued: first, increasing the valency of interaction by exchanging Cry2 for Cry2_{olig}, which forms higher-order oligomers; and second, increasing valency and concentration by co-transfection of a construct encoding Cry2_{olig} fused to mCherry (for visualization) and FUS_N and an NLS. Constructs encoding CIBN-TetR and a tetO₄-based SEAP reporter were co-transfected into HEK-293T cells together with Cry2-eYFP-FUS_N-VP16 or Cry2_{olig}-eYFP-FUS_N-VP16 constructs (yellow and green data points). Optionally, the construct encoding Cry2_{olig}-mCh-FUS_N-NLS was added (in a 2:1 plasmid amount ratio in relation to the VP16-containing construct, red and black data points). The cells were cultivated in the dark for 32 h prior to FRAP analysis. FRAP measurements were started after 10 min of blue light illumination ($2.5 \mu\text{mol m}^{-2} \text{s}^{-1}$). Images show representative nuclei directly prior to droplet bleaching; scale bar = 5 μm. Graph (left panel) shows the mean and single values of the mobile fractions calculated from the non-linear fits of $n \geq 7$ condensate recovery curves. The right panel shows the mean recovery curves of $n \geq 7$ condensates \pm SD. Pairwise comparisons were performed using a Student's *t*-test ($^* = P \leq 0.05$; $^{****} = P \leq 0.0001$).

further contained a nuclear localization sequence (NLS, Cry2_{olig}-mCh-FUS_N-NLS).

We transfected CIBN-TetR together with Cry2-eYFP-FUS_N-VP16 or Cry2_{olig}-eYFP-FUS_N-VP16 with or without additional Cry2_{olig}-mCh-FUS_N-NLS into HEK-293T cells together with a TetR-responsive reporter construct and observed condensate formation upon blue-light illumination (Figure 1B). We then analyzed the influence of the two strategies. Cry2_{olig}-enhanced clustering and increased IDR concentration, on condensate material properties by conducting FRAP experiments. We recorded the recovery of photobleached condensates (Figure 1B; Figure S1, Supporting Information) and compared the mobile fractions. Switch-

ing from Cry2 to Cry2_{olig} significantly decreased mobile fractions from 60% to 31%, as well as the apparent diffusion coefficient from $D_{\text{app}} = 0.0026 \mu\text{m}^2 \text{s}^{-1}$ to $D_{\text{app}} = 0.0017 \mu\text{m}^2 \text{s}^{-1}$ and increased the half recovery time from $t_{1/2} = 42.3 \text{ s}$ to $t_{1/2} = 63.6 \text{ s}$. The increase in IDR concentration by the modular addition of Cry2_{olig}-mCh-FUS_N-NLS further decreased the mobile fraction to 16 or 18% for Cry2-eYFP-FUS_N-VP16 and Cry2_{olig}-eYFP-FUS_N-VP16, respectively (Figure 1B).

Complementarily, we analyzed condensate number per cell, area, integrated optical density (eYFP), and circularity from the eYFP channel (Figure 2) and measured the mean mCherry signal in the nucleus and of the condensates to monitor expression

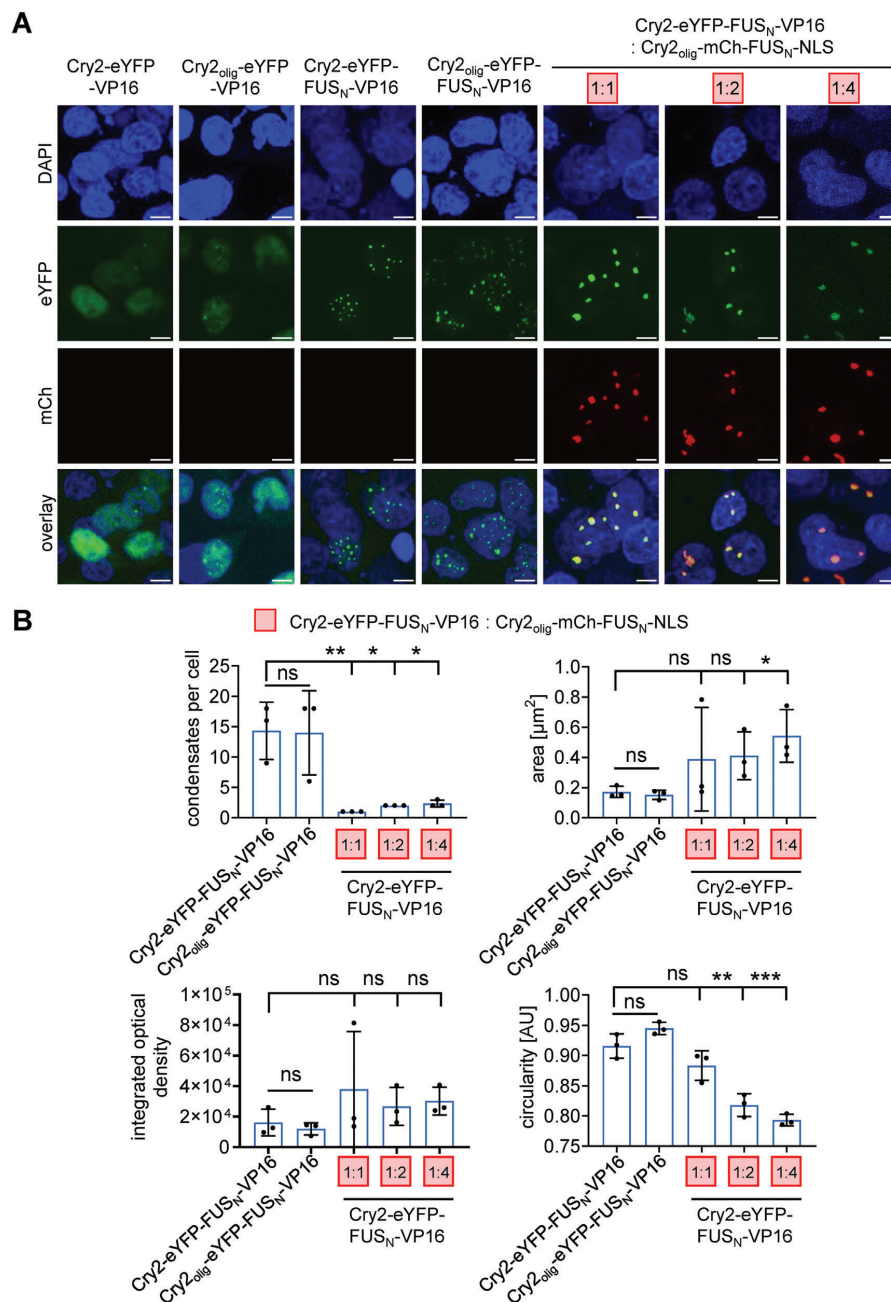


Figure 2. Microscopical characterization of the transcription factor condensates. A) Microscopy images of the condensates. HEK-293T cells were transfected with CIBN-TetR and the indicated construct combinations together with a tetO₄-based SEAP reporter (numbers in red boxes indicate the ratios of Cry2-eYFP-FUS_N-VP16 to Cry2_{olig}-mCh-FUS_N-NLS constructs). 8 h post-transfection, cells were illuminated with blue light for 72 h (2.5 $\mu\text{mol m}^{-2} \text{s}^{-1}$) and afterward analyzed by microscopy. Representative microscopy images are shown; scale bar = 5 μm . B) Quantitative analysis of the transcription

levels of Cry2_{olig}-mCh-FUS_N-NLS as a control (Figure S2, Supporting Information). Both Cry2-eYFP-FUS_N-VP16 and Cry2_{olig}-eYFP-FUS_N-VP16 yielded condensates of similar number and size. Upon the addition of Cry2_{olig}-mCh-FUS_N-NLS, the condensate number per cell was significantly decreased and further diminished with increasing the amounts of this construct. Furthermore, we observed a significant increase in the condensate area, for the highest amount of Cry2_{olig}-mCh-FUS_N-NLS. The integrated optical density of eYFP (sum of all eYFP pixel values) in the condensates did not change significantly between the conditions, suggesting similar amounts of the eYFP-containing activation domains in all conditions. With increasing amounts of Cry2_{olig}-mCh-FUS_N-NLS, we observed a dose-dependent decrease in condensate circularity. Changes in condensate morphology are often associated with distinct material properties. Whereas, circularity is considered a hallmark of liquid condensate properties, gel- or solid-like condensates with larger immobile fractions can adapt more irregular, less circular shapes. The observed decrease in circularity is therefore in agreement with previous observations (Figure 2B).^[19,33,40,41]

2.2. Altered Material Properties of Transcription Factor Condensates Affect Gene Expression Levels

To evaluate the effects of transcription factor condensates with different material properties on reporter gene expression, we analyzed transcription activity from a TetR-responsive promoter driving the expression of a secreted alkaline phosphatase (SEAP) as a reporter in HEK-293T cells. In this context, we first analyzed whether the condensates colocalized with the target promoter. To this end, we used a previously engineered U2-OS cell line with a chromosomal integration of an array of 256 repeats of the lacO operator in direct proximity to a tetO₆-responsive promoter.^[42] We stained the lacO repeats by expressing the lacO-specific binding protein LacI fused to the blue-fluorescent protein (LacI-BFP).

In the presence of the DNA-binding domain CIBN-TetR, we observed colocalization of Cry2-eYFP-FUS_N-VP16 and Cry2_{olig}-mCh-FUS_N-NLS with LacI-BFP, indicating that the transcription factor condensates were indeed localized at the promoter region (Figure 3A). The omission of the DNA-binding domain CIBN-TetR disrupted the colocalization of eYFP and mCh with the BFP-stained promoter region (Figure S3A, Supporting Information). We performed a similar experiment in HEK-293T cells using a reporter vector containing a tetO₆ and a lacO₂₅₆ array and confirmed the localization of Cry2-eYFP-FUS_N-VP16 or Cry2_{olig}-eYFP-FUS_N-VP16 with Cry2_{olig}-mCh-FUS_N-NLS at the reporter plasmids (Figure S3B, Supporting Information).

When analyzing the effect of transcription factor condensates on gene expression, potential differences in the expression levels of the different activator constructs must be considered. To ensure that the observed effects did not derive from different transcription factor expression levels, we quantified the expression levels of our eYFP-tagged transcription fac-

tors *via* flow cytometry. The observed eYFP levels are comparable between the conditions (Figure S3C, Supporting Information, eYFP expression levels). We further normalized the reporter gene activity to the flow cytometry-determined amount of transcription factor, similar to a previous study.^[10] In agreement with previous reports, Cry2-eYFP-FUS_N-VP16 yielded a 3- to fourfold increase in reporter gene expression compared to the control lacking the IDR and showing no condensate formation (Cry2-eYFP-VP16).^[10] Non-condensate-forming Cry2_{olig}-eYFP-VP16 showed 1.6-fold higher gene expression activities compared to Cry2-eYFP-VP16, likely due to increased clustering and therefore increased VP16 recruitment. Cry2_{olig}-eYFP-FUS_N-VP16 showed a 1.5-fold increase in comparison to the corresponding non-condensate-forming, FUS_N-devoid Cry2_{olig}-eYFP-VP16 construct. Interestingly, Cry2_{olig}-eYFP-FUS_N-VP16 condensates are less active than Cry2-eYFP-FUS_N-VP16 condensates and upon addition of increasing amounts of Cry2_{olig}-mCh-FUS_N-NLS to both conditions, blue-light-induced reporter expression was decreased stepwise, down to background levels (Figure 3B), although the amount of activation domains (as judged from eYFP fluorescence, Figure 2B) was unchanged. This suggests that stiff condensates of otherwise activating transcription factors, although bound to their promoter, correlate with reduced induction of transcription.

To analyze whether this principle is also functional *in vivo*, we transferred the system to mice. To this end, we first designed genetically more compact versions of the vector system to increase gene transfer efficiency in mice. We placed CIBN-TetR and Cry2-eYFP-FUS_N-VP16 on a single plasmid, either separated by posttranslational cleavage sites (T2A or a combination of T2A and P2A) or under the control of two CMV promoters in either a consecutive or bidirectional configuration (Figure S4A, Supporting Information). We tested the constructs using a SEAP reporter under the control of a TetR-responsive promoter and chose the bidirectional configuration, as it showed the highest dark-to-blue-light fold-induction, for all subsequent experiments (Figure S4B, Supporting Information). We delivered the bidirectional CIBN-TetR/Cry2-eYFP-FUS_N-VP16 construct together with a TetR-responsive luciferase reporter and increasing amounts of the Cry2_{olig}-mCh-FUS_N-NLS vector into mice *via* hydrodynamic tail vein injection. The mice were either kept in the dark or subjected to external blue light for 11 h prior to quantifying luciferase production, by whole-body bioluminescence imaging. In line with cell-culture experiments, blue light illumination activated luciferase production, which was gradually attenuated in the presence of increasing amounts of Cry2_{olig}-mCh-FUS_N-NLS (Figure 3C; Figure S4C, Supporting Information).

These results suggest that modulation of the material properties of synthetic transcription factor condensates at the promoter site by increasing valency and IDR concentration strongly impacts gene expression levels. While rather liquid condensates with a higher mobile fraction and faster recovery led to

factor condensates (only condensate forming conditions, panels 3–5). The number of condensates per cell, condensate area, integrated optical density (with regard to eYFP fluorescence), and circularity were determined. Single data points are the median of the population of one replicate, the bar represents the mean of $n = 3$ replicates \pm SD. At least 215 cells or 1619 condensates were analyzed per condition. Pairwise comparisons were performed using a Student's *t*-test ($^* = P \leq 0.05$; $^{**} = P \leq 0.01$; $^{***} = P \leq 0.001$).

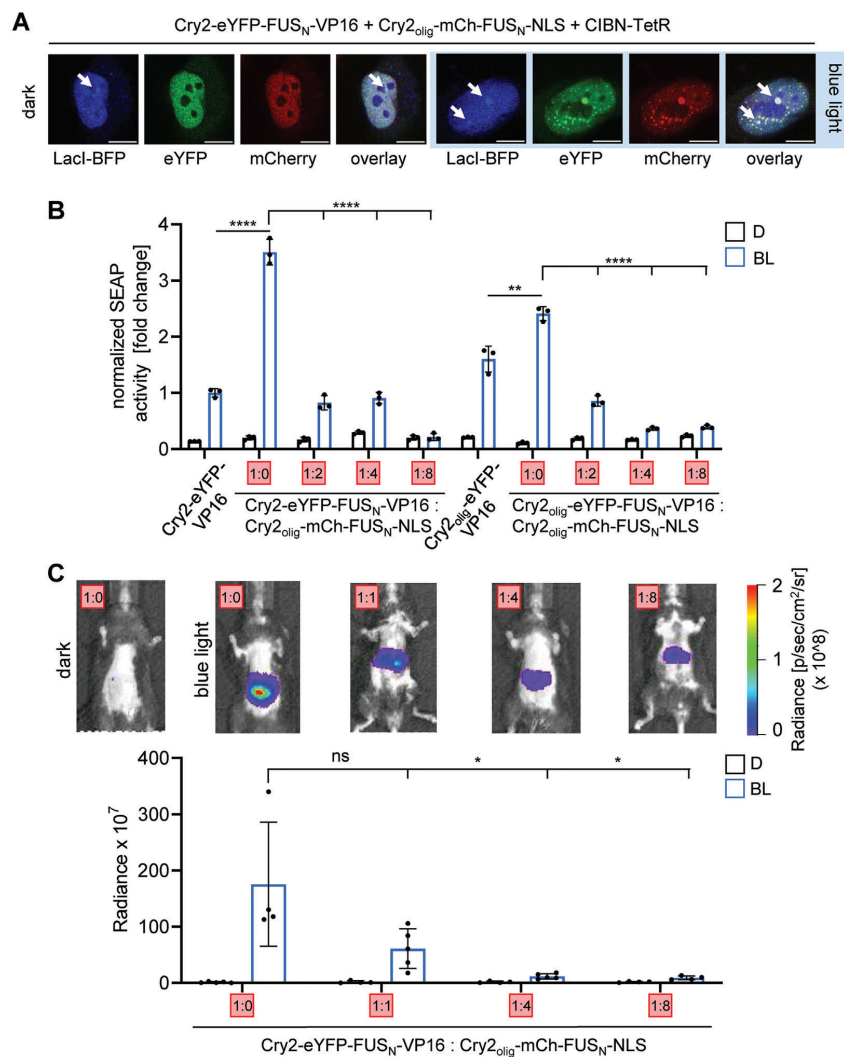


Figure 3. Influence of modified transcription factor condensate material properties on transcription. A) Colocalization of transcription factor condensates with the target promoter. U2-OS cells harboring a genomic locus with 256 lacO and 96 tetO repeats were transfected with constructs for Lacl-BFP, Cry2-eYFP-FUS_N-VP16, Cry2_{olig}-mCh-FUS_N-NLS, and CIBN-TetR. The cells were cultivated for 8 h, then illuminated for 24 h with blue light ($2.5 \mu\text{mol m}^{-2} \text{s}^{-1}$) and subjected to microscopy analysis. Scale bar = $10 \mu\text{m}$. B) Influence of transcription factor condensates on transgene expression. The indicated constructs were transfected into HEK-293T cells together with constructs for DNA-binding (CIBN-TetR) and a tetO₄-based SEAP reporter. The numbers in the red boxes indicate the approximate plasmid ratio of the VP16 to mCherry-containing constructs. Cells were cultivated for 72 h in the dark (D) or under blue light (BL, $2.5 \mu\text{mol m}^{-2} \text{s}^{-1}$) prior to quantifying SEAP and YFP production. SEAP activity values were normalized to the integrated eYFP fluorescence values of the dark samples. Data points represent the mean \pm SD ($n = 3$). C) Influence of transcription factor condensates on transgene expression in mice. Mice were hydrodynamically injected *via* the tail veins with constructs encoding CIBN-TetR and Cry2-eYFP-FUS_N-VP16 (bidirectional vector), a tetO₇-based firefly luciferase reporter, as well as the indicated ratios of Cry2_{olig}-mCh-FUS_N-NLS (red boxes, with regard to the VP16-containing construct). 8 h after plasmid injection, the mice were exposed to blue light pulses (460 nm , 10 mW cm^{-2} , 2 min on, 2 min off, alternating) for 11 h. Subsequently, luciferin was injected intraperitoneally and bioluminescence images were acquired. Mean bioluminescent radiance ($\text{p s}^{-1} \text{ cm}^{-2} \text{ sr}^{-1}$) \pm SEM is shown ($n = 4-5$) together with a representative mouse image. All pairwise comparisons were performed using a Student's *t*-test ($ns = P > 0.05$; * = $P \leq 0.05$; ** = $P \leq 0.01$; *** = $P \leq 0.001$; **** = $P \leq 0.0001$).

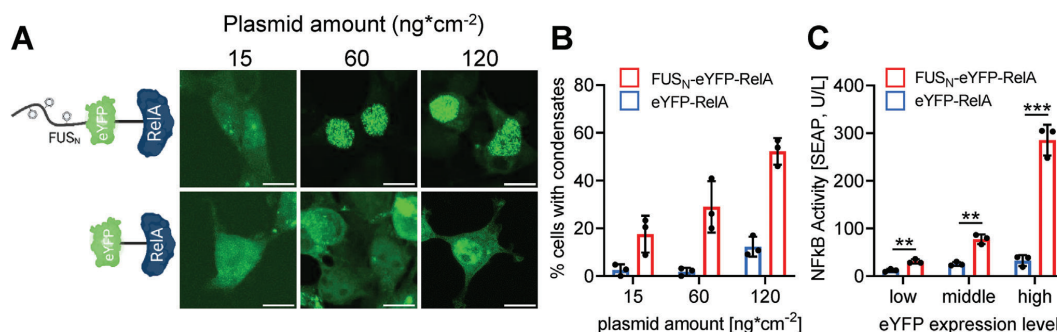


Figure 4. Influence of RelA-condensate formation on NF- κ B-responsive reporter gene expression. A) Condensate formation of RelA. Indicated amounts of expression constructs for RelA fused to eYFP and optionally FUS_N were transfected into HEK-293T cells together with an NF- κ B-responsive firefly luciferase reporter. For internal normalization, a constitutive expression vector for renilla luciferase was co-transfected. 32 h after transfection, cells were analyzed by microscopy. Scale bar = 10 μ m. Note: Minimum and maximum pixel values were adjusted differently between the panels for better visualization; quantification of the intensities is shown in Figure S5A (Supporting Information). B) Percentage of transfected cells that form at least 1 condensate. At least 103 cells per condition were analyzed. Mean percentages of $n = 3$ replicates are plotted. C) Influence of RelA condensate formation on reporter gene expression. HEK-293T cells were transfected with an NF- κ B-responsive SEAP reporter and expression plasmids for either eYFP-RelA or FUS_N-eYFP-RelA at increasing concentrations. 32 h after transfection, eYFP expression levels were determined via flow cytometry (see Figure S5B, Supporting Information). Experimental conditions with comparable eYFP expression levels (Arbitrary Units for eYFP-RelA vs. FUS_N-eYFP-RelA, respectively: low: 1 ± 0.16 vs. 1.35 ± 0.31 ; middle: 3.08 ± 0.59 vs. 3.11 ± 0.17 ; high: 14.12 ± 4.8 vs. 15.24 ± 2.54). The eYFP differences between the respective pairs are statistically not significant ($P \geq 0.05$) and were compared with regard to the amount of SEAP reporter produced. Pairwise comparisons are shown as mean \pm SD ($n = 3$). P values were calculated using a Student's t -test: ** = $P \leq 0.01$; *** = $P \leq 0.001$.

positive effects on reporter gene expression, stiffer, more dynamically arrested condensates (lower mobile fraction and slower recovery) correlated with attenuated reporter activation in mammalian cells and mice.

2.3. Impact of Condensate Formation on the Natural Transcription Factor RelA

After the characterization of our synthetic transcription factor condensates, we evaluated whether the same concept of increasing or decreasing transcription activation by modulating condensate properties could be transferred to endogenous transcription factors. We chose the transcriptional activator RelA (p65), one of the core components of the canonical NF- κ B signaling pathway.^[43]

We first started with a non-optogenetic approach by fusing RelA to eYFP (eYFP-RelA) or to FUS_N and eYFP (FUS_N-eYFP-RelA). We titrated the plasmid amounts used for transfection of HEK-293T cells and observed a dose-dependent increase in the fraction of cells that showed transcription factor condensates. Also, a low percentage of cells expressing high levels of eYFP-RelA showed the formation of clusters (Figure 4; Figure S5A, Supporting Information). We then tested the capability of the two constructs to activate transcription using an NF- κ B-responsive SEAP reporter. We titrated the plasmid amounts of eYFP-RelA and FUS_N-eYFP-RelA and quantified the eYFP expression levels via flow cytometry. To account for differences in expression levels, we compared only conditions with not significantly different eYFP expression levels and thus equal transcription factor expression levels. In agreement with the findings for the synthetic transcrip-

tion factor, condensate formation, induced by the addition of FUS_N, correlated with increased expression of the NF- κ B-responsive SEAP reporter (Figure 4C; Figure S5B, Supporting Information).

2.4. Engineering of RelA Transcription Factor Condensates with different Material Properties

Next, we evaluated the impact of light-inducible condensate stiffening on RelA activity. To this end, we fused Cry2 or Cry2_{olig} to eYFP-FUS_N-RelA and then transfected both RelA constructs (Cry2-eYFP-FUS_N-RelA or Cry2_{olig}-eYFP-FUS_N-RelA) together with Cry2_{olig}-mCh-FUS_N-NLS into HEK-293T cells. Cells were cultured in the dark or under blue light and subsequently analyzed by microscopy. Both constructs formed condensates in the dark, which might result from a combination of RelA's intrinsic property to undergo LLPS^[44] and the IDR/Cry2-containing fusion partners (Figure 5A,B). The number of condensates per cell strongly decreased upon illumination, and an increase in condensate area was observed for the Cry2_{olig} construct (Figure 5B). These findings correspond to the findings from the synthetic transcription factor (Figure 2). The eYFP integrated optical density of the condensates (reflecting the RelA amount) was similar for all conditions; only the illuminated Cry2_{olig} constructs showed an increased value. For circularity, a decrease was observed for the Cry2_{olig} constructs similar to the synthetic transcription factor, likely reflecting stiffer condensates (Figure 5B). Next, we tested the activity of the different RelA condensates on transcriptional activation using an NF- κ B-responsive dual luciferase reporter assay.^[45] When inducing Cry2/Cry2_{olig} clustering by blue light illumination, a strong drop in reporter

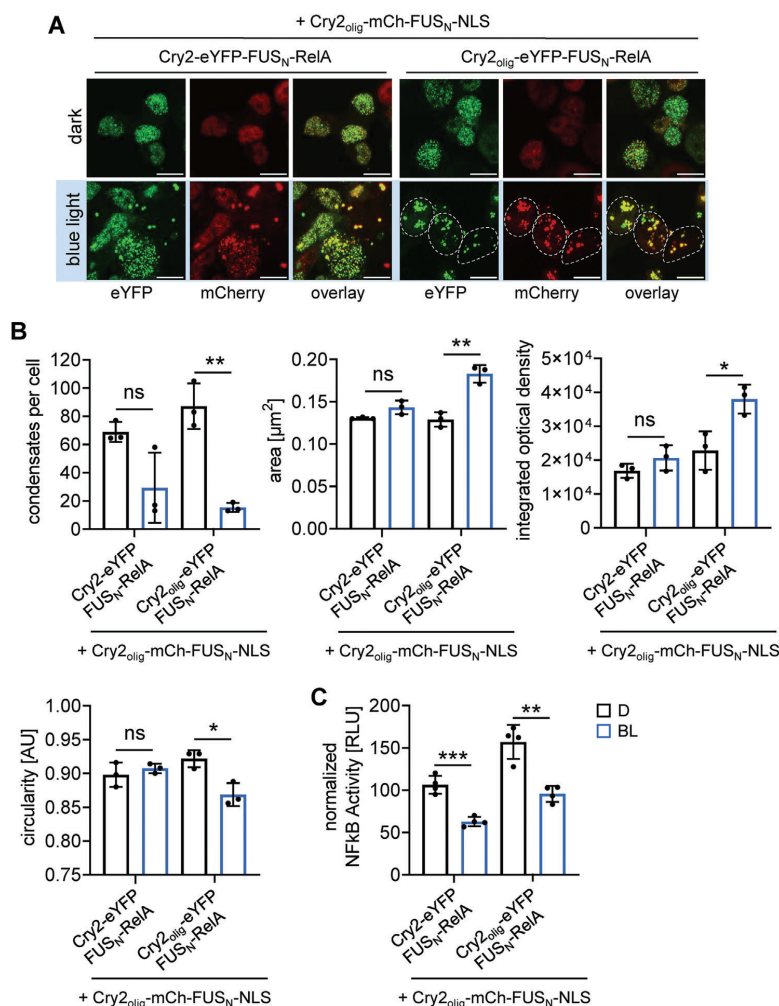


Figure 5. Optogenetic modulation of RelA-condensate material properties. A,B) Optical characterization of RelA condensates. HEK-293T cells were transfected with Cry2/Cry2_{olig}-eYFP-FUS_N-RelA, Cry2_{olig}-mCh-FUS_N-NLS, an NF- κ B-responsive firefly luciferase reporter, and a constitutive renilla luciferase reporter. 12 h post-transfection, cells were either kept in the dark or under illumination ($5 \mu\text{mol m}^{-2} \text{s}^{-1}$) for 40 h prior to microscopy analysis. The number of condensates per cell, condensate area, integrated optical density, and circularity were determined. At least 179 cells or 8219 condensates, were analyzed per condition of $n = 3$ replicates, bars represent mean \pm SD, and single data points display the median of the population of each replicate. Scale bar = $10 \mu\text{m}$. C) Influence of RelA condensates on reporter gene expression. NF- κ B-responsive firefly luciferase activity from the experiment conducted as described in A) was quantified. Values were normalized to constitutively expressed renilla luciferase activities. Means \pm SD and single values are plotted; $n = 4$. All pairwise comparisons were performed using a Student's t -test (ns = $P > 0.05$; * = $P \leq 0.05$; ** = $P \leq 0.01$; *** = $P \leq 0.001$).

gene activity was observed for both constructs. This finding is of special interest for the combination of Cry2_{olig}-eYFP-FUS_N-RelA and Cry2_{olig}-mCh-FUS_N-NLS, where the higher levels of RelA in the condensates (Figure 5B, integrated optical density) after blue-light illumination might have been expected to yield higher transcriptional activation (Figure 5C, Figure S6A, Supporting Information). Potential non-specific effects on re-

porter expression caused by the large condensates were excluded by normalizing the firefly luciferase activity with constitutively expressed renilla luciferase activity (dual luciferase assay).

We conclude from this data that stiffer transcription factor condensates (as induced here by the blue light-mediated multivalent interactions) correlate with reduced gene expression.

2.5. Downregulation of different Transcription Factor Activities by the Formation of Stiff Condensates

After demonstrating that stiff condensates of a synthetic or a natural transcription factor showed reduced gene expression, we aimed to analyze this effect more broadly by developing a strategy that allows the recruitment of different proteins into stiff condensates. For recruitment, we chose an eGFP binding nanobody (NbGFP)^[46] to capture arbitrary eGFP fusion proteins. We validated this concept by fusing NbGFP to either Cry2 or Cry2_{olig} and further inserted mCherry (mCh, for visualization), FUS_N, as well as a nuclear localization sequence (NLS, Cry2/Cry2_{olig}-mCh-FUS_N-NLS-NbGFP). We then co-transfected the construct with an eGFP-RelA expression vector and analyzed condensate formation in the dark and under blue light illumination. eGFP-RelA alone showed diffusive signals both in darkness and after blue-light illumination (Figure 6A). However, upon co-transfection with Cry2_{olig}-mCh-FUS_N-NLS and either of the NbGFP-constructs (Cry2/Cry2_{olig}-mCh-FUS_N-NLS-NbGFP), the formation of large condensates was observed upon illumination. The co-localization of the mCherry and eGFP signal in the condensates further demonstrates the effective recruitment of eGFP-RelA into the condensates.

When analyzing luciferase expression under the control of an NF- κ B-responsive promoter, a significant decrease in luciferase activity was observed under illumination compared to the dark control, with the effect being stronger for the Cry2_{olig}-based construct. This finding is in line with the previous observations and demonstrates the functionality of the recruitment-based approach for an inducible decrease in RelA-responsive gene expression (Figure 6B).

Next, we aimed at validating this approach with STAT3 and STAT6 transcription factors. To challenge the system, we used mutants with increased activity (STAT3_{Y640F}^[47] and STAT6_{V547A/T548A}^[48]) compared to the wild type. We co-transfected expression constructs for Cry2_{olig}-mCh-FUS_N-NLS-NbGFP and Cry2_{olig}-mCh-FUS_N-NLS with either STAT3_{Y640F}-eGFP or eGFP-STAT6_{V547A/T548A} vectors together with a STAT3- or STAT6-responsive luciferase reporter. The cells were further stimulated with interleukin 6 (IL-6) or interleukin 4 (IL-4) to activate STAT3 and STAT6 signaling pathways, respectively. The cells were subsequently incubated in the dark or under blue light prior to measuring luciferase activity. Upon co-transfection with the condensate-forming constructs, a 1.4- and 1.8-fold decrease in reporter output was observed for STAT3_{Y640F}-eGFP and eGFP-STAT6_{V547A/T548A} under blue light compared to the dark control, respectively (Figure 6C,D; Figure S6B,C, Supporting Information).

To confirm the binding of eGFP-RelA, STAT3_{Y640F}-eGFP, and eGFP-STAT6_{V547A/T548A} to the reporter vectors, we inserted their respective response elements into the above-described reporter vector containing the lacO₂₅₆ array. We observed colocalization of eGFP, mCherry, and BFP, suggesting that the transcription factors within the condensates are still capable of binding to DNA (Figure S7, Supporting Information).

Additionally, we tested the influence of stiff condensate formation on the transcriptional inhibitory p50 homodimer, which acts downstream of the canonical NF- κ B signaling pathway and represses transcription when bound to its target promoter.^[49] We

transfected HEK-293T cells with the NF- κ B-responsive luciferase reporter. Stimulation with TNF- α resulted in high luciferase output. This activity was strongly reduced upon co-transfection of an eGFP-p50 construct. Upon further co-transfection with Cry2_{olig}-mCh-FUS_N-NLS-NbGFP and Cry2_{olig}-mCh-FUS_N-NLS and illumination with blue light, a further 1.8-fold decrease in reporter output was observed compared to the dark control, indicating that the formation of a stiff condensate led to further strengthened transcriptional inhibition. This further indicates the sustained binding of p50 to the promoter site after stiff condensate formation, as higher luciferase activities would have been expected if the inhibitor was detached (Figure 6E; Figure S8, Supporting Information).

From these observations, we conclude that optogenetically formed, stiff condensates of activating or inhibitory transcription factors can likely be used as a broadly applicable strategy to downregulate gene expression in response to light.

2.6. Light-Controlled Downregulation of Endogenous Promoters by Stiff Condensate Formation

While all experiments above were performed with synthetic reporters as readout, we finally investigated whether the same effect could be observed for endogenous promoters, at the example of NF- κ B-responsive promoters. To this aim, we transfected HEK-293T cells either with empty vector or eGFP-RelA or eGFP-RelA, Cry2_{olig}-mCh-FUS_N-NLS-NbGFP and Cry2_{olig}-mCh-FUS_N-NLS. The cells were cultivated under blue light or in the dark prior to the extraction of total mRNA and analysis by RNAseq. For data analysis, we established a suitable threshold ($|\log_2FC| > 0.5$) and considered only genes that were deregulated more strongly. This eliminated genes that were only marginally deregulated, for example, due to minor differences in the cultivation conditions in darkness and blue light (Table S1; Figure S9, Supporting Information). Next, we filtered for genes that were previously reported to be induced by NF- κ B signaling^[50] and therefore could be bound and activated by eGFP-RelA, and affected by the condensate formation at their promoter. This step should exclude genes that were not bound by eGFP-RelA but are secondarily deregulated, for example, due to the deregulation of eGFP-RelA targets that are positive or negative regulators themselves (Table S1, Supporting Information). With this method, we obtained 15 genes that were significantly deregulated between the empty vector and eGFP-RelA conditions AND deregulated between darkness and blue light of the condensate condition (eGFP-RelA, Cry2_{olig}-mCh-FUS_N-NLS-NbGFP and Cry2_{olig}-mCh-FUS_N-NLS, Figures S10 and S11, Supporting Information). Indeed, all 15 genes were upregulated by eGFP-RelA and downregulated by condensate formation (Figure 7). Furthermore, we confirmed the deregulation of three of these genes (*TNFAIP3*, *NFKBIA*, and *CXCL1*) via qPCR and observed an up to 4.4-fold decrease in endogenous gene expression after condensate formation under illumination compared to the dark control (Figure S12, Supporting Information). The number of 15 specifically deregulated NF- κ B target genes was lower than expected, which might result, for example, from cell line specific or compensatory mechanisms of endogenous feedback mechanisms.^[51,52]

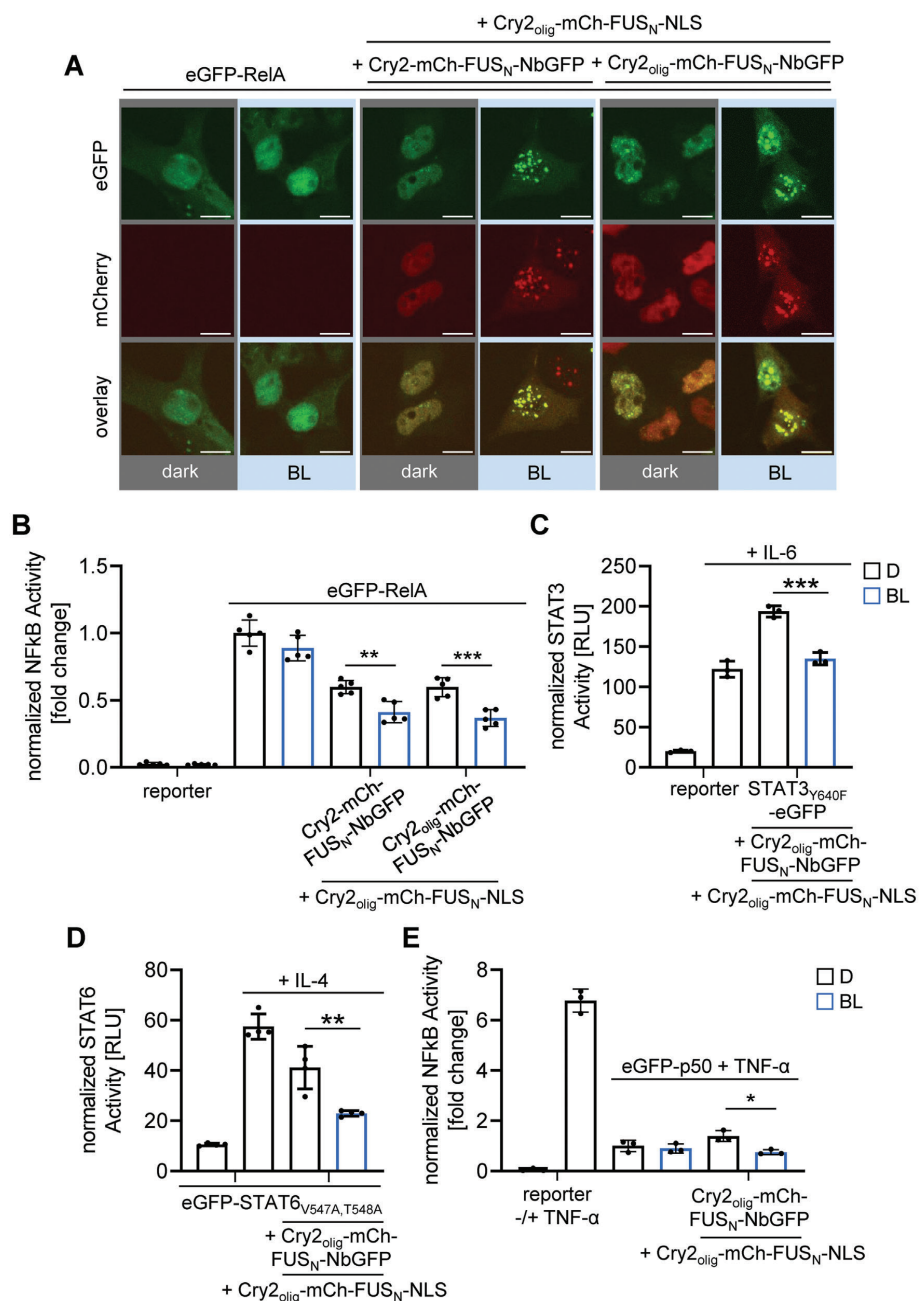


Figure 6. Influence of the formation of different transcription factors condensates on transcription activation. A) Nanobody-mediated formation of RelA condensates. HEK-293T cells were transfected with the indicated expression vectors: an NF- κ B-responsive firefly luciferase expression vector as well as a constitutive renilla luciferase construct. 8 h after transfection, cells were kept in the dark (D) or under blue light (BL) illumination ($5 \mu\text{mol m}^{-2} \text{s}^{-1}$) for 24 h prior to microscopy analysis. Scale bar = 10 μm . B) Impact of RelA condensates on NF- κ B-responsive gene expression. Cells were transfected

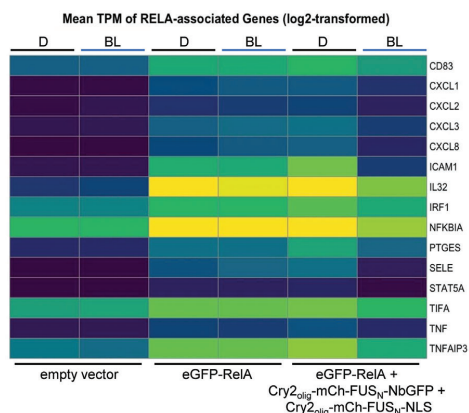


Figure 7. Impact of stiff eGFP-RelA condensates on endogenous gene expression. HEK-293T cells were transfected with the indicated expression vectors and an NF- κ B-responsive SEAP reporter. 8 h after transfection, cells were either kept in the dark (D) or under blue light illumination (BL, $5 \mu\text{mol m}^{-2} \text{s}^{-1}$) for 24 h prior to RNA extraction. Total RNA samples were subjected to RNAseq. Datasets of triplicates were pooled and 15 direct targets of eGFP-RelA were identified. Genes with a q -value ≤ 0.05 and $|\log_2\text{FC}| > 0.5$ were considered significantly deregulated. The heatmap shows their \log_2 -transformed, mean transcripts expression levels in units of kilobase million (TPM).

In conclusion, these findings further corroborate the above-described data and support the hypothesis that optogenetically induced stiff transcription factor condensates at promoter sites lead to light-inducible downregulation of transcription factor activity at synthetic and endogenous promoters (Figure 7).

3. Conclusion

Recent gene activation models suggest important roles for phase separation in the control of gene expression.^[21,53] The IDRs of cofactors, transcription factors or polymerase II mediate phase separation and thereby, effective recruitment and concentration of cofactors and activators into transcriptional condensates.^[54–56] Furthermore, condensates are capable of reconfiguring chromatin interactions to access enhancer regions through DNA looping, enabling long-range communication.^[57,58] However, the functional impact of transcriptional condensates on gene expression levels remained inconclusive. Some groups reported positive effects^[9,10,26] likely due to a higher concentration of transactivation domains at promoter regions^[27] or increased recruitment of activating cofactors.^[56] Other groups reported no additional effect in comparison to a multivalent but non-phase-

separating transcription factor^[28] or an optimum of IDRs at the promoter to achieve maximum expression levels, whereas higher IDR levels that led to condensate formation had negative effects.^[29,59] Further studies suggested mechanisms such as the reduced capability of transcription factor IDRs to recruit mediators due to changes in their sequence,^[60,61] recruitment of proteins that alter the surface tension and therefore reduce DNA binding capacity^[62,63] or sequestration of transcription factors in the cytoplasm^[64] to be involved in the downregulation of gene expression.

To investigate whether changing the material properties of transcription factor condensates could impact gene expression levels, we developed an optogenetic strategy to induce transcription factor condensates and modified their material properties by the modular addition of Cry2_{olig}-mCh-FUS_N-NLS, which increased the IDR concentration and might act as a multivalent scaffold in line with a very recent study by Hernandez-Candia *et al.*^[33] We characterized their material properties and morphology and linked them to different levels of gene expression. We observed that liquid condensates have a positive effect on gene expression in comparison to diffusive transcription factors, whereas stiffer promoter-bound transcription factor condensates result in reduced transcription. We linked functional properties to certain morphological hallmarks: stiffer condensates correlated with lower circularity, a larger area, and a lower number per cell. Inhibition of gene expression occurred despite the equal or increased transcription factor amounts within the condensates, as indicated by the fluorescent intensities of the condensates. The data on the synthetic TetR-VP16-based droplet-transcription factor and the RelA-condensates suggested that rather liquid condensates led to increased gene expression levels in comparison to diffuse transcription factors, whereas stiffer, more dynamically arrested condensates reversed this effect and led to reduced transcription activation.

The colocalization study (Figure 3A; Figures S3A,B and S7, Supporting Information) confirmed the localization of the condensates at the promoter. The smaller changes in the system, like the mutation of Cry2 to Cry2_{olig}, resulted in reduced gene expression but did not lead to morphological changes (Figure 3B, the difference between Cry2-eYFP-FUS_N-VP16 and Cry2_{olig}-eYFP-FUS_N-VP16-induced reporter gene expression, although no changes in condensate morphology or condensate number were observed (Figure 2)). A possible reason for the reduced transcriptional activity of Cry2_{olig}-eYFP-FUS_N-VP16 could be the decreased dynamics and apparent diffusion coefficient that were measured by FRAP (Figure 1).^[30,31] The larger morphological changes that occurred with Cry2_{olig}-mCh-FUS_N-NLS addition might facilitate additional inhibitory mechanisms, such as blocking the access of activating factors to endogenous promoters, due to their larger size.

as described in (A) and firefly luciferase activity was measured. Values were normalized to renilla luciferase activities. Means \pm SD and single values are plotted; values are displayed as fold changes to eGFP-RelA (dark condition). C,D) Impact of STAT3_{V640F} / STAT6_{V547A,T548A} condensates on STAT3/6-responsive gene expression. The experiment was performed as described in (A), except that eGFP-RelA was exchanged by eGFP-STAT3_{V640F} (C) or STAT6_{V547A,T548A} (D). Cells were stimulated with 5 ng mL^{-1} IL-6 or 10 ng mL^{-1} IL-4 for STAT3_{V640F} and STAT6_{V547A,T548A} experiments, respectively. E) Impact of p50 condensates on NF- κ B-responsive gene expression. The experiment was performed as described in (A), except that eGFP-RelA was exchanged by eGFP-p50. The cells were further stimulated with 5 ng mL^{-1} TNF- α , 8 h after transfection. Mean \pm SD is displayed as a fold change to eGFP-p50 (dark condition). $n = 3–5$, pairwise comparisons were performed using a Student's t -test ($^* = P \leq 0.05$; $^{**} = P \leq 0.01$; $^{***} = P \leq 0.001$).

Light is a powerful stimulus to modify protein interactions non-invasively,^[65–67] and the incorporation of the eGFP-binding nanobody enabled us to apply our system by facilitating the incorporation of arbitrary eGFP-tagged proteins into biomolecular condensates. The constructs can be used to probe protein behavior in different phase-separated conditions by modular modification of the condensate material properties, such as exchanging Cry2 with Cry2_{olig} or adding Cry2_{olig}-mCh-FUS_N-NLS.

In conclusion, we present a designer approach for the modulation of the material properties of biomolecular transcription factor condensates. We link them to distinct biological outputs using the example of transcriptional activation. We believe that the rational design of biomolecular transcription factor condensates with defined properties will enable new avenues that allow for controlling and tuning of cellular processes or the implementation of new functions. The approach presented here is likely transferable to probe and control the function of other proteins and processes in different directions of fundamental and applied research.

4. Experimental Section

Cloning: All plasmids in this study were cloned via Gibson Assembly^[68] or Aqua Cloning^[69] and are described in Table S1 (Supporting Information). Mutations and short sequences, such as linkers, were inserted with oligonucleotides and PCR. For constructs that contain multiple repeats (promoter response elements and double vectors containing two CMV promoters), *E. coli* were grown at room temperature or a maximum of 30 °C. All NF- κ B and STAT3-related reporters and templates for PCR amplification of NF- κ B and STAT3 signaling proteins were a kind gift from the laboratory of Bodo Grimbacher (Institute for Immunodeficiency, Freiburg). All sequences were confirmed by Sanger sequencing.

Illumination: All optogenetic experiments in 96-well format were conducted in black clear-bottom plates (μ CLEAR, Greiner Bio-One, catalog no. 655090) and illuminated using the optoPlate-96^[70] equipped with 470 nm LEDs (Würth Elektronik, MPN: 150141RB73100) that was programmed using the optoConfig-96.^[71] Experiments in 24- or 6-well format were illuminated with micro-controller-regulated illumination panels containing LEDs with 460 nm (LED Engin, MPN: LZ1-10B202-0000). For live cell imaging, illumination was conducted directly at the confocal microscope using a pE-4000 LED light source (460 nm, CoolLED, Andover, UK). All samples that express photosensitive proteins were handled under dim, green, safe light to avoid unwanted photoreceptor activation.

Cell Culture and Transfection: HEK-293T (DSMZ, catalog no. ACC 635) and U2OS 2-6-3^[42] cells were cultivated in Dulbecco's modified Eagle's medium (DMEM, PAN Biotech, catalog no. P04-03550) completed with fetal calf serum (FCS, 10% (v/v), PAN Biotech, catalog no. P30-3602) and penicillin-streptomycin (1% (v/v), PAN Biotech, catalog no. P06-07100) at 37 °C and 5% CO₂. They were passaged every 2–3 days after reaching a confluency of \approx 80%. For experiments, cells were seeded into multi-well plates and transfected with polyethyleneimine (PEI, 1 mg/mL in H₂O, pH 7, Polyscience, catalog no. 23966-1). Therefore, DNA and PEI were prepared separately, each in half of the total volume Opti-MEM (Thermo Fisher Scientific, catalog no. 22600-134). The two approaches were mixed, immediately vortexed for 15 s, and incubated for 15 min at room temperature. DNA/PEI mixes were then applied dropwise to the cells. Cells transfected for optogenetic experiments were then kept in darkness. If indicated, cells were stimulated 8 h after transfection with TNF- α (Merck, catalog no. H8916-10UG), IL-6 (Preprotech, catalog no. 200-06) or IL-4 (produced as previously described)^[72]. Concentrations are indicated in the figure legends. Exact plasmid combinations and amounts for each experiment are listed in Table S2 (Supporting Information).

Reporter Assays: All reporter assays (SEAP and dual-luciferase) were performed in 96-well plates (non-optogenetic experiments: Corning, cat-

alog no. 3596; optogenetic experiments: μ CLEAR, Greiner Bio-One, catalog no. 655090). 15,000 cells per well in 100 μ L DMEM were seeded 20–24 h prior to transfection. For transfection, 125 ng DNA and 0.41 μ L polyethyleneimine in 20 μ L Opti-MEM per well were used. For optogenetic experiments, illumination was started 8–12 h after transfection, and the assays were conducted 24–72 h after transfection, as indicated for each experiment. For the readout, either a Synergy 4 multimode microplate reader (BioTek Instruments Inc.), an Infinite 200Pro microplate reader (Tecan Trading AG), or a SpectraMax iD5 microplate reader (Molecular Devices GmbH) was used.

For firefly/renilla dual luciferase assays, cells were lysed by the addition of 100 μ L lysis buffer (25 mM Tris HCl⁻¹, pH 7.8, 1% Triton X-100 (v/v), 15 mM MgSO₄, 4 mM ethylene glycol tetraacetic acid (EGTA), 1 mM DTT) per well. After 5 min of incubation at room temperature (RT), cells were resuspended and split into 2 \times 40 μ L samples by transferring them into two white flat-bottom 96-well plates (Corning Incorporated, catalog no. CORN3912). The plates were spun down for 30 s at 1200 rpm to remove all bubbles. One plate was used for firefly luciferase measurement by addition of 20 μ L firefly substrate (0.47 mM luciferin in 20 mM Tricine, 2.67 mM MgSO₄, 0.1 mM EDTA, 33.3 mM DTT, 0.52 mM ATP, 0.27 mM Acetyl-CoA, 5 mM NaOH, 0.264 mM MgCO₃) per well and the other plate was used for renilla luciferase measurement by addition of 20 μ L coelenterazine (stock: 472 μ M coelenterazine in methanol; diluted 1:10 in PBS directly before measurement) per well. Both plates were measured immediately after substrate addition (program: 10 s shaking, 1000 ms integration time, endpoint measurement). Firefly values were normalized with background-subtracted renilla values.

For SEAP activity measurement, the whole supernatant was transferred into a U-bottom transparent 96-well plate (Carl Roth, catalog no. 9291.1), sealed with adhesive tape, and heated at 65 °C for 30 min. Afterward, samples were spun down for 3 min at 1250 rpm, then 80 μ L supernatant was added to 100 μ L 2x SEAP buffer (21% (v/v) diethanolamine, 20 mM L-homoarginine-hydrochloride, 1 mM MgCl₂ (pH 9.8)) in transparent flat-bottom 96-well plates (Carl Roth, catalog no. 9293.1). Directly prior to the measurement, 20 μ L para-nitrophenyl phosphate solution (pNPP, 120 mM) was added and its conversion to para-nitrophenol by SEAP was measured by absorbance at 405 nm in time intervals of 1 min. SEAP activity was calculated as described previously.^[73]

Flow Cytometry: For comparison between different constructs in reporter assays, the expression levels of the fluorescent proteins in each construct were determined by flow cytometry. Therefore, the medium was removed and cells were detached with 50 μ L trypsin/EDTA solution (PAN Biotech, catalog no. P10-023500) per well. Afterward, 150 μ L PBS supplemented with FCS (2% (v/v)) was added and cells were carefully resuspended and transferred into a transparent U-bottom 96-well plate (Greiner, catalog no. 650161). Cells were kept on ice until measurement with an Attune NxT flow (Thermo–Fisher Scientific). EGFP and eYFP were measured by excitation with a 488 nm laser and detected with a 530/30 nm emission filter (BL1) and mCherry was measured with a 561 nm excitation laser and a 620/15 nm emission filter (YL2). 15,000 cells per well were analyzed at a flow rate of 200 μ L min⁻¹. Analysis was performed using the FlowJo_v10 software. To obtain the expression levels of the eYFP-tagged transcription factor, singlets were gated and then the integrated eYFP intensity (count of singlet population multiplied by the mean eYFP fluorescence intensity of the singlet population) was calculated and used for normalization.^[10]

Microscopy and Image Analysis: For microscopy of fixed samples, coverslips (Carl Roth, catalog no. YX03.2) were placed in 24-well plates (Corning, catalog no. CORN3524) and coated with 500 μ L rat tail collagen I (Thermo–Fisher Scientific, catalog no. A1048301) at a concentration of 50 μ g mL⁻¹ diluted in 25 mM acetic acid. After 1 h of incubation at RT, the wells were washed three times with 500 μ L PBS, and 75,000 cells per well were seeded. For transfection in 24-well format, 750 ng DNA and 2.4 μ L PEI in 100 μ L OptiMEM per well were used. Illumination of optogenetic experiments was started after 8 h for time periods as indicated in the figure legends. Cells were fixed by removing the medium and adding 200 μ L methanol-free paraformaldehyde (PFA, Science Services, catalog no. E15714-S; 4% diluted in PBS (v/v)) under green safe light. After 15 min of incubation at RT in darkness, PFA was removed and cells were washed

twice with 500 μL PBS. For staining of the nuclei, 500 μL 4',6'-diamidino-2-phenylindole (DAPI, 0.2 $\mu\text{g mL}^{-1}$, Merck, catalog no. D9542) in PBS was added for 15 min at RT, then cells were washed again twice with 500 μL PBS and mounted on microscopy slides with 8.5 μL Mowiol mounting medium (2.4 g Mowiol, 6 g glycerol, 6 mL of H_2O and 12 mL of Tris/HCl (pH 8.5)). After the samples were dried, the edges were additionally fixed with transparent nail polish. All images and time series were acquired with a Zeiss LSM 880 laser scanning confocal microscope using a 63x Plan-Apochromat oil objective (NA 1.4) in z-stacks with a distance of 1 μm . DAPI was imaged with the 405 nm laser, eGFP and eYFP were excited with the 488 nm laser, and mCherry with the 561 nm laser. For colocalization experiments, only one focal plane is shown.

For quantitative image analysis, at least 2 images per replicate of a total of 3 replicates were acquired. Z-stacks were reduced to 2D maximum intensity projections. The percentage of cells that form droplets was determined by first segmenting and counting the transfected cells and then manually counting the cells with droplets. For analysis of the droplet properties, nuclei and droplets were segmented and analyzed using custom-written macros for ImageJ 2.3.0/1.53q including the Biovoxxel Toolbox v2.6.0.^[74] A threshold for a minimum 1 droplet per cell with a size of at least 0.017 μm^2 (7 pixels) was set. For droplet intensity, the RawIndDen (sum of all pixel values of the droplet) was used. All macro outputs were manually double-checked. If not stated otherwise, minimum and maximum pixel values of a channel were adjusted equally for all samples of an experiment. In overlay images, intensities may be adjusted differently for better visualization of all channels.

FRAP measurements were conducted in 35 mm glass bottom dishes (μ -Dish 35 mm, high, Ibdid cat. No. 81156) using a Tokai Hit stage top incubator under continuous illumination with the pE-4000 CoolLED (460 nm, 5 $\mu\text{mol m}^{-2} \text{s}^{-1}$). Time series of at least 300 s were acquired as z-stacks of nine focal planes with a distance of 600 nm, an interval of every 5 s, and a zoom factor of six. Four eYFP droplets were selected simultaneously with regions of interest (ROI) of $\approx 0.8 \mu\text{m}$ diameter and bleached after the first z-stack was acquired, using 100% laser power of the 488 nm laser. For analysis, droplets were manually tracked with a circular mask of constant diameter in the x, y, and z directions for 300 s. Afterward, background signals were subtracted and droplet recovery was corrected for photobleaching by normalization with the linear regression of the average fluorescence signal decrease of the nuclei. Values were normalized to the intensity before and directly after bleaching. Mobile fractions were calculated by fitting the recovery curves to an exponential plateau equation ($Y = Y_M \cdot (Y_M - Y_0) \cdot \exp(-k \cdot t) + Y_0$), Y_M = maximum population/mobile fraction, Y_0 = starting population, k = time rate constant) using GraphPad Prism 9.2.0. Half-maximum recovery time ($t_{1/2}$) and the apparent diffusion coefficient were calculated from the curve fits of the mean recovery curves, with the formulas $t_{1/2} = \ln(2)/k$ and $D_{\text{app}} = r_{\text{bleach}}^2 / (1/k)$ with a bleaching radius $r_{\text{bleach}} = 0.4 \mu\text{m}$, as previously reported.^[35,54] Please note, that we did not calculate D_{app} for curves that showed less than 20% recovery and therefore reflect extremely low dynamics leading to unreliable k values in the curve fit.

RNA Extraction and Reverse Transcription Quantitative PCR (RT-qPCR): For RNA extractions, 600,000 cells/well were seeded onto 6-well plates (Corning, catalog no. CORN3516) and 24 h later transfected with 600 μL transfection mix containing 3.750 μg total DNA and 12.375 μL PEI per well. Blue-light illumination (460 nm, 5 $\mu\text{mol m}^{-2} \text{s}^{-1}$) was started 8 h after transfection. Cells were harvested 24 h later using 1 mL TriFast (VWR, cat. no. 30–2010) per well. Total RNA was extracted according to the manufacturer's protocol. RNA integrity was verified on an agarose gel and concentrations, 260/280 and 230/280 ratios were determined with a nanodrop 1000 (Thermo–Fisher Scientific).

Reverse transcription was performed using the High Capacity Kit (Applied Biosystems, cat. no. 4368814) according to the manufacturer's protocol using 2 μg RNA. The resulting cDNA was diluted 1:20 and used for qPCR. The primers for the three NF- κ B target genes were selected from literature (NFKB1A, oAF469: 5'- ATGTCAATGCTCAGGAGCCCC-3' and oAF470: 5'-GACATCAGCCCCACTTCA-3',^[75] TNFAIP3, oAF467: 5'-CGTCCAGGTTCCAGAACCATTCC-3' and oAF468: 5'- TGGCCTGGCTCCATCTCAGTTG-3',^[76] CXCL1, oAF471: 5'-AACCGAAGTCATA-

GCCACAC-3' and oAF472: 5'-GTTGGATTGTCACTGTTCCAGC-3',^[77]) and GUS was used as housekeeping gene (oMH703/oAF481, 5'-CGTCCACCTAGAATCTGCT-3' and oMH702/oAF482, 5'-TTGCTCACAAAGGTCACAGG-3'). qPCRs were conducted with a CFX384 Touch Real-Time PCR Detection System (BioRad) in 10 μL approaches with the PowerTrack SYBR Green Mastermix (Applied Biosystems, cat. no. A46110) according to the manufacturer's protocol (fast cycling mode with default dissociation step). $\Delta\Delta\text{Ct}$ analysis was performed with the means of three technical replicates and the housekeeping gene GUS. Data is displayed as fold-changes to the eGFP-RelA containing control. Single data points display the biological replicates.

RNAseq: Sample Preparation: Experimental procedure and total RNA extraction were performed as described in section 4.7. Additionally, RNA was cleaned up using an RNeasy Mini Kit (Qiagen, cat. no. 74104) according to the manufacturer's protocol, including an on-column DNase I digest using 50 μL reactions of DNase I (New England Biolabs, cat. no. M0303). RNA integrity was verified at BGI Tech Solutions (Hong Kong) Co. using a Bioanalyzer (Agilent 2100 Bioanalyzer).

Pre-Processing: RNA-seq libraries from the 18 samples were sequenced by BGI Tech Solutions on a DNBSEQ platform using paired-end chemistry with a read length of 100 base pairs each. Each strand was sequenced across two separate lanes, generating a total of 4 FASTQ files per sample. FASTQ files were obtained from BGI and subsequently quality-controlled using FASTQC.^[78,79]

After verifying that there were no quality issues specific to individual lanes, the reads from the strand-specific sequencing replicates were pooled together. This was done to improve the accuracy and depth of coverage. After this, samples had two FASTQ files each – one for each strand.

FASTQC reported < 0.1% adapter contamination across all samples. Cutadapt^[80] was used for adapter trimming. Quality trimming was done using Q = 30 as a threshold to filter out low-quality bases using bbduk.sh from the BBMap suite.^[81] Length filtering was done using reformat.sh (BBMap) to filter out reads shorter than 50 bp.

Quantification and DGE Analysis: Transcript quantification was done using Kallisto.^[82] The reference transcriptome was obtained from Genecode (Release 38).^[83] Sleuth^[84] was used to process the transcript abundances generated by Kallisto to perform differential gene expression analysis. By setting the gene_mode parameter to TRUE while creating a sleuth object, the quantification data from the transcript level was aggregated to the gene level to perform gene-level differential expression analysis. Sleuth offers two methods to test for differential expression. The default, Likelihood Ratio Test (LRT), assesses the probability of the data under the “full” and “reduced” models. The full model assumes that gene abundances are influenced by exposure to blue light or darkness. The reduced model assumes that the treatment has no effect on gene abundance. After estimating the ratio of the two likelihoods, it returns a test statistic with its p-value. Genes with FDR-adjusted p-value < 0.05 were considered significantly differentially expressed. The Wald Test uses the full model to test whether the coefficients associated with the conditions are significantly different from zero. In this context, each coefficient represented the effect of a specific condition (darkness/ blue light exposure) on the expression of the gene. The coefficients can be treated as estimates of fold changes. To enhance the robustness of the analysis, we designated the genes detected as significantly differentially expressed by both the LRT and Wald tests as true positives. For instance, in the volcano plots, the true positive deregulated NF- κ B target genes^[50] are marked in red. The orange points (genes) above the significance threshold were considered false positives since they were reported by the Wald Test as significantly differentially expressed but not by the LRT.

Identification of direct targets of eGFP-RelA: A large list of deregulated genes was identified (Table S1, Supporting Information). To distinguish between direct and indirect NF- κ B targets, this list was compared to a list of 409 NF- κ B target genes compiled by the Gilmore lab.^[50] This list includes target genes of the NF- κ B family and genes that have a kB domain in the promoter region for potential NF- κ B binding but have not directly been shown to be targeted. Furthermore, genes with a low deregulation $\log_2\text{FC}$ ($|\log_2\text{FC}| < 0.5$) were excluded to filter out potential effects that derive from illumination or that are subject to

compensatory effects. RNAseq data is available in the BioStudies database (<http://www.ebi.ac.uk/biostudies>) under the accession number E-MTAB-13905.

Mouse Experiments: All the animals were obtained from the ECNU Laboratory Animal Centre, kept on a standard alternating 12-h light/12-h dark cycle, and given a normal chow diet (6% fat and 18% protein (wt/wt)) and water. Wild-type C57BL/6 mice (6-week-old, male) were randomly divided into four groups. The mice were hydrodynamically injected in their tail vein with a total amount of 330 μg in 2 mL (10% of the body weight in grams) of Ringer's solution (147 mM NaCl, 4 mM KCl, and 1.13 mM CaCl_2) within 3–5 s. Plasmid combinations are described in Table S2 (Supporting Information). 8 h after injection, the mice were exposed to blue light pulses (460 nm, 10 mW cm^{-2} , 2 min on, 2 min off alternating; Shenzhen Kiwi Lighting Co. Ltd.) for 11 h. The control mice were kept in the dark. For in vivo bioluminescence imaging, each mouse was intraperitoneally injected with luciferin substrate solution (150 mg kg^{-1} ; luc001, Shanghai Sciencelight Biology Science & Technology) under ether anesthesia. 5 min after luciferin injection, bioluminescence images of the mice were acquired using the IVIS Lumina II in vivo imaging system (Perkin Elmer, USA). Radiance ($\text{p s}^{-1} \text{cm}^{-2} \text{sr}^{-1}$) values were calculated for the region of interest using the Living Image 4.3.1 software.

Software: All analyses were performed with Microsoft Excel 2016 and GraphPad Prism 9.2.0. Flow cytometry data was analyzed with FlowJo_v10 and image analysis was done with ImageJ 2.3.0/1.53q including the Biovoxxel Toolbox v2.6.0.^[74] The bioluminescent mouse images were analyzed with the Living Image 4.3.1 software. VENN diagrams were generated using the InteractiVenn tool.^[85] All schemes were created with BioRender.com.

Statistics: FRAP analysis, and all bar plots from SEAP, luciferase assay, flow cytometry, or image analysis present means \pm SD. Sample size n is indicated in each figure legend. Single datapoints are displayed for all assays. Microscopy data sets were tested for normal distribution using GraphPad Prism 9.2.0. Single data points here represent the median of the not-normally distributed population of condensates or cells for each parameter (size, circularity etc.). Normalizations were performed as described in the respective figure legends.

Pairwise comparisons were performed using a two-tailed t -test with Microsoft Excel 2016 or GraphPad Prism 9.2.0. Statistical significance was considered when $P \leq 0.05$. Different P values are encoded as follows: * = $P \leq 0.05$; ** = $P \leq 0.01$; *** = $P \leq 0.001$; **** = $P \leq 0.0001$. Processing and analysis of the RNAseq data is described in detail in the experimental section 4.8.

Ethics: The experiments involving animals were approved by the East China Normal University (ECNU) Animal Care and Use Committee and in direct accordance with the Ministry of Science and Technology of the People's Republic of China on Animal Care guidelines. The protocol (protocol ID: m20221109) was approved by the ECNU Animal Care and Use Committee. All animals were euthanized after the termination of the experiments.

Supporting Information

Supporting Information is available from the Wiley Online Library or from the author.

Acknowledgements

The authors are very grateful to M. Klenzendorf and D. Gaspar for their excellent technical assistance and to L. Qiao for excellent assistance in animal work. The authors thank all members of the Weber laboratory for their helpful comments, especially N. Schneider, M. Hörner, and O. Thomas for valuable advice. The authors would like to thank the Faculty of Biology technical workshop for the construction of the illumination devices. The authors acknowledge the excellent scientific and technical assistance of the Signalling Factory Core Facility staff of the Albert-Ludwigs-University Freiburg for help on flow cytometry, especially P. Salavei and

N. Gensch. The authors acknowledge the staff of the Life Imaging Center (LIC) in the Center for Biological Systems Analysis (ZBSA) of the Albert-Ludwigs-University Freiburg for their help with microscopy resources and their excellent support in microscopy setup and image acquisition. This work was supported by the European Union (ERC, STEADY, 101053857), the German Research Foundation (Deutsche Forschungsgemeinschaft, DFG) under Germany's Excellence Strategy – CIBSS, EXC-2189, Project ID: (390939984) and under the Excellence Initiative of the German Federal and State Governments – BIOSS, EXC-294, and in part by the Ministry for Science, Research and Arts of the state of Baden-Württemberg. This work was also partially supported by the National Natural Science Foundation of China (NSFC: no.32250010, no.32261160373, no.31971346) to H.Y.

Open access funding enabled and organized by Projekt DEAL.

Conflict of Interest

The authors declare no conflict of interest.

Data and Materials Availability

The data that support the findings of this study are available from the corresponding author upon reasonable request.

Keywords

biomolecular condensates, liquid-liquid phase separation, material properties of protein condensates, optogenetics, synthetic biology

Received: February 29, 2024

Revised: March 22, 2024

Published online:

- [1] S. F. Banani, H. O. Lee, A. A. Hyman, M. K. Rosen, *Nat. Rev. Mol. Cell Biol.* **2017**, *18*, 285.
- [2] A. S. Lyon, W. B. Peeples, M. K. Rosen, *Nat. Rev. Mol. Cell Biol.* **2021**, *22*, 215.
- [3] Y. Dai, L. You, A. Chilkoti, *Nat. Rev. Bioeng.* **2023**, *1*, 466.
- [4] Y. Miao, M. Heidari, S. Mikhaleva, P. S. Tan, S. Mingu, H. Ruan, C. D. Reinkemeier, A. Obarska-Kosinska, M. Siggel, M. Beck, G. Hummer, E. Lemke, *Nature* **2023**, *617*, 162.
- [5] H. Guo, J. C. Ryan, X. Song, A. Mallet, M. Zhang, V. Pabst, A. L. Decrulle, P. Ejsmont, E. H. Wintermute, A. B. Lindner, *Cell* **2022**, *185*, 3823.
- [6] E. M. Zhao, N. Suek, M. Z. Wilson, E. Dine, N. L. Pannucci, Z. Gitai, J. L. Avalos, J. E. Toettcher, *Nat. Chem. Biol.* **2019**, *15*, 589.
- [7] Y. Shin, Y.-C. C. Chang, D. S. W. Lee, J. Berry, D. W. Sanders, P. Ronceray, N. S. Wingreen, M. Haataja, C. P. Brangwynne, *Cell* **2018**, *175*, 1481.
- [8] J. M. Eeftens, M. Kapoor, D. Michieletto, C. P. Brangwynne, *Nat. Commun.* **2021**, *12*, 5888.
- [9] M.-T. Wei, Y.-C. Chang, S. F. Shimobayashi, Y. Shin, A. R. Strom, C. P. Brangwynne, *Nat. Cell Biol.* **2020**, *22*, 1187.
- [10] N. Schneider, F. G. Wieland, D. Kong, A. A. M. M. Fischer, M. Hörner, J. Timmer, H. Ye, W. Weber, *Sci. Adv.* **2021**, *7*, eabd3568.
- [11] M. Kato, T. W. Han, S. Xie, K. Shi, X. Du, L. C. Wu, H. Mirzaei, E. J. Goldsmith, J. Longgood, J. Pei, N. V. Grishin, D. E. Frantz, J. W. Schneider, S. Chen, L. Li, M. R. Sawaya, D. Eisenberg, R. Tycko, S. L. McKnight, *Cell* **2012**, *149*, 753.

- [12] T. W. Han, M. Kato, S. Xie, L. C. Wu, H. Mirzaei, J. Pei, M. Chen, Y. Xie, J. Allen, G. Xiao, S. L. McKnight, *Cell* **2012**, *149*, 768.
- [13] A. Molliex, J. Temirov, J. Lee, M. Coughlin, A. P. Kanagaraj, H. J. Kim, T. Mittag, J. P. Taylor, *Cell* **2015**, *163*, 123.
- [14] A. Patel, H. O. Lee, L. Jawerth, S. Maharana, M. Jahnel, M. Y. Hein, S. Stoynov, J. Mahamid, S. Saha, T. M. Franzmann, A. Pozniakovski, I. Poser, N. Maghelli, L. A. Royer, M. Weigert, E. W. Myers, S. Grill, D. Drechsel, A. A. Hyman, S. Alberti, *Cell* **2015**, *162*, 1066.
- [15] S. Qamar, G. Wang, S. J. Randle, T. Knowles, M. Vendruscolo, P. S. George-hyslop, S. Qamar, G. Wang, S. J. Randle, F. S. Ruggeri, J. A. Varela, *Cell* **2018**, *173*, 720.
- [16] J. Wang, J. M. Choi, A. S. Holehouse, H. O. Lee, X. Zhang, M. Jahnel, S. Maharana, R. Lemaître, A. Pozniakovski, D. Drechsel, I. Poser, R. V. Pappu, S. Alberti, A. A. Hyman, *Cell* **2018**, *174*, 688.
- [17] W. T. Snead, A. S. Gladfelter, *Mol. Cell* **2019**, *76*, 295.
- [18] B. Tsang, I. Pritišanac, S. W. Scherer, A. M. Moses, J. D. Forman-Kay, *Cell* **2020**, *183*, 1742.
- [19] Y. Shin, J. Berry, N. Pannucci, M. P. Haataja, J. E. Toettcher, C. P. Brangwynne, *Cell* **2017**, *168*, 159.
- [20] D. Bracha, M. T. Walls, M.-T. Wei, L. Zhu, M. Kurian, J. L. Avalos, J. E. Toettcher, C. P. Brangwynne, *Cell* **2018**, *175*, 1467.
- [21] D. Hnisz, K. Shrinivas, R. A. Young, A. K. Chakraborty, P. A. Sharp, *Cell* **2017**, *169*, 13.
- [22] S. Chong, C. Dugast-Darzacq, Z. Liu, P. Dong, G. M. Dailey, C. Cattoglio, A. Heckert, S. Banala, L. Lavis, X. Darzacq, R. Tjian, *Science* **2018**, *361*, eaar2555.
- [23] A. Boija, I. A. Klein, B. R. Sabari, A. Dall'Agnesse, E. L. Coffey, A. V. Zamudio, C. H. Li, K. Shrinivas, J. C. Manteiga, N. M. Hannett, B. J. Abraham, L. K. Afeyan, Y. E. Guo, J. K. Rimel, C. B. Fant, J. Schuijers, T. I. Lee, D. J. Taatjes, R. A. Young, *Cell* **2018**, *175*, 1842.
- [24] J. E. Henninger, O. Oksuz, K. Shrinivas, I. Sagi, G. LeRoy, M. M. Zheng, J. O. Andrews, A. V. Zamudio, C. Lazaris, N. M. Hannett, T. I. Lee, P. A. Sharp, I. I. Cissé, A. K. Chakraborty, R. A. Young, *Cell* **2021**, *184*, 207.
- [25] T. Hirose, K. Ninomiya, S. Nakagawa, T. Yamazaki, *Nat. Rev. Mol. Cell Biol.* **2023**, *24*, 288.
- [26] J. Wu, B. Chen, Y. Liu, L. Ma, W. Huang, Y. Lin, *Nat. Commun.* **2022**, *13*, 2663.
- [27] D. A. Garcia, T. A. Johnson, D. M. Presman, G. Fettweis, K. Wagh, L. Rinaldi, D. A. Stavreva, V. Paakinaho, R. A. M. Jensen, S. Mandrup, A. Upadhyaya, G. L. Hager, *Mol. Cell* **2021**, *81*, 1484.
- [28] J. Trojanowski, L. Frank, A. Rademacher, N. Mücke, P. Rigaitis, K. Rippe, *Mol. Cell* **2022**, *82*, 1878.
- [29] S. Chong, T. G. W. Graham, C. Dugast-Darzacq, G. M. Dailey, X. Darzacq, R. Tjian, *Mol. Cell* **2022**, *82*, 2084.
- [30] B. Shi, W. Li, Y. Song, Z. Wang, R. Ju, A. Ulman, J. Hu, F. Palomba, Y. Zhao, J. P. Le, W. Jarrard, D. Dimoff, *Nature* **2021**, *597*, 726.
- [31] W. Li, J. Hu, B. Shi, F. Palomba, M. A. Digman, E. Gratton, *Nat. Cell Biol.* **2020**, *22*, 960.
- [32] Z. Wang, J. Lou, H. Zhang, *J. Biol. Chem.* **2022**, *298*, 101782.
- [33] C. N. Hernandez-Candia, B. R. Brady, E. Harrison, C. L. Tucker, *Nat. Chem. Biol.* **2024**, *20*, 452.
- [34] C. Guo, Z. Luo, C. Lin, *Biochemistry* **2022**, *61*, 2456.
- [35] S. J. Nair, L. Yang, D. Meluzzi, S. Oh, F. Yang, M. J. Friedman, S. Wang, T. Suter, I. Alshareedah, A. Gamliel, Q. Ma, J. Zhang, Y. Hu, Y. Tan, K. A. Ohgi, R. S. Jayani, P. R. Banerjee, A. K. Aggarwal, M. G. Rosenfeld, *Nat. Struct. Mol. Biol.* **2019**, *26*, 193.
- [36] S. Alberti, A. A. Hyman, *Nat. Rev. Mol. Cell Biol.* **2021**, *22*, 196.
- [37] Z. Wang, D. Chen, D. Guan, X. Liang, J. Xue, H. Zhao, G. Song, J. Lou, Y. He, H. Zhang, *J. Cell Biol.* **2022**, *221*, e202112024.
- [38] A. Rademacher, F. Erdel, J. Trojanowski, S. Schumacher, K. Rippe, *J. Cell Sci.* **2017**, *130*, 4213.
- [39] A. Taslimi, J. D. Vrana, D. Chen, S. Borinskaya, B. J. Mayer, M. J. Kennedy, C. L. Tucker, *Nat. Commun.* **2014**, *5*, 4925.
- [40] Y. Gao, X. Li, P. Li, **2022**, *18*, 1307.
- [41] S. Alberti, A. Gladfelter, T. Mittag, *Cell* **2019**, *176*, 419.
- [42] S. M. Janicki, T. Tsukamoto, S. E. Salghetti, W. P. Tansey, R. Sachidanandam, K. V. Prasanth, T. Ried, Y. Shav-Tal, E. Bertrand, R. H. Singer, D. L. Spector, T. Tsukamoto, T. Ried, Y. Shav-Tal, R. H. Singer, E. Bertrand, *Cell* **2004**, *116*, 683.
- [43] A. Oeckinghaus, S. Ghosh, *Cold Spring Harb. Perspect. Biol.* **2009**, *1*, a000034.
- [44] J. N. Wibisana, T. Inaba, H. Shinohara, N. Yumoto, T. Hayashi, M. Umeda, M. Ebisawa, I. Nikaido, Y. Sako, M. Okada, *PLoS Genet.* **2022**, *18*, e1010235.
- [45] P. Schneider, L. Willen, C. R. Smulski, *Methods Enzymol.* **2014**, *545*, 103.
- [46] A. Kirchofer, J. Helma, K. Schmidthals, C. Frauer, S. Cui, A. Karcher, M. Pellis, S. Muyldermans, C. S. Casas-Delucchi, C. Cardoso, H. Leonhardt, K.-P. Hopfner, U. Rothbauer, *Nat. Struct. Mol. Biol.* **2009**, *17*, 133.
- [47] R. Mori, J. Wauman, L. Icardi, J. Van Der Heyden, L. De Cauwer, F. Peelman, K. De Bosscher, J. Tavernier, *Sci. Rep.* **2017**, *7*, 1.
- [48] C. Daniel, A. Salvekar, U. Schindler, *J. Biol. Chem.* **2000**, *275*, 14255.
- [49] M. S. Hayden, S. Ghosh, *Genes Dev.* **2004**, *18*, 2195.
- [50] Boston University, "NF- κ B Gene Resources: Target Genes," can be found under, <https://www.bu.edu/nf-kb/gene-resources/target-genes/>, (accessed: October 2023).
- [51] F. Renner, M. L. Schmitz, *Trends Biochem. Sci.* **2009**, *34*, 128.
- [52] J. A. Prescott, J. P. Mitchell, S. J. Cook, *Biochem. J.* **2021**, *478*, 2619.
- [53] P. Bhat, D. Honson, M. Guttman, *Nat. Rev. Mol. Cell Biol.* **2021**, *22*, 653.
- [54] B. R. Sabari, A. D. Agnesse, A. Boija, I. A. Klein, E. L. Coffey, B. J. Abraham, N. M. Hannett, A. V. Zamudio, J. C. Manteiga, C. H. Li, Y. E. Guo, D. S. Day, J. Schuijers, E. Vasile, S. Malik, D. Hnisz, T. I. Lee, I. I. Cisse, R. G. Roeder, P. A. Sharp, A. K. Chakraborty, R. A. Young, *Science* **2018**, *3958*, eaar3958.
- [55] W. Cho, J. Spille, M. Hecht, C. Lee, C. Li, V. Grube, I. I. Cisse, *Science* **2018**, *361*, 412.
- [56] L. Ma, Z. Gao, J. Wu, B. Zhong, Y. Xie, W. Huang, Y. Lin, *Mol. Cell* **2021**, *81*, 1682.
- [57] Y. J. Kim, M. L. Jr, Y. Lee, J. Jing, J. T. Sanders, G. A. Botten, L. He, J. Lyu, Y. Zhang, M. Mettlen, P. Ly, Y. Zhou, J. Xu, *Sci. Adv.* **2023**, *9*, eadg1123.
- [58] K. Shrinivas, B. R. Sabari, E. L. Coffey, I. A. Klein, A. Boija, A. V. Zamudio, J. Schuijers, N. M. Hannett, P. A. Sharp, R. A. Young, A. K. Chakraborty, *Mol. Cell* **2019**, *75*, 549.
- [59] L. Song, X. Yao, H. Li, B. Peng, A. P. Boka, Y. Liu, G. Chen, Z. Liu, K. M. Mathias, L. Xia, Q. Li, M. Mir, Y. Li, H. Li, L. Wan, *Mol. Cell* **2022**, *82*, 4080.
- [60] S. Basu, S. D. Mackowiak, H. Niskanen, D. Knezevic, V. Asimi, S. Grosswendt, H. Geertsema, S. Ali, I. Jerković, H. Ewers, S. Mundlos, A. Meissner, D. M. Ibrahim, D. Hnisz, *Cell* **2020**, *181*, 1062.
- [61] W. Li, H. Jiang, *J. Mol. Biol.* **2022**, *434*, 167151.
- [62] Z. Wang, C. Yang, D. Guan, J. Li, H. Zhang, *Dev. Cell* **2023**, *58*, 919.
- [63] M. Takla, S. Keshri, D. C. Rubinsztein, *EMBO Rep.* **2023**, *24*, e57574.
- [64] F. Jobe, J. Simpson, P. Hawes, E. Guzman, D. Bailey, *J. Virol.* **2020**, *94*, e01380.
- [65] A. A. M. Fischer, M. M. Kramer, G. Radziwill, W. Weber, *Curr. Opin. Chem. Biol.* **2022**, *70*, 102196.
- [66] K. Kolar, C. Knobloch, H. Stork, M. Žnidarič, W. Weber, *ACS Synth. Biol.* **2018**, *7*, 1825.
- [67] K. Kolar, W. Weber, *Curr. Opin. Biotechnol.* **2017**, *47*, 112.

- [68] D. G. Gibson, L. Young, R. Y. Chuang, J. C. Venter, C. A. Hutchison, H. O. Smith, *Nat. Methods* **2009**, *6*, 343.
- [69] H. M. Beyer, P. Gonschorek, S. L. Samodelov, M. Meier, W. Weber, M. D. Zurbriggen, *PLoS One* **2015**, *10*, e0137652.
- [70] L. J. Bugaj, W. A. Lim, *Nat. Protoc.* **2019**, *14*, 2205.
- [71] O. S. Thomas, M. Hörner, W. Weber, *Nat. Protoc.* **2020**, *15*, 2785.
- [72] H. M. Beyer, O. S. Thomas, N. Riegel, M. D. Zurbriggen, W. Weber, M. Hörner, *Acta Biomater.* **2018**, *79*, 276.
- [73] S. Schlatter, M. Rimann, J. Kelm, M. Fussenegger, *Gene* **2002**, *282*, 19.
- [74] J. Brocher, "BioVoxel Toolbox v2.6.0," can be found under, <https://zenodo.org/record/8214743>, (accessed: August 2023).
- [75] A. Callegari, C. Sieben, A. Benke, D. M. Suter, B. Fierz, D. Mazza, S. Manley, *PLoS Genet.* **2019**, *15*, e1007891.
- [76] X. Jiang, H. Tian, Y. Fan, J. Chen, Y. Song, S. Wang, F. Zhu, C. Guo, L. Zhang, Y. Shi, *Clin. Vaccine Immunol.* **2012**, *19*, 1938.
- [77] D. Wang, H. Wang, J. Brown, T. Daikoku, W. Ning, Q. Shi, A. Richmond, R. Strieter, S. K. Dey, R. N. DuBois, *J. Exp. Med.* **2006**, *203*, 941.
- [78] S. Andrews, F. Krueger, A. Segonds-Pichon, L. Biggins, C. Krueger, S. Wingett, "FastQC", can be found under, <https://github.com/s-andrews/FastQC>, (accessed: October 2023).
- [79] P. Ewels, M. Magnusson, S. Lundin, M. Käller, *Bioinformatics* **2016**, *32*, 3047.
- [80] M. Martin, *EMBnet. J.* **2011**, *17*, 10.
- [81] B. Bushnell, "BBMap: A Fast, Accurate, Splice-Aware Aligner.", can be found under, <https://www.osti.gov/servlets/purl/11241166>, (accessed: October 2023).
- [82] N. L. Bray, H. Pimentel, P. Melsted, L. Pachter, *Nat. Biotechnol.* **2016**, *34*, 525.
- [83] GENCODE Consortium, "Genome v38 Transcriptome", can be found under, <https://www.gencodegenes.org/human/>, (accessed: October 2023).
- [84] H. Pimentel, N. L. Bray, S. Puente, P. Melsted, L. Pachter, *Nat. Methods* **2017**, *14*, 687.
- [85] R. Heberle, H. Meirelles, G. V. Silva, F. R. Telles, G. P. Minghim, *BMC Bioinformatics* **2015**, *16*, 169.

Bibliography

- [1] Holly V. Goodson and Erin M. Jonasson. “Microtubules and Microtubule-Associated Proteins”. In: *Cold Spring Harbor Perspectives in Biology* 10.6 (Jan. 6, 2018). Company: Cold Spring Harbor Laboratory Press Distributor: Cold Spring Harbor Laboratory Press Institution: Cold Spring Harbor Laboratory Press Label: Cold Spring Harbor Laboratory Press Publisher: Cold Spring Harbor Lab, a022608. ISSN: , 1943-0264. DOI: 10.1101/cshperspect.a022608. URL: <http://cshperspectives.cshlp.org/content/10/6/a022608> (visited on 10/14/2024).
- [2] April L. Risinger and Lin Du. “Targeting and extending the eukaryotic druggable genome with natural products: cytoskeletal targets of natural products”. In: *Natural Product Reports* 37.5 (May 1, 2020), pp. 634–652. ISSN: 1460-4752. DOI: 10.1039/c9np00053d.
- [3] Thomas D. Pollard. “Actin and Actin-Binding Proteins”. In: *Cold Spring Harbor Perspectives in Biology* 8.8 (Jan. 8, 2016). Company: Cold Spring Harbor Laboratory Press Distributor: Cold Spring Harbor Laboratory Press Institution: Cold Spring Harbor Laboratory Press Label: Cold Spring Harbor Laboratory Press Publisher: Cold Spring Harbor Lab, a018226. ISSN: , 1943-0264. DOI: 10.1101/cshperspect.a018226. URL: <http://cshperspectives.cshlp.org/content/8/8/a018226> (visited on 10/21/2024).
- [4] Matthias Schaks, Grégory Giannone, and Klemens Rottner. “Actin dynamics in cell migration”. In: *Essays in Biochemistry* 63.5 (Sept. 24, 2019), pp. 483–495. ISSN: 0071-1365. DOI: 10.1042/EBC20190015. URL: <https://doi.org/10.1042/EBC20190015> (visited on 08/23/2024).
- [5] Tim Lämmermann and Ronald N. Germain. “The multiple faces of leukocyte interstitial migration”. In: *Seminars in Immunopathology* 36.2 (Mar. 1, 2014), pp. 227–251. ISSN: 1863-2300. DOI: 10.1007/s00281-014-0418-8. URL: <https://doi.org/10.1007/s00281-014-0418-8> (visited on 06/26/2023).
- [6] Roshia Ali et al. “Jasplakinolide Attenuates Cell Migration by Impeding Alpha-1-syntrophin Protein Phosphorylation in Breast Cancer Cells”. In: *The Protein Journal*

- 40.2 (Apr. 1, 2021), pp. 234–244. ISSN: 1875-8355. DOI: 10.1007/s10930-021-09963-y. URL: <https://doi.org/10.1007/s10930-021-09963-y> (visited on 08/23/2024).
- [7] Louise P. Cramer. “Role of actin-filament disassembly in lamellipodium protrusion in motile cells revealed using the drug jasplakinolide”. In: *Current Biology* 9.19 (Oct. 7, 1999). Publisher: Elsevier, pp. 1095–1105. ISSN: 0960-9822. DOI: 10.1016/S0960-9822(99)80478-3. URL: [https://www.cell.com/current-biology/abstract/S0960-9822\(99\)80478-3](https://www.cell.com/current-biology/abstract/S0960-9822(99)80478-3) (visited on 08/23/2024).
- [8] G. S. Ou, Z. L. Chen, and M. Yuan. “Jasplakinolide reversibly disrupts actin filaments in suspension-cultured tobacco BY-2 cells”. In: *Protoplasma* 219.3 (May 1, 2002), pp. 168–175. ISSN: 1615-6102. DOI: 10.1007/s007090200018. URL: <https://doi.org/10.1007/s007090200018> (visited on 08/23/2024).
- [9] A. G. Bodnar et al. “Extension of life-span by introduction of telomerase into normal human cells”. In: *Science (New York, N.Y.)* 279.5349 (Jan. 16, 1998), pp. 349–352. ISSN: 0036-8075. DOI: 10.1126/science.279.5349.349.
- [10] Vera L. Bonilha. “Retinal pigment epithelium (RPE) cytoskeleton *in vivo* and *in vitro*”. In: *Experimental Eye Research*. Retinal pigment epithelial cell culture: Current standards and technical criteria for model systems 126 (Sept. 1, 2014), pp. 38–45. ISSN: 0014-4835. DOI: 10.1016/j.exer.2013.09.015. URL: <https://www.sciencedirect.com/science/article/pii/S0014483513002819> (visited on 10/21/2024).
- [11] Yan-Jun Liu et al. “Confinement and Low Adhesion Induce Fast Amoeboid Migration of Slow Mesenchymal Cells”. In: *Cell* 160.4 (Feb. 12, 2015), pp. 659–672. ISSN: 0092-8674. DOI: 10.1016/j.cell.2015.01.007. URL: <https://www.sciencedirect.com/science/article/pii/S0092867415000082> (visited on 05/11/2023).
- [12] Carsten Baltés et al. “Actin stabilization in cell migration”. In: *Frontiers in Cell and Developmental Biology* 10 (Aug. 11, 2022). Publisher: Frontiers. ISSN: 2296-634X. DOI: 10.3389/fcell.2022.931880. URL: <https://www.frontiersin.org/journals/cell-and-developmental-biology/articles/10.3389/fcell.2022.931880/full> (visited on 07/05/2024).
- [13] Steven J. Collins, Robert C. Gallo, and Robert E. Gallagher. “Continuous growth and differentiation of human myeloid leukaemic cells in suspension culture”. In: *Nature* 270.5635 (Nov. 1977). Publisher: Nature Publishing Group, pp. 347–349. ISSN: 1476-4687. DOI: 10.1038/270347a0. URL: <https://www.nature.com/articles/270347a0> (visited on 10/21/2024).
- [14] G. D. Birnie. “The HL60 cell line: a model system for studying human myeloid cell differentiation”. In: *The British Journal of Cancer. Supplement* 9 (Dec. 1988), p. 41. URL: <https://pmc.ncbi.nlm.nih.gov/articles/PMC2149104/> (visited on 10/21/2024).

- [15] Michael Mihlan et al. “Neutrophils: Amoeboid Migration and Swarming Dynamics in Tissues”. In: *Frontiers in Cell and Developmental Biology* 10 (Apr. 11, 2022). Publisher: Frontiers. ISSN: 2296-634X. DOI: 10.3389/fcell.2022.871789. URL: <https://www.frontiersin.org/journals/cell-and-developmental-biology/articles/10.3389/fcell.2022.871789/full> (visited on 07/25/2024).
- [16] George J. Todaro and Howard Green. “QUANTITATIVE STUDIES OF THE GROWTH OF MOUSE EMBRYO CELLS IN CULTURE AND THEIR DEVELOPMENT INTO ESTABLISHED LINES”. In: *Journal of Cell Biology* 17.2 (May 1, 1963), pp. 299–313. ISSN: 0021-9525. DOI: 10.1083/jcb.17.2.299. URL: <https://doi.org/10.1083/jcb.17.2.299> (visited on 10/27/2024).
- [17] Melissa M. St Amand, John A. Hanover, and Joseph Shiloach. “A comparison of strategies for immortalizing mouse embryonic fibroblasts”. In: *Journal of Biological Methods* 3.2 (May 23, 2016). Number: 2 Publisher: POL Scientific, p. 1. ISSN: TBA. DOI: 10.14440/jbm.2016.110. URL: <https://polscientific.com/journal/JBM/3/2/10.14440/jbm.2016.110> (visited on 10/27/2024).
- [18] Mengfei Chen et al. “Role of MEF feeder cells in direct reprogramming of mousetail-tip fibroblasts”. In: *Cell Biology International* 33.12 (Dec. 1, 2009). Publisher: John Wiley & Sons, Ltd, pp. 1268–1273. ISSN: 1095-8355. DOI: 10.1016/j.cellbi.2009.06.004. URL: <https://onlinelibrary.wiley.com/doi/10.1016/j.cellbi.2009.06.004> (visited on 10/27/2024).
- [19] Shengli Dong, Mazvita Maziveyi, and Suresh K. Alahari. “Primary Tumor and MEF Cell Isolation to Study Lung Metastasis”. In: *Journal of Visualized Experiments : JoVE* 99 (May 20, 2015), p. 52609. DOI: 10.3791/52609. URL: <https://pmc.ncbi.nlm.nih.gov/articles/PMC4542731/> (visited on 10/27/2024).
- [20] Szymon Janyga et al. “CD4+ cells in autoimmune thyroid disease”. In: *Endokrynologia Polska* 72.5 (2021). Number: 5, pp. 572–583. ISSN: 2299-8306. DOI: 10.5603/EP.a2021.0076. URL: https://journals.viamedica.pl/endokrynologia_polska/article/view/EP.a2021.0076 (visited on 10/21/2024).
- [21] **Karen Anne-Marie Ullrich et al. “IL-3 receptor signalling suppresses chronic intestinal inflammation by controlling mechanobiology and tissue egress of regulatory T cells”. In: *Gut* 72.11 (Nov. 1, 2023). Publisher: BMJ Publishing Group Section: Inflammatory bowel disease, pp. 2081–2094. ISSN: 0017-5749, 1468-3288. DOI: 10.1136/gutjnl-2023-329818. URL: <https://gut.bmj.com/content/72/11/2081> (visited on 07/05/2024).**
- [22] Ricardo Piña et al. “Ten Approaches That Improve Immunostaining: A Review of the Latest Advances for the Optimization of Immunofluorescence”. In: *International Journal of Molecular Sciences* 23.3 (Jan. 2022). Number: 3 Publisher: Multidisciplinary Digital Publishing Institute, p. 1426. ISSN: 1422-0067. DOI: 10.3390/ijms23031426. URL: <https://www.mdpi.com/1422-0067/23/3/1426> (visited on 10/08/2024).

- [23] Nicholas APS Buss et al. “Monoclonal antibody therapeutics: history and future”. In: *Current Opinion in Pharmacology*. Anti-infectives • New technologies 12.5 (Oct. 1, 2012), pp. 615–622. ISSN: 1471-4892. DOI: 10.1016/j.coph.2012.08.001. URL: <https://www.sciencedirect.com/science/article/pii/S1471489212001488> (visited on 10/08/2024).
- [24] Virginia Bayer. “An Overview of Monoclonal Antibodies”. In: *Seminars in Oncology Nursing*. Immunotherapy in Oncology 35.5 (Oct. 1, 2019), p. 150927. ISSN: 0749-2081. DOI: 10.1016/j.soncn.2019.08.006. URL: <https://www.sciencedirect.com/science/article/pii/S0749208119301093> (visited on 10/08/2024).
- [25] Michael D. Huber and Larry Gerace. “The size-wise nucleus: nuclear volume control in eukaryotes”. In: *The Journal of Cell Biology* 179.4 (Nov. 19, 2007), pp. 583–584. ISSN: 1540-8140, 0021-9525. DOI: 10.1083/jcb.200710156. URL: <https://rupress.org/jcb/article/179/4/583/45049/The-size-wise-nucleus-nuclear-volume-control-in> (visited on 10/04/2024).
- [26] Teresa A. Larsen et al. “The Structure of DAPI Bound to DNA”. In: *Journal of Biomolecular Structure and Dynamics* 7.3 (Dec. 1, 1989). Publisher: Taylor & Francis _eprint, pp. 477–491. ISSN: 0739-1102. DOI: 10.1080/07391102.1989.10508505. URL: <https://doi.org/10.1080/07391102.1989.10508505> (visited on 10/04/2024).
- [27] Debapriya Banerjee and Samir Kumar Pal. “Dynamics in the DNA Recognition by DAPI: Exploration of the Various Binding Modes”. In: *The Journal of Physical Chemistry B* 112.3 (Jan. 1, 2008). Publisher: American Chemical Society, pp. 1016–1021. ISSN: 1520-6106. DOI: 10.1021/jp077090f. URL: <https://doi.org/10.1021/jp077090f> (visited on 10/04/2024).
- [28] Jan Kapuscinski. “DAPI: a DNA-Specific Fluorescent Probe”. In: *Biotechnic & Histochemistry* 70.5 (Jan. 1, 1995). Publisher: Taylor & Francis _eprint, pp. 220–233. ISSN: 1052-0295. DOI: 10.3109/10520299509108199. URL: <https://doi.org/10.3109/10520299509108199> (visited on 10/04/2024).
- [29] Daniele Zink, Nicolas Sadoni, and Ernst Stelzer. “Visualizing chromatin and chromosomes in living cells”. In: *Methods* 29.1 (Jan. 1, 2003), pp. 42–50. ISSN: 1046-2023. DOI: 10.1016/S1046-2023(02)00289-X. URL: <https://www.sciencedirect.com/science/article/pii/S104620230200289X> (visited on 10/04/2024).
- [30] Jonas Bucevičius, Gražvydas Lukinavičius, and Rūta Gerasimaitė. “The Use of Hoechst Dyes for DNA Staining and Beyond”. In: *Chemosensors* 6.2 (June 2018). Number: 2 Publisher: Multidisciplinary Digital Publishing Institute, p. 18. ISSN: 2227-9040. DOI: 10.3390/chemosensors6020018. URL: <https://www.mdpi.com/2227-9040/6/2/18> (visited on 10/04/2024).

- [31] Alexander Belyy et al. “Structure of the Lifeact–F-actin complex”. In: *PLOS Biology* 18.11 (Nov. 20, 2020). Publisher: Public Library of Science, e3000925. ISSN: 1545-7885. DOI: 10.1371/journal.pbio.3000925. URL: <https://journals.plos.org/plosbiology/article?id=10.1371/journal.pbio.3000925> (visited on 10/02/2024).
- [32] Sabrina Pospich, Felipe Merino, and Stefan Raunser. “Structural Effects and Functional Implications of Phalloidin and Jasplakinolide Binding to Actin Filaments”. In: *Structure* 28.4 (Apr. 7, 2020), 437–449.e5. ISSN: 0969-2126. DOI: 10.1016/j.str.2020.01.014. URL: <https://www.sciencedirect.com/science/article/pii/S0969212620300411> (visited on 10/02/2024).
- [33] Julia Riedl et al. “Lifeact: a versatile marker to visualize F-actin”. In: *Nature Methods* 5.7 (July 2008), pp. 605–607. ISSN: 1548-7091, 1548-7105. DOI: 10.1038/nmeth.1220. URL: <https://www.nature.com/articles/nmeth.1220> (visited on 10/02/2024).
- [34] Naomi Courtemanche, Thomas D. Pollard, and Qian Chen. “Avoiding artefacts when counting polymerized actin in live cells with LifeAct fused to fluorescent proteins”. In: *Nature Cell Biology* 18.6 (June 2016). Publisher: Nature Publishing Group, pp. 676–683. ISSN: 1476-4679. DOI: 10.1038/ncb3351. URL: <https://www.nature.com/articles/ncb3351> (visited on 10/02/2024).
- [35] F M Boyce and N L Bucher. “Baculovirus-mediated gene transfer into mammalian cells.” In: *Proceedings of the National Academy of Sciences* 93.6 (Mar. 19, 1996). Publisher: Proceedings of the National Academy of Sciences, pp. 2348–2352. DOI: 10.1073/pnas.93.6.2348. URL: <https://www.pnas.org/doi/abs/10.1073/pnas.93.6.2348> (visited on 08/21/2024).
- [36] Scott Forth and Tarun M. Kapoor. “The mechanics of microtubule networks in cell division”. In: *Journal of Cell Biology* 216.6 (May 10, 2017), pp. 1525–1531. ISSN: 0021-9525. DOI: 10.1083/jcb.201612064. URL: <https://doi.org/10.1083/jcb.201612064> (visited on 10/20/2024).
- [37] Sandrine Etienne-Manneville. “Microtubules in Cell Migration”. In: *Annual Review of Cell and Developmental Biology* 29 (Volume 29, 2013 Oct. 6, 2013). Publisher: Annual Reviews, pp. 471–499. ISSN: 1081-0706, 1530-8995. DOI: 10.1146/annurev-cellbio-101011-155711. URL: <https://www.annualreviews.org/content/journals/10.1146/annurev-cellbio-101011-155711> (visited on 10/20/2024).
- [38] Florian Huber et al. “Cytoskeletal crosstalk: when three different personalities team up”. In: *Current Opinion in Cell Biology*. Cell architecture 32 (Feb. 1, 2015), pp. 39–47. ISSN: 0955-0674. DOI: 10.1016/j.ceb.2014.10.005. URL: <https://www.sciencedirect.com/science/article/pii/S0955067414001276> (visited on 10/14/2024).

- [39] M. Bishr Omary, Pierre A. Coulombe, and W. H. Irwin McLean. “Intermediate Filament Proteins and Their Associated Diseases”. In: *New England Journal of Medicine* 351.20 (Nov. 11, 2004). Publisher: Massachusetts Medical Society _eprint: <https://www.nejm.org/doi/pdf/10.1056/NEJMra040319>, pp. 2087–2100. ISSN: 0028-4793. DOI: 10.1056/NEJMra040319. URL: <https://www.nejm.org/doi/full/10.1056/NEJMra040319> (visited on 10/14/2024).
- [40] Kausalya Murthy and Patricia Wadsworth. “Myosin-II-Dependent Localization and Dynamics of F-Actin during Cytokinesis”. In: *Current Biology* 15.8 (Apr. 26, 2005). Publisher: Elsevier, pp. 724–731. ISSN: 0960-9822. DOI: 10.1016/j.cub.2005.02.055. URL: [https://www.cell.com/current-biology/abstract/S0960-9822\(05\)00228-9](https://www.cell.com/current-biology/abstract/S0960-9822(05)00228-9) (visited on 10/21/2024).
- [41] Ilan Spector et al. “Latrunculins: Novel Marine Toxins That Disrupt Microfilament Organization in Cultured Cells”. In: *Science* 219.4584 (Feb. 4, 1983). Publisher: American Association for the Advancement of Science, pp. 493–495. DOI: 10.1126/science.6681676. URL: <https://www.science.org/doi/abs/10.1126/science.6681676> (visited on 08/25/2024).
- [42] Y. Kashman, A. Groweiss, and U. Shmueli. “Latrunculin, a new 2-thiazolidinone macrolide from the marine sponge *latrunculia magnifica*”. In: *Tetrahedron Letters* 21.37 (Jan. 1, 1980), pp. 3629–3632. ISSN: 0040-4039. DOI: 10.1016/0040-4039(80)80255-3. URL: <https://www.sciencedirect.com/science/article/pii/0040403980802553> (visited on 08/25/2024).
- [43] Martine Coué et al. “Inhibition of actin polymerization by latrunculin A”. In: *FEBS Letters* 213.2 (Mar. 23, 1987), pp. 316–318. ISSN: 0014-5793. DOI: 10.1016/0014-5793(87)81513-2. URL: <https://www.sciencedirect.com/science/article/pii/0014579387815132> (visited on 04/04/2024).
- [44] Ikuko Fujiwara et al. “Latrunculin A Accelerates Actin Filament Depolymerization in Addition to Sequestering Actin Monomers”. In: *Current Biology* 28.19 (Oct. 8, 2018). Publisher: Elsevier, 3183–3192.e2. ISSN: 0960-9822. DOI: 10.1016/j.cub.2018.07.082. URL: [https://www.cell.com/current-biology/abstract/S0960-9822\(18\)31044-3](https://www.cell.com/current-biology/abstract/S0960-9822(18)31044-3) (visited on 08/25/2024).
- [45] Khalid A. El Sayed et al. “Latrunculin A and Its C-17-O-Carbamates Inhibit Prostate Tumor Cell Invasion and HIF-1 Activation in Breast Tumor Cells”. In: *Journal of Natural Products* 71.3 (Mar. 1, 2008). Publisher: American Chemical Society, pp. 396–402. ISSN: 0163-3864. DOI: 10.1021/np070587w. URL: <https://doi.org/10.1021/np070587w> (visited on 08/25/2024).
- [46] Jörg Renkawitz et al. “Adaptive force transmission in amoeboid cell migration”. In: *Nature Cell Biology* 11.12 (Dec. 2009). Publisher: Nature Publishing Group, pp. 1438–1443. ISSN: 1476-4679. DOI: 10.1038/ncb1992. URL: <https://www.nature.com/articles/ncb1992> (visited on 08/25/2024).

- [47] M. R. Bubb et al. “Jasplakinolide, a cytotoxic natural product, induces actin polymerization and competitively inhibits the binding of phalloidin to F-actin”. In: *The Journal of Biological Chemistry* 269.21 (May 27, 1994), pp. 14869–14871. ISSN: 0021-9258.
- [48] Takashi Iizuka et al. “Miuraenamides A and B, Novel Antimicrobial Cyclic Depsipeptides from a New Slightly Halophilic Myxobacterium: Taxonomy, Production, and Biological Properties”. In: *The Journal of Antibiotics* 59.7 (July 2006). Publisher: Nature Publishing Group, pp. 385–391. ISSN: 1881-1469. DOI: 10.1038/ja.2006.55. URL: <https://www.nature.com/articles/ja200655> (visited on 08/23/2024).
- [49] Lisa Karmann et al. “Total Syntheses and Biological Evaluation of Miuraenamides”. In: *Angewandte Chemie International Edition* 54.15 (2015). eprint: <https://onlinelibrary.wiley.com/doi/pdf/10.1002/anie.201411212>, pp. 4502–4507. ISSN: 1521-3773. DOI: 10.1002/anie.201411212. URL: <https://onlinelibrary.wiley.com/doi/abs/10.1002/anie.201411212> (visited on 10/25/2023).
- [50] Shuaijun Wang et al. “Actin stabilizing compounds show specific biological effects due to their binding mode”. In: *Scientific Reports* 9.1 (July 5, 2019). Number: 1 Publisher: Nature Publishing Group, p. 9731. ISSN: 2045-2322. DOI: 10.1038/s41598-019-46282-w. URL: <https://www.nature.com/articles/s41598-019-46282-w> (visited on 10/25/2023).
- [51] James E Bear and Jason M Haugh. “Directed migration of mesenchymal cells: where signaling and the cytoskeleton meet”. In: *Current Opinion in Cell Biology*. Cell adhesion and migration 30 (Oct. 1, 2014), pp. 74–82. ISSN: 0955-0674. DOI: 10.1016/j.ceb.2014.06.005. URL: <https://www.sciencedirect.com/science/article/pii/S0955067414000763> (visited on 10/22/2024).
- [52] R. J. Hawkins and R. Voituriez. “Mechanisms of Cell Motion in Confined Geometries”. In: *Mathematical Modelling of Natural Phenomena* 5.1 (2010). Number: 1 Publisher: EDP Sciences, pp. 84–105. ISSN: 0973-5348, 1760-6101. DOI: 10.1051/mmnp/20105104. URL: <https://www.mmnp-journal.org/articles/mmnp/abs/2010/01/mmnp20105p84/mmnp20105p84.html> (visited on 10/22/2024).
- [53] Tim Lämmermann et al. “Rapid leukocyte migration by integrin-independent flowing and squeezing”. In: *Nature* 453.7191 (May 2008). Publisher: Nature Publishing Group, pp. 51–55. ISSN: 1476-4687. DOI: 10.1038/nature06887. URL: <https://www.nature.com/articles/nature06887> (visited on 10/23/2024).
- [54] Doriane Vesperini et al. “Characterization of immune cell migration using microfabrication”. In: *Biophysical Reviews* 13.2 (Apr. 1, 2021), pp. 185–202. ISSN: 1867-2469. DOI: 10.1007/s12551-021-00787-9. URL: <https://doi.org/10.1007/s12551-021-00787-9> (visited on 05/15/2023).

- [55] Karin Legerstee and Adriaan B. Houtsmuller. “A Layered View on Focal Adhesions”. In: *Biology* 10.11 (Nov. 2021). Number: 11 Publisher: Multidisciplinary Digital Publishing Institute, p. 1189. ISSN: 2079-7737. DOI: 10.3390/biology10111189. URL: <https://www.mdpi.com/2079-7737/10/11/1189> (visited on 02/01/2023).
- [56] Bernhard Wehrle-Haller. “Structure and function of focal adhesions”. In: *Current Opinion in Cell Biology*. Cell structure and dynamics 24.1 (Feb. 1, 2012), pp. 116–124. ISSN: 0955-0674. DOI: 10.1016/j.ceb.2011.11.001. URL: <https://www.sciencedirect.com/science/article/pii/S0955067411001475> (visited on 08/25/2024).
- [57] Makoto Nagano et al. “Turnover of Focal Adhesions and Cancer Cell Migration”. In: *International Journal of Cell Biology* 2012 (Jan. 26, 2012). Publisher: Hindawi, e310616. ISSN: 1687-8876. DOI: 10.1155/2012/310616. URL: <https://www.hindawi.com/journals/ijcb/2012/310616/> (visited on 10/26/2022).
- [58] Ellen J. Ezratty, Michael A. Partridge, and Gregg G. Gundersen. “Microtubule-induced focal adhesion disassembly is mediated by dynamin and focal adhesion kinase”. In: *Nature Cell Biology* 7.6 (June 2005). Publisher: Nature Publishing Group, pp. 581–590. ISSN: 1476-4679. DOI: 10.1038/ncb1262. URL: <https://www.nature.com/articles/ncb1262> (visited on 09/29/2024).
- [59] Dong-Hwee Kim and Denis Wirtz. “Predicting how cells spread and migrate”. In: *Cell Adhesion & Migration* 7.3 (May 5, 2013). Publisher: Taylor & Francis _eprint, pp. 293–296. ISSN: 1933-6918. DOI: 10.4161/cam.24804. URL: <https://doi.org/10.4161/cam.24804> (visited on 10/26/2022).
- [60] U. S. Schwarz et al. “Calculation of Forces at Focal Adhesions from Elastic Substrate Data: The Effect of Localized Force and the Need for Regularization”. In: *Biophysical Journal* 83.3 (Sept. 1, 2002), pp. 1380–1394. ISSN: 0006-3495. DOI: 10.1016/S0006-3495(02)73909-X. URL: <https://www.sciencedirect.com/science/article/pii/S000634950273909X> (visited on 04/04/2024).
- [61] Nathalie Q. Balaban et al. “Force and focal adhesion assembly: a close relationship studied using elastic micropatterned substrates”. In: *Nature Cell Biology* 3.5 (May 2001). Number: 5 Publisher: Nature Publishing Group, pp. 466–472. ISSN: 1476-4679. DOI: 10.1038/35074532. URL: https://www.nature.com/articles/ncb0501_466 (visited on 02/27/2023).
- [62] Manuel Théry. “Micropatterning as a tool to decipher cell morphogenesis and functions”. In: *Journal of Cell Science* 123.24 (Dec. 15, 2010), pp. 4201–4213. ISSN: 0021-9533. DOI: 10.1242/jcs.075150. URL: <https://doi.org/10.1242/jcs.075150> (visited on 08/20/2024).

- [63] Elisa D’Arcangelo and Alison P McGuigan. “Micropatterning Strategies to Engineer Controlled Cell and Tissue Architecture in Vitro”. In: *BioTechniques* 58.1 (Jan. 1, 2015). Publisher: Taylor & Francis _eprint: <https://doi.org/10.2144/000114245>, pp. 13–23. ISSN: 0736-6205. DOI: 10.2144/000114245. URL: <https://doi.org/10.2144/000114245> (visited on 08/21/2024).
- [64] Amy Brock et al. “Geometric Determinants of Directional Cell Motility Revealed Using Microcontact Printing”. In: *Langmuir* 19.5 (Mar. 1, 2003). Publisher: American Chemical Society, pp. 1611–1617. ISSN: 0743-7463. DOI: 10.1021/1a026394k. URL: <https://doi.org/10.1021/1a026394k> (visited on 08/21/2024).
- [65] Ning Wang et al. “Micropatterning tractional forces in living cells”. In: *Cell Motility* 52.2 (2002). _eprint: <https://onlinelibrary.wiley.com/doi/pdf/10.1002/cm.10037>, pp. 97–106. ISSN: 1097-0169. DOI: 10.1002/cm.10037. URL: <https://onlinelibrary.wiley.com/doi/abs/10.1002/cm.10037> (visited on 08/21/2024).
- [66] Kristopher A. Kilian et al. “Geometric cues for directing the differentiation of mesenchymal stem cells”. In: *Proceedings of the National Academy of Sciences* 107.11 (Mar. 16, 2010). Publisher: Proceedings of the National Academy of Sciences, pp. 4872–4877. DOI: 10.1073/pnas.0903269107. URL: <https://www.pnas.org/doi/abs/10.1073/pnas.0903269107> (visited on 08/21/2024).
- [67] Ammar Azioune et al. “Chapter 8 - Protein Micropatterns: A Direct Printing Protocol Using Deep UVs”. In: *Methods in Cell Biology*. Ed. by Lynne Cassimeris and Phong Tran. Vol. 97. Microtubules: in vivo. Academic Press, Jan. 1, 2010, pp. 133–146. DOI: 10.1016/S0091-679X(10)97008-8. URL: <https://www.sciencedirect.com/science/article/pii/S0091679X10970088> (visited on 08/20/2024).
- [68] Pierre-Olivier Strale et al. “Multiprotein Printing by Light-Induced Molecular Adsorption”. In: *Advanced Materials (Deerfield Beach, Fla.)* 28.10 (Mar. 9, 2016), pp. 2024–2029. ISSN: 1521-4095. DOI: 10.1002/adma.201504154.
- [69] D. Axelrod et al. “Mobility measurement by analysis of fluorescence photobleaching recovery kinetics”. In: *Biophysical Journal* 16.9 (Sept. 1, 1976). Publisher: Elsevier, pp. 1055–1069. ISSN: 0006-3495. DOI: 10.1016/S0006-3495(76)85755-4. URL: [https://www.cell.com/biophysj/abstract/S0006-3495\(76\)85755-4](https://www.cell.com/biophysj/abstract/S0006-3495(76)85755-4) (visited on 08/21/2024).
- [70] Anne K. Kenworthy. “What’s past is prologue: FRAP keeps delivering 50 years later”. In: *Biophysical Journal* 122.18 (Sept. 19, 2023), pp. 3577–3586. ISSN: 0006-3495. DOI: 10.1016/j.bpj.2023.05.016. URL: <https://www.sciencedirect.com/science/article/pii/S0006349523003284> (visited on 08/21/2024).

- [71] K Jacobson and J Wojcieszyn. “The translational mobility of substances within the cytoplasmic matrix.” In: *Proceedings of the National Academy of Sciences* 81.21 (Nov. 1984). Publisher: Proceedings of the National Academy of Sciences, pp. 6747–6751. DOI: 10.1073/pnas.81.21.6747. URL: <https://www.pnas.org/doi/abs/10.1073/pnas.81.21.6747> (visited on 08/21/2024).
- [72] E D Salmon et al. “Spindle microtubule dynamics in sea urchin embryos: analysis using a fluorescein-labeled tubulin and measurements of fluorescence redistribution after laser photobleaching.” In: *Journal of Cell Biology* 99.6 (Dec. 1, 1984), pp. 2165–2174. ISSN: 0021-9525. DOI: 10.1083/jcb.99.6.2165. URL: <https://doi.org/10.1083/jcb.99.6.2165> (visited on 08/21/2024).
- [73] Marco Fritzsche et al. “Analysis of turnover dynamics of the submembranous actin cortex”. In: *Molecular Biology of the Cell* 24.6 (Mar. 15, 2013). Publisher: American Society for Cell Biology (mboc), pp. 757–767. ISSN: 1059-1524. DOI: 10.1091/mbc.e12-06-0485. URL: <https://www.molbiolcell.org/doi/full/10.1091/mbc.e12-06-0485> (visited on 08/21/2024).
- [74] Mark Skamrahl et al. “Simultaneous Quantification of the Interplay Between Molecular Turnover and Cell Mechanics by AFM–FRAP”. In: *Small* 15.40 (2019). _eprint: <https://onlinelibrary.wiley.com/doi/pdf/10.1002/smll.201902202>, p. 1902202. ISSN: 1613-6829. DOI: 10.1002/smll.201902202. URL: <https://onlinelibrary.wiley.com/doi/abs/10.1002/smll.201902202> (visited on 08/22/2024).
- [75] Marco Fritzsche and Guillaume Charras. “Dissecting protein reaction dynamics in living cells by fluorescence recovery after photobleaching”. In: *Nature Protocols* 10.5 (May 2015). Publisher: Nature Publishing Group, pp. 660–680. ISSN: 1750-2799. DOI: 10.1038/nprot.2015.042. URL: <https://www.nature.com/articles/nprot.2015.042> (visited on 08/21/2024).
- [76] Elisabeth E. Charrier et al. “A novel method to make viscoelastic polyacrylamide gels for cell culture and traction force microscopy”. In: *APL Bioengineering* 4.3 (July 2, 2020), p. 036104. ISSN: 2473-2877. DOI: 10.1063/5.0002750. URL: <https://doi.org/10.1063/5.0002750> (visited on 08/22/2024).
- [77] Sam C. P. Norris et al. “Photodegradable Polyacrylamide Gels for Dynamic Control of Cell Functions”. In: *ACS Applied Materials & Interfaces* 13.5 (Feb. 10, 2021). Publisher: American Chemical Society, pp. 5929–5944. ISSN: 1944-8244. DOI: 10.1021/acsami.0c19627. URL: <https://doi.org/10.1021/acsami.0c19627> (visited on 08/22/2024).
- [78] Rachel J. Jerrell and Aron Parekh. “Polyacrylamide Gels for Invadopodia and Traction Force Assays on Cancer Cells”. In: *JoVE (Journal of Visualized Experiments)* 95 (Jan. 4, 2015), e52343. ISSN: 1940-087X. DOI: 10.3791/52343. URL: <https://www.jove.com/t/52343/polyacrylamide-gels-for-invadopodia-traction-force-assays-on-cancer> (visited on 08/22/2024).

- [79] Cynthia Mann and Deborah Leckband. “Measuring Traction Forces in Long-Term Cell Cultures”. In: *Cellular and Molecular Bioengineering* 3.1 (Mar. 1, 2010), pp. 40–49. ISSN: 1865-5033. DOI: 10.1007/s12195-010-0108-0. URL: <https://doi.org/10.1007/s12195-010-0108-0> (visited on 08/22/2024).
- [80] Ajinkya Ghagre et al. “Pattern-Based Contractility Screening, a Reference-Free Alternative to Traction Force Microscopy Methodology”. In: *ACS Applied Materials & Interfaces* 13.17 (May 5, 2021). Publisher: American Chemical Society, pp. 19726–19735. ISSN: 1944-8244. DOI: 10.1021/acsami.1c02987. URL: <https://doi.org/10.1021/acsami.1c02987> (visited on 04/24/2023).
- [81] Keil J. Regehr et al. “Biological implications of polydimethylsiloxane-based microfluidic cell culture”. In: *Lab on a Chip* 9.15 (2009). Publisher: Royal Society of Chemistry, pp. 2132–2139. DOI: 10.1039/B903043C. URL: <https://pubs.rsc.org/en/content/articlelanding/2009/1c/b903043c> (visited on 08/22/2024).
- [82] Soumyabrata Banik et al. “The revolution of PDMS microfluidics in cellular biology”. In: *Critical Reviews in Biotechnology* 43.3 (Apr. 3, 2023). Publisher: Taylor & Francis _eprint: <https://doi.org/10.1080/07388551.2022.2034733>, pp. 465–483. ISSN: 0738-8551. DOI: 10.1080/07388551.2022.2034733. URL: <https://doi.org/10.1080/07388551.2022.2034733> (visited on 08/22/2024).
- [83] Jong Seob Choi, Yunxian Piao, and Tae Seok Seo. “Fabrication of a circular PDMS microchannel for constructing a three-dimensional endothelial cell layer”. In: *Bioprocess and Biosystems Engineering* 36.12 (Dec. 1, 2013), pp. 1871–1878. ISSN: 1615-7605. DOI: 10.1007/s00449-013-0961-z. URL: <https://doi.org/10.1007/s00449-013-0961-z> (visited on 08/22/2024).
- [84] Fu-Qiang Nie et al. “On-chip cell migration assay using microfluidic channels”. In: *Biomaterials* 28.27 (Sept. 1, 2007), pp. 4017–4022. ISSN: 0142-9612. DOI: 10.1016/j.biomaterials.2007.05.037. URL: <https://www.sciencedirect.com/science/article/pii/S0142961207004516> (visited on 08/22/2024).
- [85] Mohamad Anis Bin Ramlan, Ryota Toyohara, and Toshiro Ohashi. “Effect of width of microchannel device on behavior of collective cell migration”. In: *Journal of Biomechanical Science and Engineering* 18.4 (2023). Num Pages: 23-00536, pp. 23–00536. DOI: 10.1299/jbse.23-00536.
- [86] Mélina L. Heuzé et al. “Cell Migration in Confinement: A Micro-Channel-Based Assay”. In: *Cell Migration: Developmental Methods and Protocols*. Ed. by Claire M. Wells and Maddy Parsons. Totowa, NJ: Humana Press, 2011, pp. 415–434. ISBN: 978-1-61779-207-6. DOI: 10.1007/978-1-61779-207-6_28. URL: https://doi.org/10.1007/978-1-61779-207-6_28 (visited on 08/21/2024).

- [87] Malcolm S. Steinberg, Peter B. Armstrong, and R. E. Granger. “On the recovery of adhesiveness by trypsin-dissociated cells”. In: *The Journal of Membrane Biology* 13.1 (Dec. 1, 1973), pp. 97–128. ISSN: 1432-1424. DOI: 10.1007/BF01868223. URL: <https://doi.org/10.1007/BF01868223> (visited on 08/23/2024).
- [88] Jens Friedrichs et al. “A practical guide to quantify cell adhesion using single-cell force spectroscopy”. In: *Methods. Nanoimaging Methods for Biomedicine* 60.2 (Apr. 1, 2013), pp. 169–178. ISSN: 1046-2023. DOI: 10.1016/j.ymeth.2013.01.006. URL: <https://www.sciencedirect.com/science/article/pii/S1046202313000170> (visited on 08/23/2024).
- [89] André Meister et al. “FluidFM: Combining Atomic Force Microscopy and Nanofluidics in a Universal Liquid Delivery System for Single Cell Applications and Beyond”. In: *Nano Letters* 9.6 (June 10, 2009). Publisher: American Chemical Society, pp. 2501–2507. ISSN: 1530-6984. DOI: 10.1021/nl901384x. URL: <https://doi.org/10.1021/nl901384x> (visited on 08/23/2024).
- [90] Caroline Hayot et al. “Characterization of the activities of actin-affecting drugs on tumor cell migration”. In: *Toxicology and Applied Pharmacology* 211.1 (Feb. 15, 2006), pp. 30–40. ISSN: 0041-008X. DOI: 10.1016/j.taap.2005.06.006. URL: <https://www.sciencedirect.com/science/article/pii/S0041008X05003625> (visited on 04/04/2024).
- [91] Florian A. Gegenfurtner et al. “Transcriptional effects of actin-binding compounds: the cytoplasm sets the tone”. In: *Cellular and Molecular Life Sciences* 75.24 (Dec. 1, 2018), pp. 4539–4555. ISSN: 1420-9071. DOI: 10.1007/s00018-018-2919-4. URL: <https://doi.org/10.1007/s00018-018-2919-4> (visited on 07/25/2024).
- [92] Ying Liu and Makoto Ojika. “Genomic Analysis of the Rare Slightly Halophilic Myxobacterium “Paraliomyxa miuraensis” SMH-27-4, the Producer of the Antibiotic Miuraenamide A”. In: *Microorganisms* 11.2 (Feb. 2023). Number: 2 Publisher: Multidisciplinary Digital Publishing Institute, p. 371. ISSN: 2076-2607. DOI: 10.3390/microorganisms11020371. URL: <https://www.mdpi.com/2076-2607/11/2/371> (visited on 10/25/2023).
- [93] **Caroline A. Evans et al. “Metastasising Fibroblasts Show an HDAC6-Dependent Increase in Migration Speed and Loss of Directionality Linked to Major Changes in the Vimentin Interactome”. In: *International Journal of Molecular Sciences* 23.4 (Jan. 2022). Number: 4 Publisher: Multidisciplinary Digital Publishing Institute, p. 1961. ISSN: 1422-0067. DOI: 10.3390/ijms23041961. URL: <https://www.mdpi.com/1422-0067/23/4/1961> (visited on 07/05/2024).**

- [94] **Alexandra A.M. Fischer et al.** “Engineering Material Properties of Transcription Factor Condensates to Control Gene Expression in Mammalian Cells and Mice”. In: *Small* n/a (n/a), p. 2311834. ISSN: 1613-6829. DOI: 10.1002/sml1.202311834. URL: <https://onlinelibrary.wiley.com/doi/abs/10.1002/sml1.202311834> (visited on 08/06/2024).
- [95] Macfarlane Burnet. “The Thymus Gland”. In: *Scientific American* 207.5 (1962). Publisher: Scientific American, a division of Nature America, Inc., pp. 50–57. ISSN: 0036-8733. URL: <https://www.jstor.org/stable/24936350> (visited on 10/09/2024).
- [96] J. F. a. P. Miller. “The discovery of thymus function and of thymus-derived lymphocytes”. In: *Immunological Reviews* 185.1 (2002). _eprint: <https://onlinelibrary.wiley.com/doi/pdf/10.1034/j.1600-065X.2002.18502.x>, pp. 7–14. ISSN: 1600-065X. DOI: 10.1034/j.1600-065X.2002.18502.x. URL: <https://onlinelibrary.wiley.com/doi/abs/10.1034/j.1600-065X.2002.18502.x> (visited on 10/09/2024).
- [97] Gerard Wagemaker et al. “Interleukin-3”. In: *Biotherapy* 2.4 (Oct. 1, 1990), pp. 337–345. ISSN: 1573-8280. DOI: 10.1007/BF02170083. URL: <https://doi.org/10.1007/BF02170083> (visited on 10/09/2024).

Note: Entries in the bibliography that are written in **bold characters** indicate that I am (co-)author of this article.

Appendix A

Protocols

A.1 Cell culture

You need: (if not stated otherwise work under the cell culture bench, all cells were kept in the incubator at 37°C and 5% CO₂.)

- DMEM F12 Medium + 10% FBS, 1% Glutamax, and 1% Penicillin/Streptomycin.
- RPMI Medium + 10% FBS, 1% Glutamax, and 1% Penicillin/Streptomycin.
- PBS.
- Cell culture flask.
- Pipettes.
- Trypsin.
- Centrifuge.

A.1.1 Cell passaging

- RPE-1 and MEF cells.
 1. Use DMEM F12 Medium.
 2. Remove old medium and rinse with PBS.
 3. Add 1 mL of trypsin and put in incubator for three minutes.
 4. Gently shake the cell flask to detach cells from the flask.
 5. Add another milliliter of cell medium to stop the effects of trypsin and centrifuge the mixture at 1300 rpm for three minutes.

6. Remove the liquid and re-suspend the cells at the desired concentration.
 7. Keep 20% confluency of cells and discard the unused ones.
 8. Repeat two to three times a week.
- HL60 cells.
 1. Use RPMI Medium.
 2. Discard half of the medium.
 3. Transfer the other half into a new cell flask and refill it.
 4. Repeat one to two times a week.
 - CD4+ cells.
 1. The cells I worked with did not divide any further, so here I only describe how to take care of them before they could be used in an experiment.
 2. Use RPMI Medium.
 3. Centrifuge cells at 1000 rpm for five minutes.
 4. Discard liquid and re-suspend cells in medium.
 5. Repeat three times and re-suspend cells at desired concentration.

A.1.2 Cell seeding

- RPE-1, MEFs and CD4+ cells.
 1. Plasma activate glass bottom dish or glass cover slip for three minutes.
 2. For RPE-1 and MEF cells: cover activated side with fibronectin (concentration $25 \mu\text{g mL}^{-1}$).
 3. For CD4+ cells: cover the activated side with VCAM-1 (concentration $5 \mu\text{g mL}^{-1}$).
 4. Incubate at room temperature for one hour (seal with parafilm to avoid evaporation).
 5. For RPE-1 and MEF cells: seed around 100 000 cells per dish.
 6. For CD4+ cells seed around 1 Million cells per dish.
- HL60 cells and neutrophils are non adherent cells. To seed them one prepares PDMS microstructures. The protocol for these is given at A.3.

A.1.3 Differentiation of HL60 cells

To differentiate HL60 cells into neutrophils, one adds 1.3% of DMSO to the cell medium and incubates them for two days. As soon as the cells start to spread, they are differentiated into neutrophils.

A.2 Fixation and staining of cells

Starting point: Cells seeded and fully adhered to a glass cover slip, glass bottom dish or similar.

You need:

- 4% PFA.
- Triton X100 (0.1% solution).
- PBS.
- BSA (3% solution).
- Phalloidin-iFluor 555 or phalloidin polyclonal antibodies.
- Fluoromount G+DAPI.

A.2.1 PFA fixation

(if not stated otherwise operate under the chemical hood.)

1. Remove cell medium (aspirate liquid always at the corner of the sample to not accidentally remove cells from the sample).
2. Rinse sample three times with PBS.
3. Completely cover cells with 4% PFA for ten minutes (in a 6-well plate around 700 μ L of PFA are sufficient per well).
4. Remove PFA and wash samples three times with PBS for five minutes each time.
5. Fixed cells can be stored at 4°C and protected from light in PBS before further processing.

A.2.2 Phalloidin staining

(if not stated otherwise operate under the chemical hood.)

1. Dissolve cell membrane using Triton X100 for ten minutes.
2. Wash sample three times with PBS.
3. One hour of incubation with BSA to block unspecific bindings.
4. One hour of a 1:1000 phalloidin in BSA solution (cover the samples with aluminum foil to avoid bleaching).

5. Wash cells three times with PBS.
6. Mount samples with Flouromount G+DAPI.
7. Store samples at 4 °C and protected from light.

A.2.3 Direct immunostaining (paxillin)

(if not stated otherwise operate under the chemical hood.)

1. Dissolve cell membrane using Triton X100 for ten minutes.
2. Wash sample three times with PBS.
3. One hour of incubation with BSA to block unspecific bindings.
4. One hour of a 1:1000 paxillin antibodies in BSA solution (cover the samples with aluminum foil to avoid bleaching).
5. Wash cells three times with PBS.
6. Mount samples with Flouromount G+DAPI.
7. Store samples at 4 °C and protected from light.

A.3 PDMS microfabrication and cell migration

(If not stated otherwise operate at room temperature.)

You need:

- PDMS compound A and B.
- Fine scale.
- Speedmixer.
- Vacuum chamber.
- Oven.
- Glass bottom dish.
- Epoxy mold.
- pll-g-PEG or fibronectin.
- PBS.

- Cell culture medium.
- Hoechst (final concentration $250 \text{ ng } \mu\text{L}^{-1}$).

Protocol:

1. Mix PDMS compounds A and B in a 10:1 ratio in a plastic cup.
2. Punch a hole in the lid of the plastic cup (otherwise the cup might burst in the vacuum speed mixer).
3. Mix PDMS in speed mixer (program 5 = 1300rpm at 0.01 bar for 5 minutes).
4. Pour PDMS in epoxy mold and remove air bubbles by placing the mold in a vacuum chamber.
5. Cure the PDMS inside an oven at 80°C for at least 90 minutes.
6. Use a scalpel and cut the PDMS from the mold (always cut away from you and never put a finger in the way you are cutting).
7. Punch four inlet holes in the PDMS chip and remove dust by using a scotch tape.
8. Plasma activate the PDMS chip and the glass bottom dish for three minutes.
9. Attach the PDMS chip into the glass bottom dish and fill the chip either with pll-g-PEG or fibronectin (make sure to only use one of the holes, so you do not trap air inside the channels).
10. Incubate for one hour and rinse with PBS three times.
11. Completely submerge in the exact same cell culture medium you use for the cells at least for one hour before adding cells (PDMS is porous, so the PDMS needs to saturate before adding cells).
12. At the same time add Hoechst to the cells and incubate for 30 minutes in incubator before changing the medium and activate the microscopes temperature and CO₂ control unit.
13. Seed around 100 000 cells in one of the inlets.
14. Place dish under the microscope and set time laps experiments (adjust the intervals of pictures according to the Nyquist criterion).

A.4 PAA gel

You need: (if not stated otherwise, operate at room temperature and under the chemical hood.)

- Ethanol (70%).
- 3-ATPS (3-acryl-propyl-trimethoxysilane).
- Glass cover slips (25 mm).
- Shaker.
- Acrylamide.
- Bis-acrylamide.
- PBS.
- APS (ammoniumpersulfoxide).
- TEMED.
- Pure water.
- Sonicator.

A.4.1 Acryl-silanization of cover slips

1. Immerse cover slips in ethanol and sonicate for 10 minutes.
2. Immerse in fresh ethanol and dry it on a paper towel.
3. Incubate cover slips in a 0.5% solution of 3-APTS in ethanol for one hour on a shaker (Cover with parafilm to avoid evaporation).
4. Immerse cover slips in fresh ethanol and let it dry on paper towel. Silanized cover slips can be stored for several months.

A.4.2 Poly-acrylamide hydrogel

1. Mix 200 μL of 20% acrylamide, 96 μL 1% bis-acrylamide and 198.5 μL PBS to obtain a 12 kPa gel. The stock solutions should not be older than 4 weeks.
2. Vortex the mix for 30 sec and degas with Ar for 2 min to remove oxygen. Add APS (10% in MilliQ, 1:100 v/v, always use fresh solution) and TEMED (1:1000 v/v) to solution. Resuspend with pipette after each addition.

3. To improve homogeneity, it is recommended to add the APS first and mix and then add the TEMED.
4. Quickly pipette 12 μL droplets of gel solution onto acryl-silanized coverslips and cover with the top coverslips. To transfer micropatterns, the top coverslip should be patterned beforehand (as describe in A.5).
5. Allow the gel to polymerize at room temperature for 10 min.
6. Put the gels in PBS for 1 h or longer to make it swell, and then remove the top coverslip to obtain a hydrogel film attached to an acryl-silanized coverslip (push the coverslip in parallel to the glass surface, avoid damaging hydrogel).

A.5 Micropatterning

You need:

- Glass cover slips (diameter 25 mm) or glass bottom dish.
- pll-g-PEG (poly-L-lysine grafted Poly ethylene Glycol) (concentration: 1 mM).
- Pure water.
- Parafilm.
- Fibronectin ($25 \mu\text{g mL}^{-1}$).

A.5.1 PEG coating

(If not stated otherwise operate at room temperature.)

Glass cover slip

1. Rinse glass cover slips with ethanol (70%) and dry them on a paper towel.
2. Plasma activate glass cover slips in a plasma oven for three minutes.
3. At the same time, prepare a plastic dish and line it with parafilm.
4. Place a 50 μL droplet of the pll-g-PEG solution on the parafilm for each glass cover slip.
5. After activation place the activated side of the glass cover slip on the PEG droplet.
6. Place a wet tissue inside the plastic dish and seal it with parafilm to avoid evaporation.
7. Incubate for one hour at room temperature before patterning.

Glass bottom dish

1. Plasma activate glass bottom dish in a plasma oven for three minutes.
2. Optional: To reduce the amount of PEG needed, put a PDMS stencil in the plasma oven together with the glass bottom dish and attach it to the glass bottom after activation.
3. Place a 100 μ L droplet of the pll-g-PEG solution inside of the glass bottom dish. If you added a PDMS stencil, it is sufficient to fill the wells of the stencil.
4. Close the lid of the glass bottom dish, to avoid evaporation.
5. Incubate for one hour at room temperature before patterning.

A.5.2 Deep UV

(If not stated otherwise operate at room temperature.)

1. Use the PEG coated glass cover slips.
2. rinse them with pure water.
3. Activate the quartz photomask in a deep UV-cleaner for five minutes.
4. place a 4.5 μ L droplet of pure water at every sport where you want to place a glass cover slip on the chrome side of the photomask (the chrome side will be tainted in a faint gold).
5. Place the glass cover slips on the water droplets with the PEG coated side facing the photomask.
6. Use two plastic pipette tips to remove air bubbles underneath the glass cover slip by gently pressing against the glass.
7. Place the photomask with the glass cover slips inside the deep UV cleaner with the quartz side facing the UV lamp (the quartz side is silver) and irradiate it for six minutes.
8. Lift the glass cover slips from the photomask by pouring pure water on top and wait for the glass cover slips to float.
9. Place 50 μ L droplets of fibronectin for each glass cover slip in a parafilm lined plastic dish.

10. Place the patterned glass cover slips with the patterned area facing the fibronectin on the droplets.
11. Place a wet tissue inside the plastic dish and seal it with parafilm to avoid evaporation.
12. Incubate for one hour and rinse three times with PBS before seeding cells.

A.5.3 PRIMO

(If not stated otherwise operate at room temperature.)

1. Use the PEG coated glass bottom dish (or the PEG coated glass cover slips).
2. Calibrate the PRIMO with a glass bottom dish marked with highlighter.
3. Add the photoinitiator PLPP to the glass bottom dish.
4. Load the wanted .tif mask for the patterns.
5. Set exposure time (an exposure time of around 30 seconds per pattern is sufficient).
6. Rinse the dish three times with PBS (this step is important, as PLPP is toxic to cells).
7. Add fibronectin and cover all patterned area with it.
8. Incubate for one hour before rinsing with PBS and seeding cells.

A.6 Fluorescence recovery after photobleaching

You need:

- BacMam solution (Cell Light).
- Cell culture medium (depending on cell type).
- Cell Tak (for non adherent cells).
- Fibronectin coated glass bottom dish (concentration $25 \mu\text{g mL}^{-1}$).

A.6.1 BacMam treatment

1. Seed 100 000 cells in a glass bottom dish (for RPE-1 cells: wait at least 6 hours for them to fully adhere).
2. Add BacMam solution according to the following formula:

$$V_{\text{BacMam}} = \frac{\text{Nb. of cells} \cdot \text{ppc}}{10^8} \text{mL}$$

where “*ppc*” means “particles per cell” and is a cell type dependent value. For CD4+ and RPE-1 cells this value is 30, resulting in a total amount of BacMam solution of $V_{\text{BacMam}} = 30\mu\text{L}$.

3. Put cells in incubator (37°C, 5% CO₂) for 2 days before using them for FRAP experiments.

A.6.2 FRAP measurement

1. Activate temperature and CO₂ control unit and set it to 37°C and 5% CO₂. Wait at least 30 minutes for the system so settle.
2. Seed BacMam treated cells in a fibronectin coated glass bottom dish (for RPE-1 cells) or a Cell Tak coated glass bottom dish (for CD4+ cells).
3. Place glass bottom dish under microscope and start FRAP measurements.
4. Measure intensities at three different ROIs:
 - (i) The ROI where the bleaching happens.
 - (ii) A spot inside the cell to measure the overall bleaching.
 - (iii) A spot outside the cell to measure the background signal.